Improved Convergence Rate of Multi-Group Scattering Moment Tallies for Monte Carlo Neutron Transport Codes

by

Adam Nelson

A dissertation submitted in partial fulfillment
of the requirements for the degree of
Doctor of Philosophy
(Nuclear Engineering and Radiological Sciences)
in the University of Michigan
2014

Doctoral Committee:

Professor William R. Martin, Chair
Associate Professor Yves F. Atchade
Adjunct Assistant Professor Benjamin S. Collins
Professor Thomas J. Downar

NDPP

ACKNOWLEDGMENTS

Finally, after 22 years, I am done with school.

I said those words in mid-2009 as I completed my Master's degree. That lasted until that very same fall when my work decided to institute a fellowship program for current employees to obtain their graduate degrees full-time. Due to an apparent short term memory loss issue, I was the first to sign up.

Before I ever left my work for my new life as a student, I was fortunate to be the beneficiary of a world-class education while working for both Dr. Don Dei and Dr. Bruce Bingman. I am forever in debt to these two gentlemen, their unmatchable strategic thinking, ingenuity, experience, and ability to seemingly know everything about everything created a highly educational environment for me to quickly mature in to an experienced engineer.

Soon after achieving candidacy status at Michigan, I began helping out with both the MPACT and the OpenMC development teams. Working with these groups not only provided a solid foundation to exercise classroom knowledge in a more production environment, but provided for long-lasting friendships with some of the future leaders in our industry, of which I am very grateful.

I would also like to thank my committee members, Prof. Yves Atchade, Prof. Benjamin Collins, and Prof. Thomas J. Downar for their mentoring and generous donation of time and experience to my own research. Of course, it goes without saying that my sincerest gratitude goes to my advisor, Professor William Martin, whose wisdom, patience, and kindness provided me with the environment I needed to complete this work.

I am ever grateful to my parents, Don and Laura, for their constant support and encouragement from day one. I realize this more than ever now that I have my own children, Oren and Rhett. I only hope I can provide them the same environment I had while growing up.

Oren and Rhett themselves deserve a special thank you as well. Both of these little guys can put a smile on my face faster than any single thing in this world.

Last, but not least, I owe everything in the world to the patience, strength, and constant reassurance of my wife and best friend, Jordan. Thank you Jordan, I love you.

With that, I can again say: *finally, after 27 years I am done with school.*

TABLE OF CONTENTS

Chapter

LIST OF FIGURES

LIST OF TABLES

LIST OF APPENDICES

LIST OF ACRONYMS

ACE A Compact ENDF

CASL Consortium for Advanced Simulation of Light Water Reactors

CDF Cumulative Distribution Function

CI Confidence Interval

CM Center-of-Mass

ENDF Evaluated Nuclear Data File

FGK Free-Gas Kernel

LAB Laboratory

MC Monte Carlo

MGXS Multi-Group Cross Sections

MOC Method of Characteristics

NDPP Nuclear Data Pre-Processor

LANL Los Alamos National Laboratory

LINAC Linear Accelerator

LWR Light Water Reactor

PDF Probability Distribution Function

RPI Rensselaer Polytechnic Institute

ABSTRACT

Multi-group scattering moment matrices are critical to the solution of the multi-group form of the neutron transport equation, as they are responsible for describing the change in direction and energy of neutrons. These matrices, however, are difficult to correctly calculate from the measured nuclear data with both deterministic and stochastic methods. Calculating these parameters when using deterministic methods requires a set of assumptions which do not hold true in all conditions. These quantities can be calculated accurately with stochastic methods, however doing so is computationally expensive due to the poor efficiency of tallying scattering moment matrices.

This work presents an improved method of obtaining multi-group scattering moment matrices from a Monte Carlo neutron transport code. This improved method of tallying the scattering moment matrices is based on recognizing that all of the outgoing particle information is known a priori and can be taken advantage of to increase the tallying efficiency (therefore reducing the uncertainty) of the stochastically integrated tallies. In this scheme, the complete outgoing probability distribution is tallied, supplying every one of the scattering moment matrices elements with its share of data. In addition to reducing the uncertainty, this method allows for the use of a track-length estimation process potentially offering even further improvement to the tallying efficiency.

Unfortunately, to produce the needed distributions, the probability functions themselves must undergo an integration over the outgoing energy and scattering angle dimensions. This integration is too costly to perform during the Monte Carlo simulation itself and therefore must be performed in advance by way of a pre-processing code.

The new method increases the information obtained from tally events and therefore has a significantly higher efficiency than the currently used techniques. The improved method has been implemented in a code system containing a new pre-processor code, NDPP, and a Monte Carlo neutron transport code, OpenMC. This method is then tested in a pin cell problem and a larger problem designed to accentuate the importance of scattering moment matrices. These tests show that accuracy was retained while the figure-of-merit for generating scattering moment matrices and fission energy spectra was significantly improved.

CHAPTER 1

Introduction

The degree of optimization of a nuclear reactor system is highly-dependent upon the accuracy and precision of the calculation methodologies employed and the ability of the designers to efficiently explore the design envelope. This statement holds true whether the design effort be geared towards a refueling of an existing design or a brand new effort. Unfortunately, these two factors are typically inversely related: if one wants to use more accurate methodologies, more time is required and less design iterations can be explored. In the specific discipline of this thesis, reactor core physics, these competing effects are balanced by utilizing relatively high-fidelity methods to generate input parameters and/or corrections for lower-fidelity methods. The higher-fidelity methods are used for a few select cases with small dimensionality (e.g., a single fuel rod) whereas the low-fidelity methods are utilized for a large number of cases, each with a larger dimensionality (e.g., the entire core through life and during various planned and unplanned evolutions which must be analyzed). There is a desire, motivated by both safety and economic concerns, to increase the accuracy of relatively high-fidelity methods to propagate the accuracy gains to the lower order methods. In this way the overall accuracy of the final design can be increased while still allowing for a large number of design iterations to be performed.

The goal of this dissertation is to further enable this ideal by reducing the cost of applying high-fidelity methods to provide information towards the lower-fidelity methods. This will be achieved by using Monte Carlo neutron transport to generate multi-group cross section libraries to be used by deterministic neutron transport codes. This work will specifically focus on reducing the time needed to determine the exiting speed and angle of a neutron following a collision event with a nuclide.

The main quantity of interest (of which others are derived) for performing neutronic analysis of a reactor is the neutron flux, a measure of the neutron track-length per unit volume per unit time, which can be readily used to determine the fission power generation rate among other important quantities. The flux is determined by way of solving the Boltzmann transport equation [1], which requires knowledge of nuclide properties called cross sections. The solution to the transport equation is a function dependent upon seven dimensions: the neutron's location, direction-of-motion, kinetic energy, and the time. The transport equation can currently be solved by either Monte Carlo (MC) methods or via numerical (deterministic) techniques.

To solve the equation using deterministic methods, the dimensionality of the problem is first reduced via a combination of discretization techniques and other approximations. The discretization techniques are applied to the space, energy, and angle dimensions and lead to both truncation errors and/or large computational costs. The approximations include assuming dimensions away such as the time in steady-state analyses and representing the neutron direction of motion with a functional expansion, as well as any homogenization that may be required by the discretization methods. The flexibility of deterministic transport offers reactor designers with a methodology with knobs to tweak which can allow for quickly running but low-fidelity analysis models to moderate-fidelity models which require a significant amount of computation power.

Before deterministic methods can be used, a library of parameters called Multi-Group Cross Sections (MGXS) must be generated. These MGXS libraries (discussed in Chapter 2) are the result of lumping the behavior of neutrons in a given reactor system in groups characterized by the neutron's energy. As will be seen, the determination of multi-group cross sections require knowledge of the neutron distribution before the cross sections can be accurately determined. Since the neutron distribution is not known when one is trying to find the neutron distribution, then the distribution will have to be estimated using a myriad of approximations. This estimation process requires the guiding hand of an expert, weeks of time, and an inevitable comparison of the resultant deterministic transport calculations with both experimental results and Monte Carlo calculations.

MC neutron transport methods [2], on the other hand, have the capability to solve the transport equation without making approximations to the dimensions of space, direction, energy, and if desired, even time. The input to MC codes include the geometric and material information of the problem to model, as well as continuous-energy neutron reaction data. This reaction data is based on a large library of measurements performed at facilities such as the Rensselaer Polytechnic Institute (RPI) Linear Accelerator (LINAC) in Troy, New York. Since this data is measured, it of course contains measurement uncertainties. MC uses this data when simulating the life of a neutron in the modeled problem and thus can only provide an answer as accurate as the measured reaction data.

Of course, MC methods do not come without their own penalty, or their would be no reason for deterministic transport. MC integration replaces the truncation error of deterministic transport with an error of its own: stochastic uncertainty. This uncertainty comes about because MC methods sample the behavior of a finite population of neutrons according to the probability distribution functions described by the continuous-energy reaction data. MC methods produce stochastic uncertainties for a certain recorded quantity (called a tally) which reduce proportional to the square root of the number of neutron histories simulated. That is to say, if one wants to reduce an uncertainty by a factor of 10, then a factor of 100 more histories must be simulated. Since reactors are quite large systems and a high degree of precision is needed to model their complex behavior, this has required a very large number of histories (on the order of hundreds of billions) which has only recently become somewhat feasible [3].

Recent work [4–11] has investigated the use of MC to replace many of the approximations necessary when creating a MGXS library. The ultimate end goal is to have a hybrid system where Monte Carlo is used on a local basis to calculate multi-group cross sections and the deterministic transport solver is used to come up with a core-wide solution to the neutron distribution problem. As Chapter 3 will discuss, certain types of multi-group cross section data require significantly more computational time to produce than the others if they were to be calculated with a Monte Carlo solver. These are the scattering moment matrices which describe the probabilities of neutrons emerging from a scattering collision in a certain energy group and with a particular direction.

1.1 Thesis Objective

The goal of this work is to significantly reduce the stochastic uncertainty of a multi-group cross section library generated by the Monte Carlo method of neutron transport for a fixed number of simulated histories. Since a specific class of library parameters, the scattering moment matrices, are the most limiting in terms of tallying efficiency, the majority of work will be aimed at increasing their tallying efficiency to match the other required parameters.

1.2 Thesis Outline

- Chapter 2 derives the multi-group form of the neutron transport equation with the double-differential scattering kernel expanded with Legendre moments. This derivation includes a discussion of the approximations inherent within the method and presents an overview of how measured nuclear data is translated to the multi-group form for use by a deterministic transport solver. In discussing this library generation process, the need for a more accurate Monte Carlo-based means of generating such libraries will be identified.

- Chapter 3 first discusses the information necessary to understand using Monte Carlo neutron transport as a means to generate multi-group cross section libraries. This includes discussing the measure of tally uncertainties, the types of tallies available, and how the specific quantities of interest in library generation would be tallied with a Monte Carlo code. Finally, this chapter puts the Monte Carlo-based scheme to test by using it to generate libraries for two problems of interest. During the course of this evaluation it is identified that the scattering moment matrices are generally the least efficient of tally types needed and identifies a potential means for significantly increasing the efficiency; this method is referred to as the Improved Method. Finally, this improved method is investigated enough to understand that the method will not be successful without pre-processing the continuous-energy data into a more easily worked with form.

- Chapter 4 defines the mathematical formulations used to represent neutron reactions in a continuous-energy data library. This discussion is necessary in order to facilitate understanding of the computations performed in Chapter 5.

- Chapter 5 describes, in detail, the operations performed by the pre-processor identified in Chapter 3. This pre-processor is called NDPP.

- Chapter 6 tests the results of NDPP for correctness by way of performing spot-checks on the output data and by using the data with the improved method of tallying to ensure that the entire method reproduces the answer to within sufficient accuracy. Next, the improved method with NDPP data will be used to study the actual impact on tallying efficiency in order to understand if the method is actually useful.

- Chapter 7 summarizes the implications of the improved method of tallying and identifies future work which may be performed to further increase the benefit.

CHAPTER 2

Angular Expansion and Multi-Group Approximations

The continuous-energy steady-state neutron transport equation, Eq. (2.1), describes the balance of neutrons through the six dimensions of space ($\vec{r}$), the neutron's energy (E), and the neutron's direction of motion ($\vec{\Omega}$) [1,2]. This equation is used to solve for the angular flux distribution, $\psi\left(E,\vec{r},\vec{\Omega}\right)$.

$$\begin{aligned}\vec{\Omega}\cdot\nabla\psi\left(E,\vec{r},\vec{\Omega}\right)&+\Sigma_t\left(E,\vec{r}\right)\psi\left(E,\vec{r},\vec{\Omega}\right)\\ &=\int_0^\infty\int_{4\pi}\Sigma_s\left(E'\rightarrow E,\vec{r},\vec{\Omega}'\cdot\vec{\Omega}\right)\psi\left(E',\vec{r},\vec{\Omega}'\right)d\Omega' dE'\\ &\quad+\frac{1}{k_{eff}}\left[\int_0^\infty\int_{4\pi}\frac{1}{4\pi}\nu\Sigma_f\left(E'\rightarrow E,\vec{r}\right)\psi\left(E',\vec{r},\vec{\Omega}'\right)d\Omega' dE'\right]\end{aligned}\tag{2.1}$$

The angular flux is the neutron angular density distribution multiplied by the speed of the neutron. With this definition, the quantity $\psi\left(E,\vec{r},\vec{\Omega}\right)dVd\Omega dE$ represents the total distance traveled by neutrons per unit time in the infinitesimally small volume dV centered at the location $\vec{r}$ with energies dE about E and directions of motion within the infinitesimally small solid angle $d\Omega$ around the direction of motion $\vec{\Omega}$. Other quantities in Eq. (2.1) are:

- The total probability of interaction per unit length traveled at a given energy and location ($\Sigma_t\left(E,\vec{r}\right)$)
- The probability per unit length that a neutron will undergo a scattering collision at a given energy, direction and location and be transferred to energy E and direction $\vec{\Omega}$ ($\Sigma_s\left(E'\rightarrow E,\vec{r},\vec{\Omega}'\cdot\vec{\Omega}\right)$)

- The probability per unit length that neutrons will be produced by fission at a given energy producing neutrons according to a distribution in outgoing energies E $(\nu\Sigma_f(E' \rightarrow E, \vec{r}))$

The final term to define in this equation is k_{eff}; this quantity represents the neutron multiplication factor and is essentially the quantity which balances the neutron sources with the losses via leakage and absorption. k_{eff} is referred to as either the neutron multiplication factor or the eigenvalue of the system. The name “neutron multiplication factor” provides an indication of its physical meaning: if a random neutron is injected into the system, the value of k_{eff} represents, on average, how many new neutrons will be produced due to fission of that beginning source neutron.

These six dimensions result in an equation which is difficult to solve numerically without making further approximations. This chapter will focus on two approximations which are typically made to the continuous-energy steady-state neutron transport equation in order to reduce this dimensionality. Doing so allows the transport equation to be solved for problems of interest in a sufficiently timely and accurate manor. These two approximations act on the angular and energy dimensions, respectively. The following sections present these beginning with the angular approximation, with a final discussion on a few more approximations commonly made to the multi-group form of the neutron transport equation.

2.1 Angular Expansion of the Scattering Source

A common technique used to reduce the dimensionality of an expression is to perform a functional expansion of the equation over certain dimensions. The direction of motion, $\vec{\Omega}$, can be represented in such a way.

To begin, consider the expansion of the angular flux with spherical harmonics functions, Y_ℓ^m, as the basis functions of choice. In the steps detailed below, the Y_ℓ^m functions are as discussed in References [12, 13].

By the definition of orthogonal functions and spherical harmonics in particular, these flux harmonics can be used to regenerate the original function, supposing enough orders are applied. This expansion is shown in Eq. (2.2). The resultant coefficients of the expansion are shown in Eq. (2.3).

$$\psi\left(E, \vec{r}, \vec{\Omega}\right) = \sum_{\ell=0}^{\infty} \frac{2\ell+1}{4\pi} \sum_{m=-\ell}^{\ell} \psi_\ell^m(E, \vec{r})\, Y_\ell^m\left(\vec{\Omega}\right) \tag{2.2}$$

$$\psi_\ell^m(E,\vec{r}) = \int_{4\pi} \psi\left(E,\vec{r},\vec{\Omega}\right) Y_\ell^m\left(\vec{\Omega}\right) d\vec{\Omega} \tag{2.3}$$

Next, consider the scattering source from the original transport equation; this is the first term on the right hand side of Eq. (2.1) and is usually called the "double-differential scattering kernel". This term represents the transfer of a neutron exiting at energy E and direction $\vec{\Omega}$ after undergoing a scattering collision at all other energies and angles. The change in angle, represented by $\vec{\Omega}' \cdot \vec{\Omega}$, can first be replaced by a single variable, μ, since the change in the neutron's pre- and post-collision direction is not dependent upon the pre-collision direction. Next, another functional expansion can be applied to the double-differential cross section to replace μ with a series of harmonics, just as was done with the flux. Instead of applying spherical harmonics, however, μ will be treated with Legendre polynomials. These Legendre polynomials are another set of orthogonal bases which have a useful relation to spherical harmonics which will soon be exploited. This expansion is shown in Eq. (2.4) and the coefficients (or moments) of the expansion are found in Eq. (2.5).

$$\Sigma_s(E' \to E,\vec{r},\mu) = \sum_{\ell=0}^{\infty} \frac{2\ell+1}{2} \sum_{\ell=0}^{\infty} \Sigma_{s,\ell}(E' \to E,\vec{r}) P_\ell(\mu) \tag{2.4}$$

$$\Sigma_{s,\ell}(E' \to E,\vec{r}) = \int_{-1}^{1} \Sigma_s(E' \to E,\vec{r},\mu) P_\ell(\mu) d\mu \tag{2.5}$$

If the Legendre expansion of the double-differential scattering cross section and spherical harmonic expansion of the angular flux are inserted into the scattering source term, the spherical harmonic addition theorem can then be applied. When this is performed, the resultant scattering source term is shown in (2.6). In this equation, R_ℓ^m are the "real spherical harmonics" and result from the spherical harmonic addition theorem and the multiplication of the Y_ℓ^m with its complex conjugate.

$$\int_0^\infty \int_{4\pi} \Sigma_s(E' \to E,\vec{r},\mu) \psi\left(\vec{r},\vec{\Omega}'\right) d\Omega' dE' =$$

$$\int_0^\infty \sum_{l=0}^{\infty} \frac{2\ell+1}{4\pi} \Sigma_{s,\ell}(E' \to E,\vec{r}) \sum_{m=-\ell}^{\ell} \psi_\ell^m(E',\vec{r}) R_\ell^m\left(\vec{\Omega}\right) dE' \tag{2.6}$$

Up to this point, the angular flux has been expanded in terms of spherical harmonics and the scattering cross section expanded with Legendre polynomials in order to approximate the angular dependence with a finite sum of spherical harmonic moments which contain that angular dependence. When this revised source term is used in the continuous-energy transport equation, the equation shown in Eq. (2.7) is obtained. The reader should be aware that the angular variable is still present in the remaining terms of the transport equation: this dimension is treated in various ways by different approximations used in deterministic transport. Some of these approximations do include applying the spherical harmonics expansion to the flux in the remaining terms, called the P_n method. The specifics of how the angular variable is treated in the remaining terms are not relevant to the needs of this work and so will not be discussed further.

$$\begin{aligned}\vec{\Omega}\cdot\nabla\psi\left(E,\vec{r},\vec{\Omega}\right)+\Sigma_t(E,\vec{r})\psi\left(E,\vec{r},\vec{\Omega}\right) \\ =\int_0^\infty\sum_{l=0}^{\infty}\frac{2\ell+1}{4\pi}\Sigma_{s,\ell}(E'\rightarrow E,\vec{r})\sum_{m=-\ell}^{\ell}R_\ell^m\left(\vec{\Omega}\right)\psi_\ell^m(E',\vec{r})dE' \\ +\frac{1}{k_{eff}}\left[\int_0^\infty\int_{4\pi}\frac{1}{4\pi}\nu\Sigma_f(E'\rightarrow E,\vec{r})\psi\left(E',\vec{r},\vec{\Omega}'\right)d\Omega'dE'\right]\end{aligned} \tag{2.7}$$

Up to this point, no approximations have been made. The flux and cross section expansions are accurate so long as an infinite number of orders are used. Unfortunately, practical needs dictate that this expansion be truncated to a finite order, L. For reactor analysis applications L is typically only as high two or three; shielding applications can apply many more due to the extreme anisotropy of the systems being modeled. The continuous-energy transport equation truncated to an angular order of L is shown in Eq. (2.8). This equation is the starting point for multi-group theory discussed in the next section.

$$\begin{aligned}\vec{\Omega}\cdot\nabla\psi\left(E,\vec{r},\vec{\Omega}\right)+\Sigma_t(E,\vec{r})\psi\left(E,\vec{r},\vec{\Omega}\right) \\ =\int_0^\infty\sum_{l=0}^{L}\frac{2\ell+1}{4\pi}\Sigma_{s,\ell}(E'\rightarrow E,\vec{r})\sum_{m=-\ell}^{\ell}R_\ell^m\left(\vec{\Omega}\right)\psi_\ell^m(E',\vec{r})dE' \\ +\frac{1}{k_{eff}}\left[\int_0^\infty\int_{4\pi}\frac{1}{4\pi}\nu\Sigma_f(E'\rightarrow E,\vec{r})\psi\left(E',\vec{r},\vec{\Omega}'\right)d\Omega'dE'\right]\end{aligned} \tag{2.8}$$

2.2 Multi-Group Theory

2.2.1 Energy Discretization

Now that the scattering source has been reduced in complexity, the next dimension to simplify is the neutron energy. The multi-group approximation which follows is employed in nearly every deterministic transport code.

To begin, consider the entire energy range expected in the problem; for reactor analysis this is typically zero to twenty MeV. The next step is to bin the energies in G energy groups. These groups are numbered such that group 1 is the fastest energy group, say from six to twenty MeV, and the largest group index (group G) is the lowest energy group. See Appendix B for example group structures.

With this binning in place, the flux can be integrated over these group boundaries to create the group-wise counterpart, ψ_g. This integral over the energy is shown in Eq. (2.9).

$$\psi_g\left(\vec{r},\vec{\Omega}\right) = \int_{E_g}^{E_{g-1}} \psi\left(E,\vec{r},\vec{\Omega}\right) dE \tag{2.9}$$

The next step is to integrate the transport equation the previous section finished with, Eq. (2.8), over the energy within a single group. This step yields the form shown in Eq. (2.10); with the changes highlighted in red. The definition of ψ_g is applied when it was straight-forward to do so.

$$\begin{aligned}
&\vec{\Omega}\cdot\nabla\psi_g\left(\vec{r},\vec{\Omega}\right) + \int\limits_{E_g}^{E_{g-1}} \Sigma_t(E,\vec{r})\psi\left(E,\vec{r},\vec{\Omega}\right)dE \\
&\quad = \sum_{g'=1}^{G}\int\limits_{E_{g'}}^{E_{g'-1}}\int\limits_{E_g}^{E_{g-1}}\sum_{l=0}^{L}\frac{2\ell+1}{4\pi}\Sigma_{s,\ell}(E'\rightarrow E,\vec{r})\sum_{m=-\ell}^{\ell}R_\ell^m\left(\vec{\Omega}\right)\psi_\ell^m(E',\vec{r})\,dE\,dE' \\
&\qquad + \frac{1}{k_{eff}}\left[\frac{1}{4\pi}\sum_{g'=1}^{G}\int\limits_{E_{g'}}^{E_{g'-1}}\int\limits_{E_g}^{E_{g-1}}\int\limits_{4\pi}\nu\Sigma_f(E'\rightarrow E,\vec{r})\psi\left(E',\vec{r},\vec{\Omega}'\right)d\Omega'\,dE\,dE'\right]
\end{aligned} \tag{2.10}$$

Three terms still remain which can be further simplified: the total reaction term, the scattering, and fission source terms. These will be treated by multiplying the terms by unity in the useful form of $\frac{\psi_g}{\psi_g}$ as shown in Eq. (2.11).

$$\begin{aligned}
&\vec{\Omega}\cdot\nabla\psi_g\left(\vec{r},\vec{\Omega}\right)+\frac{\int\limits_{E_g}^{E_{g-1}}\Sigma_t\left(E,\vec{r}\right)\psi\left(E,\vec{r},\vec{\Omega}\right)dE}{\psi_g\left(\vec{r},\vec{\Omega}\right)}\psi_g\left(\vec{r},\vec{\Omega}\right)\\
&=\sum_{g'=1}^{G}\frac{\int\limits_{E_{g'}}^{E_{g'-1}}\int\limits_{E_g}^{E_{g-1}}\sum\limits_{l=0}^{L}\frac{2\ell+1}{4\pi}\Sigma_{s,\ell}\left(E'\rightarrow E,\vec{r}\right)\sum\limits_{m=-\ell}^{\ell}R_{\ell}^{m}\left(\vec{\Omega}\right)\psi_{\ell}^{m}\left(E',\vec{r}\right)dEdE'}{\psi'_g\left(\vec{r},\vec{\Omega}'\right)}\psi'_g\left(\vec{r},\vec{\Omega}'\right)\\
&+\frac{1}{k_{eff}}\left[\sum_{g'=1}^{G}\frac{1}{4\pi}\frac{\int\limits_{E_{g'}}^{E_{g'-1}}\int\limits_{E_g}^{E_{g-1}}\int\limits_{4\pi}\nu\Sigma_f\left(E'\rightarrow E,\vec{r}\right)\psi\left(E',\vec{r},\vec{\Omega}'\right)d\Omega' dEdE'}{\psi'_g\left(\vec{r},\vec{\Omega}'\right)}\psi'_g\left(\vec{r},\vec{\Omega}'\right)\right]
\end{aligned}\tag{2.11}$$

These three red terms in Eq. (2.11) are collected and replaced with their more concise forms provided in Eqs. (2.12), (2.13), and (2.14). These three quantities define what are called the MGXS. It can be seen that these MGXS are equivalent to the average cross section in the energy group, weighted by the angular neutron flux.

$$\Sigma_{t,g}\left(\vec{r},\vec{\Omega}\right)=\frac{\int\limits_{E_g}^{E_{g-1}}\Sigma_t\left(E,\vec{r}\right)\psi\left(E,\vec{r},\vec{\Omega}\right)dE}{\psi_g\left(\vec{r},\vec{\Omega}\right)}\tag{2.12}$$

$$\nu\Sigma_{f,g'\rightarrow g}\left(\vec{r},\vec{\Omega}\right)=\frac{\int\limits_{E_{g'}}^{E_{g'-1}}\int\limits_{E_g}^{E_{g-1}}\int\limits_{4\pi}\nu\Sigma_f\left(E'\rightarrow E,\vec{r}\right)\psi\left(E',\vec{r},\vec{\Omega}'\right)d\Omega'\,dE\,dE'}{\psi'_g\left(\vec{r},\vec{\Omega}'\right)}\tag{2.13}$$

$$\Sigma_{s,g'\rightarrow g}\left(\vec{r},\vec{\Omega}',\mu\right)=\frac{\int\limits_{E_{g'}}^{E_{g'-1}}\int\limits_{E_g}^{E_{g-1}}\sum\limits_{l=0}^{L}\frac{2\ell+1}{4\pi}\Sigma_{s,\ell}\left(E'\rightarrow E,\vec{r}\right)\sum\limits_{m=-\ell}^{\ell}R_{\ell}^{m}\left(\vec{\Omega}\right)\psi_{\ell}^{m}\left(E',\vec{r}\right)dE'}{\psi'_g\left(\vec{r},\vec{\Omega}'\right)}\tag{2.14}$$

When the substitutions of Eqs. (2.12), (2.13), and (2.14) are made into Eq. (2.11), the result is shown in Eq. (2.15). This is the multi-group transport equation in its most "pure" form; that is, without any multi-group approximations yet applied.

$$\begin{aligned}
&\vec{\Omega}\cdot\nabla\psi_g\left(\vec{r},\vec{\Omega}\right)+\Sigma_{t,g}\left(\vec{r},\vec{\Omega}\right)\psi_g\left(\vec{r},\vec{\Omega}\right)= \\
&\qquad=\sum_{g'=1}^{G}\sum_{l=0}^{\infty}\frac{2\ell+1}{4\pi}\Sigma_{s,\ell,g'\to g}\left(\vec{r}\right)\sum_{m=-\ell}^{\ell}\psi_{\ell,g'}^{m}\left(\vec{r}\right)R_{\ell}^{m}\left(\vec{\Omega}\right)dE' \\
&\qquad\qquad+\frac{1}{k_{eff}}\left[\sum_{g'=1}^{G}\frac{1}{4\pi}\nu\Sigma_{f,g'\to g}\left(\vec{r},\vec{\Omega}\right)\psi_{g'}\left(\vec{r},\vec{\Omega}'\right)d\Omega'\right] \qquad (2.15)
\end{aligned}$$

The MGXS in Eqs. (2.12), (2.13), and (2.14) are not yet useful, however. The cross sections contain a dependence on the neutron's incoming angle which is computationally inefficient and undesirable. These data would either need to be functionally expanded with spherical harmonics as was done with the flux previously, or provided in some other form which describes the angular dependence. This marks the first of the approximations which need to be made in order to allow multi-group theory to be a useful method. To remove this angular dependence on the data, one of the following two paths are typically taken: the "flux separability" approximation or the "Consistent-P" approximation. Note that after this discussion, the remainder of this work will exclusively utilize the flux separability approximation.

2.2.2 Flux Separability Approximation

The flux separability approximation begins by assuming that the energy dependence of the angular flux is not a function of the neutron angle. This approximation allows the angular dependence to be removed from the multi-group cross sections as shown by example for the total cross section in Eq. (2.16). Eq. (2.16) shows the application of the flux separability approximation by allowing the energy and angular dependence to be treated by two functions multiplied by each other, $\phi(E,\vec{r})$ and $W\left(\vec{r},\vec{\Omega}\right)$. The $W\left(\vec{r},\vec{\Omega}\right)$ terms can then be pulled out of the numerator and denominator integrals and thus cancel out.

$$\begin{aligned}\Sigma_{t,g}\left(\vec{r},\vec{\Omega}\right) &= \frac{\int_{E_g}^{E_{g-1}} \Sigma_t(E,\vec{r})\psi\left(E,\vec{r},\vec{\Omega}\right)dE}{\int_{E_g}^{E_{g-1}} \psi\left(E,\vec{r},\vec{\Omega}\right)dE} \\ &\approx \frac{\int_{E_g}^{E_{g-1}} \Sigma_t(E,\vec{r})\phi(E,\vec{r})\,W\left(\vec{r},\vec{\Omega}\right)dE}{\int_{E_g}^{E_{g-1}} \phi(E,\vec{r})\,W\left(\vec{r},\vec{\Omega}\right)dE} \\ &\approx \frac{\int_{E_g}^{E_{g-1}} \Sigma_t(E,\vec{r})\phi(E,\vec{r})\,dE}{\int_{E_g}^{E_{g-1}} \phi(E,\vec{r})\,dE}\end{aligned} \tag{2.16}$$

The same assumption can be applied to the fission production and scattering equations, yielding their new definitions shown in Eqs. (2.17) and (2.18), respectively.

$$\nu\Sigma_{f,g'\to g}\left(\vec{r},\vec{\Omega}'\right) \approx \frac{\int_{E_{g'}}^{E_{g'-1}} \int_{E_g}^{E_{g-1}} \nu\Sigma_f(E'\to E,\vec{r})\phi(E,\vec{r})\,dE\,dE'}{\int_{E_{g'}}^{E_{g'-1}} \phi(E',\vec{r})\,dE'} = \nu\Sigma_{f,g'\to g}(\vec{r}) \tag{2.17}$$

$$\Sigma_{s,\ell,g'\to g}\left(\vec{r},\vec{\Omega}'\right) \approx \frac{\int\limits_{E_{g'}}^{E_{g'-1}} \int\limits_{E_g}^{E_{g-1}} \frac{1}{4\pi}\Sigma_{s,0}(E'\to E,\vec{r})\psi_0^0(E',\vec{r})\,dE dE'}{\int_{E_{g'}}^{E_{g'-1}} \phi(E,\vec{r})\,dE'} = \Sigma_{s,g'\to g}(\vec{r}) \tag{2.18}$$

2.2.3 Consistent-P Approximation

Unfortunately, the flux separability approximation does not work well near material discontinuities where neutrons coming from one direction can have an entirely different within-group energy distribution than from another direction due to differing absorption or scattering characteristics of a region. A common way to treat this was first derived by Bell, Hansen, and Sandmeier in 1967 [14].

This Consistent-P approximation begins by expanding the angular flux using the previously discussed angular flux moments as weighting functions for only the total (Eq. (2.19)) and scattering cross sections (Eq. (2.20)). The fission cross section was not included in this treatment by Bell et al due to their main focus on one-dimensional shielding problems which were the predominant deterministic transport application at the time. In applications of this method today, the fission cross section is commonly assumed to be independent of $\vec{\Omega}$ since a method as simple as the Consistent-P approximation can not be applied in the case of $\nu\Sigma_f$ due to the presence of effective neutron multiplication factor.

$$\Sigma^m_{t,\ell,g}(\vec{r}) = \frac{\int\limits_{E_g}^{E_{g-1}} \Sigma_t(E,\vec{r})\psi^m_\ell(E,\vec{r})\,dE}{\int\limits_{E_g}^{E_{g-1}} \psi^m_\ell(E,\vec{r})\,dE} \tag{2.19}$$

$$\Sigma^m_{s,\ell,g'\to g}(\vec{r}) = \frac{\int\limits_{E_{g'}}^{E_{g'-1}} \int\limits_{E_g}^{E_{g-1}} \Sigma_{s,\ell}(E'\to E,\vec{r})\psi^m_\ell(E',\vec{r})\,dE\,dE'}{\int\limits_{E_{g'}}^{E_{g'-1}} \psi^m_\ell(E',\vec{r})\,dE'} \tag{2.20}$$

Now, plugging these terms in the transport equation (while suppressing the spatial dimensions, $\vec{r}$, for the moment), Eq. (2.21) is obtained.

$$\begin{aligned}\vec{\Omega}\cdot\nabla\psi_g\left(\vec{\Omega}\right) + \Sigma^m_{t,\ell,g}\psi^m_{\ell,g} = \\ \sum_{g'=1}^{G}\sum_{l=0}^{L}\frac{2\ell+1}{4\pi}\sum_{m=-\ell}^{\ell}\Sigma^m_{s,\ell,g'\to g}R^m_\ell\left(\vec{\Omega}\right)\psi^m_{\ell,g'} \\ + \frac{1}{k_{eff}}\left[\sum_{g'=1}^{G}\frac{1}{4\pi}\nu\Sigma_{f,g'\to g}\psi_{g'}\left(\vec{\Omega}'\right)\right]\end{aligned} \tag{2.21}$$

The total cross section moment, $\Sigma^m_{t,\ell,g}$, can then be moved to the right hand side and placed for convenience with the scattering moments. This step shown in Eq. (2.22).

$$\begin{aligned}\vec{\Omega}\cdot\nabla\psi_g\left(\vec{\Omega}\right) + \cancel{\Sigma^m_{t,\ell,g}\psi^m_{\ell,g}} = \\ \sum_{g'=1}^{G}\sum_{l=0}^{L}\frac{2\ell+1}{4\pi}\sum_{m=-\ell}^{\ell}\left(\Sigma^m_{s,\ell,g'\to g} - \Sigma^m_{t,\ell,g'}\right)R^m_\ell\left(\vec{\Omega}\right)\psi^m_{\ell,g'} \\ + \frac{1}{k_{eff}}\left[\sum_{g'=1}^{G}\frac{1}{4\pi}\nu\Sigma_{f,g'\to g}\psi_{g'}\left(\vec{\Omega}'\right)\right]\end{aligned} \tag{2.22}$$

Next, the isotropically-weighted total cross section can be added to both sides, recovering the familiar form. This step shown in Eq. (2.23).

$$\begin{aligned}\vec{\Omega}\cdot\nabla\psi_g\left(\vec{\Omega}\right)+\Sigma_{t,g}\psi_g &= \\ &\sum_{g'=1}^{G}\sum_{l=0}^{L}\frac{2\ell+1}{4\pi}\sum_{m=-\ell}^{\ell}\left(\Sigma^m_{s,\ell,g'\to g}-\Sigma^m_{t,\ell,g'}+\Sigma_{t,g}\right)R^m_\ell\left(\vec{\Omega}\right)\psi^m_{\ell,g'} \\ &+\frac{1}{k_{eff}}\left[\sum_{g'=1}^{G}\frac{1}{4\pi}\nu\Sigma_{f,g'\to g}\psi_{g'}\left(\vec{\Omega}'\right)\right]\end{aligned} \tag{2.23}$$

Finally, the scattering source term, which now has two additional total cross section terms, can be combined to create a separate term, called $\tilde{\Sigma}^m_{s,\ell,g'\to g}$ in this work. This term is defined by Eq. (2.24). In this term, $\delta_{g',g}$ denotes that the total cross section moments are only subtracted from the diagonal of the original scattering moments.

$$\tilde{\Sigma}^m_{s,\ell,g'\to g}\left(\vec{r}\right)=\Sigma^m_{s,\ell,g'\to g}\left(\vec{r}\right)+\left(\Sigma_{t,g}\left(\vec{r}\right)-\Sigma^m_{t,\ell,g}\delta_{g',g}\left(\vec{r}\right)\right) \tag{2.24}$$

One additional step can be taken (and is commonly done so) if desired to reduce the data dimensionality further. In this step, the total m moments of a given l^{th} order are assumed to be separable in energy (as was done with the flux separability approximation). In this case, the scattering moment is as shown in Eq. (2.25) [12].

$$\tilde{\Sigma}_{s,\ell,g'\to g}\left(\vec{r}\right)=\sum_{m=-\ell}^{\ell}\tilde{\Sigma}^m_{s,\ell,g'\to g}\left(\vec{r}\right) \tag{2.25}$$

Using the consistent-P approximation with the above modification, the multi-group transport approximation is as shown in Eq. (2.26). This form is desirable since it removes the angular dependence of the multi-group cross sections but maintains the accuracy of the initial multi-group transport equation.

$$\begin{aligned}\vec{\Omega}\cdot\nabla\psi_g\left(\vec{\Omega}\right)+\Sigma_{t,g}\psi_g\left(\vec{\Omega}\right) &= \\ &\sum_{g'=1}^{G}\sum_{l=0}^{L}\frac{2\ell+1}{4\pi}\tilde{\Sigma}_{s,\ell,g'\to g}\left(\vec{r}\right)\sum_{m=-\ell}^{\ell}R^m_\ell\left(\vec{\Omega}\right)\psi^m_{\ell,g'} \\ &+\frac{1}{k_{eff}}\left[\sum_{g'=1}^{G}\frac{1}{4\pi}\nu\Sigma_{f,g'\to g}\psi_{g'}\left(\vec{\Omega}'\right)\right]\end{aligned} \tag{2.26}$$

2.3 Additional Approximations Relating to Multi-Group Theory

Before finalizing the multi-group transport equation, two more minor approximations are typically applied in deterministic codes. These are to first include the neutron production via (n,xn) reactions as well as to simplify the fission neutron source term.

These (n,xn) neutron production reactions typically occurs at energies greater than a few MeV; for example, the threshold of the $(n,2n)$ reaction for ^{238}U is around 6.18 MeV. These reactions are typically folded into the scattering cross section with appropriate adjustments made to maintain the neutron balance due to the neutron producing (n,xn) reactions. This modification is shown in Eq. (2.27). In this equation, $\nu_{scatt,g'\rightarrow g}$ is simply referred to as the average yield term for all scattering reactions. Eq. (2.27) also shows adjustments needed to be made to the absorption cross section to maintain the neutron balance, if this is provided as an input to a deterministic transport solver.

$$\begin{gathered}\hat{\Sigma}_{s,\ell,g'\rightarrow g} = \nu_{scatt,g'\rightarrow g}\tilde{\Sigma}_{s,\ell,g'\rightarrow g} \\ \hat{\Sigma}_{a,g} = \Sigma_{a,g} - \left(\nu_{scatt,g'\rightarrow g} - 1\right)\tilde{\Sigma}_{s,\ell,g'\rightarrow g}\end{gathered} \tag{2.27}$$

The final approximation to introduce is a condensation of the fission matrix, $\nu\Sigma_{f,g'\rightarrow g}$ into two terms: the fission production term $(\nu\Sigma_{f,g'})$ and the fission energy spectra, χg. This is done because, for light water reactors, the outgoing probability distribution of fission neutron energies is not strongly dependent upon the incoming energy. Thus this dependence can be removed as is shown in Eq. (2.28) and Eq. (2.29) so that only two vectors, each of length G are needed as opposed to a complete $G\times G$ fission matrix.

$$\chi_g = \frac{\sum\limits_{g'=0}^{G} \nu\Sigma_{f,g'\rightarrow g}\psi_{g'}}{\sum\limits_{g=0}^{G}\sum\limits_{g'=0}^{G} \nu\Sigma_{f,g'\rightarrow g}\psi_{g'}} \tag{2.28}$$

$$\nu\Sigma_{f,g'} = \sum_{g=0}^{G} \nu\Sigma_{f,g'\rightarrow g} \tag{2.29}$$

2.4 Multi-Group Cross Section Library Generation

2.4.1 Difficulty In Library Generating

After the steps discussed in preceding sections are taken, the transport equation is as shown in Eq. (2.30). Approximations were made along the way in truncating the angular expansion to order L, applying either the flux separability or consistent-P approximations, inserting scattering production neutrons into the scattering term, and splitting the fission matrix into the two distinct terms, $\nu\Sigma_{f,g}$ and χ_g.

$$\begin{aligned}\vec{\Omega}\cdot\nabla\psi_g\left(\vec{r},\vec{\Omega}\right)+\Sigma_{t,g}\left(\vec{r}\right)\psi_g\left(\vec{r}\right) = &\\ \sum_{g'=1}^{G}\sum_{l=0}^{L}\frac{2\ell+1}{4\pi}\hat{\Sigma}_{s,\ell,g'\to g}\left(\vec{r}\right)&\sum_{m=-\ell}^{\ell}R_\ell^m\left(\vec{\Omega}\right)\psi_{\ell,g'}^m\left(\vec{r}\right)\\ &+\frac{1}{k_{eff}}\left[\sum_{g'=1}^{G}\frac{\chi_g\left(\vec{r}\right)}{4\pi}\nu\Sigma_{f,g'}\left(\vec{r}\right)\psi_{g'}\left(\vec{r}\right)\right]\end{aligned} \tag{2.30}$$

Whatever the approximations made along the way, one should notice that the MGXS terms require knowledge of the flux distribution. However, the flux distribution is the result of the transport equation. This yields a chicken-or-egg problem: the determination of the flux requires multi-group cross sections, but the determination of the multi-group cross sections requires knowledge of the flux for use as the weighting function. An iterative approach would eventually yield an accurate solution to this quandary. Unfortunately, a completely iterative approach would be quite expensive computationally due to the hundreds of billions of unknowns which may need to be solved for during the analysis of just one of the many single steady-state calculations. Instead, a typical approach taken is to make an "informed guess" of what the flux distribution is and to use that during the generation of the multi-group cross section library to use during the solution of the transport equation.

The main driver of the difficulties encountered is to be able to quantify the effect of the resonances in the continuous-energy cross section data. The resonances are the sharp peaks seen in the absorption cross section for ^{238}U at 298 K is shown in Figure 2.1 [15]. These resonances are present at energies from roughly 1 eV to 100 keV, at which point their presence becomes difficult to measure adequately.

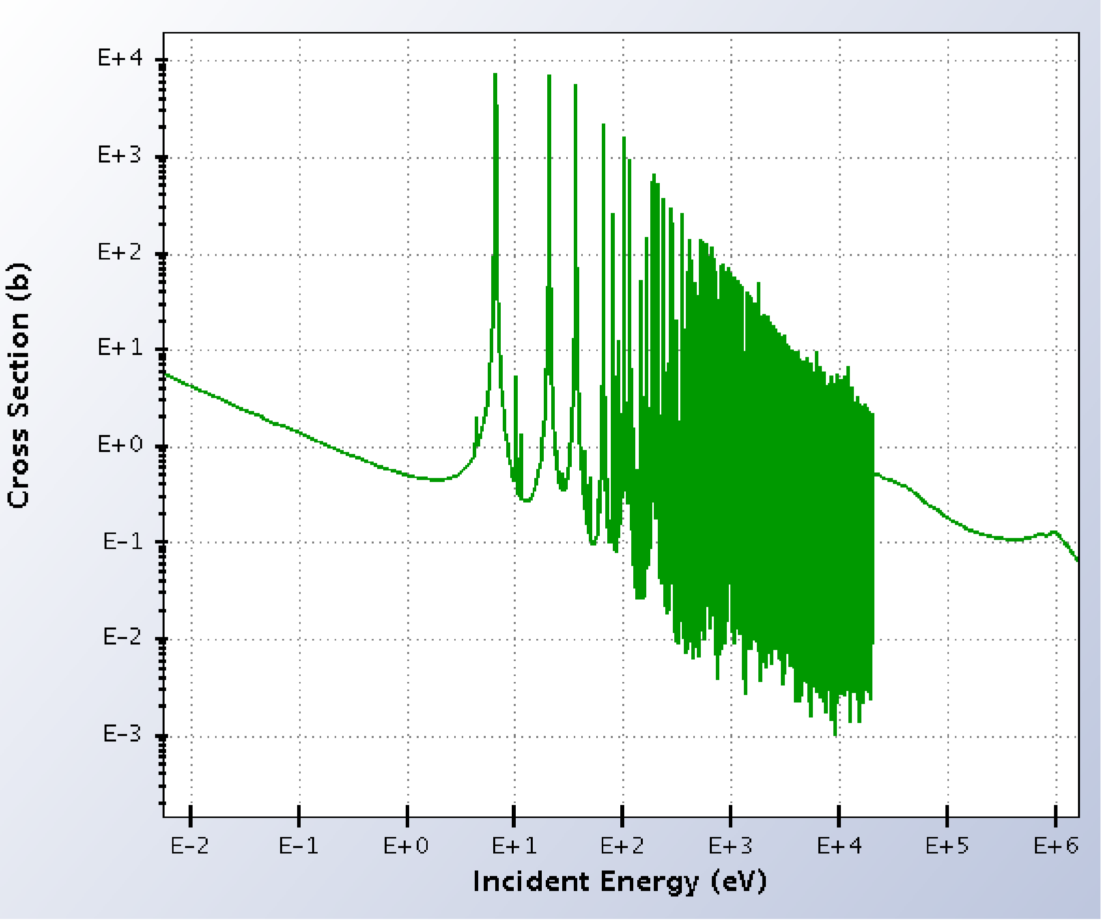

Figure 2.1: $^{238}U\ (n,\gamma)$ Cross Section

2.4.2 Typical Path

The exact methodology used to generate this informed flux guess is, in practice, specific to each reactor class and vendor based on experience with the design in question. Regardless, this is an expensive engineering process requiring on the order of man-weeks to man-months to perform. The general process is depicted in Figure 2.2 found in Chapter 9 ("Lattice Physics Computations") of the Nuclear Engineering Handbook [12].

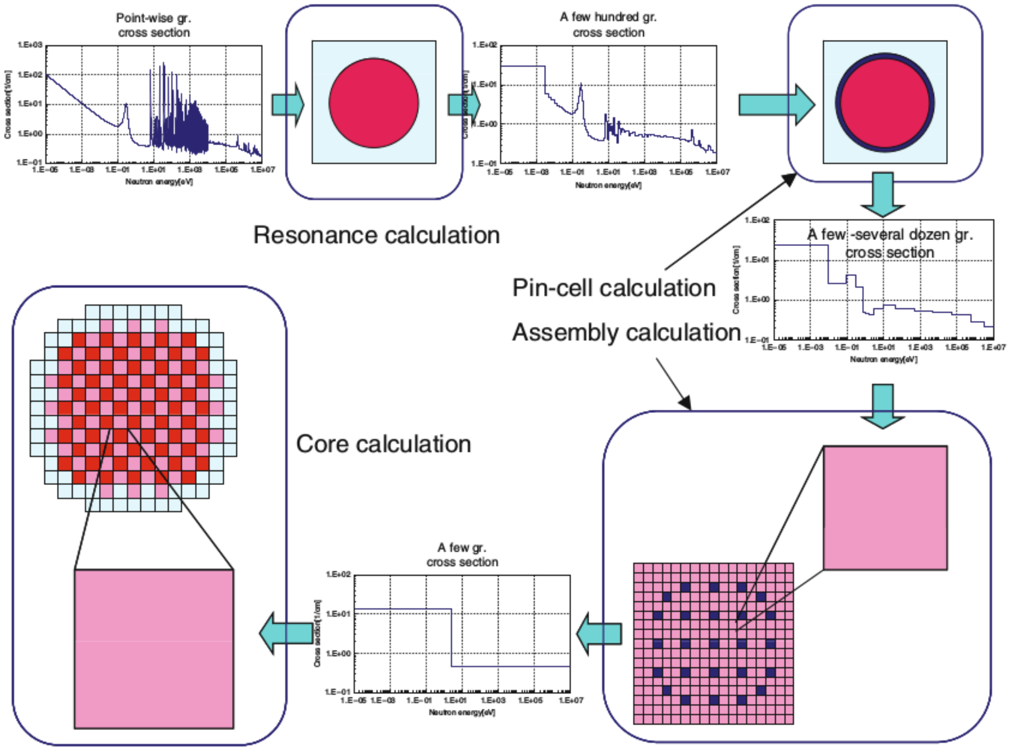

Figure 2.2: Overview of Traditional Multi-Group Cross Section Library Generation Scheme

This scheme reduces to a process where fidelity in the energy dimension is progressively replaced with spatial fidelity in terms of both the problem size and degree of heterogeneity modeled. The following steps are taken:

1. Estimate the flux spectra for a representative problem with significantly reduced spatial and angular dimensionality but using an “ultra-fine” group structure.
    (a) This representative problem can be an infinite homogeneous problem but more modern analyses are typically performed with a simplified reactor fuel pin described in 1-D polar or 2-D Cartesian geometry with only a single resonant isotope and moderator represented.
2. Use this “ultra-fine group” flux spectra as a weighting function to generate cross sections of a coarser group structure, called the “fine” group structure (with up to hundreds of groups)
3. The fine group structure is then used in a calculation for each heterogeneous, multi-nuclide fuel pin, generating a multi-group library with around 50 to 150 groups with one set of data for each unique pin type.

4. This multi-group structure is next used in a fuel assembly-sized problem for each typical fuel assembly in the core being analyzed.

5. The flux spectra obtained in these assembly problems is then used to collapse the fine group structure to a "multi" or "few" group structure (with anywhere between two and tens of groups).

Note that the depiction of the above scheme does not consider the modifications necessary to account for the energy spectrum which results from the infinite boundary conditions. Other schemes are necessary to correct for these cases (such as when a fuel rod is adjacent to a highly absorbing control rod).

Unfortunately, the flux spectra for even a homogeneous system with a single nuclide with resonances can not be analytically calculated. Instead, the effect of these resonances on the flux spectra in this simplest of cases is treated by a variety of assumptions about the probability of scattering into and out of a resonance while a neutron is slowing down from fission energies (around 0.7 MeV) to the thermal range (less than 0.625 eV). These resonances approximations are referred to as the narrow resonance, narrow resonance-infinite mass, and intermediate resonance approximations. [1,16]. The resonance problem becomes more difficult when one begins to consider overlapping resonances, either from the same nuclide (as is the case at higher energies due to Doppler broadening) or when another isotope is present which is also a resonant absorber. This is further exacerbated when spatial heterogeneity is introduced and resonances in adjacent pins can affect the flux spectra in the cell currently being analyzed.

2.4.3 Monte Carlo as a Library Generation Tool?

The above discussion leads to the conclusion that the determination of MGXS libraries requires many approximations. These approximations, combined with the other inherent approximations in deterministic transport require the application of an experiment-to-calculation correction factor be applied to the final analysis of a core design. In practice, the "experiment" is either an actual critical facility, or more recently, a Monte Carlo calculation. Adjustments are also made to k_{eff} to account for these issues, among others.

Instead of pursuing this torturous path, recent effort has been spent evaluating the Monte Carlo method to stochastically determine the MGXS library of interest [4–11]. Since Monte Carlo techniques can deal directly with the continuous-energy data and exact geometric representations, the Monte Carlo solver can be used to go straight to the assembly-level calculation depicted in Figure 2.2. This, of course, would not remove all the approximations necessary, since accurately determining the spatial and energetic flux distribution to generate cross sections defeats the purpose of performing the final core design calculation due to the chicken-or-egg problem discussed previously. Some of the remaining approximations would have to deal with treatment of the neutron leakage spectra on boundary surfaces, as well as the core state points to analyze (including temperature distributions, depletion conditions, et cetera) and how to interpolate the resultant data between these state points. These approximations are present regardless of the MGXS generation path chosen.

Chapter 3 presents an implementation of this approach in order to identify its weaknesses.

CHAPTER 3

Monte Carlo for the Generation of Multi-Group Cross Sections

The previous chapter identified a need for utilizing Monte Carlo methods to generate multi-group cross sections for use by a deterministic transport code. This chapter will focus on performing this task and identifying and improving barriers towards achieving this result.

This investigation, and all that follow in this work, will be performed using the OpenMC [17] Monte Carlo neutron transport code written primarily by the Massachusetts Institute of Technology, though with users and developers active everywhere due to the open nature of the code.

3.1 Monte Carlo Tallying

Monte Carlo neutron transport codes sample the behavior of the neutron population distribution in some system. The results of this simulation are provided by accumulating, or "tallying", certain information as it occurs during the neutron transport. This information includes quantities such as the neutron flux, the total reaction rate, and the neutron absorption rate. These tallies are simply integrals of a the neutron population distribution (that is, the angular flux) multiplied by some response function. This is mathematically described in Equation (3.1), for tally T. Again in this equation, $\vec{r}$ is the spatial location, $\vec{\Omega}$ is a unit-vector in the direction of neutron motion, E' is the neutron's energy, E is the outgoing energy of the particle after a certain event, and μ is the cosine of the change in angle of the pre- and post-event neutron. The bounds of the integrals (not shown) represent the portion of phase space that the tally should be concerned with. In OpenMC parlance, these bounds are referred to as the filters. The response function, $R\left(\vec{r},\vec{\Omega},E',E,\mu\right)$, is defined by the response desired. The last two quantities, E and μ only exist when there is an outgoing component of the response function; for example with a scattering collision where the neutron's energy and angle are changed. As an example of the tallying process, if the flux is desired to be tallied, then the response function is simply unity; if the total reaction rate is desired, then the response function is $\Sigma_t(\vec{r}, E')$.

$$T = \int dE' \int dE \int d\vec{r} \int d\vec{\Omega} R\left(\vec{r}, \vec{\Omega}, E', E\right) \psi\left(\vec{r}, \vec{\Omega}, E'\right) \tag{3.1}$$

Of course, these integrals are not analytically or numerically solved by the MC code; instead they are stochastically estimated by way of two types of tally estimators which will be discussed later. Before this discussion can be had though, it is instructive to understand the method of stochastic integration and how to estimate the variance of that result.

When stochastically estimating a quantity, such as the tally shown in Eq. (3.1), the sample mean of the quantity is as shown in Eq. (3.2).

$$\bar{X} = \frac{1}{N} \sum_{i=1}^{N} x_i \tag{3.2}$$

Since Monte Carlo integration is a stochastic process limited to a finite sample size, it comes with a stochastic uncertainty. Therefore, the variance of the sample mean must be determined in addition to the mean. This variance is as shown in Eq. (3.3).

$$s_{\bar{X}}^2 = \frac{1}{N-1} \left(\frac{1}{N} \sum_{i=1}^{N} x_i^2 - \bar{x}^2 \right) \tag{3.3}$$

Eq. 3.3 shows that as the number of histories, N, is increased, the variance of the sample mean will decrease. The degree that this uncertainty is reduced is a well known result, shown in Eq. (3.4). This formula shows that the variance of the mean can be reduced by increasing the number of tally realizations, N, and that this reduction rate is proportional to $N^{-1/2}$

$$s_{\bar{X}} = \frac{s_X}{\sqrt{N}} \tag{3.4}$$

The two types of estimators mentioned earlier are the collision estimators and track-length estimators.

Collision estimators essentially accumulate results every time the event of interest occurs. That is, the Eq. (3.1) integral reduces to simply that shown in Eq. (3.5). In this equation, W_{tot} is the total particle weight simulated, w_i is the pre-collision weight of the particle undergoing the event to be recorded, and the set $i \in V$ means that the event occurred within the volume of phase space represented by P. In other words, if the event occurred such that it met the bounds of the particular tally filter and the sampled reaction is of the desired type, then it will be scored.

$$T = \frac{1}{W_{tot}} \sum_{i \in P} w_i \tag{3.5}$$

This estimator requires that a collision event has actually occurred. This limits the efficiency of the tally as there can be few realizations (N in Eq. (3.4)) in areas which have a low probability of events occurring.

The track-length estimator aims to improve this weakness of the collision estimator by scoring results every time a neutron history travels a known distance within a tally filter. The general estimator in this case is shown in Eq. (3.6). In this equation, TL_i is the length traversed by the particle within the spatial filter of interest; the term $i \in V$ refers to the complete set of distances traversed by a particle within the region of interest; R_i is the response function evaluated at the particle's angle and energy and in the volumetric region of interest; the weight quantities W_{tot} and w_i hold the same meaning they did for the collision estimator.

$$T = \frac{1}{W_{tot}} \sum_{i \in V} TL_i w_i R_i \tag{3.6}$$

These track-length tallies are powerful, however they cannot be applied universally: tally scores which require outgoing particle information (e.g., a post-collision outgoing energy) are not eligible for track-length estimation since the collision did not actually occur.

3.2 Tally Types Required to Generate a Library

As discussed in Chapter 2, deterministic transport solvers using the Multi-Group Approximation require group-wise data for the following quantities: a total interaction cross section ($\Sigma_{t,g}$), the scattering cross section with the scattering angle expanded in Legendre polynomials (called the scattering moments, $\Sigma_{s,l,g' \rightarrow g}$), the fission neutron production cross section ($\nu\Sigma_{f,g}$), the average fission spectrum (χ_g)), and finally the fission energy release cross section ($\kappa\Sigma_{f,g}$) to be used when reconstructing power from flux. The tallying of most of these quantities is straight-forward; however the tallying of scattering and scattering production moments requires further discussion, found below.

3.2.1 Scattering and Scattering Production Moment Matrices Tallies

The multi-group scattering kernel moments are defined as shown in Eq. (3.7). In this equation (and the remainder of this paper), n is the nuclide, MT is the reaction channel, i is the tally region, E and g are the outgoing energy and energy group, E' and g' are the incoming energy and energy group, N is the number density, σ_s is the microscopic scattering cross section, $\vec{r}$ is the location in space, μ is the laboratory frame change-in-angle, $P_l(\mu)$ is the Legendre polynomial of order l evaluated at μ, $f_{n,MT}$ represents the multi-variate Probability Distribution Function (PDF) of transferring from energy E' to E with a change-in-angle of μ, ψ is the angular flux, and finally ϕ is the scalar flux. The sum over reaction channels includes only the scattering collisions: elastic, inelastic level, inelastic continuum, and (n,xn) collisions. The effect of neutron multiplication via (n,xn) collisions can be included by multiplying the integrand in Eq. (3.7) by the reaction multiplicity. This process yields the scattering production moment estimator shown in Eq. (3.8).

$$\Sigma_{s,l,g'\to g,i}\phi_{g',i} = \sum_{n} N_n \sum_{MT_n} \int\limits_{V_i} \int\limits_{E_{g'}}^{E_{g'-1}} \int\limits_{E_g}^{E_{g-1}} \int\limits_{4\pi} \int\limits_{-1}^{1} \Big[\sigma_{s,n,MT}(E') f_{n,MT}(E' \to E,\mu) \times P_l(\mu)\psi\left(E',\vec{r},\vec{\Omega}\right) d\mu\, d\vec{\Omega}\, dE\, dE'\, dr^3\Big] \tag{3.7}$$

$$\hat{\Sigma}_{s,l,g'\to g,i}\phi_{g',i} = \sum_{n} N_n \sum_{MT_n} \int\limits_{V_i} \int\limits_{E_{g'}}^{E_{g'-1}} \int\limits_{E_g}^{E_{g-1}} \int\limits_{4\pi} \int\limits_{-1}^{1} \Big[Y_{n,MT}(E')\sigma_{s,n,MT}(E') f_{n,MT}(E' \to E,\mu) \times P_l(\mu)\psi\left(E',\vec{r},\vec{\Omega}\right) d\mu\, d\vec{\Omega}\, dE\, dE'\, dr^3\Big] \tag{3.8}$$

The most commonly used method to tally the above equations was derived by E. L. Redmond in 1997 [4]. Redmond derived two classes of methods of doing so, referred to as the *Direct* and *Explicit* methods. The *Direct* methods are analog tallying methods; that is, the μ from Eq. (3.7) obtained in the Monte Carlo transport scattering process is tallied directly. The *Explicit* methods force a sampling of a finite number of (E,μ) points of $f_{n,MT}(E',E,\mu)$ per scattering collision at the incoming energy E', with the weight of each score adjusted according to the relative probability of each energy-angle bin for the encountered scattering reaction. In this way, the *Explicit* method provides more information about the encountered angular distribution at each collision than the Direct method.

The *Direct* and *Explicit* classes each include two specific methods: tallying of the angular distribution in a histogram representation (referred to as the Direct-f(μ) and Explicit-f(μ) methods); and tallying directly to the Legendre moments (referred to as the Direct-P$_n$ and Explicit-P$_n$ methods).

The P_n methods are more memory compact than the *f(μ)* methods, but can require more computations during the transport process as the Legendre polynomial needs to be evaluated for every order of interest with the sampled scattering angle as the argument. The Direct-P$_n$ approach is the method currently implemented in both the Serpent [5] and OpenMC [17] Monte Carlo transport solvers. No implementation of the *Explicit* classes in production codes are known to the authors of this paper, including the work done by Redmond. Since the Direct-P$_n$ is the only method used in production, this work will not use the Direct-f(μ) and Explicit methods as comparison standards.

The scattering production version of the Direct-P$_n$ is shown in Eq. (3.9). In this equation, μ_i is the sampled scattering angle and $\omega_{i,out}$ is the particle weight after the collision. If the scattering moment (vice scattering production moment) estimator is required, the pre-collision weight is used instead. This is because $\frac{\omega_{i,out}}{\omega_{i,in}}$ is the number of neutrons produced, or the yield. The tally estimator is a sum over all events which are incoming group g', to outgoing group g, in a region of interest V, and for the nuclides of interest (n). Since this estimator only records the tallied change in angle and energy transfer (by using $g' \rightarrow g$ tally filters), it incurs a tallying inefficiency in that only one entry of the scattering matrix receives information for every scattering event.

$$\hat{\Sigma}_{s,l,g'\rightarrow g,i}\phi_{g',i} = \sum_{event\; i\in n,g',g,V} \omega_{i,out}\, P_l(\mu_i) \tag{3.9}$$

Now that the main method used to generating scattering moment matrices is understood, it would be worthwhile to understand the tallying efficiency of all Monte Carlo MGXS tallies, as well as the efficiency of the Direct-P$_n$ tally compared to the other types of tallies (such as the total reaction rate, etc.) needed to generate a library.

For the remainder of this work, the Direct-P$_n$ estimator will be referred to as the "analog" estimator since it is an analog tallying scheme of the scattering reaction.

3.3 Application of Monte Carlo Tallies for Generating A Cross Section Library

To analyze the performance of Monte Carlo for the task at hand, two markedly different cases will be examined: a library generated for the case of single pin cell with data obtained only for each material; and a library generated for a 5x5 array of 21 fuel rods, two water-filled guide tubes and two Pyrex-filled guide tubes with library data obtained for each pin and concentric rings within each pin type to capture the resonance self-shielding effect.

Each of these models are described in Appendix A. As a reminder, all libraries in this work were generated using the flux separability approximation discussed in Section 2.2.2.

3.3.1 Pin-Cell Model

The first case to consider is a hot-zero power UO_2 pin cell with typical beginning of cycle material parameters. This model provides the simplest production-level scenario which could be used to generate cross sections. The pin cell is fully defined (including input files) in Appendix A.

This pin cell was fully instrumented with tallies to produce a macroscopic MGXS library using the 47-group structure discussed in Appendix B. These tallies included up to P_2 scattering production matrices and the total fission energy spectra data. This calculation was performed by tallying over one billion histories with 1.9 million discarded histories to converge the fission source. A forty-seven group structure was utilized for applicability to production problems and because few-group structures (i.e., two or four groups) have such broad structures that tallying efficiency is not a major concern.

Due to the large size of data, not every outgoing group will be quantitatively examined for every material and scattering order. Therefore one group each from the fast, epithermal, and thermal energy regimes for only the fuel and the moderator will be discussed. The groups to be examined are groups 4, 14, and 44. Group 4 has energy bounds of 1.35 to 2.23 MeV. This group was chosen simply because it is high enough in energy to contain interesting inelastic collision physics but low enough in energy to provide reasonably low uncertainties. Group 14 has energy bounds of 29.0 to 47.8 eV; this group is above the free-gas cutoff, but the presence of a large ^{238}U resonance at roughly 37 eV makes this group slightly more interesting. Finally, group 44 has energy bounds of 0.0428 to 0.0569 eV; this group was chosen because it contains the 600K thermal energy of 0.0517 eV.

This analysis will begin by comparing the reported relative uncertainties of the generated multi-group cross sections as a function of the number of histories. The types included in this analysis are the total cross section (Σ_t), the fission production cross section ($\nu\Sigma_f$), the P_0 through P_2 scattering moments ($\Sigma_{s,0}$, $\Sigma_{s,1}$, and $\Sigma_{s,2}$ respectively),and the fission spectra (χ). These data were generated for each of the 47 groups, including the energy transfer matrix $g' \rightarrow g$ for the scattering moments. The outgoing data for the scattering moments are condensed to one single-value for each incoming group, including the proper propagation of error. All data are tallied using track-length estimators where possible, but collision estimators were applied when outgoing information is required in the case of the scattering moments and fission spectra.

Figures 3.1 and 3.2 show this behavior for the fast group, group 4, in the fuel and moderator, respectively. Figures 3.3 and 3.4 show the same for the epithermal group, group 14, and Figures 3.5 and 3.6 show this information for the thermal group, group 44.

All cases show that the largest uncertainties are observed in $\Sigma_{s,1}$, $\Sigma_{s,2}$, and sometimes the χ data. When these data are furthest from zero (in the fast group for all cases), they lag behind the least. On the other hand, when these values become close to zero (such as when scattering becomes mostly isotropic in the epithermal range or when the fission spectra approaches zero), the relative uncertainties have values larger than 10% after even one billion histories. This study can be summarized by saying that if one wanted to ensure that all data was certain to within 0.1% for just an isotropic problem, then a total of 100 million histories would be required, driven by the groups 14 and 44 fuel $\Sigma_{s,0}$ data.

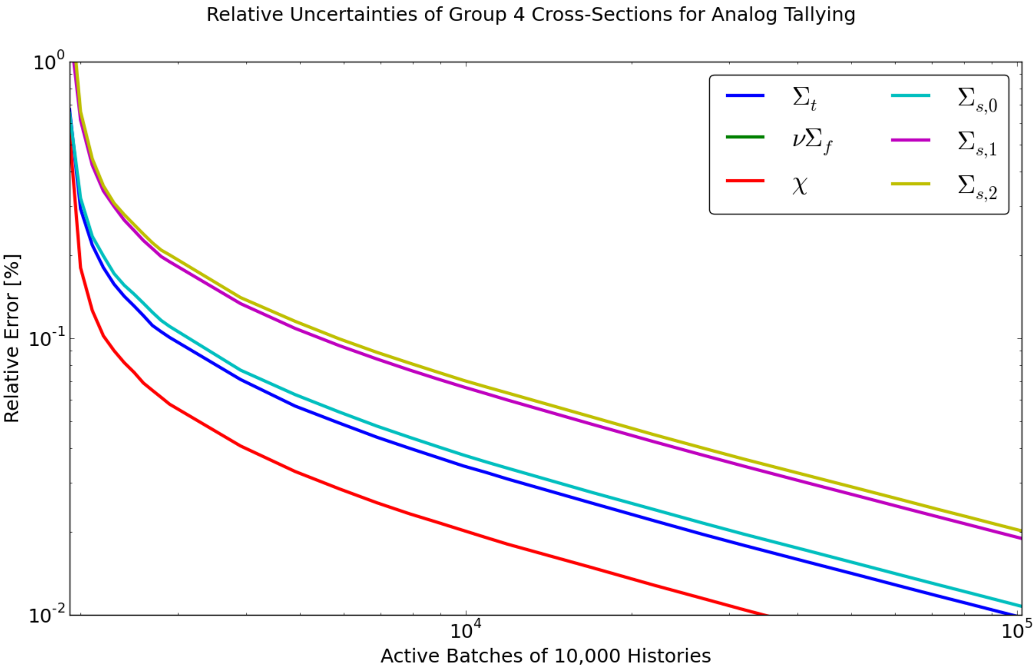

Figure 3.1: Fuel Uncertainty Convergence in Group 4

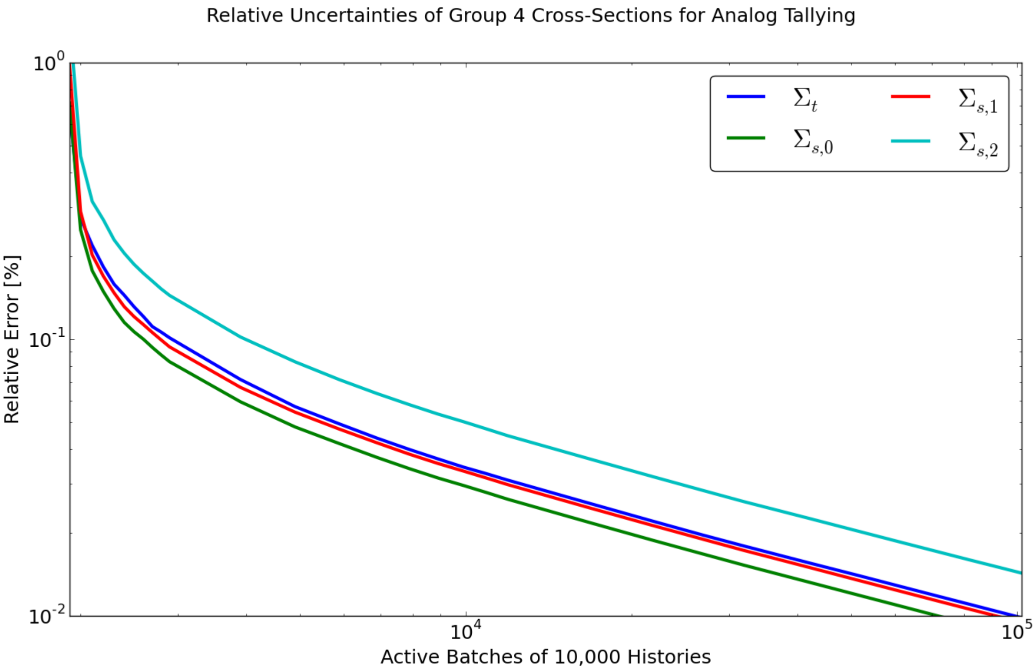

Figure 3.2: Moderator Uncertainty Convergence in Group 4

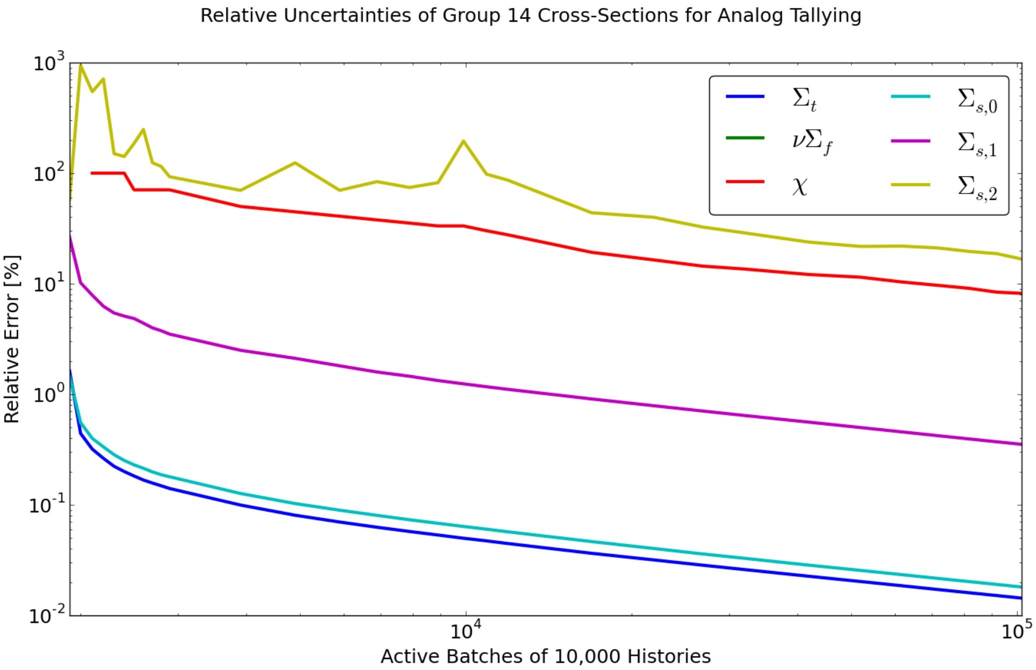

Figure 3.3: Fuel Uncertainty Convergence in Group 14

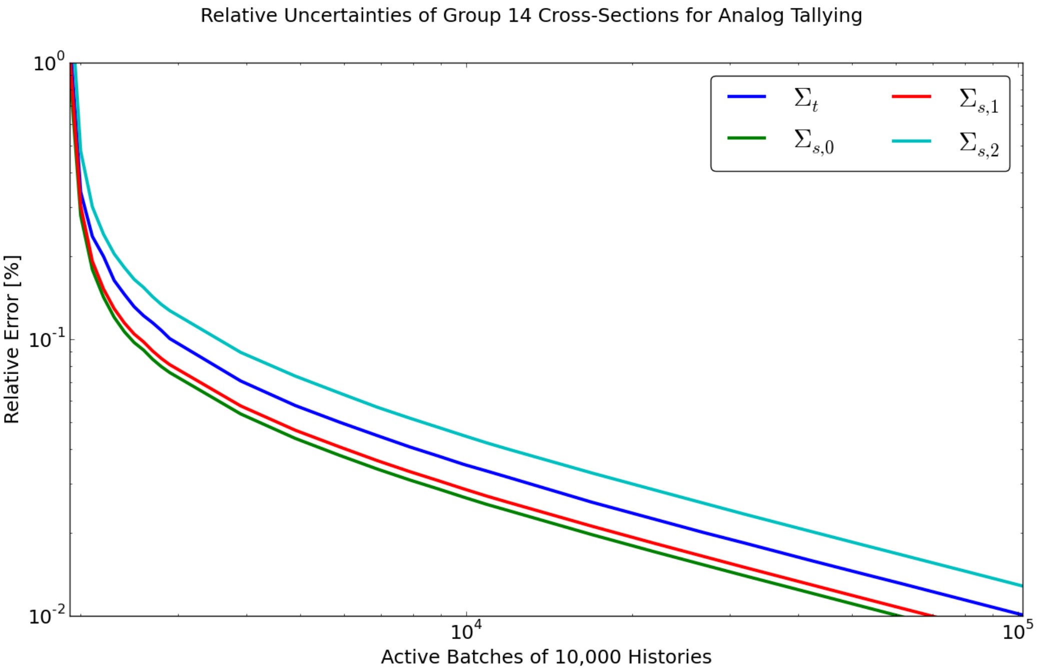

Figure 3.4: Moderator Uncertainty Convergence in Group 14

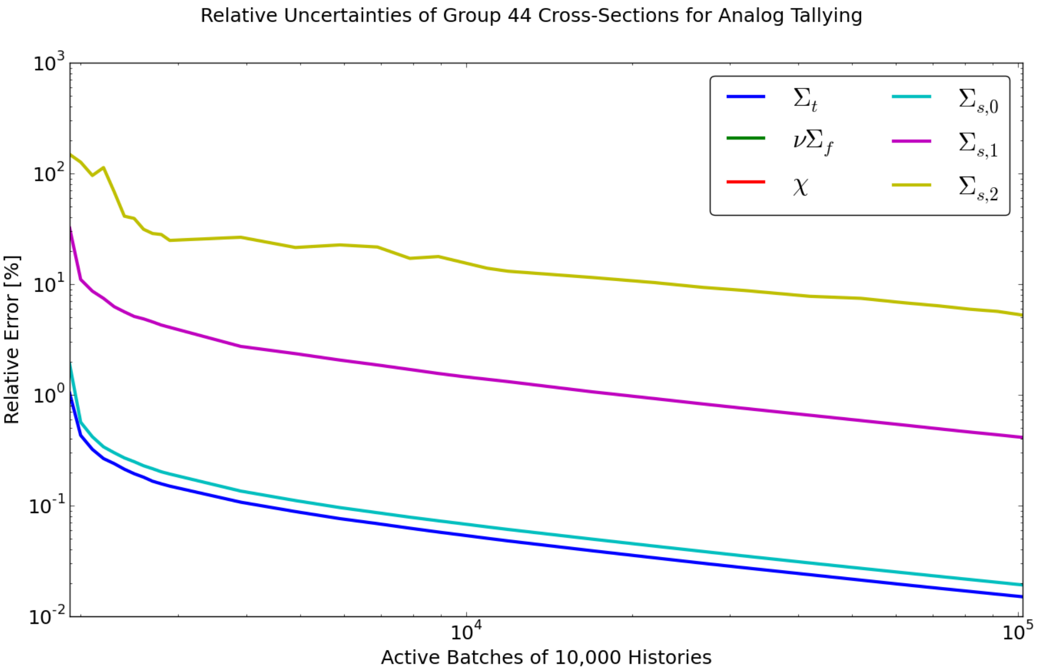

Figure 3.5: Fuel Uncertainty Convergence in Group 44

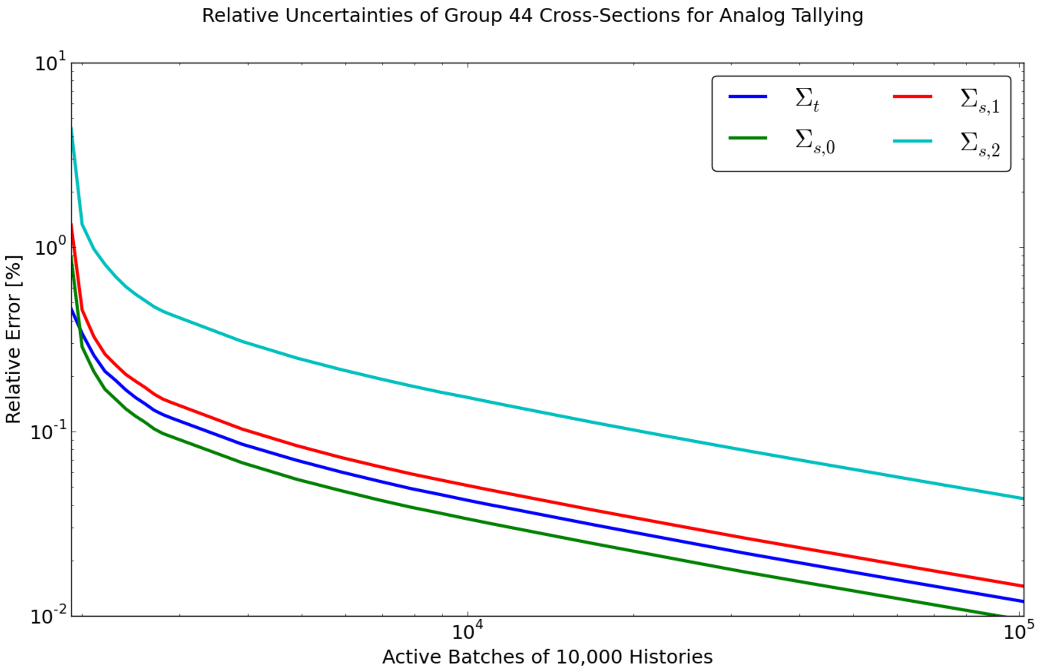

Figure 3.6: Moderator Uncertainty Convergence in Group 44

The next result to investigate is how well an integral parameter is predicted despite the above uncertainties. This integral parameter will be the calculated eigenvalue of the pin cell when the newly-generated MGXS library is used by a deterministic transport code in a model of a pin cell with the exact same model description. The MPACT [18] Method of Characteristics (MOC) code was used for this effort. MPACT was chosen because it is an accessible deterministic transport code which can handle pin-cell geometry faithfully and supports up to P_5 anisotropic scattering. The input for this model can also be found in Appendix A. In this model, a ray spacing of 0.005 cm is used. The angular quadrature is Chebyshev-Yamamoto (with 32 azimuthal and 3 polar angles). The fission source and eigenvalue are converged to 10^{-6}.

This analysis was performed with libraries generated at varying OpenMC histories and with both P_0 and P_2 scattering treatments. The results of the P_0 calculation are shown in Figure 3.7; Figure 3.8 shows the same information has the y-axis in terms of the percent-mille (pcm) bias between the MPACT solution and the 1 billion particle OpenMC solution. The same results are shown for P_2 scattering in Figures 3.9 and 3.10.

The one billion history OpenMC eigenvalue is 1.181820 ± 0.000029; the final P_0 MPACT eigenvalue is 1.1775166 while the P_2 eigenvalue is 1.1777991. These values yield final biases of -364 and -340 pcm, respectively. Since this bias was quite large, the models were compared for consistency and the same sort of system even set up and run in a similar, but independent, code system: the Serpent Monte Carlo code [5] was used to generate the cross sections and a different MOC code, OpenMOC [19], was used to perform the deterministic transport calculation. The results were the same. Yoshioka [9] performed a similar analysis - generating multi-group cross sections with Monte Carlo and providing the results to a transport solver using a similar pin cell model. Yoshioka found that the eigenvalue bias was around 300-400 pcm when using sixteen groups; they did not study the bias further than identifying that it exists. This gives some indication that the bias is to be expected and not a flaw that is unique to the methods used in the analysis discussed in this section.

Some of this bias can be attributable to the spatial and angular discretization schemes used in the MOC method (as well as any other deterministic transport method). However, the portion of the bias which is introduced by the multi-group approximation could be improved by:

- Utilize a finer energy group structure:
  - Doing so can reduce the errors due to the above weaknesses.
- Further discretization of the cross section generation regions:
  - Only one set of macroscopic cross sections were generated for each material type; that is, the spatial variation in the self-shielding is not accounted for with one set of cross sections.
- Utilize an anisotropic weighting flux for cross section generation:
  - This study used an isotropic weighting flux due to the flux separability approximation.
  - This can lead to a mis-prediction in the amount of neutrons being reflected back into the fuel from the moderator as the neutrons near the fuel-gap-clad and clad-moderator interfaces should be encountering cross sections which depend strongly on their direction of motion.

Next, when examining the convergence trajectory, it is seen that the MPACT solution can not be considered “converged” until roughly 10,000 batches (or 100 million active histories) as this is the point at which the eigenvalue begins to vary by less than around 10 pcm.

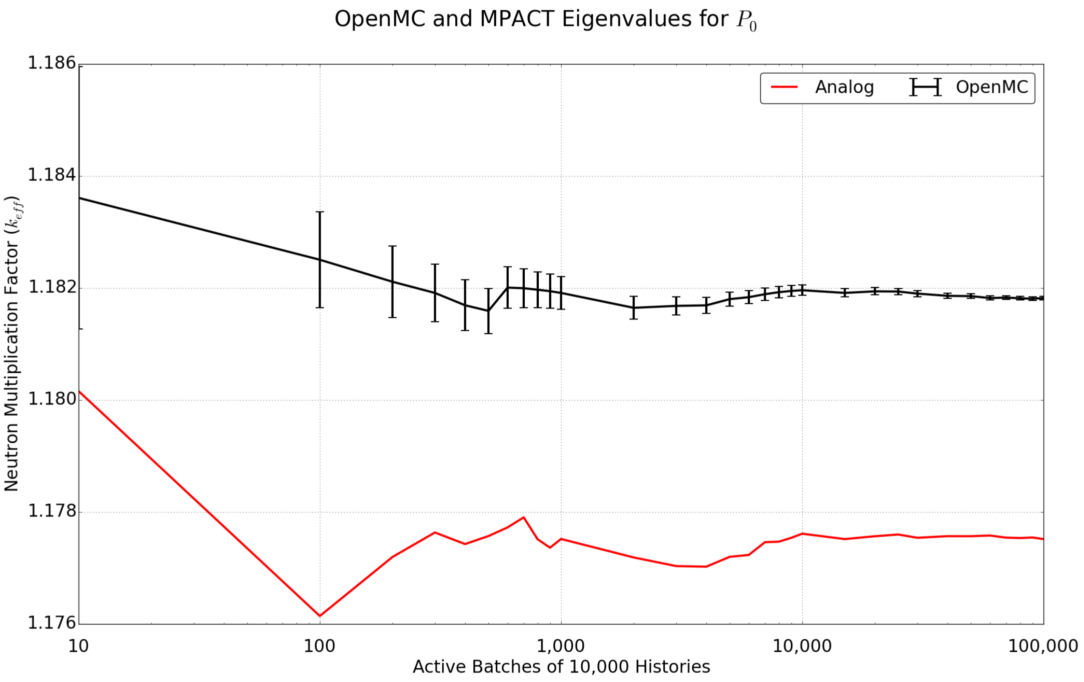

Figure 3.7: Pin Cell Problem MPACT P_0 Eigenvalue Convergence

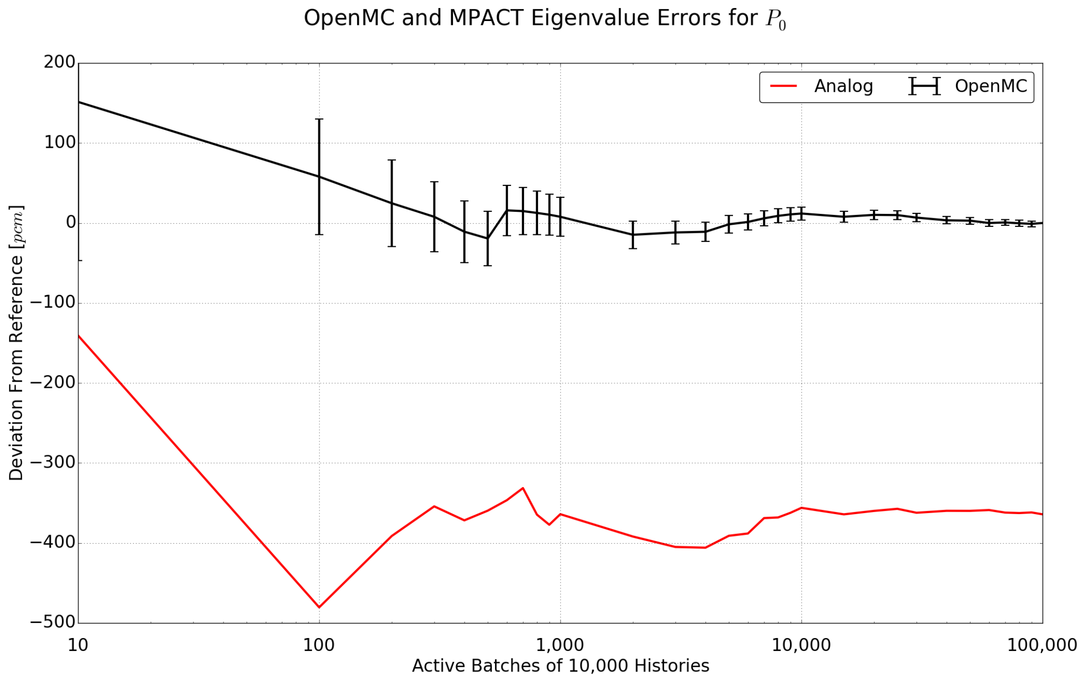

Figure 3.8: Pin Cell Problem MPACT P_0 Eigenvalue Convergence [pcm]

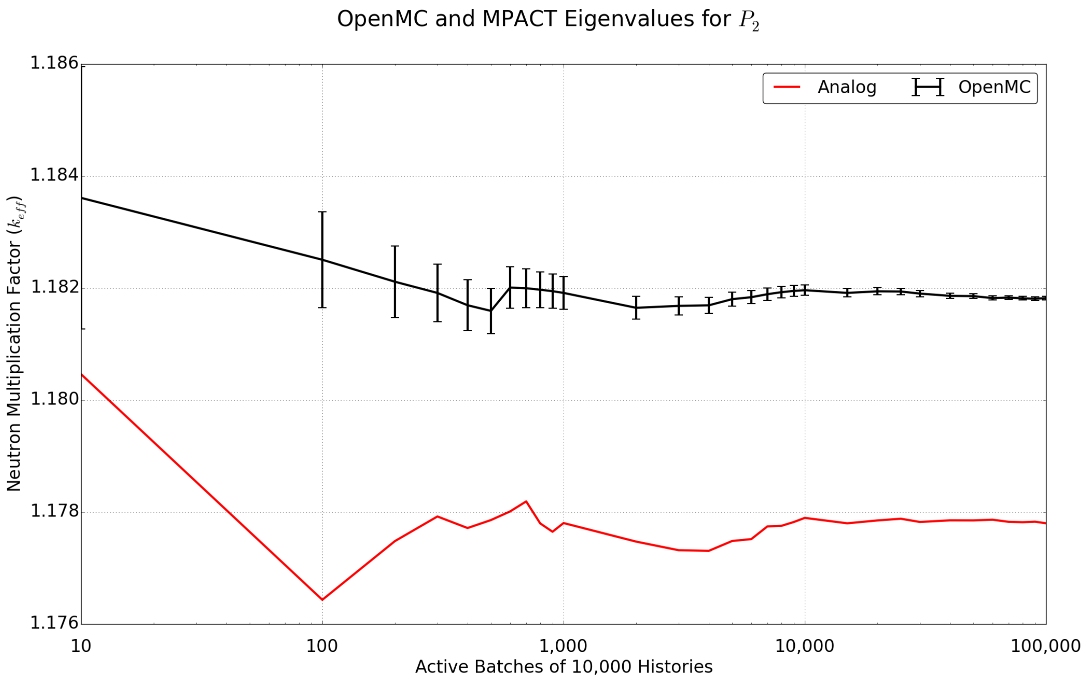

Figure 3.9: Pin Cell Problem MPACT P_2 Eigenvalue Convergence

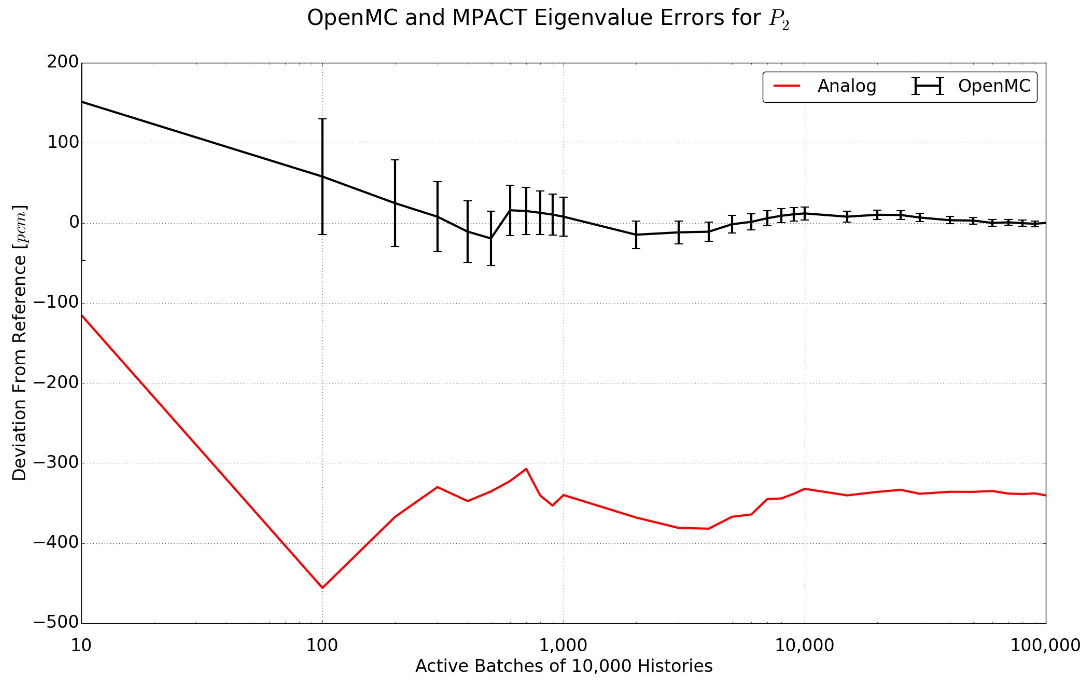

Figure 3.10: Pin Cell Problem MPACT P_2 Eigenvalue Convergence [pcm]

3.3.2 Sub-Assembly Model

The second case to consider is a hot-zero power 5x5 array consisting of 21 fuel rods, two water-filled guide tubes and two Pyrex-filled guide tubes as described in Appendix A. The tallies were set up such that each material within each pin produced its own tallies, and further, each fuel pellet and Pyrex rod were subdivided into five and two (respectively) tally regions of equal volume. This approach resulted in a total of 194 total tally regions, each capturing data to generate all the different macroscopic MGXS types using the same 47-group structure used for the pin-cell. Finally, these tallies included up to P_2 scattering production matrices and the total fission energy spectra data. This calculation was also performed with one billion active histories with nine million discarded histories to converge the fission source.

To minimize the data, this examination will only concern itself with the eigenvalue and pin power convergence after being run in the MPACT code. The individual groups for each tally region can be ignored since their behavior will follow that shown for the pin-cell, just with higher relative uncertainties due to the smaller fraction of histories which enter into each tally's respective volume.

Like the pin-cell model, this analysis was performed in MPACT with libraries generated by OpenMC at OpenMC history counts and with both P_0 and P_2 scattering treatments. This model is described thoroughly in Appendix A. In this model, a ray spacing of 0.005 cm is used. The angular quadrature is Chebyshev-Yamamoto (with 32 azimuthal and 3 polar angles). The fission source and eigenvalue are converged to 10^{-6}.

The results of the P_0 effort are shown in Figure 3.11; Figure 3.12 shows the same information but is normalized with the y-axis being the pcm bias between the MPACT solution and the 1 billion particle OpenMC solution. The same results are shown for P_2 scattering in Figures 3.13 and 3.14.

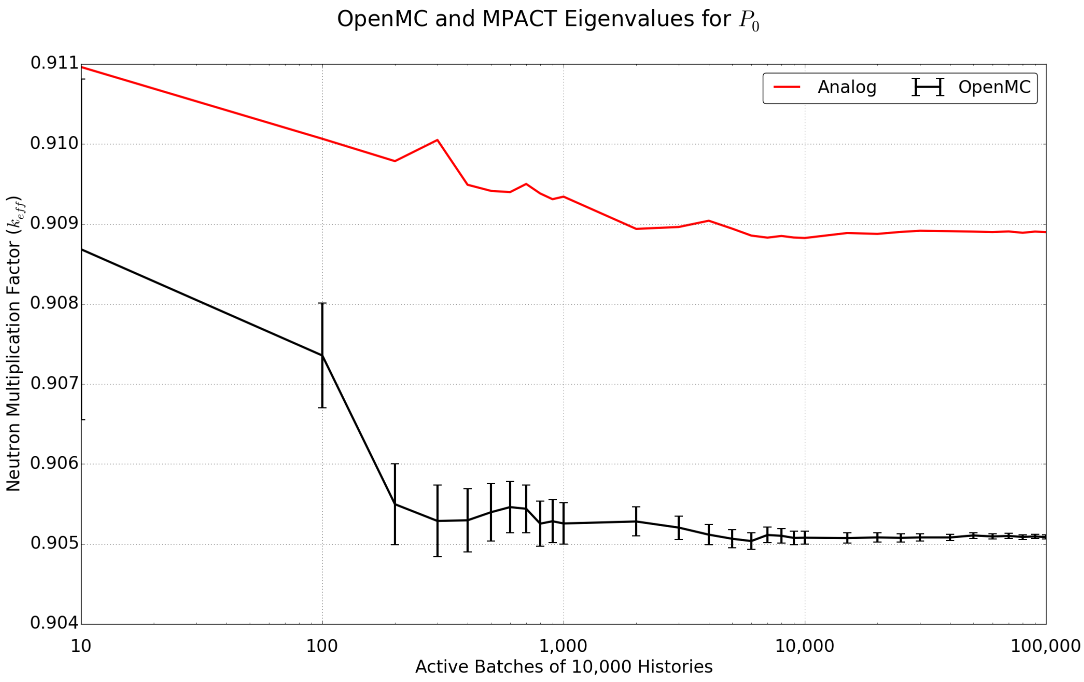

Figure 3.11: Sub-Assembly Problem MPACT P_0 Eigenvalue Convergence

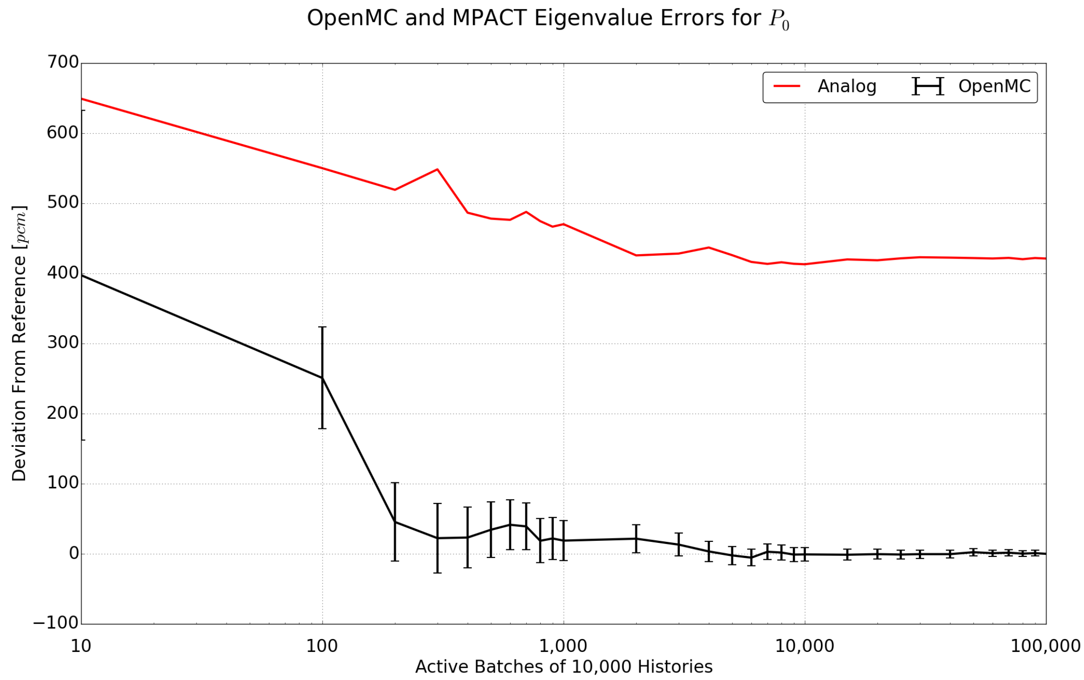

Figure 3.12: Sub-Assembly Problem MPACT P_0 Eigenvalue Convergence [pcm]

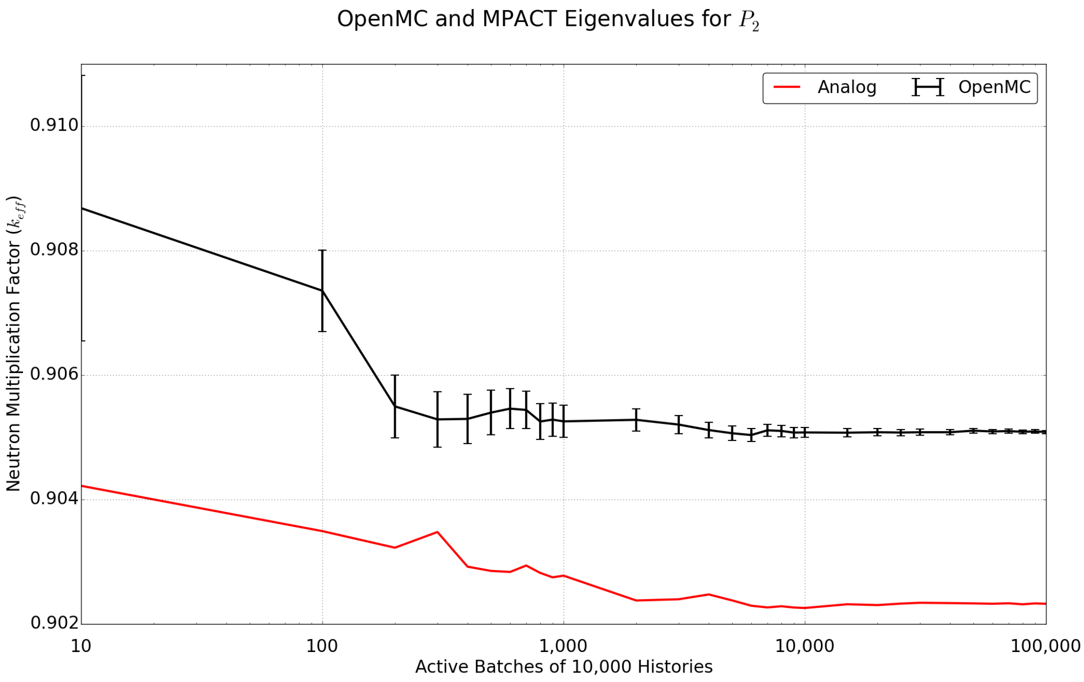

Figure 3.13: Sub-Assembly Problem MPACT P_2 Eigenvalue Convergence

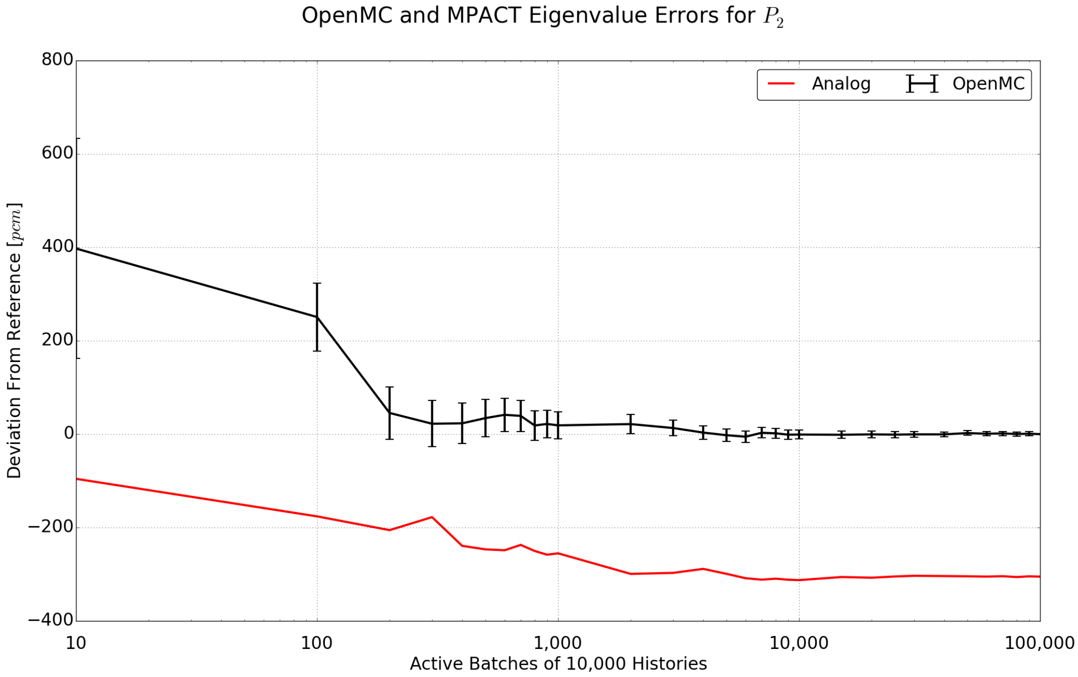

Figure 3.14: Sub-Assembly Problem MPACT P_2 Eigenvalue Convergence [pcm]

The one billion history OpenMC eigenvalue is 0.905086 ± 0.000026; the final P_0 MPACT eigenvalue is 0.9088986 while the P_2 eigenvalue is 0.9023248. These values yield final biases of 421 and -305 pcm, respectively.

A general observation can be made that the MGXS library generation requires around 10,000 batches (100 million histories) to obtain sufficiently converged results for this model after the non-negligible entries in the scattering moment matrices have been sufficiently converged.

Of course, the value of k_{eff} is not the only calculated quantity to consider: the other is the power distribution. To that end, Figures (3.15) and (3.16) show the convergence of the maximum pin power error (top) and the root-mean-squared error (bottom) of all 21 fuel-bearing pins. In this case, the maximum pin power error is defined as the percent difference between the pin power of the highest-power pin in the sub-assembly value at the particular batch count and the OpenMC reference peak pin power presented in Appendix A. The root-mean-squared is the same, but showing the root-mean-square error of all the fuel pins.

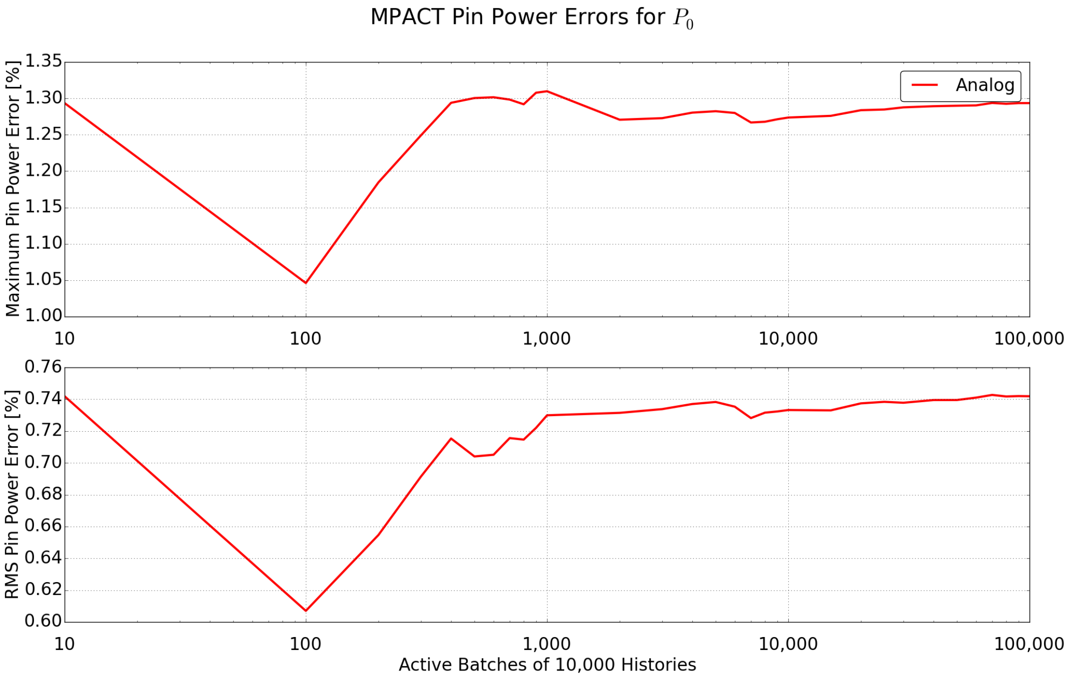

Figure 3.15: Sub-Assembly Problem MPACT P_0 Pin Power Convergence

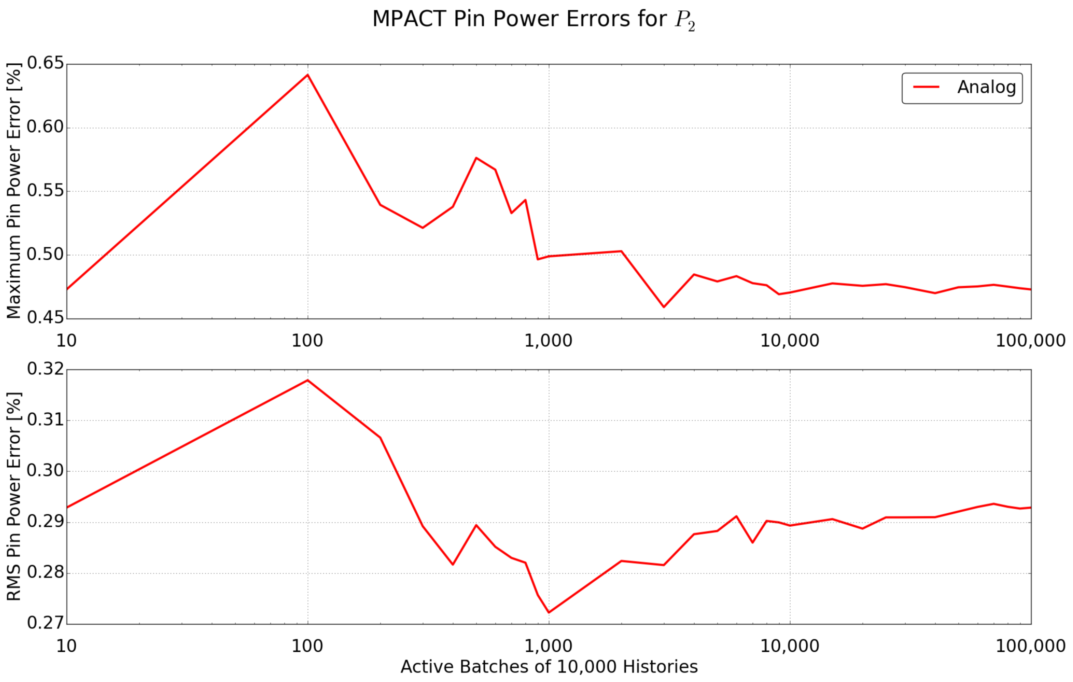

Figure 3.16: Sub-Assembly Problem MPACT P_2 Pin Power Convergence

Figure (3.15) shows that the error in the hottest pin eventually converges to an error of roughly 1.29% when using P_0 scattering in MPACT after around 1,000 batches, or 10 million active histories. The root-mean-square error also converges at roughly the same time to a value of 0.74%. When using P_2 scattering (Figure (3.16)) the hottest pin error drops to around 0.47% and the root-mean-square error to around 0.29%; both occur at around 100 million active histories.

3.3.3 Application Summary

The above analysis found that a grand total of 100 million active histories was required before the library could truly become useful. One hundred million histories is a very large number, especially for a single pin cell out of the many different types of pins and operating conditions which would need to be examined. Further, the cross section tallies were set up only on a material basis and thus did not describe the spatial self-shielding effect of fuel resonances. Adding tallies to sufficiently describe this effect would require even more histories since the phase-space volume represented by each tally would be reduced. This is prohibitively expensive and will not efficiently allow for a system where MC-generated MGXS libraries are applied on a local basis for a global deterministic transport solver.

The above work also showed that quantities which required tallying information about the outgoing particle (the scattering moment matrices and fission spectra) are the least efficient of the cross sections to be tallied. This was both because the presence of outgoing information precludes the use of track-length estimators, but also because the tallying efficiency diminishes as the number of outgoing dimensions to integrate (such as outgoing energy and scattering angle) increases. This latter phenomena is best explained by observation of Eq. (3.4). Since there are more dimensions to integrate, the number of samples per filter is decreased thus increasing the stochastic uncertainty. If this weakness could be improved then the tallying efficiency could be increased significantly and the cost of utilizing Monte Carlo methods to generate MGXS libraries would be commensurately reduced. Accomplishing this task is the goal of this dissertation.

3.4 Improved Method of Tallying Outgoing Distribution Information

As stated, the goal is to improve upon the tallying efficiency of data needed for generating a MGXS library. More specifically, this effort is targeted at the least efficient of this data: the scattering moment matrices, $\Sigma_{s,l}$. When investigating potential options, it is prudent to begin examining work performed by others.

3.4.1 Previous Work

A major potential candidate for help in improving the tallying efficiency is one previously mentioned, the Explicit-P$_n$ method by Redmond. This method directly sampled the Legendre moments, but attempted to sample from more of the angular distribution at each scattering event to improve the span of information tallied at each collision. This approach works by determining the contribution to a set of equi-probable angular bins and energy groups and scores a weighted result for each. This weighting is determined by finding the probability of a neutron scattering event into the target angle bin and group pair. This is typically done in the Center-of-Mass (CM) frame and then converted to the Laboratory (LAB) frame for scoring, though the specifics depend on the exact law in use. Unfortunately, this method requires knowledge of which scattering angle results in an outgoing energy which matches a group boundary. This boundary information is unique to each incoming energy, nuclide and reaction channel and would therefore need to be calculated at the time of a collision or a priori. Further, this method still samples a finite set of points (determined by the number of angle/energy bins chosen by the user); while more information is provided about the distribution, it still provides limited information while incurring a large run-time penalty.

3.4.2 Options Not Pursued

Anther method which, to the author's knowledge, has not been published could have been investigated for improving the tallying efficiency. In this method, multiple "virtual" scatters are simulated at the time of tallying such that more of the energy and angle dimensions are explored per collision. This can be then further expanded by using these "virtual" collisions to enable track-length tallies.

The first item, sampling a number of "virtual" scatters per actual scatter, is a simplified implementation of Redmond's Explicit-P_n method since the "virtual" samples are not targeted to particular groups like they are in Explicit-P_n. This method shares the down side of having to incur the cost of calling the scattering routines multiple times per collision event.

The second item, using these "virtual" collisions to enable track-length tallies is a viable option, so long as the run-time impact is not too burdensome. Unfortunately, the scattering kinematics routines, some of the costliest in a Monte Carlo simulation, must be called for every nuclide in the material every time a neutron passes through that material. This additional computation cost will add up quickly.

These methods were implemented by the author in a customized version of OpenMC and tested on an infinite homogeneous mixture of ^{1}H and ^{235}U with the same 47-group structure discussed in Appendix B and 900,000 active histories. The "virtual" scatters were sampled four times for every tally event (whether it be collision or track-length).

For the first method (which is simply a collision implementation), the P_0 and P_1 uncertainties were improved by 11 and 46%, respectively. Unfortunately the additional computational burden of this method slowed down the OpenMC simulation by nearly 65%. In terms of the figure-of-merit (defined in Eq. (3.10)), this method yielded a factor of two improvement compared with Direct-P_n in the P_0 data, but actually reduced performance for P_1 as the figure-of-merit was 25% lower than the equivalent Direct-P_n value.

$$FOM = \frac{1}{\sigma^2 t} \tag{3.10}$$

The second method (a track-length implementation) fared slightly better. The run time was reduced by 76% and the total figure-of-merit for P_0 and P_1 were increased by only factors of 5.8 and 1.3, respectively.

These results imply that the method can yield a modest improvement, though not without a significant decrement to the computational burden. For these reasons, this option was not considered for further examination.

3.4.3 Improved Method

The Explicit-P_n method discussed by Redmond and the options presented in the previous section all relied entirely on increasing the number of samples of Eqs. (3.7) and (3.8) when tallying the results in order to improve the tallying efficiency. This was done such that reaction channels, outgoing energies, and scattering angle could be more finely resolved with each collision, leading to a reduction in the variance of the tally. However, the increased number of samples provided only a modest improvement for a large computational cost and is therefore considered to be not useful for practical applications. Note that the production moment integral, Eq. (3.8), is provided for readability below as Eq. (3.11).

$$\hat{\Sigma}_{s,l,g'\to g,i}\phi_{g',i} = \sum_{n} N_n \sum_{MT_n} \int_{V_i} \int_{E_{g'}}^{E_{g'-1}} \int_{E_g}^{E_{g-1}} \int_{4\pi} \int_{-1}^{1} \left[Y_{n,MT}(E')\sigma_{s,n,MT}(E') f_{n,MT}(E' \to E,\mu) \right.$$
$$\left. \times P_l(\mu)\psi\left(E',\vec{r},\vec{\Omega}\right) d\mu\, d\vec{\Omega}\, dE\, dE'\, dr^3 \right] \quad (3.11)$$

Instead, consider the following approach. The desired integral (Eq. (3.11)) can be split in to two parts: the conditional probability function describing the outgoing particle distribution in energy and angle given that a particle is generating path-length about location $\vec{r}$, and the probability that a particle generated path-length about location $\vec{r}$. The conditional probability, $h_{l,g}(E',\vec{r})$, is defined in Eqs (3.12). The probability of a particle generating path-length in a particular phase-space is the angular flux, $\psi\left(E',\vec{r},\vec{\Omega}\right)$. With this nomenclature, the scattering production integral can be simplified as is shown in Eq. (3.12b).

$$h_{l,g}(E',\vec{r}) = \sum_{n} N_n \sum_{MT_n} Y_{n,MT}(E')\sigma_{s,n,MT}(E') \int_{E_g}^{E_{g-1}} \int_{-1}^{1} f_{n,MT}(E' \to E,\mu) P_l(\mu) d\mu\, dE \quad (3.12a)$$

$$\hat{\Sigma}_{s,l,g'\to g,i}\phi_{g',i} = \int_{V_i} \int_{E_{g'}}^{E_{g'-1}} \int_{4\pi} h_{l,g}(E',\vec{r})\, \psi\left(E',\vec{r},\vec{\Omega}\right) d\vec{\Omega}\, dE'\, dr^3 \quad (3.12b)$$

So far all that has been done is the terms have been combined in to convenient groupings, based on the conditional probability and the probability of the condition occurring.

Luckily, $h_{l,g}(E',\vec{r})$ has two properties which make it useful to our purposes. First, every quantity (and distribution) on the right-hand side of Eq. (3.12a) is present in the ACE library. More importantly, this library is already in use by the Monte Carlo neutron transport code. Second, since all the information in Eq. (3.12a) is already known, it can be deterministically evaluated.

These two factors mean that the Monte Carlo *does not need to stochastically integrate this eight-dimensional integral* (ten, if you count the sum over isotopes and their reaction channels). Instead, the Monte Carlo only needs to be relied upon to estimate the three dimensions of space, incoming energy, and particle direction (V_i, E', and $\vec{\Omega}$). Fortunately, these are the same dimensions which must be resolved for every other major quantity of interest for the generation of MGXS libraries since most multi-group data are flux-weighted quantities.

This combined deterministic and stochastic estimation is called both deterministic scoring [20], or expected value scoring [21]. While the exact improvement can not be explicitly determined (as it is highly dependent upon the functions being integrated), it has been shown that the variance of these reduced dimensionality integrals is *always* smaller than the standard sample-mean estimator [21,22].

This conclusion stands to reason because it is effectively a restatement of the following: the stochastically integrated results will be more certain if all known information is included. In terms more specific to the application at hand: every time a scattering event is tallied, there is not a single outgoing energy and scattering angle scored. Instead, the entire continuum of possible outgoing energy and scattering angles is tallied. Every one of the $G \times G$ elements in the scattering matrix, for every L order receives its applicable data.

This method has an additional benefit which as of yet has not been discussed. When presenting the Direct-P$_n$ and other methods, it was noted that only collision estimators could be used for the scattering moment matrices since a track-length tally does not tally an actual sampled collision and thus no outgoing information would be known by the tally. Now that the conditional probability describing the outgoing particle distribution is considered known and deterministically integrated, scattering moment matrix tallies can be used with a track-length estimator form. This is a very useful finding, as it means not only will the variance be improved due to more information being tallied, but more information will be tallied more frequently due to the track-length estimator.

The acts of deterministically integrating some of these quantities and the summing of the complete set of known data to every $G \times G \times L$ tally unfortunately requires time to compute. Therefore the improvement in tallying efficiency has to be weighed against the additional computational cost before the method can be considered useful. This work will therefore focus on determining the reduction in relative uncertainties as well as the computational cost of doing so.

3.4.3.1 Practical Application of Improved Method

The form developed in Eqs. (3.12) can be further developed to represent the form the MC solver would more practically utilize during the tallying process. First, the known conditional probability data ($h_{l,g}\left(E',\vec{r}\right)$) can be rewritten as is shown in Eqs. (3.13) and (3.14) for the scattering moment and scattering production moment estimators, respectively. These data have been normalized by the cross sections for reasons of reducing memory, which will be discussed in Chapter 5.

$$f_{n,E'\to g,l}(E') = \frac{\sum\limits_{MT}\sigma_{s,n,MT}(E')\int\limits_{E_g}^{E_{g-1}}\int\limits_{-1}^{1} P_l(\mu)\, f_{n,MT}(E',E,\mu)d\mu\, dE}{\sum\limits_{MT}\sigma_{s,n,MT}(E')} \tag{3.13}$$

$$\hat{f}_{n,E'\to g,l}(E') = \frac{\sum\limits_{MT}Y_{n,MT}(E')\sigma_{s,n,MT}(E')\int\limits_{E_g}^{E_{g-1}}\int\limits_{-1}^{1} P_l(\mu)\, f_{n,MT}(E',E,\mu)d\mu\, dE}{\sum\limits_{MT}\sigma_{s,n,MT}(E')} \tag{3.14}$$

Next, the scattering and scattering production moment matrices tally estimator which uses this information can be written using a track-length estimator, as are shown in Eqs. (3.15) and (3.16).

$$\Sigma_{s,l,g'\to g,i}\phi_{g',i} = \sum_{event\, i\in g',V} \omega_i\, TL_i\, N - N\sigma_{s,n}(E')\, f_{n,E'\to g,l}(E') \tag{3.15}$$

$$\hat{\Sigma}_{s,l,g'\to g,i}\phi_{g',i} = \sum_{event\, i\in g',V} \omega_i\, TL_i\, N_n\sigma_{s,n}(E')\, \hat{f}_{n,E'\to g,l}(E') \tag{3.16}$$

For completeness, these can also be written in the form of the collision estimator, which requires a collision with a specific nuclide to have occurred. These estimators are shown in Eqs. (3.17) and (3.18).

$$\Sigma_{s,l,g'\to g,i}\phi_{g',i} = \sum_{event\, i\in n,g',V} \omega_i\, f_{n,E'\to g,l}(E') \tag{3.17}$$

$$\hat{\Sigma}_{s,l,g'\rightarrow g,i}\phi_{g',i} = \sum_{event\, i\in n,g',V} \omega_i \hat{f}_{n,E'\rightarrow g,l}(E') \tag{3.18}$$

The deterministic integration shown in Eqs. (3.13) and (3.14) is, unfortunately, a computationally complicated integral that is expensive to compute. This threatens to remove the gains in tallying efficiency of this proposed improved method. Therefore, to save computation time, a pre-processing code should be written which computes these quantities before the particle transport phase ever begins. This pre-processor requires as input the continuous-energy, ACE formatted input data, the desired multi-group cross section energy group structure, a list of the nuclides and temperatures needed. This data is then used to produce a set of angular distributions for an array of incoming energy values with the probability distribution functions integrated over the outgoing energy group, and expanded in Legendre polynomials.

3.4.3.2 Improved Method Example

To visualize the benefits of the method, consider the following simulation of tallying randomly sampled scattering distributions when using both the analog method of scattering and the improved method presented above.

This simulation will randomly select from incoming energies between 1.25 and 1.5 eV according to a uniform probability distribution. These energies were chosen simply because this energy range has a nearly equal probability of scattering to the next lowest energy group (with a group boundary of 0.625 eV) and scattering back in to the initial group.

For the analog method of tallying, the simulation then randomly sampled the outgoing energy and angle using elastic (target-at-rest) kinematics off of hydrogen. This outgoing information was then used in the Direct-P_n formulation to tally directly to P_2 scattering moment matrices as is shown in Eq. (3.9).

For the improved method, the integral in Eq. (3.13) was evaluated at the nearest energy points in the ACE data, 1.25 and 1.5 eV. These two distributions, with the reference solution at the average incoming energy (1.375 eV) are shown in Figure 3.17. In this plot, the left plot shows the distribution in the down-scatter group and the left plot shows the self-scatter distribution. The same sampled incoming energy was used to interpolate to the appropriate scattering moment matrices. To aid in visualization, the distributions were expanded from their Legendre coefficients in to the complete scattering angle distribution (using 1,001 points) for each outgoing energy group.

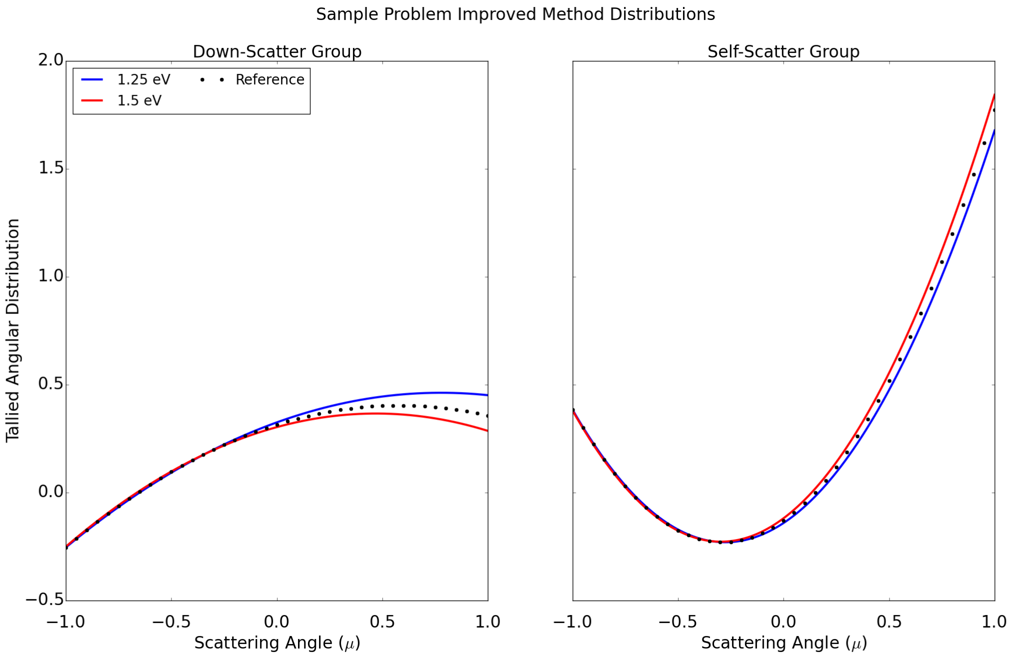

Figure 3.17: Improved Method Data at Various Energies

Since the improved method can only be calculated on an incoming energy grid (as thats how the data is provided, as discussed in Chapter 4), Figure 3.17 provides visual indication of the need for interpolating the distributions, though in practice it will be done by interpolating moments and not the distribution points themselves.

This simulation was run using 1, 10, 1,000, and 100,000 samples of the incoming energy. The results of these simulations are shown in Figures 3.18 through 3.21. In these figures the left plots are for the down-scatter group and the right-most plots are for scattering in to the same plot. The top set of plots show the analog distribution (in red), the improved method distribution (in blue), and the analytically calculated expected distribution denoted by the black circles. Finally, the bottom plots show the absolute error of the percent deviation from the reference distribution of each method. Before examining the figures, it is important to note that the vertical asymptotes seen in the errors are simply due to the reference distribution either crossing zero or the calculated distributions moving from being less than to greater than (or vice versa) the reference solution.

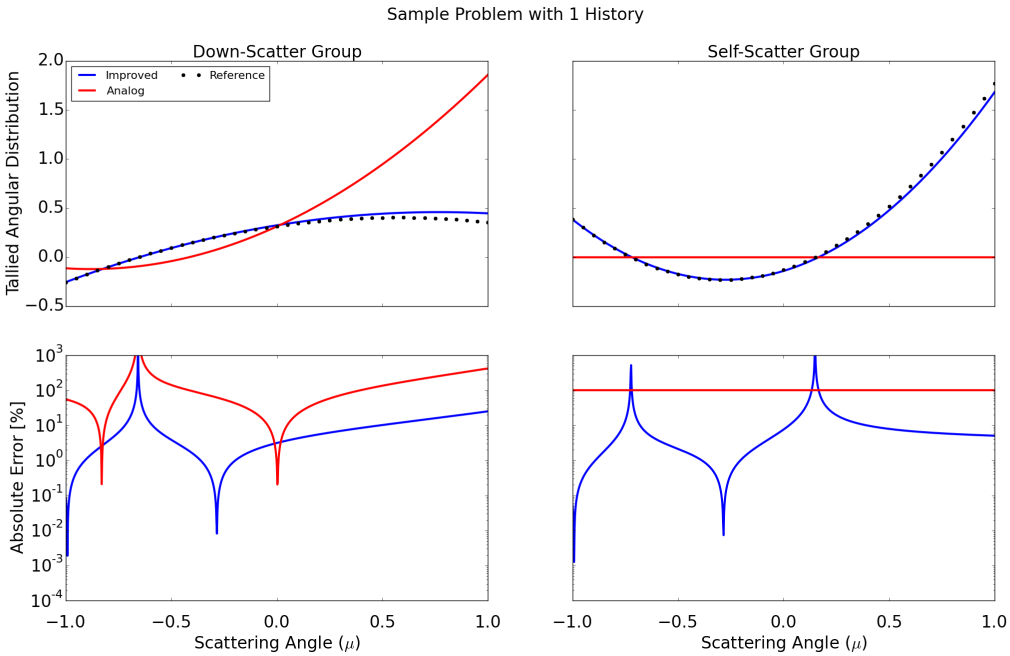

Figure 3.18: Sample Problem After 1 History

After only one sample, one would not typically expect that a two-group angular distribution could be accurately determined. This is confirmed by the percent error in the analog solution, which has errors on the order of 100% for the down-scatter group. Since the single sample taken happened to be a down-scatter event, the self-scatter group still has a null distribution; the tally does not yet learned that self-scatters are possible. Figure 3.18, however, shows that the improved method has errors between 1 and 10% in both groups, a one to two magnitude improvement over the analog.

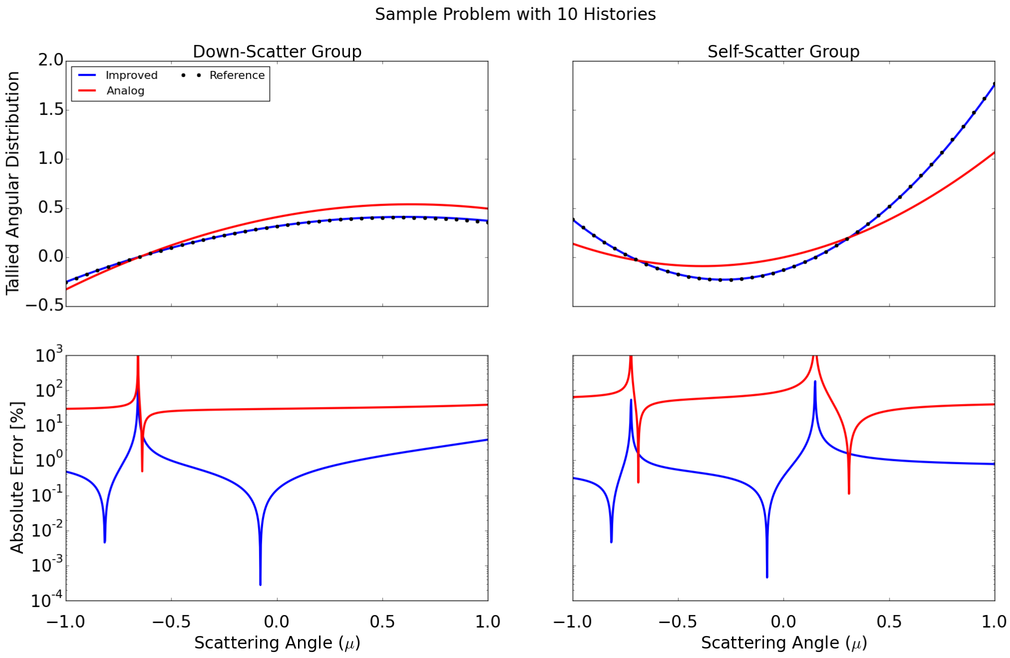

Figure 3.19: Sample Problem After 10 Histories

After 10 histories, the analog method recognizes that self-scatter can occur. The analog error is now between 10 and 100%, and the improved method is mostly below 1% with some areas above.

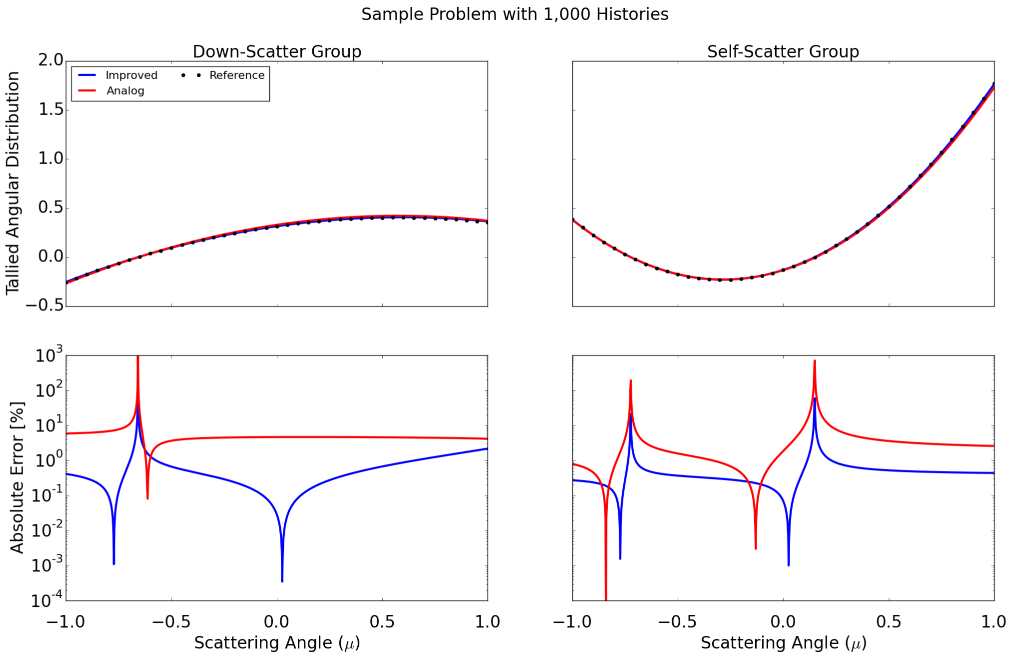

Figure 3.20: Sample Problem After 1,000 Histories

After 1,000 histories, the analog method has approached the accuracy levels of the improved method as it was after one history.

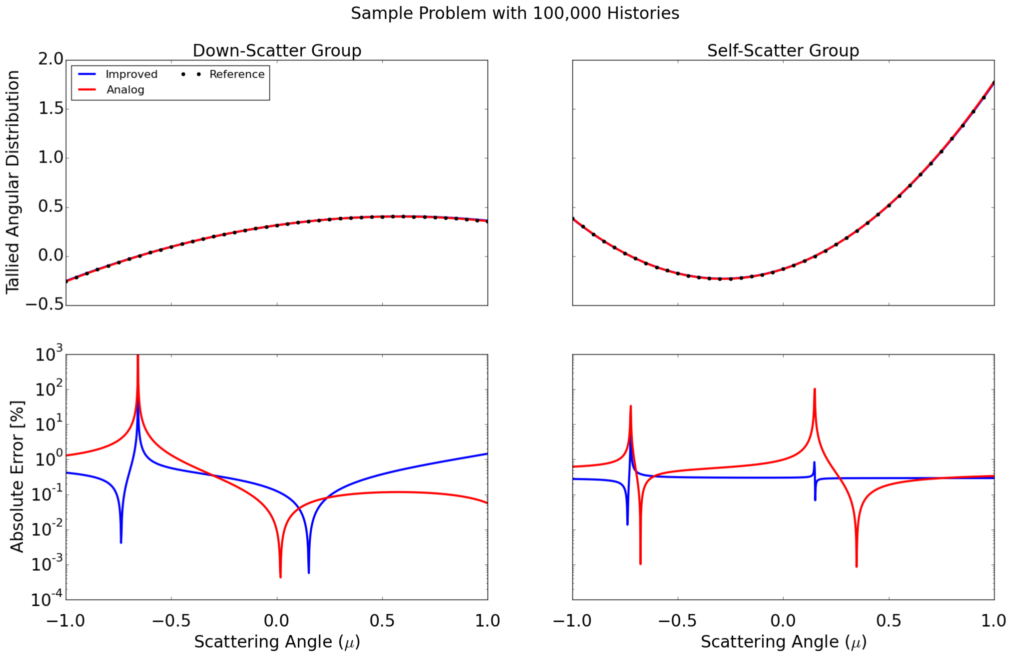

Figure 3.21: Sample Problem After 100,000 Histories

Finally, the improved method and analog method seem to perform equally well after 100,000 histories.

This simulation can also be used to understand the variance reduction of the method. The calculated relative uncertainty of these methods is shown for only the 10 and 100,000 history case for the P_1 and P_2 moments for the down-scatter group in Table 3.1. The self-scatter uncertainties do not provide any more information than the down-scatter and so are not shown. In this table a substantial improvement in the uncertainty is observed in the improved method data, even after only 10 histories. Further, the relative uncertainty is not a strong function of the scattering order for the improved method, but it is for the analog method. This is because all of the scattering moment matrices are populated with all the known information at once.

Table 3.1: Down-Scatter Uncertainty

Case	P_1 Uncertainty	P_2 Uncertainty
Analog @ 10 Histories	0.3874	1.6829
Improved @ 10 Histories	0.1044	0.0854
Analog @ 100,000 Histories	0.3511	1.2888
Improved @ 100,000 Histories	0.0793	0.0654

3.4.3.3 Improved Method Summary

This improved method of tallying the scattering moment matrices is based on recognizing that all of the outgoing particle information is known a priori. This can be taken advantage of to increase the tallying efficiency (reducing the uncertainty) of the stochastically integrated tallies since the complete outgoing probability distribution is tallied. Each tally event supplies every one of the $G \times G$ elements in the scattering matrix, for every L order, with its share of data.

In addition to reducing the uncertainty, this method allows for the use of a track-length estimation process potentially offering even further improvement to the tallying efficiency.

This method is an act of mining the continuous-energy ACE data library for useful data which can improve the Monte Carlo tallying. The same method can also be applied towards the fission energy spectrum as well as the determination of the photon source in a coupled neutron-photon problem, though these applications are not investigated in this work.

For example, the pre-processed fission spectra information for the prompt, delayed, and total neutron spectra are shown in Eq. (3.19).

$$\chi_{p,n,E'\to g}(E') = P_{n,MT}(E') \int\limits_{E_g}^{E_{g-1}} \chi_{p,n,MT}(E',E)dE \tag{3.19a}$$

$$\chi_{d,c,n,E'\to g}(E') = \int\limits_{E_g}^{E_{g-1}} Y_{c,n}(E)\chi_{d,c,n,MT}(E',E)dE \tag{3.19b}$$

$$\chi_{t,n,E'\to g}(E') = (1-\beta_{t,n})\chi_{p,n,E'\to g}(E') + \sum_{precursor\, c}^{C} \beta_{c,n}\chi_{d,c,n,E'\to g}(E') \tag{3.19c}$$

The next chapter (Chapter 4 will discuss the reaction types and kinematics equations relevant to this pre-processor; the chapter which follows that (Chapter 5) will discuss the pre-processor itself.

CHAPTER 4

Scattering Reaction Distributions in Monte Carlo Codes

Before discussing the detailed methods used to perform integration of the double-differential scattering kernel, it would be useful for the reader to have an understanding of the current mathematical models used to describe the reaction mechanics of the outgoing neutrons from these reactions. This chapter will therefore present an overview of the types of collisions with secondary particles which are encountered by neutrons in a typical fission reactor and then move on to the mathematical representation of these reactions in Evaluated Nuclear Data File (ENDF) [15] and/or ACE data [23].

4.1 Typical Scattering Mechanisms

The scattering reactions eject neutrons which are emitted at a different energy and direction of motion than the original incoming neutron. For the case of some reactions more than one of these secondary neutrons are produced.

These reactions can be categorized into one of the following, each of which will be discussed in subsequent sections:

1. Inelastic Scattering
2. Elastic Resonance Scattering
3. Elastic Potential Scattering

4.1.1 Inelastic Scattering

In an inelastic collision, a neutron is momentarily absorbed, forming a compound nucleus which then promptly decays, ejecting a neutron (or multiple neutrons). These reactions are called inelastic collisions because the nucleus is left in an excited state and thus kinetic energy is not conserved. In order to form the compound nucleus, the incoming neutron must have a kinetic energy such that a certain threshold energy is exceeded; this threshold is typically in the keV range, though its magnitude depends on the nuclear structure of the target nucleus. Since the target nucleus is left in an excited state, the ejected neutron can be emitted with a substantially lower kinetic energy than the neutron which was initially absorbed [2].

For the purposes of experimental measurement of the reaction channel and modeling in a Monte Carlo simulation, inelastic scattering reactions are separated into three distinct categories: inelastic level collisions, inelastic continuum collisions and neutron multiplying collisions.

Inelastic level collisions $\left(n, n'_k\right)$ are where measurement data is to a sufficient resolution that the reaction outgoing probability distribution functions can be isolated. These levels are typically the lower energy inelastic collisions since measurement efficiency is improved at lower energies.

Inelastic continuum collisions (n, n'_c) are essentially the catch-all for inelastic level collisions in which the energy levels can not be identified independently and thus their aggregate effect is combined into one reaction channel. This occurs as neutron energy increases along with the nuclear shell level density.

Neutron multiplying collisions (n, xn) are treated as inelastic collisions which produce multiple neutrons. While these could be separated into level and continuum-type measurements, since the threshold energy for producing multiple neutrons is quite high (approximately 6.17 MeV for ^{238}U), only a continuum type effect can be sufficiently measured.

4.1.2 Elastic Resonance Scattering

Elastic resonance scattering is a subset of inelastic scattering collisions but with one important distinction: the target nucleus is left in the ground state. In this case, kinetic energy is conserved and the kinematic equations for this case match closely with elastic potential scattering. Like inelastic scattering, elastic resonance scattering also requires a threshold energy be exceeded before it becomes energetically feasible.

4.1.3 Elastic Potential Scattering

Elastic potential scattering is when a neutron collides with a target nucleus but a compound nucleus is not formed. This case can be considered to follow typical “billiard-ball” collision kinematics. These reactions take place across the entire energy range and are typically the only scattering reaction that occurs when neutron energy is less than a few electron-Volts.

Since this reaction can occur at very low energies, it requires discussion of how the kinematics change when the incoming neutron's energy becomes comparable to the energy of the thermal motion of the target nucleus and the molecular or crystal structure binding energies. The kinematics equations of both of these situations become more difficult. For the case of a thermal motion of the target, the target has a velocity distribution with a known probability distribution function (specifically, a Maxwellian). For the case when the neutron energy approaches a magnitude near the molecular or lattice binding levels, then the constrained motion of the target nuclide must also be taken into account. The effect of thermal motion on the scattering kinematics is typically only accounted for when the neutron's energy is less than $400kT$, where k is the Boltzmann constant and T is the material temperature. This value of $400kT$ is around 10eV at room temperature but when the target nuclide is hydrogen the thermal motion must be accounted for at all neutron energies. Note that the value of $400kT$ is current convention but this value can change in the future, as it has in the past. The effects due to molecular or lattice binding, if present, also begin to be non-negligible as the neutron's energy becomes less than a few electron-Volts.

4.2 Representation of Secondary Particle Kinematics in Modern Data and Monte Carlo Codes

This section will present an overview of the ACE format [23], then discuss the mathematical modeling used in the ACE system for each of the above collision types of interest including the conversion from the CM to the LAB frame, if necessary.

4.2.1 ACE Format Overview

ACE data libraries are produced by the NJOY [24] code developed by Los Alamos National Laboratory (LANL). The ACE data output from NJOY is essentially a more computer-usable form of the originating ENDF/B data with data points thinned and distribution information converted to more useful forms. Each ACE library can contain data for multiple nuclides with data at multiple temperatures. For most traditional cases, all of the data contained in ACE is repeated for every temperature point. ACE data can be written in one of two formats: ASCII (called Type 1), or binary (called Type 2).

The ACE data begins with header information which includes information needed about the nuclide and library itself such as the nuclide identification, processed temperature, data source, and various information about how much data is contained in the library and where. After the header information, cross sections are provided on a uniform energy grid for the total, total absorption, elastic scattering; this is called the ESZ block. Later data blocks include those which define the following:

1. The list of ENDF/B reaction types (MT numbers) which are provided in the data (in the MTR block).
2. The shell level energies (Q-values) for inelastic collisions (LQR block).
3. the number of emitted neutrons from a reaction and whether or not data is in the LAB or CM frame (TYR block).
4. Cross sections for the provided reaction types (SIG block).
5. Angular distributions for reactions containing emitted neutrons (AND block).
6. Energy and energy-angle distributions for reactions which have emitted neutrons (DLW block).

The representation of angle, energy, and energy-angle distributions is of interest to this discussion and will be expanded upon further as needed to describe the mathematical modeling of the previously discussed reaction types.

4.2.2 Inelastic Scattering Representation

The three types of inelastic collisions represented (inelastic level, inelastic continuum, and neutron producing reactions) each have different ways to be represented mathematically. As one would expect, the inelastic level collisions are more precisely defined with Law 3. The remaining types of collisions are described with more general PDFs. The cross sections of these inelastic scattering reactions do not require Doppler broadening due to their lack of resonances. In addition, the outgoing neutron energy spectra and angular distributions are independent of temperature.

The energy distributions needed for some scattering descriptions are provided in the DLW block of the corresponding reaction channels. The angular distributions are either combined with the energy distribution to produce an energy-angle distribution, or the reaction is assumed to be isotropic in the CM system. Modern (ENDF/B-VII.0 [25] and

ENDF/B-VII.1 [15]) evaluations utilize the following ACE laws to describe the distributions:

1. Level Scattering (Law 3)
2. Evaporation Spectrum (Law 9)
3. Kalbach-87 Formalism (Law 44)
4. Continuous Energy-Angle Tabular Distribution (Law 61)

4.2.2.1 Law 3: Level Scattering

Law 3 is used exclusively for inelastic level collisions. This Law is very compact, requiring only two numbers to define the energy distribution for the entire energy domain. Law 3 is shown in Eqs. (4.1). In these equations, A is the atomic-weight ratio of the target nucleus, μ_{CM} is the CM frame scattering angle, E_{CM} is the outgoing energy in the CM frame, and Q is the nucleus shell energy level of interest. The L_1 and L_2 parameters are provided by the Law; they are not energy-dependent and therefore only one of each needs to be provided for each instance of this Law. This distribution does not contain angular information; instead, the angular distribution is either supplied separately or assumed to be isotropic in the laboratory frame when this law is used for inelastic scattering reactions.

$$L_1 = \left(\frac{A+1}{A}\right)|Q| \tag{4.1a}$$

$$L_2 = \left(\frac{A}{A+1}\right)^2 \tag{4.1b}$$

$$E_{CM} = L_2 * (E' - L_1) \tag{4.1c}$$

$$E_{LAB} = E_{CM} + \left[E' + 2\mu_{CM}(A+1)\sqrt{E' E_{CM}}\right] / (A+1)^2 \tag{4.1d}$$

4.2.2.2 Law 9: Evaporation Spectrum

Some evaluations of inelastic continuum reactions and neutron multiplying reactions utilize an evaporation spectrum to represent the outgoing energy distribution. The functional form of this spectra is shown in Eqs. (4.2). This distribution does not contain angular information; instead, the angular distribution is either supplied separately or assumed to be isotropic in the laboratory frame when this law is used for inelastic scattering reactions.

In these equations, T is the fitting parameter (referred to as the effective temperature) and U is the value used to limit the maximum energy of the spectra (referred to as the restriction energy). The application of the restriction energy is shown in Eq. (4.3). There is only one restriction energy provided for each set of data, but the effective temperature is provided at a set of incoming energy values with interpolation schemes defined between these points.

$$x = \frac{E' - U}{T} \tag{4.2a}$$

$$C = T^2 \left[1 - e^{-x} (1 + x)\right] \tag{4.2b}$$

$$f(E' \to E) = \begin{cases} \frac{Ee^{-\frac{E}{T}}}{C}, & \text{if } 0 \le E \le E' - U \\ 0, & \text{otherwise} \end{cases} \tag{4.2c}$$

$$0 \le E \le E' - U \tag{4.3}$$

4.2.2.3 Law 44: Kalbach-87 Formalism

The Kalbach-87 formalism is a relatively recent introduction into ENDF which is gradually replacing many other Law types due to the compactness and high accuracy [26]. Law 44 is essentially a tabular distribution in outgoing energy, with a tabular PDF and Cumulative Distribution Function (CDF) defining the outgoing energy distribution and a continuous function describing the angular distribution. The angular portion requires two parameters, A, and R, each of which are functions of the the incoming and outgoing energies. The function describing the angular distribution is shown in Eq. (4.4). The Law can be used to describe outgoing parameters in either the CM or LAB frames, though it is mostly used to describe CM distributions. Rules for interpolation are provided to determine the outgoing distribution at values between the provided points; the interpolation can either be histogram or linear-linear interpolation. Finally, the incoming energy distributions can also be interpolated between; usually by linear-linear interpolation.

$$f(\mu, E', E) = \frac{A(E', E)}{2\sinh(A(E', E))} \left[\cosh(A(E', E)\mu) + R(E', E)\sinh(A(E', E)\mu)\right] \tag{4.4}$$

4.2.2.4 Law 61: Continuous Energy-Angle Tabular Distribution

Law 61 is similar to Law 44 except the angular distribution is described with a tabular PDF and CDF defined over a fixed number of outgoing angles. The outgoing angular distribution also contains rules for interpolation; either histogram or linear-linear interpolation can be used.

4.2.2.5 Conversion From Center-of-Mass to Laboratory Frames

The outgoing energy and/or scattering angle is provided in the CM frame for the above inelastic collisions as opposed to being provided in the LAB frame. Before these CM frame distributions can be useful, they must first be converted to the LAB frame of reference. The conversion for inelastic level (Law 3) data is easily handled in the same fashion as the target-at-rest elastic scattering and will be discussed concurrently in Section 4.2.3 and shown in Eqs. (4.6). The conversion for Laws 9, 44 and 61, on the other hand, require a separate more complicated treatment which will be discussed in the following paragraphs.

These continuum reactions with outgoing information provided in the CM frame require a complicated conversion algorithm due to there being multiple LAB frame outgoing energies that are possible for a given CM frame outgoing energy. The method used to perform this conversion by the NJOY [24] code is discussed in the Methods for Processing ENDF/B-VII manual [16]. In this method, the conversion is performed for every incoming energy necessary. The method can be summarized as adaptively building the energy transfer probability distribution by fixing the outgoing energy in the LAB frame while sweeping over the CM energy and angles. The equations of this method are shown in Eqs. (4.5). The final form of this method yields Legendre moments of the angular distribution which is the desired end-product of this work.

$$J = \sqrt{\frac{E_{LAB}}{E_{CM}}} = \frac{1}{\sqrt{1 + c^2 - 2c\mu}} \tag{4.5a}$$

$$c = \frac{\sqrt{E'/E_{LAB}}}{(A+1)} \tag{4.5b}$$

$$\omega = (\mu - c)\,J \tag{4.5c}$$

$$\mu_{min} = \frac{1}{2c}\left(1 + c^2 - \frac{E_{CM,max}}{E_{LAB}}\right)J \tag{4.5d}$$

$$E_{LAB,max} = E'\left(\sqrt{\frac{E_{CM,max}}{E'}} + \frac{1}{A+1}\right)^2 \tag{4.5e}$$

$$f_{l,LAB}(E', E_{LAB}) = \int_{\mu_{min}}^{1} f_{CM}(E', E_{CM}, \omega)\, P_l(\mu)\, J\, d\mu \tag{4.5f}$$

In these equations, A is the atomic weight ratio, J is the CM to LAB Jacobian, μ is the LAB cosine, ω is the CM cosine, $P_l(\mu)$ is the Legendre polynomial evaluated at the LAB cosine value, E' is the incoming energy as before, E_{LAB} is the LAB outgoing energy, E_{CM} is the CM outgoing energy, and $E_{CM,max}$ is the maximum possible CM outgoing energy as described by the ACE data.

4.2.3 Elastic Scattering Representation

As previously discussed, there are two types of elastic scattering: resonance and potential scattering. Since both are described by kinematics equations where both momentum and energy are conserved, the same mathematical treatment is applied to both. For this reason, the ACE data does not distinguish between resonance elastic and potential scattering; both share the same MT identifier of 2.

The elastic scattering cross sections are complicated functions with resonance peaks and valleys due to the resonant scatters; this data therefore undergoes Doppler broadening. In addition, the outgoing neutron energy spectra and angular distributions are dependent on temperature since the target-in-motion and bound-atom effects are functions of temperature.

The required angular distributions are provided in the AND block of the ACE data. Angular data in an AND block can either be provided as an isotropic distribution, an equi-probably histogram distribution with 32 bins, or a tabular distribution. The tabular distribution, like the tabular distributions for the outgoing energy, includes a set of points at various cosine values as well as the PDF and CDF values. Finally, these distributions also include instructions on whether to use histogram or linear-linear interpolation. These angular distributions are provided in the CM frame.

The following sections discuss the methodologies used to generate scattering kernels for target-at-rest kinematics (billiard ball collisions), target-in-motion kinematics (via the free-gas kernel) and when molecular and/or lattice binding effects become important (with thermal scattering tables).

4.2.3.1 Target-at-Rest Elastic Scattering

For target-at-rest kinematics, the energy distributions needed for the outgoing neutrons can be calculated based on first-principles once the cosine of the change-in-angle or its probability distribution function is known. The Legendre moments of the target-at-rest outgoing distribution can be found as described in Eqs. (4.6). Since the outgoing energy depends on the change-in-angle, the Legendre moment integration (Eq. (4.6d)) includes the integral over the outgoing energy as well.

$$R = A\sqrt{1+\frac{Q(A+1)}{AE'}} \tag{4.6a}$$

$$\omega = \frac{E'(A+1)^2 - E\left(1+R^2\right)}{2RE} \tag{4.6b}$$

$$\mu = \frac{1+R\omega}{\sqrt{1+R^2+2R\omega}} \tag{4.6c}$$

$$f_l(E') = \int_{\omega(E_{low})}^{\omega(E_{high})} f(E',\omega)P_l(\mu[\omega])\,d\omega \tag{4.6d}$$

In these equations, A is the atomic weight ratio, R is the effective mass ratio, Q is the inelastic level energy if applicable, μ is the LAB cosine, ω is the CM cosine, $P_l(\mu)$ is the Legendre polynomial evaluated at the LAB cosine value, E' is the incoming energy, and E is the LAB outgoing energy. These equations apply equally to inelastic level collisions; in this case the effective mass ratio is used to modify the atomic weight ratio to ensure correct kinematics.

4.2.3.2 Free-Gas Kernel For Elastic Collisions With A Target-in-Motion

If a collision is elastic and the incoming energy is below a cutoff value (typically 10 eV), then elastic collisions are to be treated via target-in-motion kinematics. The Free-Gas Kernel (FGK) is one such target-in-motion scheme. Such target-in-motion schemes modify the standard elastic scattering kernel to account for the fact that the target nuclide may not be at rest, but in fact can have a non-negligible velocity according to a Maxwellian thermal distribution. This phenomena, and associated kinematics equations, are discussed in many nuclear engineering textbooks with a good summary presented in Hébert [13]. The equations developed in Hébert (and presented below as Eqs. (4.7) below) make use of $S(\alpha,\beta)$ notation of the kernel, where the momentum and energy transfer are represented by the terms α and β, respectively. The method shown in Eqs. (4.7), the outgoing angular distribution is assumed to be isotropic in the CM frame; this assumption yields the $\frac{1}{2}$ term in Eq. (4.7d). The terms in Eqs. (4.7) are the same used elsewhere in this document.

$$\alpha = \frac{E+E'-2\mu\sqrt{EE'}}{AkT} \tag{4.7a}$$

$$\beta = \frac{E-E'}{kT} \tag{4.7b}$$

$$S(\alpha,\beta) = \frac{exp\left(-\frac{(\alpha+\beta)^2}{4\alpha}\right)}{2\sqrt{\pi\alpha}} \tag{4.7c}$$

$$f_{FGK}(E',E,\mu) = \frac{1}{2kT}\left(\frac{A+1}{A}\right)^2\sqrt{\frac{E}{E'}}S(\alpha,\beta) \tag{4.7d}$$

4.2.3.3 Molecular and Lattice Effects: Thermal Scattering Tables

For the purposes of this document, the discussion of specific thermal scattering mechanisms is better left to other references such as the book by Williams [27]. This work will discuss the form of the thermal scattering data (commonly called $S(\alpha,\beta)$ tables). This data is divided into three categories: coherent elastic scattering, incoherent elastic scattering, and inelastic scattering. Note that in the case of lattice and molecular scattering, the terms *elastic* and *inelastic* refer to the complete molecule or lattice and not a specific nucleus being in an excited state or not. Coherent elastic scattering occurs in crystalline structures and is characterized by Bragg edges in the angular distribution. Incoherent elastic scattering refers to the elastic scattering in a hydrogenous solid. Both incoherent and coherent elastic scattering leave the neutron with the same pre- and post-collision energies; in this case only the angle changes. Finally, inelastic scattering (for thermal scattering purposes) is the general case when the system is left with latent vibrational or rotational energy post-collision; it is applicable to all material types. All of the energy and angle distributions of thermal scattering tables are presented in the LAB frame.

The coherent elastic scattering change-in-angle is given by a discrete value which depends on the value of the scattered Bragg edge and the incoming (and outgoing) energy of the particle. This relationship is shown in Eq. (4.8); E_i in this case is the energy of the scattered Bragg edge.

$$\mu = 1 - \frac{E_i}{E'} \tag{4.8}$$

For incoherent elastic scattering, the thermal scattering tables present a series of discrete values of μ, each of which are equally likely.

Finally, for inelastic scattering, three formulations are used in the thermal scattering data to represent the outgoing energy: equi-probable discrete outgoing energies, unequally probable discrete outgoing energies, and continuous outgoing energies provided in tabular format. Each of these three outgoing energy representations contains discrete and equi-probable outgoing cosines.

The continuous outgoing energies are provided in a tabular format. There exists one table for each of a set of incoming neutron energies. The distribution at each incoming energy provides a list of outgoing energies, each with the associated values of the PDF and CDF. Rules for interpolation are also provided in order to determine the outgoing distribution at values between the provided points. These interpolation types can either be histogram or linear-linear interpolation. Finally, the incoming energy distributions can also be interpolated, usually by linear-linear interpolation. Note that this work strictly uses ACE libraries using the discrete outgoing energy representation; only limited data has been released containing the continuous energy distributions.

CHAPTER 5

The Nuclear Data Pre-Processor

This work has thus far shown that there is a need to improve the efficiency of tallying MGXS, has identified a method (called the improved method) to achieve this, and finally discussed that the method can not be realized in a production environment without some form of pre-processing of the continuous-energy nuclear data into a form more readily tallied. This chapter discusses the implementation of this pre-processor in a code written especially for the task, called the Nuclear Data Pre-Processor (NDPP).

Before discussing NDPP specifics, it is instructive to explore the requirements on NDPP; what it must provide and how the data is best presented. The goal of NDPP is to determine the previously discussed scattering moment and scattering production moments. These were the same equations developed in Chapter 3, Eqs. (3.13), and (3.14) though now the temperature dependence of the data can be acknowledged with the inclusion of the material temperature (T). These new forms are shown below as Eqs. (5.1) and (5.2).

$$f_{n,E'\to g,l}(E',T) = \frac{\sum\limits_{MT} \sigma_{s,n,MT}(E',T) \int\limits_{E_g}^{E_{g-1}} \int\limits_{-1}^{1} P_l(\mu)\, f_{n,MT}(E',E,\mu,T) d\mu\, dE}{\sum\limits_{MT} \sigma_{s,n,MT}(E',T)} \tag{5.1}$$

$$\hat{f}_{n,E'\to g,l}(E',T) = \frac{\sum\limits_{MT} Y_{n,MT}(E') \sigma_{s,n,MT}(E',T) \int\limits_{E_g}^{E_{g-1}} \int\limits_{-1}^{1} P_l(\mu)\, f_{n,MT}(E',E,\mu,T) d\mu\, dE}{\sum\limits_{MT} \sigma_{s,n,MT}(E',T)} \tag{5.2}$$

Great care must be taken when integrating these functions so the improved tallying method can provide results which maintain the high level of accuracy expected from Monte

Carlo neutron transport codes. On the other hand, this pre-processed data must be stored in memory during the Monte Carlo simulation in order to use the improved method. The above two goals imply that the desired accuracy must be balanced with memory usage, as is commonly the case in engineering computations. Fortuitously, NDPP run time is not a factor since this data pre-processing will typically only be performed once for every new upstream data release (that is, once every few years when a new ENDF evaluation is released).

The integrals shown in the above equations are functions of the incoming energy (E') and material temperature (T). The first thing to notice is how this incoming energy dependence should be represented; this will be discussed in a later section, but it suffices for now to simply state that this continuous incoming energy dependence will be replaced with point-wise values and an interpolation scheme to obtain results between the provided points. This approach is the exact same taken in the upstream ACE and ENDF data. The same can be done for the temperature dependence of the nuclear data (T); a table will exist at each temperature needed and interpolation rules provided to generate values for intermediate temperatures.

Next, one notices that every incoming energy value will have at most $G \times L$ discrete values for the scattering quantities, G being the number of energy groups and L the Legendre expansion order desired. Therefore, the data library produced by NDPP would be $\mathcal{O}(N_{E'} \times G \times L)$, with $N_{E'}$ being the number of incoming energy points. This can become prohibitively large as the number of groups and scattering orders used in deterministic transport codes can be in the range of around 50 to 150 groups with up to P_3 data. Fortuitously, there are ways around this impending memory issue including:

1. Intelligently choosing incoming energy points to reduce the value of $N_{E'}$;
2. Employing a thinning algorithm which removes incoming energy points which do not provide an accuracy benefit;
3. Setting transfer values less than a threshold to zero;
4. Taking advantage of the fact that the $f_{n,MT}(E' \rightarrow g)$ will have values of 0 for many values of g by utilizing a sparse storage format;
5. Organizing the data in such a way that the incoming energy dependence is minimized.

The first and second items will be the subject of Section 5.1.3; items three and four will be discussed together in Section 5.1.6. The last item affects the discussion throughout the remainder of this chapter and therefore warrants exploration at this time.

The cross sections for elastic scattering are temperature dependent while inelastic cross sections do not have a measurable temperature dependence, as discussed in Chapter 4. Further, the elastic scattering angular distribution ($f_{n,MT}$) also becomes dependent upon the temperature when thermal motion of the target nuclide and binding effects are non-negligible (i.e., at low energies). Inelastic reactions do not occur at low enough energies for this to be of concern and therefore their angular distributions are not affected by temperature. The above two points show that the temperature dependence for the scattering and scattering production integrals is entirely contained within the terms for elastic scattering ($MT = 2$).

With this knowledge, the scattering kernels can be re-written as shown in Eqs. (5.3) and (5.4) where 2 is used to denote an MT of 2. The temperature dependence in this format is entirely contained within the first term of each the numerator and denominator. Therefore if NDPP can produce two sets of data, one temperature-dependent (that is, elastic) and another temperature-independent (inelastic), then the amount of information needed for each temperature will be drastically reduced. This is highly desirable since the elastic data requires significantly fewer incoming energy points than the inelastic data as will be seen in Sections 5.1.3 and 5.1.6.

$$f_{n,E'\to g,l}(E',T) = \frac{\sigma_{s,n,2}(E',T)\overline{f_{n,2}}(E',T) + \overline{\sigma f_{n,inel}}(E')}{\sigma_{s,n,2}(E',T) + \sum\limits_{MT\neq 2} \sigma_{s,n,MT}(E')} \tag{5.3a}$$

$$\overline{f_{n,2}}(E',T) = \int\limits_{E_g}^{E_{g-1}} \int\limits_{-1}^{1} P_l(\mu)\, f_{n,2}(E',E,\mu,T)d\mu\, dE \tag{5.3b}$$

$$\overline{\sigma f_{n,inel}}(E') = \sum_{MT\neq 2} \sigma_{s,n,MT}(E') \int\limits_{E_g}^{E_{g-1}} \int\limits_{-1}^{1} P_l(\mu)\, f_{n,MT}(E',E,\mu)d\mu\, dE \tag{5.3c}$$

$$\hat{f}_{n,E'\to g,l}(E',T) = \frac{\sigma_{s,n,2}(E',T)\overline{f_{n,2}}(E',T) + \overline{Y\sigma f_{n,inel}}(E')}{\sigma_{s,n,2}(E',T) + \sum\limits_{MT\neq 2} \sigma_{s,n,MT}(E')} \tag{5.4a}$$

$$\overline{Y\sigma f_{n,inel}}(E') = \sum_{MT\neq 2} Y_{n,MT}(E')\sigma_{s,n,MT}(E') \int\limits_{E_g}^{E_{g-1}} \int\limits_{-1}^{1} P_l(\mu)\, f_{n,MT}(E',E,\mu)d\mu\, dE \tag{5.4b}$$

In conclusion, NDPP is required to provide separate data for $\overline{f_{n,2}}(E',T)$ and $\overline{\sigma f_{n,inel}}(E')$ (or $\overline{\sigma Y f_{n,inel}}(E')$, if scattering production data is requested), each of which can be provided on their own independent E' grids. The cross section values in the denominator and in front of $\overline{f_{n,2}}$ will be provided at "on-the-fly" by the Monte Carlo code.

The following sections will discuss the details of how NDPP calculates the required data and will also summarize the changes needed to a Monte Carlo code to allow it to be able to use this data.

5.1 NDPP Implementation

NDPP is written in Fortran 2003 using modern software development practices, utilizing the object-oriented programming paradigm, and written in a version-controlled environment (Git). NDPP is production-ready and available for all to use due to the open source software model used. The open source model was used to both complement OpenMC [17] and its open development model as well as to ensure the widest adoption possible. The source code is hosted by GitHub, a central server which provides source code hosting, issue tracking, and documentation hosting. The source code is available at https://github.com/ndpp/ndpp and the documentation is available at http://ndpp.github.io. To improve performance, NDPP has been parallelized using both distributed (using MPI [28]) and shared memory (using OpenMP [29]) paradigms.

The overall flow of the code is simply:

1. Gather user input;
2. Read ACE data;
3. Process the scattering data:
    (a) Set the incoming energy points to use;
    (b) Parse the ACE data to a common format;
    (c) Perform the integration over outgoing energy and/or angle for each incoming energy point for each reaction type
    (d) Thin the data;
4. Write the results for later use in a Monte Carlo solver.

Each of these functional areas will be discussed in this section's subsections.

To aid in comprehension of NDPP, an example nuclide will be used where appropriate in the discussion of scattering integration: Zirconium-90 (^{90}Zr) as evaluated in the ENDF/B-VII.0 ACE data provided with the MCNP5 version 1.60 release [23]. The data used here has been processed at a temperature of 600K. This particular isotope was chosen due to its variety of inelastic reaction types in the energy range of interest to thermal reactor designers (0 to 20MeV), though the methods discussed are applicable to all nuclides. The atomic weight ratio (or A) of ^{90}Zr is 89.1324. The ^{90}Zr scattering data in ENDF-B/VII.0 is described by the following reactions with threshold energies less than 20 MeV:

- Elastic, MT=2
- Inelastic scatter with two ejected neutrons, $(n,2n)$, threshold of 12.1 MeV, MT=16
- Inelastic scatter with an ejected α, $(n,n\alpha)$, threshold of 10.0 MeV, MT=22
- Inelastic scatter with an ejected proton, (n,np), threshold of 8.45 MeV, MT=28
- First inelastic level, (n,n_1), threshold of 1.78 MeV, MT=51
- Second inelastic level, (n,n_2), threshold of 2.21 MeV, MT=52
- Third inelastic level, (n,n_3), threshold of 2.35 MeV, MT=53
- Fourth inelastic level, (n,n_4), threshold of 2.77 MeV, MT=54
- Fifth inelastic level, (n,n_5), threshold of 2.78 MeV, MT=55
- Sixth inelastic level, (n,n_6), threshold of 3.11 MeV, MT=56
- Seventh inelastic level, (n,n_7), threshold of 3.35 MeV, MT=57
- Eigth inelastic level, (n,n_8), threshold of 3.49 MeV, MT=58
- Ninth inelastic level, (n,n_9), threshold of 3.60 MeV, MT=59
- Inelastic continuum, (n,n_c), threshold of 1.19 MeV, MT=91

The cross sections for these reactions (with the different inelastic levels combined into one green (n,inelastic) line) are shown in Figure (5.1).

5.1.1 User Input

NDPP shares as much code as possible with OpenMC. The input file format and project structure will therefore be familiar to those experienced with OpenMC.

The input parameters for NDPP are provided in two files: *ndpp.xml* and *cross_sections.xml*. These files make use of the eXtensible Markup Language (*XML*) format. The *ndpp.xml* file provides NDPP with the options the user wishes to use when processing a set of nuclides. The set of nuclides to evaluate is provided in *cross_sections.xml*,

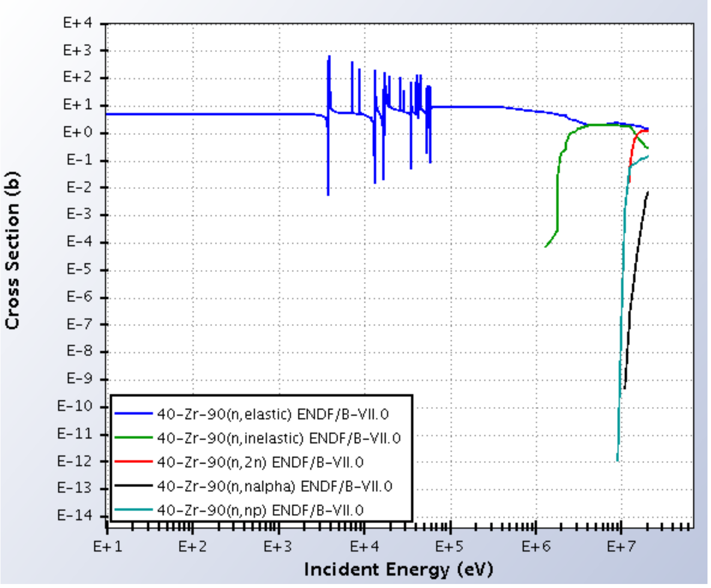

Figure 5.1: Zirconium-90 Scattering Reaction Cross Sections

which is compatible with the equivalent *cross_sections.xml* file used to define the data libraries available for use in OpenMC. The user input provided in the *ndpp.xml* includes the scattering order, the energy group structure, whether or not scattering-production data is to be produced, the number of angular samples to take when performing numerical integration, the cutoff energy to apply for the free-gas scattering kernel, the type of output file to produce (ASCII, or binary) and the tolerances for thinning the data, and finally the number of shared memory (OpenMP) threads to use during the processing.

A sample *ndpp.xml* and *cross_sections.xml* file can be found in Appendix C.

5.1.2 Reading of ACE Data

NDPP, like OpenMC, utilizes a library listing file (typically named *cross_sections.xml*) to obtain a list of ACE files to be used with associated meta-data to aid in reading them. This file is similar to the *xsdir* file utilized by MCNP [23]. NDPP uses this file as the definition of all nuclide and temperature libraries to be processed. This was chosen to follow the same format as is used in OpenMC so that a user can pass their entire ACE library through NDPP and have all improved moment data available for all nuclides and temperatures that could be expected to be present in their OpenMC models. In addition to providing the data locations, this file allows the user to set the free-gas cutoff energy on a nuclide-specific basis.

For each of the nuclide libraries listed in the *cross_sections.xml* file, the ACE data is read from disk creating an ACE object in memory for each nuclide which is essentially an objectified representation of the ACE library. NDPP can read either Type 1 (ASCII) or Type 2 (binary) ACE libraries.

5.1.3 Generation of The Scattering Data Incoming Energy Grid

The output of the NDPP data will be a tabular set of values for the pre-processed data. Since the end use of this data is in a continuous-energy MC code, the data must be interpolable between the provided incoming energy points. The number of points chosen must be kept sufficiently small such that the interpolation is accurate enough, but with few enough points that the memory burden of this NDPP data is not overwhelming. As discussed in the introduction to this chapter, the elastic and inelastic data have been separated (see Eqs. (5.3) and (5.4)), each with their own incoming energy grid and criterion for selecting points. The following discussion will be separated into one specific to elastic scattering and another specific to inelastic scattering.

5.1.3.1 Elastic Grid Generation

The initial template for the elastic grid is the union energy grid used in the ACE data for all reaction channels described in the model. This grid contains points mainly used to describe the cross section variation in the data. The next step is to take all of the incoming energy points for the outgoing distribution data and combine this with the initial template. There are likely to be duplicate values in these two grids, but the merging algorithm used for this purpose takes care to remove duplicates as they are encountered.

The combining of the above two grids is to ensure that the variation of outgoing distributions is well described to avoid introducing any extra error. These steps were quite simple and merely laid the framework for the next step which is absolutely necessary to achieve the desired interpolation accuracy.

To understand the next and final category of points needed in the incoming energy grid, consider the example nuclide, ^{90}Zr. When undergoing elastic scattering, a neutron collides with this isotope at energy E', the minimum possible outgoing (when assuming target-at-rest kinematics) is $\left(\frac{A-1}{A+1}\right)^2 E'$, or $0.9561E'$. If the energy group which contains E' spans $[0.9561E', E']$, then the percentage of neutrons which are emitted to the current group from E' is 100% and all other groups receive 0% of the outgoing neutrons. Conversely, if the energy group which contains E' has a lower group boundary exactly equal to E', then the current group receives an infinitesimally small percentage of the neutrons and a combination of the lower energy group receives nearly all of the outgoing data. There is clearly some transition between these extremes which must be captured; hence the need for points added to the incoming energy grid.

To illustrate this effect, Figure (5.2) shows the ^{90}Zr elastic scattering kernel as a function of the incoming energy (on the x-axis) and the scattering moment (on the y-axis) from E' to the outgoing group who has an upper bin boundary of 9.12 keV (taken from the C5G7 [30] group structure discussed in Table B.1 of Appendix B). This figure shows that the transfer to group 3 is zero when E' is above a certain threshold, or critical point, and increases linearly with decreasing energy until achieving a moment of 1.0 when E' is equal to the group boundary (denoted by the black vertical line).

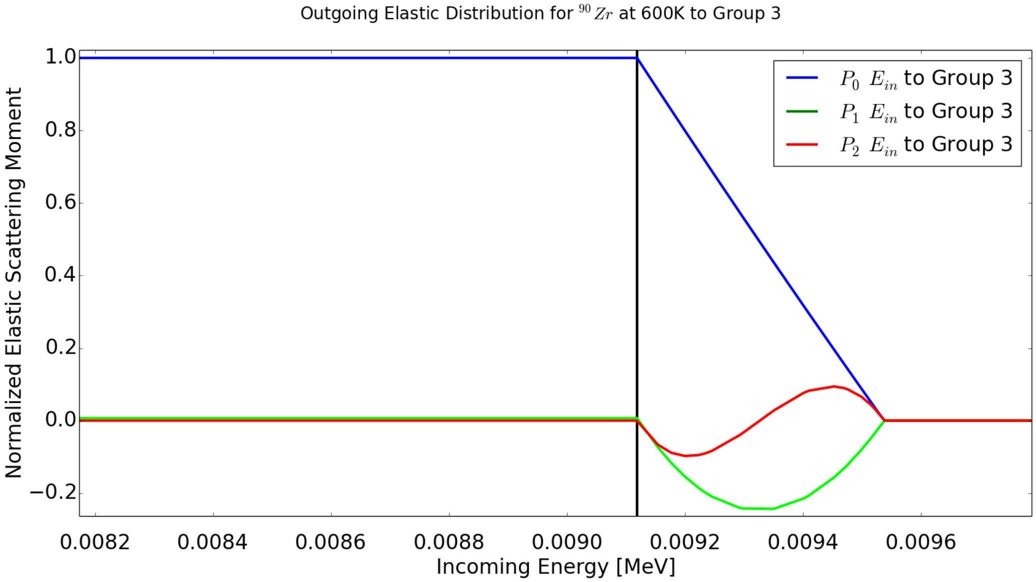

Figure 5.2: Zirconium-90 Elastic Scattering Reaction Moments, Down-Scatter to Group 3

The P_1 moment has a parabolic shape and the P_2 function has the shape of a third-order polynomial between these two points. These shapes are a measure of the degree of anisotropy of the angular distribution; as will be seen in the next figure, this can not be taken as a general rule of thumb. Regardless of the exact shape, enough points must be chosen to allow for interpolation to capture this shape adequately.

For target-at-rest kinematics, the value of the each of the critical energies is found by solving Eq. (4.6) for E' with $\omega = -1$ and E equal to each of the group boundaries. The resultant equation specific to elastic scattering with target-at-rest kinematics is shown in Eq. (5.5). This equation shows that the critical points are dependent upon the mass of the target nuclide; as A increases, the critical point becomes closer and closer to the group boundary, E_g. Now that the critical points are known, fifty points are added (though this is user-selectable) to the grid from $E_{crit,low}$ to $E_{crit,high}$ with equal-lethargy spacing.

$$E_{crit,high} = \left(\frac{A+1}{A-1}\right)^2 E_g \tag{5.5}$$

For the free-gas kernel, these critical points exist for both down-scattering and up-scattering. This phenomenon is shown again with the example nuclide by moving to lower energies as shown in Figure (5.3). In this figure, group 6 is to the left of the black line and group 5 is to the right. This figure shos that the energies below the group boundary of 0.625 eV still contribute to group five, implying that up-scatter is present. The P_1 and P_2 moments show oscillatory behavior in the same range; though at this energy note that the shape does not go as a polynomial of degree $N+1$ as was seen in Figure 5.2. Thus, for the case of free-gas kernel scattering, there is a critical point both above (down-scattering) and below (for up-scattering) the group boundary.

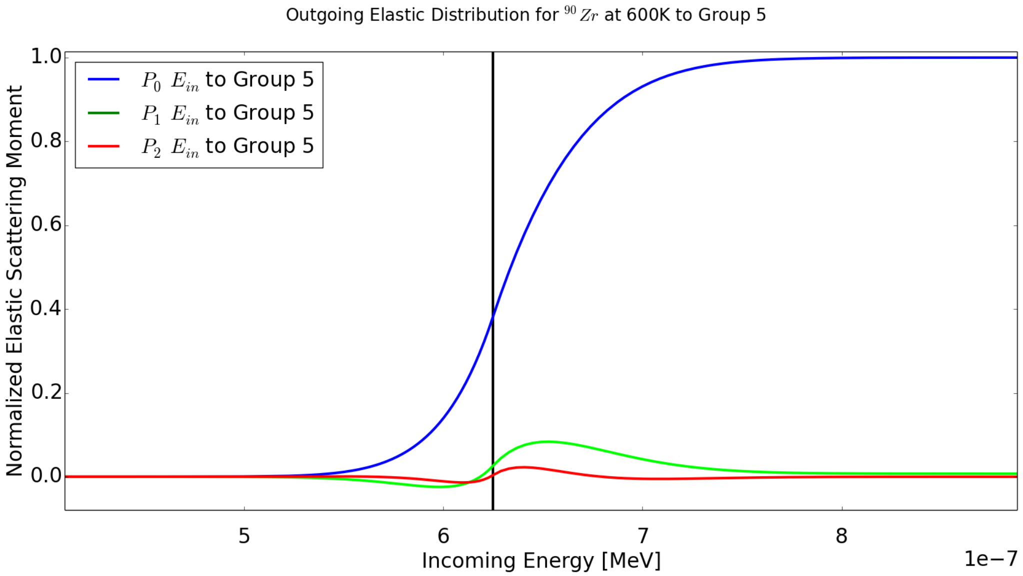

Figure 5.3: Zirconium-90 Elastic Scattering Reaction Moments, Up-Scatter to Group 5

The critical points for the case of free-gas scattering can not be explicitly determined due to the thermal Maxwellian which describes the thermal motion containing tails in the PDF which extend from zero to ∞; instead critical values were chosen which bound the expected data for all cases inspected. These critical points are shown in Eq. (5.6). The lower point simply uses two times the mean thermal energy as the cutoff while the upper point was chosen to expand the difference between the elastic $E_{crit,high}$ in Eq. (5.5) by a factor of 7. Both of these values were not explicitly derived, but instead were iterated upon to find values which provide useful results in all cases. Now that the critical points are known, fifty points are added (though this is user-selectable) to the grid from $E_{crit,low}$ to

$E_{crit,high}$ with equal-lethargy spacing.

$$E_{crit,low} = E_g - 2kT\frac{A+1}{A} \tag{5.6a}$$

$$E_{crit,high} = \left(7\left(\frac{A+1}{A-1}\right)^2 - 6\right)E_g \tag{5.6b}$$

Critical points are more difficult with thermal scattering libraries. The phenomena still exists, but the data provided in the files is not sufficient to intelligently generate these critical points. Instead, NDPP searches through inelastic incoherent reaction data (where the outgoing energy is different than the incoming energy) for the critical points by comparing outgoing energy values and group boundaries. Since this incoming energy grid is tabular, NDPP uses interpolation to determine where the incoming energy value should be in order to approximately place the outgoing energy at a group boundary. These points are then added to the incoming energy grid. Finally, NDPP creates a very fine incident energy grid by adding a user-selectable number of incoming energy points for every point that exists in the data. The current default for this value is 50 new points for every group with energies applicable to the thermal scattering library. This helps to generate more continuous and interpolatable angular distribution for coherent elastic reactions where the value of μ is defined exactly by the incoming energy and Bragg energy level (Eq. (4.8)).

5.1.3.2 Inelastic Grid Generation

The inelastic incoming energy grid begins from the same place that the elastic grid began: the merged grids of the points in the union energy grid for cross sections and the incoming energy points in the energy- and angle-distributions for the individual reaction channels. However, it would be excessive to keep all points below the minimum inelastic threshold energy as their outgoing distributions are all zero; these points are consequently discarded.

As one would expect, there are also critical points for the inelastic reactions. For example, these points can be seen in Figure 5.4 which shows the inelastic scattering moments from all energies to group 1.

There exists two critical points for every reaction channel and outgoing energy group. The upper critical point corresponds to when the CM change-in-angle (ω) is +1 and the lower point corresponds to when ω is -1. Like the elastic target-at-rest critical point derivation, the critical points can be found by solving Eq. (4.6) for E' with $\omega \pm 1$ and E equal to each of the group boundaries [16]. The results of this are shown in in Eqs. (5.7). These relations simplify to the same as those for elastic target-at-rest kinematics when the binding energy, Q, is set to 0. Now that the critical points are known, fifty points are added (though

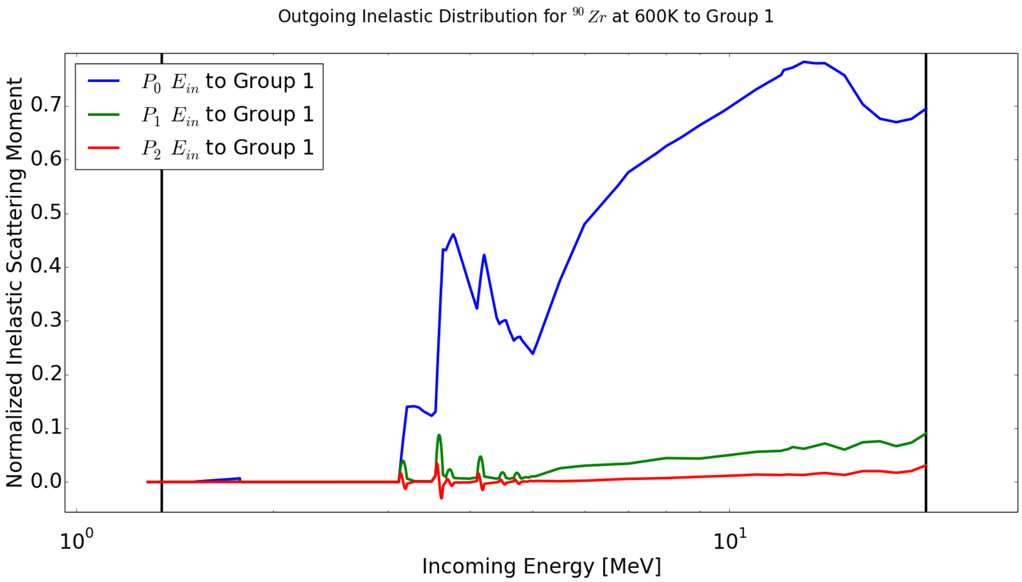

Figure 5.4: Zirconium-90 Inelastic Scattering Reaction Moments, Scatter to Group 1

this is again user-selectable) to the grid from $E_{crit,low}$ to $E_{crit,high}$ with equal-lethargy spacing. Since the fifty points are added for every group and inelastic reaction channel, the inelastic grid should be expected to be significantly larger than the elastic grid.

$$E_F = \frac{A+1}{A} E_g \tag{5.7a}$$

$$D = \left[A^2\left(1+\frac{E_F}{-Q}\right)-1\right]\frac{E_F}{-Q} \tag{5.7b}$$

$$F_{low} = \frac{1-\sqrt{D}}{1+\frac{E_F}{-Q}} \tag{5.7c}$$

$$E_{crit,low} = \frac{-Q\frac{A+1}{A}}{1-\left(\frac{F_{low}}{A}\right)^2} \tag{5.7d}$$

$$F_{high} = \frac{1+\sqrt{D}}{1+\frac{E_F}{-Q}} \tag{5.7e}$$

$$E_{crit,high} = \frac{-Q\frac{A+1}{A}}{1-\left(\frac{F_{high}}{A}\right)^2} \tag{5.7f}$$

5.1.4 ACE Data Parsing

The next step performed by NDPP is to put the data on a common grid to generalize the integration that may be performed to be as independent of the ACE Law as is possible. Note that this is not done for the energy distribution of inelastic reactions described by Laws 3 and 9; in these reactions the energy distribution is fully defined by simple Laws and changing their form would yield a loss of both accuracy and computational efficiency.

For the cases which are not Laws 3 and 9, NDPP first takes most of the ACE angular, energy and energy-angle distributions discussed in Chapter 4 and converts each to a 3-D tabular representation to improve the efficiency of integration. The dimensions of this table are $(\mu\,Points) \times (Outgoing\,Energy) \times (Incoming\,Energy)$ (in Fortran column-major format) and the size of these dimensions depend upon user input and the ACE data itself. The μ dimension is the same for every ACE distribution, and contains a user-specified number of equally-spaced angular points between $[-1,1]$. The outgoing energy is as specified in the ACE data: angular-only distributions have an outgoing energy dimension of 1; energy-angle distributions have a dimension for outgoing energy corresponding to the number of outgoing energy points specified in the ACE data. The incoming energy points for this reaction type data are the same as is specified by the ACE data specific to the reaction distribution data.

This table is filled by proceeding through each incoming energy point of the distribution data, stepping through each outgoing energy point (if present), and converting whichever format is utilized to evaluate $f(E', E, \mu)$ at the desired value of μ and storing the result in the corresponding table location.

This table will lose some accuracy in the angular dimension relative to the original ACE distributions, but this accuracy is a function of the number of angular points used. NDPP's default value for the number of angular points is 2001 (i.e., a μ spacing of 0.001), minimizing this truncation error. Since a large portion of reactions contain angular data in tabular distributions with significantly fewer points, this angular spacing is overly fine and will have a negligible effect on accuracy; the accuracy will only be lost in the case of the Law 44 (Kalbach-87 Formalism) data where the angular variable is treated by a continuous function. Even in this case, the angular spacing is considered fine enough that this will not be an issue.

5.1.5 Scattering Data Integration and Combination

Now that the incoming energy grid of the output library is known, the code begins determining Eqs. (5.8), (5.9) and (5.10), which were discussed previously with Eqs. (5.3) and

(5.4).

$$\overline{f_{n,2}}(E',T) = \int_{E_g}^{E_{g-1}} \int_{-1}^{1} P_l(\mu)\, f_{n,2}(E',E,\mu,T) d\mu\, dE \tag{5.8}$$

$$\overline{\sigma f_{n,inel}}(E') = \sum_{MT \neq 2} \sigma_{s,n,MT}(E') \int_{E_g}^{E_{g-1}} \int_{-1}^{1} P_l(\mu)\, f_{n,MT}(E',E,\mu) d\mu\, dE \tag{5.9}$$

$$\overline{Y\sigma f_{n,inel}}(E') = \sum_{MT \neq 2} Y_{n,MT}(E')\sigma_{s,n,MT}(E') \int_{E_g}^{E_{g-1}} \int_{-1}^{1} P_l(\mu)\, f_{n,MT}(E',E,\mu) d\mu\, dE \tag{5.10}$$

From a high-level view, this is done by proceeding through each energy on the applicable incoming energy grid (i.e., elastic and inelastic), and for each reaction channel calculating the double integral as appropriate, multiplying by the appropriate cross section and neutron yield if needed, and summing the result to the total quantity. This process is the same for nuclidic ACE libraries and thermal scattering tables, though the thermal scattering tables put all data in the elastic reaction channels. This is a straight-forward process, but the details of performing the integration require further explanation. This step will be explained in detail in the following sections for the following cases:

1. Target-at-rest elastic and inelastic level (Law 3) calculations
2. Free-Gas kernel elastic reactions
3. Law 9 inelastic calculations
4. Other inelastic calculations
5. Thermal scattering table calculations

5.1.5.1 Target-At-Rest Elastic and Inelastic Level Integration

Eqs. (4.6) from Chapter 4 provided the governing equations which must be solved to convert elastic (target-at-rest) and inelastic level collisions from the CM to LAB frames while also producing the Legendre moment of the angular distribution. For clarity, these equations are provided below as Eqs. (5.11).

$$R = A\sqrt{1+\frac{Q(A+1)}{AE'}} \tag{5.11a}$$

$$\omega = \frac{E'(A+1)^2 - E\left(1+R^2\right)}{2RE} \tag{5.11b}$$

$$\mu = \frac{1+R\omega}{\sqrt{1+R^2+2R\omega}} \tag{5.11c}$$

$$f_l(E') = \int_{\omega(E_{low})}^{\omega(E_{high})} f(E',\omega)P_l(\mu[\omega])\,d\omega \tag{5.11d}$$

NDPP follows this prescription for these reactions. These steps are provided in order below:

1. R is calculated according to Eq. (5.11a).
2. The upper and lower bounds of integration for the ω variable are found by solving Eq. (5.11b) for $E = E_{g-1}$ and $E = E_g$, respectively.
3. Trapezoidal integration is performed over $f(E',\omega)P_l(\mu[\omega])$ with μ determined by Eq. (5.11c).

5.1.5.2 Free-Gas Kernel Elastic Integration

Eqs. (4.7) in Chapter 4 provided the governing equations which must be solved for free-gas kernel kinematics. To aid in this discussion, these equations are repeated below as Eqs. (5.12).

The derivation of Eqs. (5.12) assume an isotropic distribution (in the CM frame) exists; this assumption is responsible for the $\frac{1}{2}$ term in Eq. (5.12d). However, inspection of the ACE data shows this is an approximation which is not always true as a small contribution of a linear anisotropic component can exist. Therefore, the last equation in Eqs. (5.12) was modified by removing the $\frac{1}{2}$ (which represents an isotropic angular distribution) and replacing it with $f(E',\mu)$. Performing this operation, multiplying by the Legendre moment, integrating over μ and over the energy group of interest yields the relation to be integrated to find the Legendre moments of a group, shown in Eq. (5.12e).

$$\alpha = \frac{E+E'-2\mu\sqrt{EE'}}{A\,kT} \tag{5.12a}$$

$$\beta = \frac{E-E'}{kT} \tag{5.12b}$$

$$S(\alpha,\beta) = \frac{exp\left(-\frac{(\alpha+\beta)^2}{4\alpha}\right)}{2\sqrt{\pi\alpha}} \tag{5.12c}$$

$$f_{FGK}(E',E,\mu) = \frac{1}{2kT}\left(\frac{A+1}{A}\right)^2\sqrt{\frac{E}{E'}}S(\alpha,\beta) \tag{5.12d}$$

$$f_{FGK,l,g}(E') = \frac{1}{kT}\left(\frac{A+1}{A}\right)^2\sqrt{\frac{E}{E'}}\int_{E_g}^{E_{g-1}}\int_{-1}^{1} S(\alpha,\beta)\, f_{elastic}(E',\omega[\mu])\, P_l(\mu)\, d\mu\, dE \tag{5.12e}$$

Before examining the integration of the free-gas kernel, it would be useful to understand its behavior with respect to the variables of integration, μ and E. Consider again the example nuclide ^{90}Zr at room temperature (kT = 2.53E-8 MeV) with an isotropic elastic scattering angular distribution. Figures 5.5 through 5.7 show the angular distribution of the $S(\alpha,\beta)$ function (Eq. (5.12c)) with incoming energies at varying multiples of the thermal energy. These incoming energies correspond to 0.0253 eV, 25.3 eV, and 25.3 keV. The outgoing energy in this case is chosen to be the energy such that the CM cosine of the change-in-angle is exactly zero (0.0247 eV, 24.7 eV, and 24.7 keV, respectively).

These cases show us that the $S(\alpha,\beta)$ function approaches a Dirac-delta function centered about a certain value of μ when E' becomes much larger than kT. This makes sense because the target-at-rest elastic kernel relationship between outgoing energy and the change-in-angle *is* a Dirac-delta: there is only one E for every μ. At energies lower than this, the motion of the nuclei allows there to be a continuous spread of angles which produce the same outgoing energy.

Figures (5.8) through (5.10) show the free-gas kernel function integrated over μ as a function of outgoing energy at the same multiples of the thermal energy. For convenience, the x-axis in these plots is outgoing energy divided by the thermal energy. The P_0 through P_2 moments are included for completeness. These cases show three specific behavior of the function with respect to E which will be useful when integrating:

- The derivative of the kernel is clearly discontinuous at $E = E'$ and the range of integration should be split here.
- The 25.3 eV case begins to approach the expected outgoing energy distribution for a target-at-rest, save for the up-scatter and the presence of a low-energy tail.
- The 25.3 keV case (which does look very much like typical target-at-rest kinematics) has some numerical issues due to the integration of the angular variable.

The numerical issues in the 25.3 keV case could have been removed with tighter integration parameters when generating these figures, but were left to show why special care is

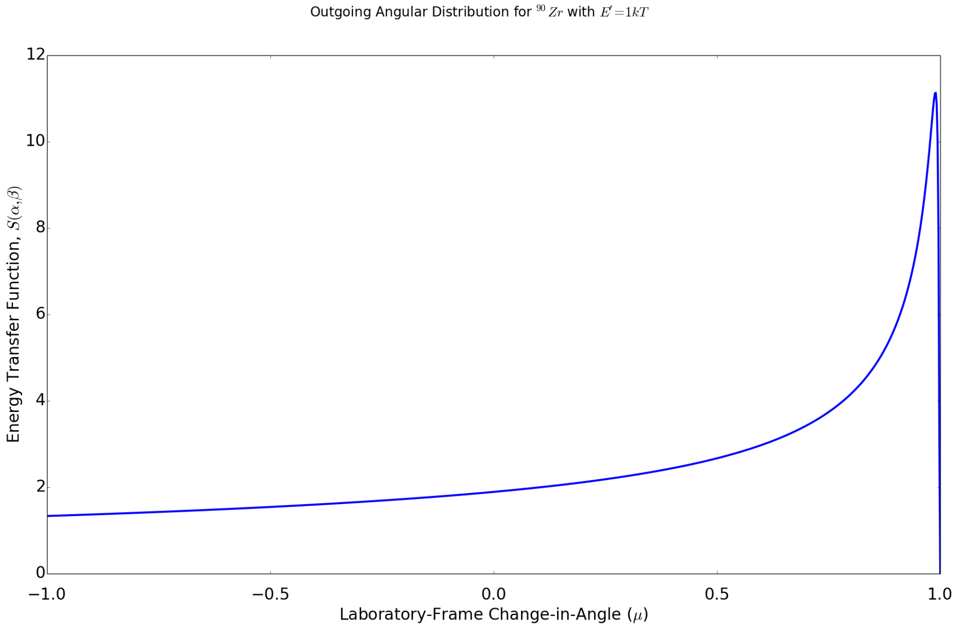

Figure 5.5: Zirconium-90 S (α,β) Function at 0.0253 eV

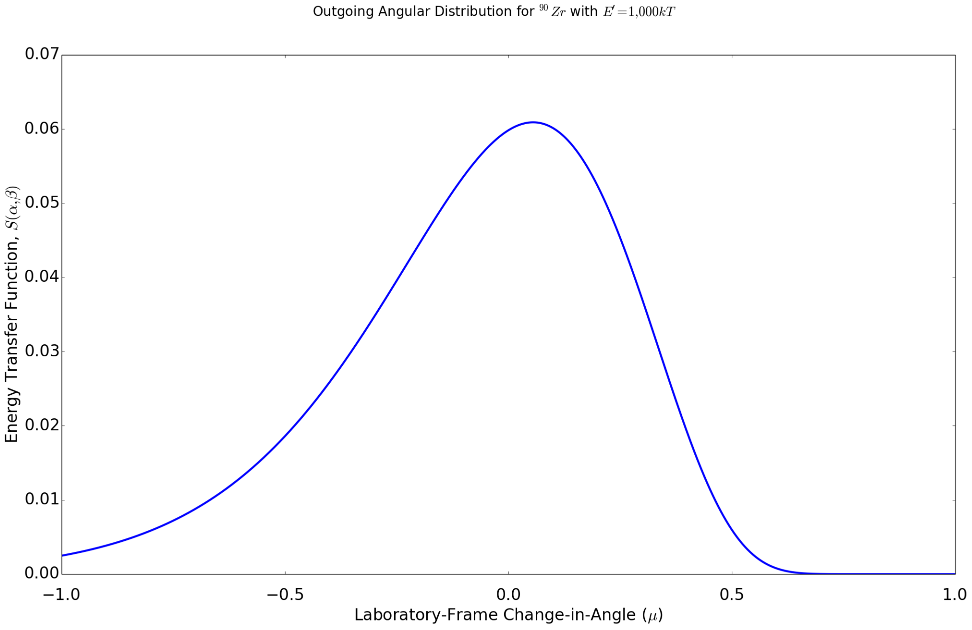

Figure 5.6: Zirconium-90 S (α,β) Function at 25.3 eV

needed when the relationship between energy and angle approaches a Dirac-delta function. The approach taken for NDPP will be discussed shortly.

Now that the functional behavior of the free-gas kernel is better understood, the discus-

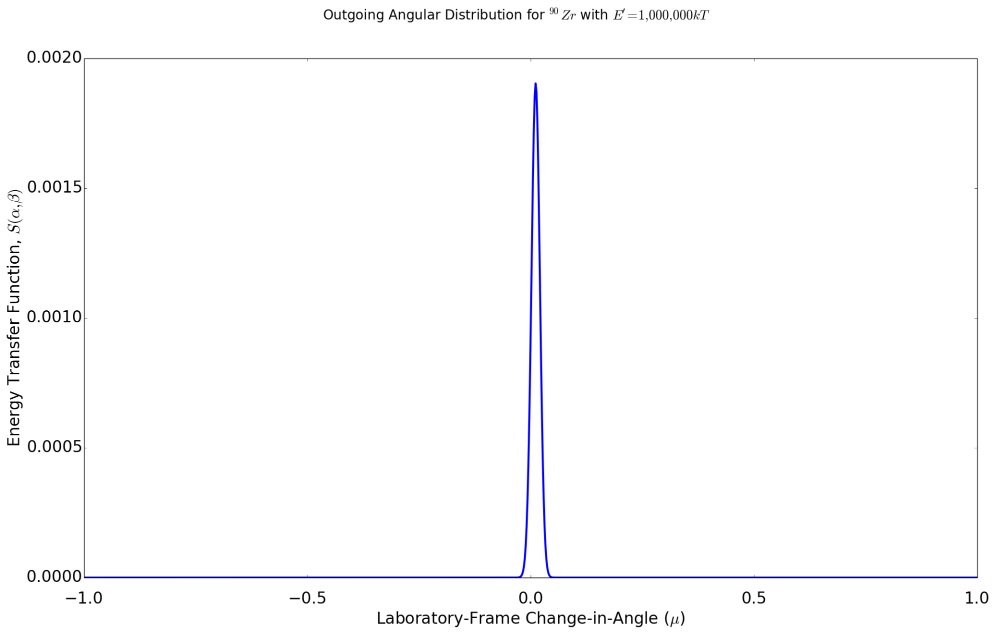

Figure 5.7: Zirconium-90 $S(\alpha,\beta)$ Function at 25.3 keV

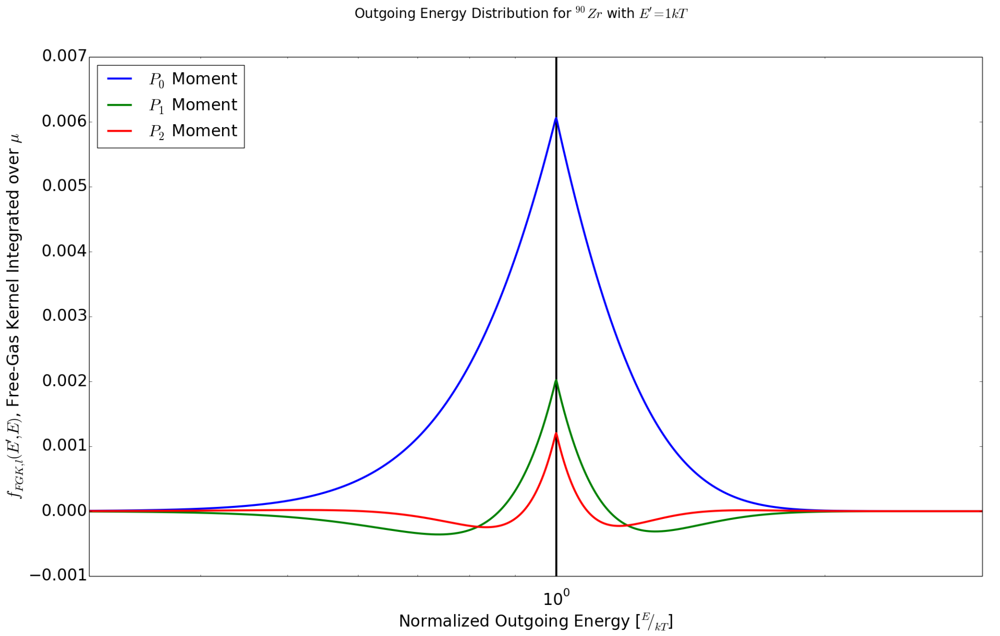

Figure 5.8: Zirconium-90 Free-Gas Kernel at 0.0253 eV

sion can move on to the actual integration techniques used. The integration of Eq (5.12e) is essentially an adaptive Simpson's integration [31] over each of the outgoing energy and μ. The outgoing energy integration is performed after the angle integration at the outgoing

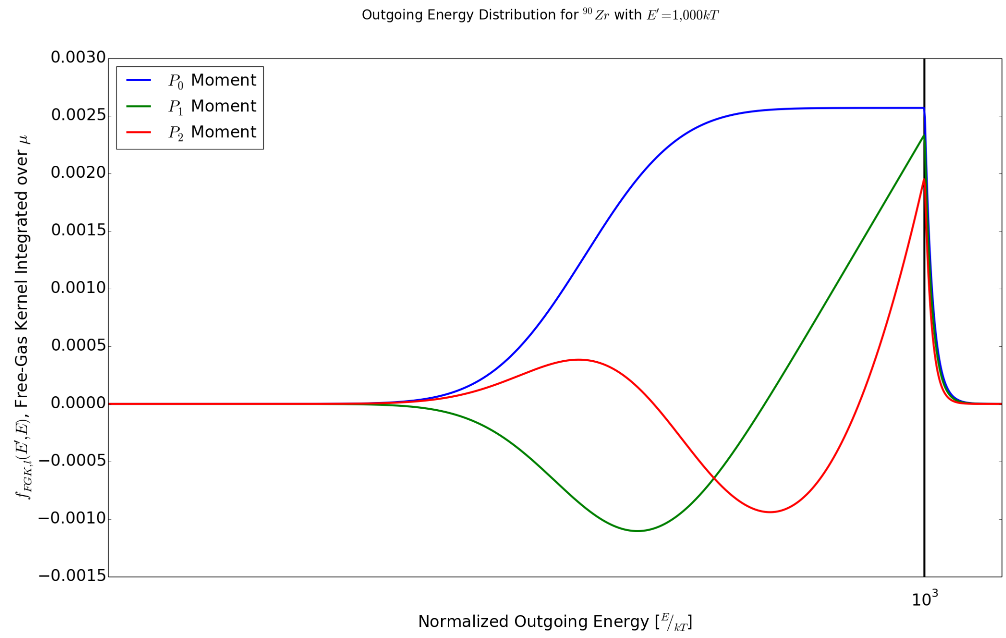

Figure 5.9: Zirconium-90 Free-Gas Kernel at 25.3 eV

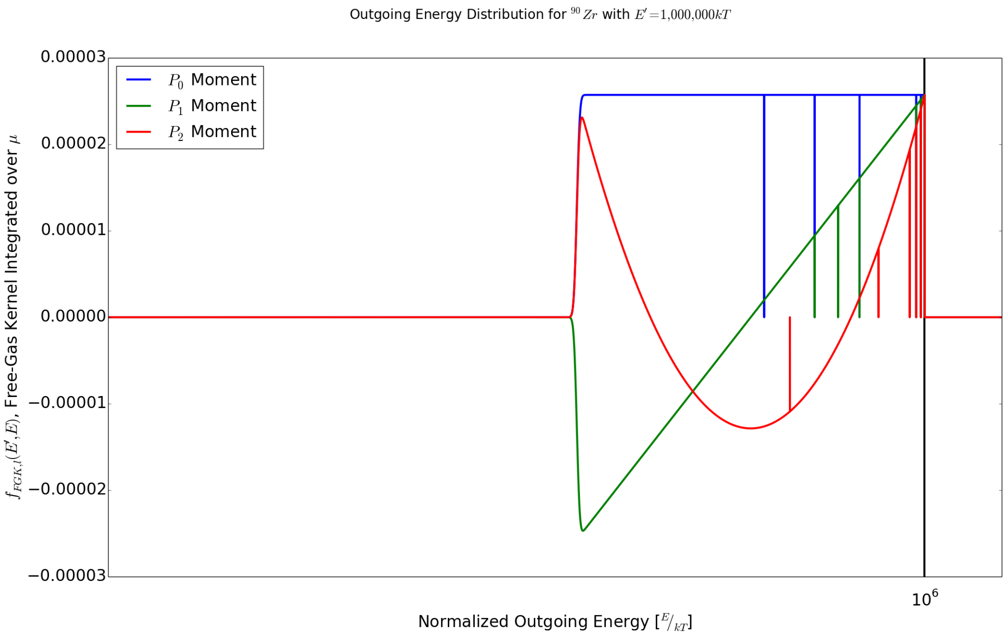

Figure 5.10: Zirconium-90 Free-Gas Kernel at 25.3 keV

energy point of interest (of which these points are determined adaptively, of course).

When performing the adaptive angular integration, a root finding algorithm (Brent's method [32]) is used to find the points when the $S(\alpha,\beta)$ function reaches a user-specified fraction of the maximum value in $\mu \in [-1, 1]$. This allows the adaptive integration to hone in on portion of the angular domain which contains the important information and is useful when the $S(\alpha,\beta)$ approaches a Dirac-delta as shown in Figure 5.7. The integration over μ is performed to the left and right of the maximum value of the function separately and then combined. This is in order to improve accuracy again when dealing with Dirac-delta like functions.

For the outgoing energy adaptive integration, the only special treatment needed is to set integration break points at both the group boundaries and outgoing energy values which correspond to the discontinuity previously discussed when $E' = E$ and another for when $E = \left(\frac{A-1}{A+1}\right)^2 E'$; this last point is merely used to improve the adaptive integration performance between the constant portion of the P_0 moment in Figure 5.9 and the more rapidly decreasing region at values less than $\left(\frac{A-1}{A+1}\right)^2 E'$.

Before leaving this topic, it should be noted that other, more accurate, formulations of target-in-motion kinematics exist [33–35] which could have been utilized for this work. These options were not chosen because the OpenMC code does not yet support other formulations besides the free-gas kernel and thus chosing other kernels would not allow for a consistent comparison between tallying methods.

5.1.5.3 Law 9 Inelastic Integration

The evaporation spectrum in Law 9 is used for some inelastic continuum and neutron production reactions in nuclides such as ^{12}C and For these cases, the evaporation spectrum (see Eq. (4.2)) is used to define the outgoing energy and a separate angular distribution is provided (though it is usually isotropic) and is always defined in the laboratory system. In this case, the angle and energy distributions are considered separate: the angular bounds of integration are always $[-1, 1]$ regardless of the outgoing energy bounds. This means that the angle and energy integrations are separable and the integral to solve is shown in Eq. (5.13).

$$f_{Law\,9,l,g}(E') = \int_{E_g}^{E_{g-1}} f_{Law\,9}(E' \to E)\,dE \int_{-1}^{1} g(\mu) P_l(\mu)\,d\mu \tag{5.13}$$

The integral over the angular distribution (called $g(\mu)$ in this case) is simply a trapezoidal integration over the tabular distribution created when doing the ACE processing discussed in Section 5.1.4.

The integral over the energy distribution can be solved analytically. This analytical solution is shown in Eq. (5.14) for the case when $0 \leq E \leq E' - U$ (otherwise the integral is nil).

$$x = \frac{E' - U}{T} \tag{5.14a}$$

$$C = T^2\left[1 - e^{-x}(1+x)\right] \tag{5.14b}$$

$$\int_{E_g}^{E_{g-1}} f_{Law9}(E' \rightarrow E)\,dE = \frac{-T}{C}\left(\left(e^{-E_{g-1}/T}\left(T + E_{g-1}\right)\right) - \left(e^{-E_g/T}\left(T + E_g\right)\right)\right) \tag{5.14c}$$

5.1.5.4 Inelastic Energy-Angle Distribution Integration

A majority of inelastic continuum and neutron production reaction distributions are described by either Kalbach-87 formalism (Law 44) or a continuous energy-angle tabular distribution (Law 61). These reactions are typically provided in the CM frame, but can also exist in the LAB frame. If these distributions are provided in the LAB frame, then trapezoidal integration is performed over both the outgoing energy and change-in-angle. If the data is provided in the CM frame, then the frame must be converted to the LAB frame as discussed in Section 4.2.2.5. The equations used in this transformation are provided in Eqs. (4.5) and are also repeated below for clarity as Eqs. (5.15).

$$J = \sqrt{\frac{E_{LAB}}{E_{CM}}} = \frac{1}{\sqrt{1 + c^2 - 2c\mu}} \tag{5.15a}$$

$$c = \frac{\sqrt{E'/E_{LAB}}}{(A+1)} \tag{5.15b}$$

$$\omega = (\mu - c)\,J \tag{5.15c}$$

$$\mu_{min} = \frac{1}{2c}\left(1 + c^2 - \frac{E_{CM,max}}{E_{LAB}}\right)J \tag{5.15d}$$

$$E_{LAB,max} = E'\left(\sqrt{\frac{E_{CM,max}}{E'}} + \frac{1}{A+1}\right)^2 \tag{5.15e}$$

$$f_{l,LAB}(E', E_{LAB}) = \int_{\mu_{min}}^{1} f_{CM}(E', E_{CM}, \omega)\,P_l(\mu)\,J\,d\mu \tag{5.15f}$$

This integration is performed by setting up a grid of E_{LAB} points per outgoing energy group; the default value for the number of these points is 20, though this is an available option to the user). Each point on this outgoing energy grid is then used to calculate the following parameters (in the order listed):

1. c and μ_{min} are calculated directly

2. E_{LAB} is found using the equation for J

3. ω is determined

4. J is determined

5. The corresponding probability distribution function for the calculated E_{cm} is determined from the ACE data

6. A portion of $f_{l,LAB}(E', E_{LAB})$ is integrated over the outgoing energy using trapezoidal integration with the newly acquired E_{LAB} distribution as a single sample for the integration.

5.1.5.5 Thermal Scattering Table Integration

Thermal scattering tables (referred to as $S(\alpha,\beta)$ tables) are described by three types of reactions: coherent elastic, incoherent elastic, and inelastic. As discussed in Chapter 4, the coherent elastic reactions have no energy loss, and thus the incoming and outgoing energies are equal. The incoherent elastic and incoherent inelastic reactions do have a change in energy described by either discrete outgoing energies or continuous energies with corresponding probability distribution functions and cumulative distribution functions.

These energies are trivial to integrate over outgoing groups; discrete data can simply be summed in the group of interest and the cumulative distribution for the continuous data readily provides the outgoing energy integral.

The change in angle can be described by discrete values determined by the incoming energy (for coherent elastic in Eq. (4.8)) or with discrete fixed angles (as for incoherent elastic and inelastic data). The discrete values of μ are equally trivial to integrate and need no further discussion.

5.1.6 Data Thinning

The scattering data created by NDPP has a size which scales like $\mathcal{O}(N_{E'} \times G \times L)$. This file size can grow quite large and bears an undue computational burden on the downstream Monte Carlo code. To that end, NDPP provides two means to thin the data and reduce the total file size. These are: forcing values below a threshold to zero (increasing transfer matrix sparsity), and removing incoming energy points which provide no more information than interpolation would provide.

The first method, called the printing tolerance, steps through each incoming energy point and searches through all outgoing groups to see if the isotropic moment is less than a user-defined threshold (the *print_tol* parameter, which defaults to 1E-8). When found, the value of the isotropic moment (and the values of all higher order moments) is set to 0 and the remaining outgoing group information is re-normalized. This method reduces the storage requirements because NDPP uses a sparse storage format for the outgoing data. This sparse storage does not remove the requirement to store all the zeros, but instead makes it such that the outgoing group information is only stored from the first to the last group which is non-zero. This means that for incoming energy points which only scatter into the same group, there will only be one outgoing group which needs to be stored.

The second method of grid reduction is simply called grid thinning; this method actually removes incoming energy points from the grid. This method works by stepping through every incoming energy point and seeing if interpolating from the neighboring points reproduces the calculated value to within a user-specified tolerance (the *thin_tol* parameter, which defaults to zero). If so, then that point can be removed from the grid, saving memory. This thinning is performed after the printing tolerance is applied so that the additional sparsity can be taken advantage of when thinning the data.

To evaluate the performance of these thinning methods, consider again the example nuclide ^{90}Zr. Tables 5.1 and 5.2 show applicable size information for both before and after thinning with both the seven-group structure discussed previously and a larger forty-seven group structure with energy bounds which match those used in the HELIOS 47-group library (see Appendix B). Each of these cases was evaluated with P_2 data being calculated. The un-thinned case had a printing tolerance of 10^{-10} and a thinning tolerance of 0. The thinned case had the printing tolerance set to 10^{-10} and the thinning tolerance set to a still very tight tolerance of $10^{-5}\%$.

Table 5.1: Seven Group Thinning Performance

Case	Elastic Points	Elastic Storage	Inelastic Points	Inelastic Storage
Un-Thinned	5,280	0.13 MB	2,573	0.37 MB
Thinned	2,079	0.06 MB	2,332	0.28 MB
Reduction	61%	54%	9%	24%

These tables show that the thinning worked as desired. A majority of the thinning is present on the elastic grid since most of the thinned points were those from the cross section incoming energy grid which were not needed. The inelastic grid was barely thinned in both cases, implying that the grid generation was adequately placing points where needed and the number of them was slightly (but not overwhelmingly) too much. Also evident is

Table 5.2: Forty-Seven Group Thinning Performance

Case	Elastic Points	Elastic Storage	Inelastic Points	Inelastic Storage
Un-Thinned	7,603	0.47 MB	18,963	16.38 MB
Thinned	4,285	0.37 MB	17,230	11.22 MB
Reduction	44%	21%	9%	32%

how the data storage grows with increasing number of groups. Finally, it is clear that the majority of the storage is taken up by inelastic data which fortunately does not need to be repeated for different temperatures. This was the goal of the splitting of the data.

Note that these thinning parameters are still quite fine and further memory savings can be achieved by increasing the tolerances further, perhaps as far as 0.1% to be consistent with standard practice when generating ACE libraries. However, since the appropriate number to use is dependent on the problem to analyze, sensitivity studies of these thinning parameters are left to the potential users of the method. For now it suffices to show that the data storage penalty is a strong function of the thinning tolerances chosen.

5.1.7 Writing Output

The data created by NDPP can store the results of the above calculations in either ASCII or binary files (similar to the ACE Type 1 and Type 2 files). This data is currently written such that each nuclide/temperature combination has a separate file. A *ndpp_lib.xml* file is also written which describes the meta-data (such as group structure and user-options) as well as describing each library such that the Monte Carlo code can access the data. Note that thermal scattering tables, as far as NDPP are concerned, are no different than any other nuclidic library but all reaction types are left with the temperature-dependent elastic data vice being split between inelastic and elastic.

Each library file contains the data listed below in the order provided. The item in italics is the data name and, if provided, the length. For example, *array[N,M]* is a variable called array which contains N rows and M columns of data.

1. *name*: Nuclide name
2. *kT*: Temperature
3. *NG*: Number of groups
4. *E_bins[NG+1]*: Energy group structure in ascending order
5. *scatt_type*: Whether or not Legendre or tabular output is provided (currently not used)

6. *scatt_order*: The scattering order of the Legendre data
7. *nuinel_present*: Whether or not inelastic scattering production data is present in addition to standard inelastic scattering data
8. *chi_present*: Whether or not the fission spectra data is included
    - Note that this feature has not yet been fully implemented though it is included in the data format for future expansion
9. *mu_bins*: The number of angular bins used when integrating
10. *thin_tol*: The thinning tolerance applied to the data
11. Elastic scattering data, $\overline{f_{n,2}}(E',T)$:
    (a) *NE_el*: Number of incoming energy points
    (b) *E_el[NE_el]*: Incoming energy grid
    (c) *group_index_el[NG+1]*: Location in *E_el* of each group boundary
    (d) For every incoming energy point:
        i. *gmin*: Minimum outgoing group
        ii. *gmax*: Maximum outgoing group
        iii. *data[gmin:gmax, scatt_order]*: Outgoing data for each Legendre order
12. Inelastic scattering data, $\overline{\sigma f_{n,inel}}(E')$:
    (a) *NE_inel*: Number of incoming energy points
    (b) *E_inel[NE_inel]*: Incoming energy grid
    (c) *group_index_inel[NG+1]*: Location in *E_inel* of each group boundary
    (d) For every incoming energy point:
        i. *gmin*: Minimum outgoing group
        ii. *gmax*: Maximum outgoing group
        iii. *data[gmin:gmax, scatt_order]*: Outgoing data for each Legendre order
    (e) If *nuinel_present* is true, retrieve inelastic production data at every incoming energy point, $\overline{\sigma Y f_{n,inel}}(E')$:
        i. *gmin*: Minimum outgoing group
        ii. *gmax*: Maximum outgoing group

        iii. *data[gmin:gmax, scatt_order]*: Outgoing data for each Legendre order

13. If *chi_present* is true:
    (a) *NE_chi*: Number of incoming energy points for fission spectra grid
    (b) *NP_chi*: Number of delayed neutron precursor groups
    (c) *E_chi[NE_chi]*: Incoming energy grid
    (d) *chi_total[NG,NE_chi]*: Outgoing total fission spectra
    (e) *chi_prompt[NG,NE_chi]*: Outgoing prompt fission spectra
    (f) For each delayed neutron precursor group, *p*:
    (g) *chi_delayed,p[NP,NG,NE_chi]*: Outgoing delayed fission spectra for precursor group *p*
    - Note that this feature has not yet been fully implemented though it is included in the data format for future expansion

5.2 OpenMC Implementation

To make use of the data produced by NDPP, a Monte Carlo code needed to be modified to take advantage of the data. OpenMC was chosen as the code to use because it is readily available, written in a modern dialect of Fortran (Fortran 2003), and is considered to have reactor analysis capabilities comparable to other widely used codes such as MCNP [23] and Serpent [5].

The changes necessary to OpenMC were trivial: the corresponding NDPP data for each nuclide in the problem needed to be loaded into memory (with non-useful pieces discarded), and a new type of tally score created which uses the NDPP scattering, scattering and production instead of the traditional tallying schemes previously implemented. Since the NDPP data allows for track-length estimators to be used, each of these score types were implemented for both collision and track-length estimators. These tallies can also be tallied on a material (macroscopic) or nuclidic (microscopic) basis. The scattering data tallies can be tallied for all moments at once or only for a single requested moment. Finally, all these different types of scores can be tallies using either isotropic flux weighting (per the flux separability approximation), or with spherical harmonic flux moment weighting (to support the Consistent-P approximation).

The scattering and scattering-production tally scoring essentially occurs as follows for each nuclide to be tallied (which is all the nuclides in a material if determining macroscopic cross sections):

- For each of the elastic and inelastic data:
    - A binary search is performed over the set of incoming energy points which exist in the current incoming group to determine the location of the particle's incoming energy on the NDPP grid.
    - These locations are used to logarithmically interpolate the outgoing distribution at the particle's incoming energy.
- The elastic and inelastic data are combined into a single distribution for all orders requested using the cross section values for the current nuclide at the current energy which have already been determined by OpenMC.
- This entire distribution (and all orders) are then tallied in the correct locations.

The modifications to OpenMC discussed above will be merged into the main branch of OpenMC and will be available for use shortly after the publication of this dissertation.

CHAPTER 6

Improved Method Performance

This dissertation has thus far identified an area in which Monte Carlo neutron transport is lacking, discussed a potential fix, and then described the implementation of said fix. However, this work has not yet shown the theorized benefits of the improved method. Doing so means determining if the method produces results of sufficient accuracy, and then identifying if the perceived benefits are real and, most importantly, useful. This chapter provides these measures for the improved method and the NDPP & OpenMC implementation of the method.

This study will be done by first examining the accuracy of the data output by NDPP before it is used by any Monte Carlo code. After this is performed, the data will be applied to realistic problems to determine the quality of the sufficiently converged multi-group cross sections. This quality comparison means examining the cross sections themselves as well as the subsequent value of k_{eff} and pin power distributions obtained when utilizing these cross sections. Finally, the stated benefit of the improved method is the improved efficiency of tallying MGXS with outgoing distribution information. This claim will be tested by comparing the tallying efficiency of these MGXS with the same data with the original tallying method by examining the points at which the cross sections produced by both methods can be considered sufficiently converged as well as the magnitude of the stochastic uncertainties.

The problems to be analyzed in this chapter are the same as examined in Chapter 3: a UO_2 pin cell and a 5x5 sub-assembly problem. Like before, the HELIOS forty-seven group structure [36] will be used in all cases of this chapter. The energy bounds of this structure can be found in Table B.2 of Appendix B. All NDPP data was sourced from the ENDF/B-VII.0-based ACE files supplied with MCNP6. A thinning tolerance of 1E-5% and a printing tolerance of 1E-10 was applied, and 501 angular points were used for numerical integration of the angular distribution (yielding an angular spacing of 0.004). Data was generated for up to P_2 scattering. Note that all the uncertainties reported herein are in terms of the 95% Confidence Interval (CI) as they were in Chapter 3.

6.1 Point-Wise Accuracy Comparison

In this section, OpenMC was used to sample a scattering distribution for a set of incoming energy points using the analog method of tallying. These were then compared to the corresponding distributions produced by NDPP at the same energies.

All of the OpenMC models used in this analysis were infinite in space and composed of a single nuclide. OpenMC was run in fixed-source mode with a spatially flat monoenergetic and isotropic neutron source with a total of 30 million histories. Tallies were set up to score the P_0 through P_2 scattering moments for outgoing energies corresponding to the 47-group structure. The incoming energy filter was set up to tightly contain the incoming energy of interest for each case; the bin was chosen to be very thin such that only neutrons nearly exactly at the energy of interest will contribute to the collected data.

Five cases were analyzed in order to test the different classes of reactions encountered by NDPP:

1. Elastic scattering with target-at-rest kinematics
2. Elastic scattering with target-in-motion kinematics (i.e., the free-gas kernel)
3. Inelastic level scattering
4. Inelastic continuum scattering
5. Thermal scattering ($S(\alpha,\beta)$) kinematics

The first four cases utilize ^{90}Zr as the target nucleus while the last uses ^{1}H in H_2O. The results of these cases are described in the following sections.

In all of these figures, the top plot shows the NDPP data (in red) and the average value of the OpenMC tallied data (in black); the OpenMC data contains the 95% CI as error bars,though these are often difficult to discern due to the large number of histories that were simulated. The x-axis in both cases is the outgoing energy of the multi-group data. The bottom plot shows the absolute error (in percent) between the NDPP and OpenMC data (in red); the black line shows the 95% CI of the tallys relative uncertainty for comparison. Finally, the dashed vertical line represents the incoming energy.

6.1.1 Elastic Target-at-Rest Comparison

The first case was chosen to evaluate the ability of NDPP to calculate distributions for elastic scattering with a target-at-rest. The now familiar example nuclide ^{90}Zr was used for this case at an incoming energy of 48.15 eV. This energy was chosen because it is an energy above the 400*kT* free-gas treatment cutoff of 20.7 eV and below the inelastic threshold, ensuring this test only contains elastic collisions with the target nuclide but without the application of the free gas kernel. In addition, this energy is slightly above a group break point, meaning both self-scatter and down-scatter will be observed.

The P_0, P_1, and P_2 results for this case are shown in Figures 6.1, 6.2, and 6.3, respectively. For all orders it is difficult to discern any differences between the mean values; in addition, the percent differences between the two are always lower than the stochastic error. This gives good confidence that NDPP accurately handles elastic scattering with target-at-rest kinematics accurately.

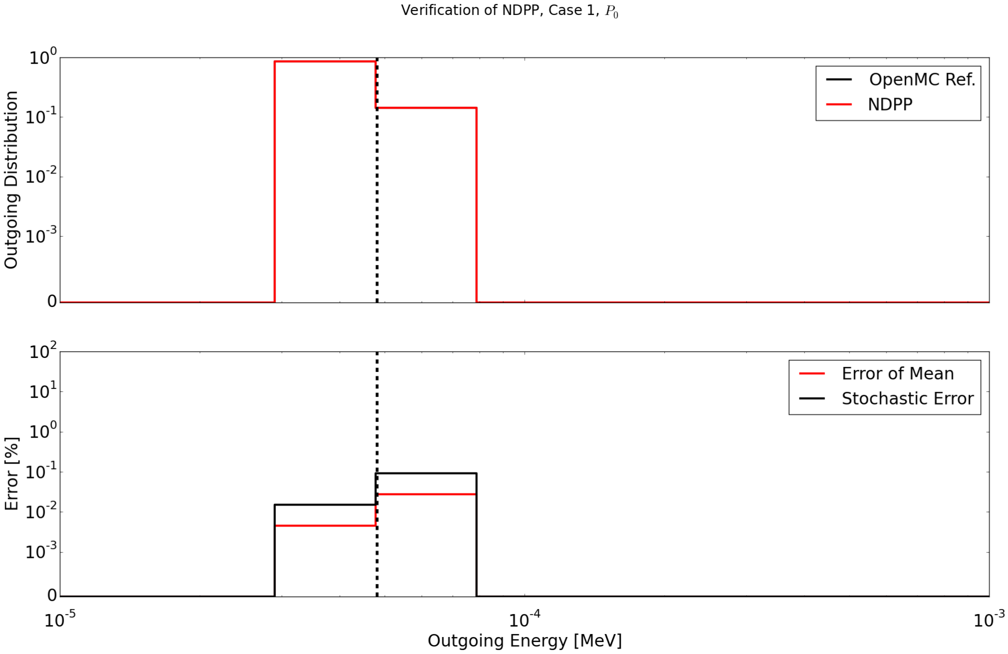

Figure 6.1: Case 1: Elastic, Target-At-Rest, with P_0 Scattering

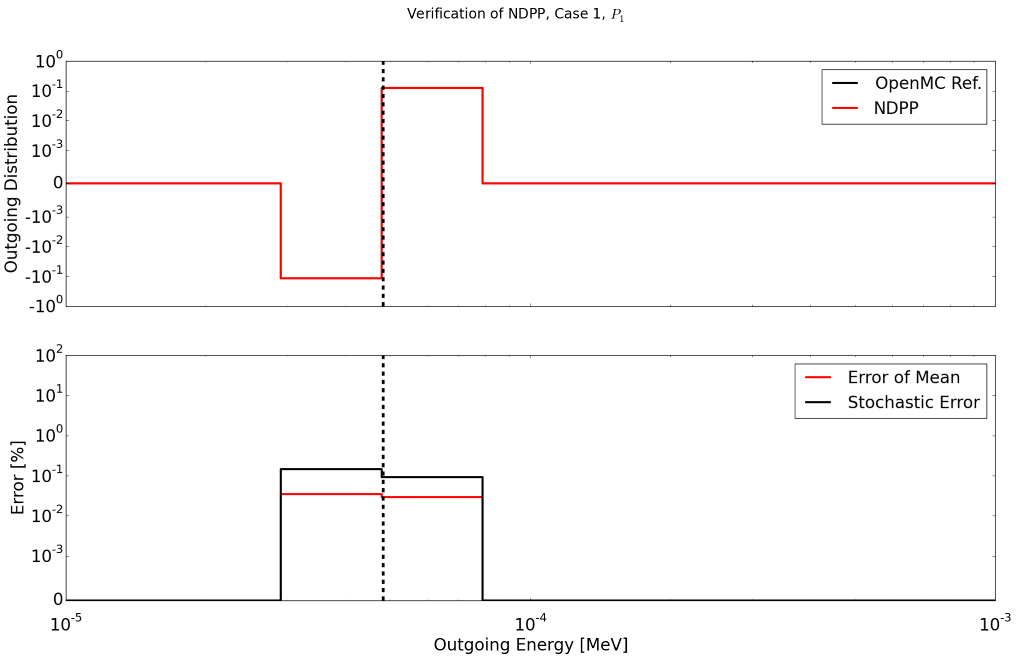

Figure 6.2: Case 1: Elastic, Target-At-Rest, with P_1 Scattering

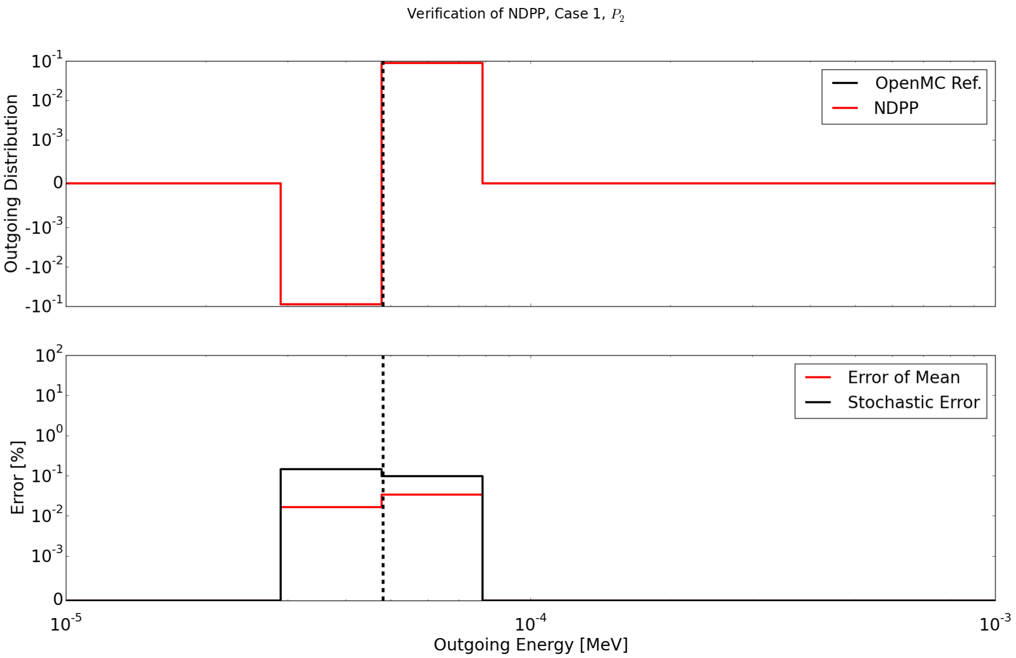

Figure 6.3: Case 1: Elastic, Target-At-Rest, with P_2 Scattering

6.1.2 Elastic Target-in-Motion Comparison

Case two was designed to test the free-gas kernel implementation in NDPP again with ^{90}Zr as the target nuclide. The model in this case is the same as in the previous, except that the incoming energy of interest is now below the free-gas threshold energy. In this case 1.05 eV was chosen. This point is between two group boundaries, 1.0137 and 1.0722 eV, and thus down- and up-scatter will be observed. The results of this case are shown in Figures 6.4 through 6.6 for the P_0 through P_2 data, respectively. Like the target-at-rest case, these results show again that the NDPP data is always within the 95% CI bounds and therefore matches the reference well.

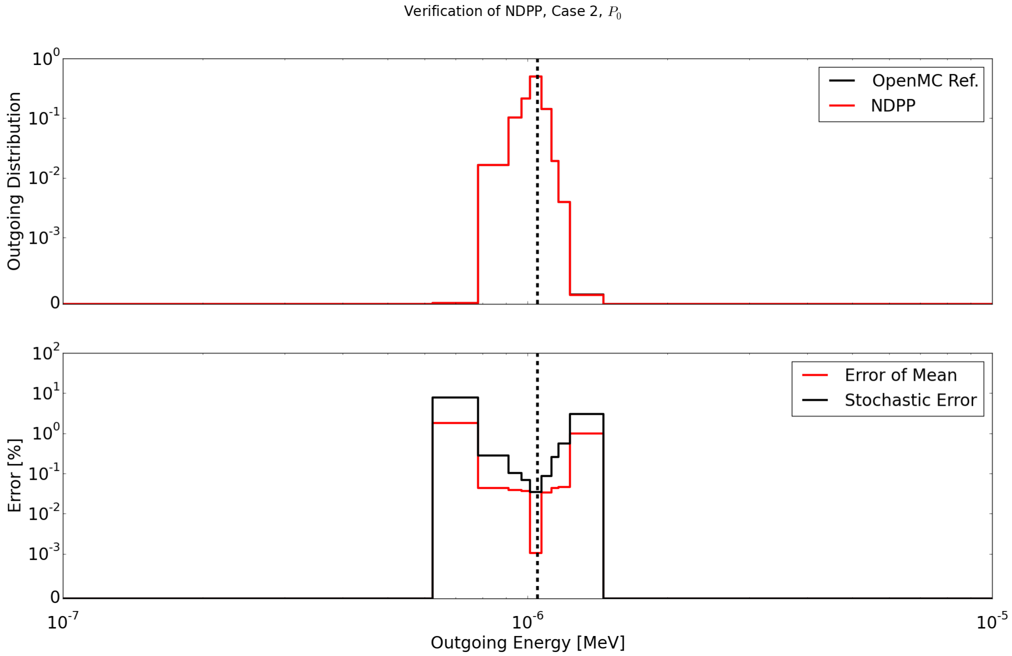

Figure 6.4: Case 2: Elastic, Target-In-Motion, with P_0 Scattering

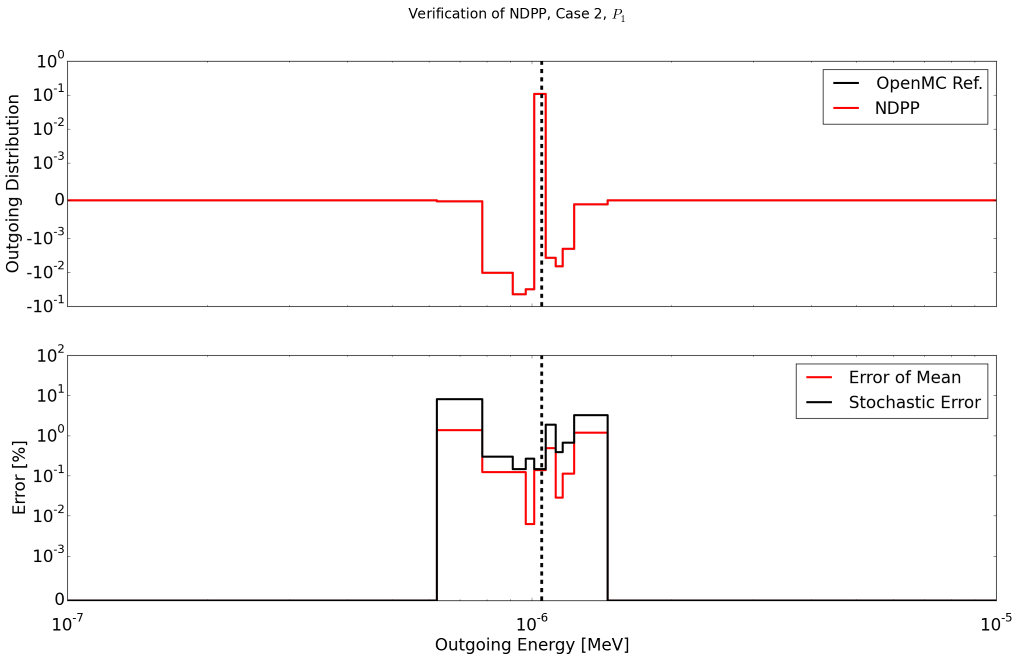

Figure 6.5: Case 2: Elastic, Target-In-Motion, with P_1 Scattering

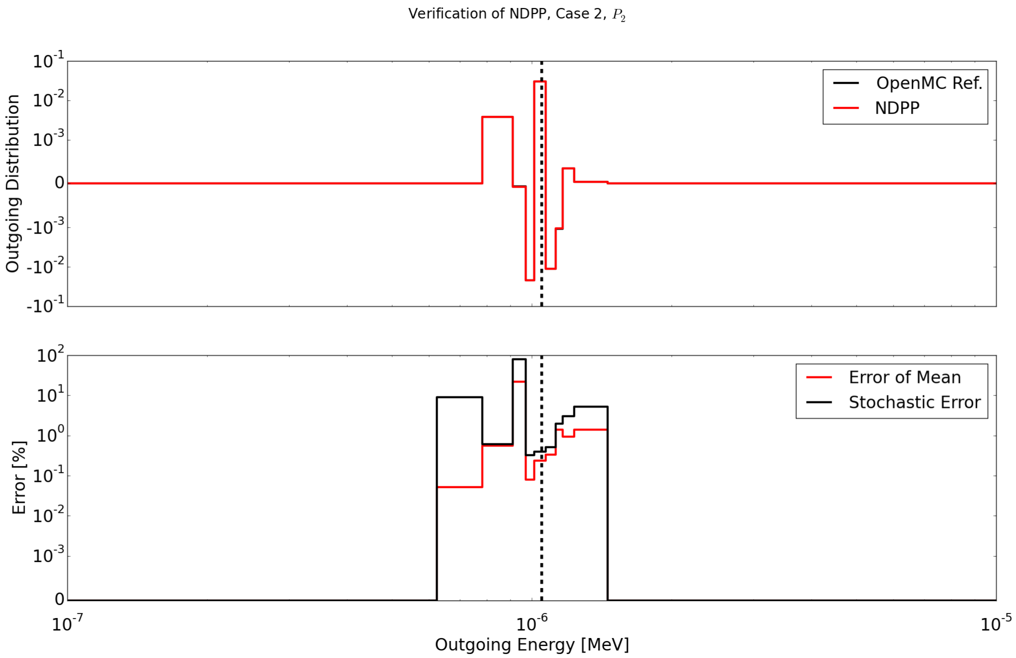

Figure 6.6: Case 2: Elastic, Target-In-Motion, with P_2 Scattering

6.1.3 Inelastic Level Comparison

Case three exercised the ability to calculate inelastic level collision distributions described by Law 3. ^{90}Zr is again the target. The energy of this problem, 3.0 MeV, was chosen so that a single inelastic level channel, (n,n_2), represents the majority of inelastic collisions and the inelastic collisions represent a sizable portion of all scattering collisions. The elastic cross section at this energy is 2.8 barns; the total inelastic cross section is 50% of this and the (n,n_2) cross section is slightly more than 50% of the total probability of an inelastic collision. The continuum cross section is three orders of magnitude lower than the (n,n_2) cross section.

These results are shown in Figures 6.7 through 6.9 for the P_0 through P_2 data, respectively. The outgoing energy distribution, best shown in Figure 6.7, shows two distinct outgoing energy regimes; the first is in the group containing the incoming energy and the second begins near 1 MeV. The first regime is due to the elastic scattering while the second regime is due to the outgoing inelastic neutrons. Each of these regimes shows good agreement. This is to be expected as the elastic (target-at-rest) kinematics and inelastic level kinematics are describes by the same equations as discussed in Chapters 4 and 5.

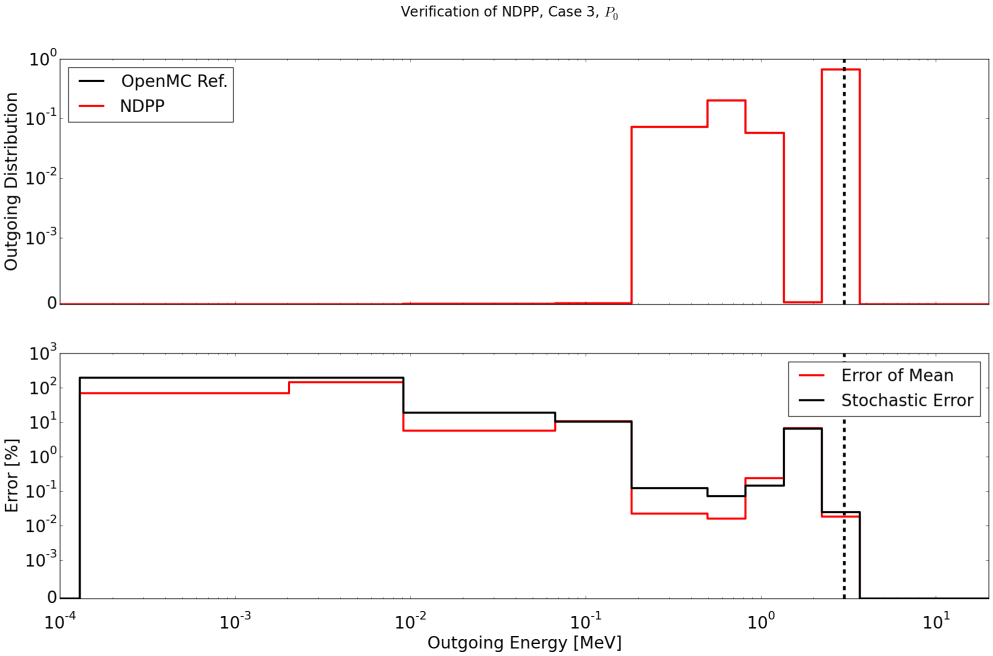

Figure 6.7: Case 3: Inelastic Level, with P_0 Scattering

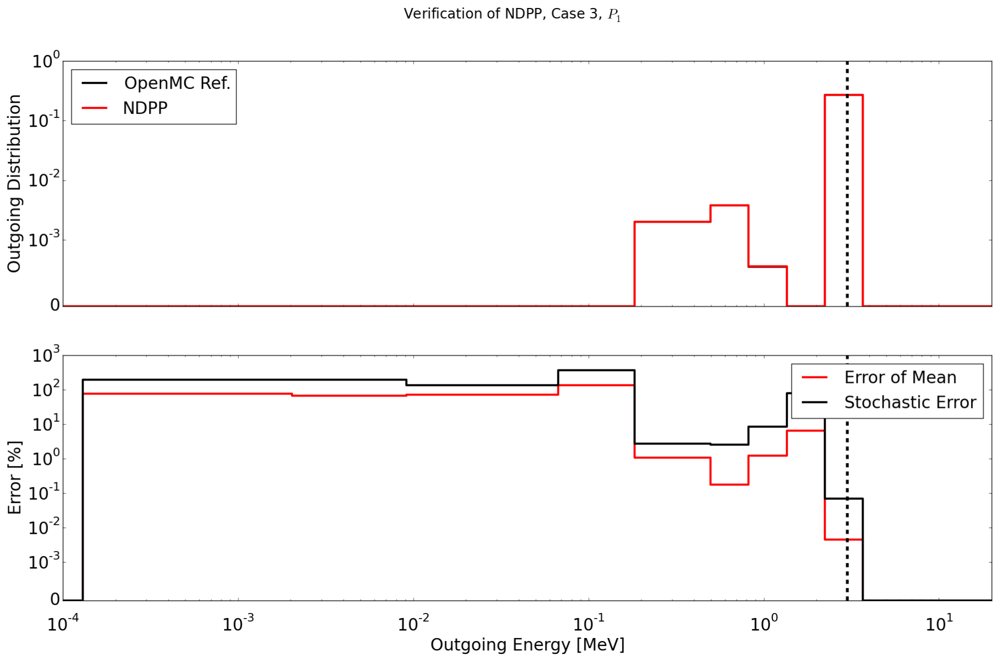

Figure 6.8: Case 3: Inelastic Level, with P_1 Scattering

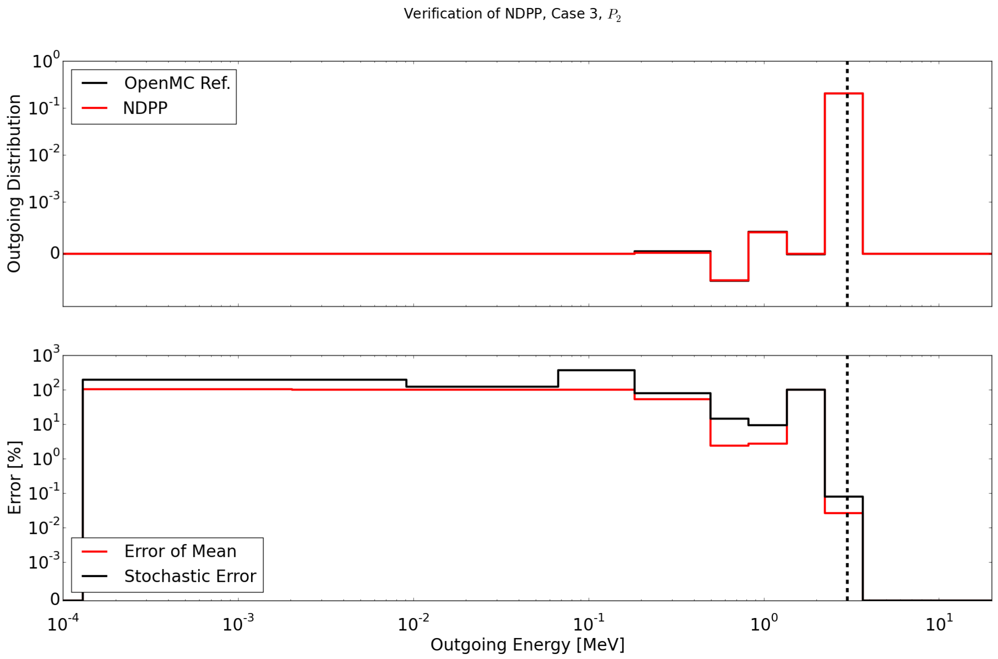

Figure 6.9: Case 3: Inelastic Level, with P_2 Scattering

6.1.4 Inelastic Continuum Comparison

Case four is the final case using ${}^{90}Zr$ as the target. The energy of this case, 6.0653 MeV, was chosen such that inelastic continuum scattering was the predominant inelastic reaction with a cross section of 1.81 barns. This continuum reaction was 92% of the total inelastic cross section and 85% as large as the elastic cross section. The continuum reaction for this nuclide is represented by a Law 61 tabular energy-angle distribution in the CM frame and therefore requires the complicated integration routine of Eq. (5.15).

Figures 6.10 through 6.12 show the results for the P_0 through P_2 data, respectively. The elastic peak just below the incoming energy can be seen as well as the smooth outgoing distribution of the continuum reaction. These data show that some outgoing groups contain values for the error of the mean is larger than the stochastic error. From this data it is expected that the error of the means would only increase as the number of histories is increased. This, therefore, is an expected source of bias in the analyses using NDPP data. The numerical integration procedure used to integrate Law 61 could make use of a higher number of samples.

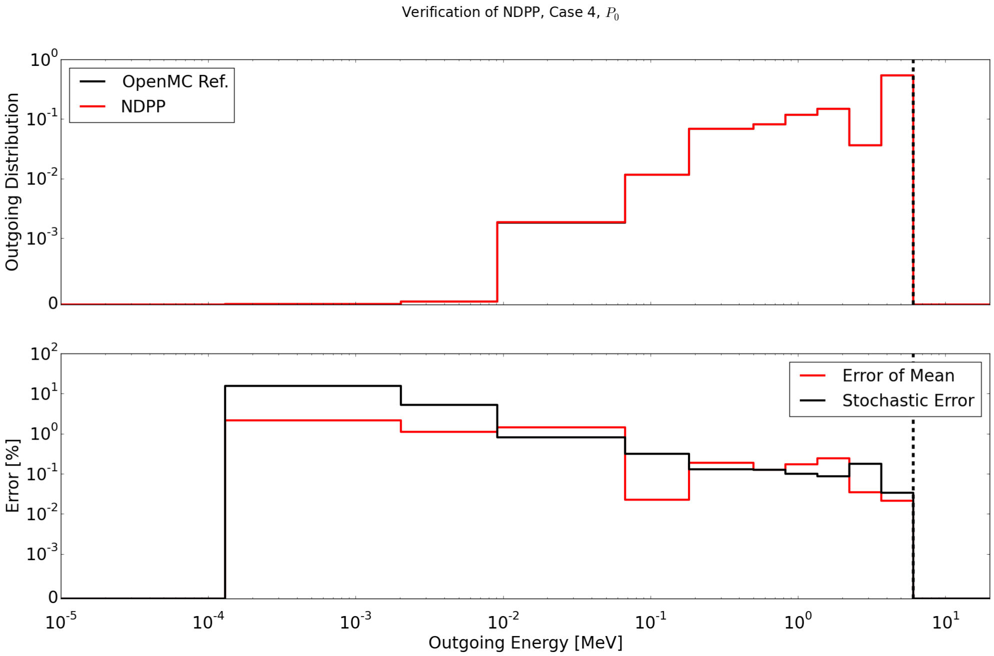

Figure 6.10: Case 4: Inelastic Continuum, with P_0 Scattering

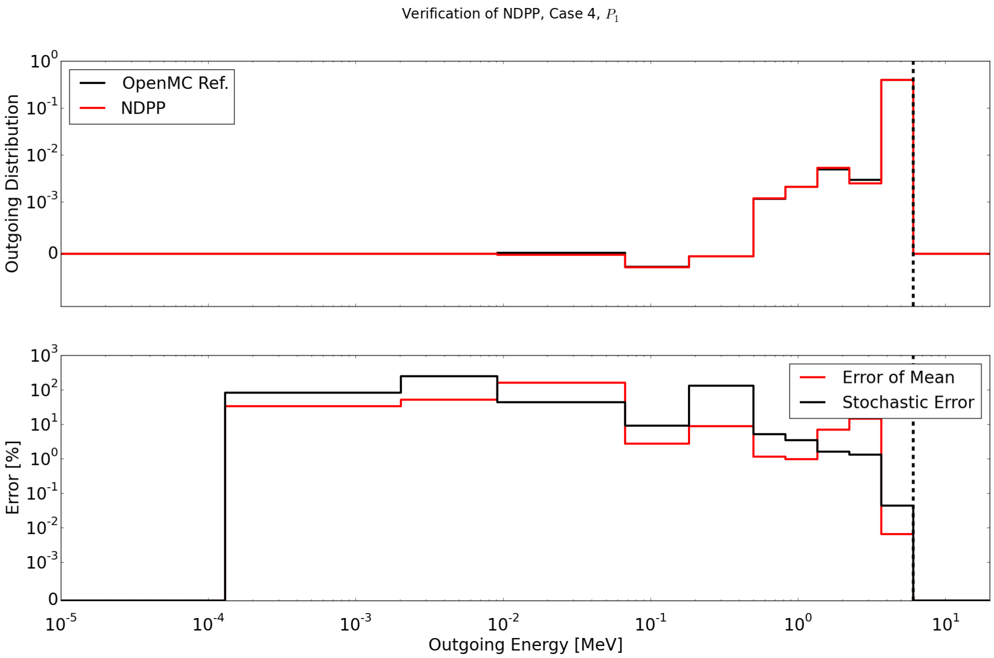

Figure 6.11: Case 4: Inelastic Continuum, with P_1 Scattering

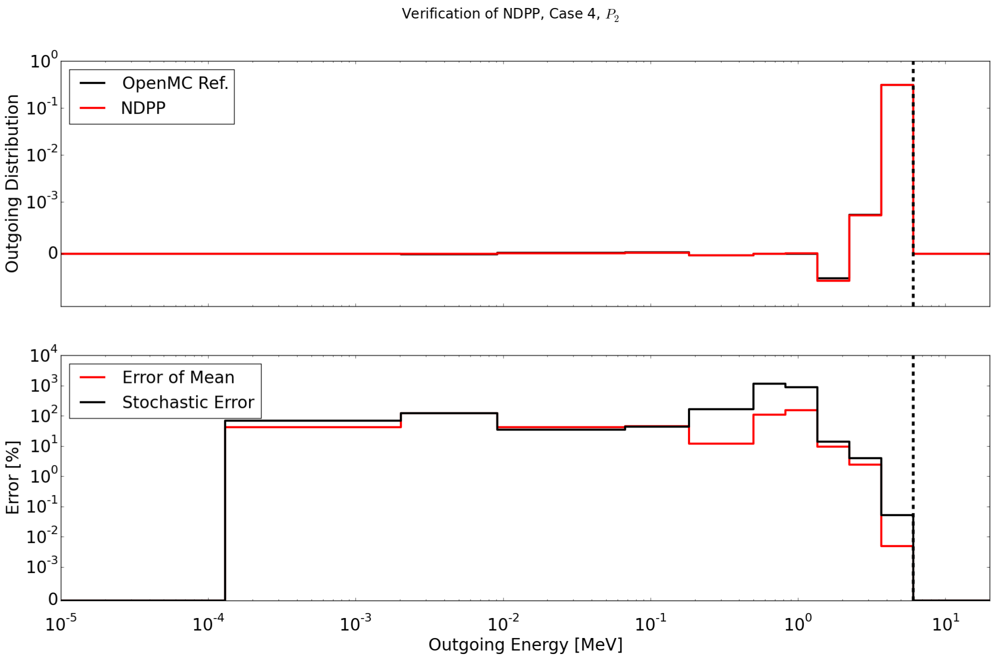

Figure 6.12: Case 4: Inelastic Continuum, with P_2 Scattering

6.1.5 Thermal Scattering Tables Comparison

The next case tests the ability of NDPP to calculate the scattering data of thermal scattering tables. This problem used ^1H with the H-H_2O thermal scattering table applied. The incoming energy was 1.05 eV ensuring that only $S\ (\alpha,\beta)$ scattering is encountered in the OpenMC calculation. These results are shown in Figures 6.13 through 6.15 for the P_0 through P_2 data, respectively. Excellent agreement is again seen.

Note that the relative error goes to zero in multiple locations because the thermal scattering tables (as calculated by NJOY [24]) contain discrete outgoing energies; the groups that do not contain any of this set of energies therefore have a zero probability.

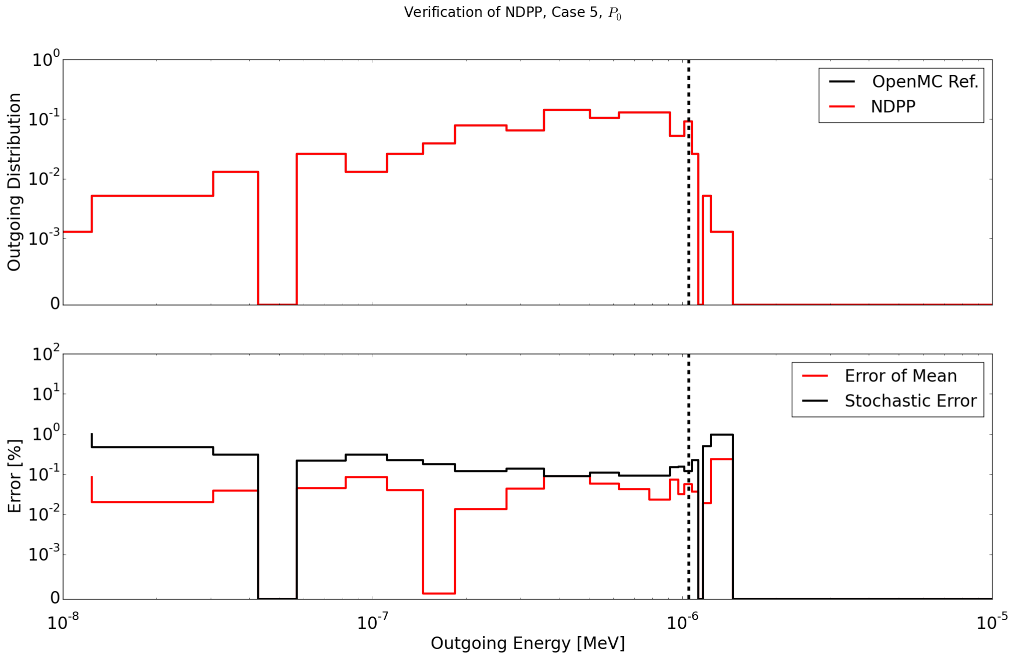

Figure 6.13: Case 5: $S\ (\alpha,\beta)$, with P_0 Scattering

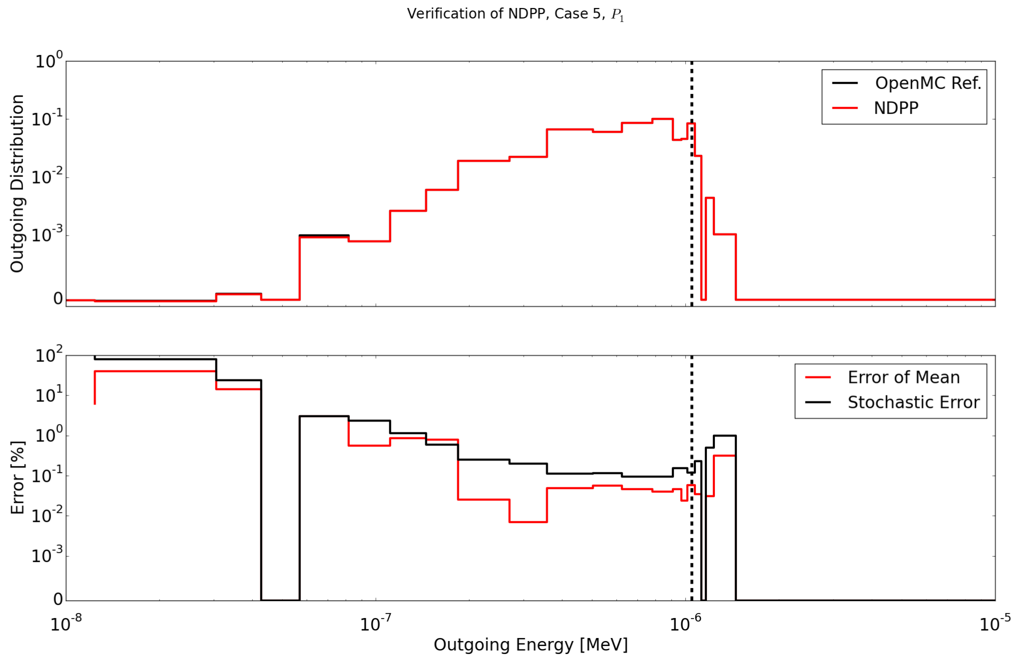

Figure 6.14: Case 5: $S(\alpha,\beta)$, with P_1 Scattering

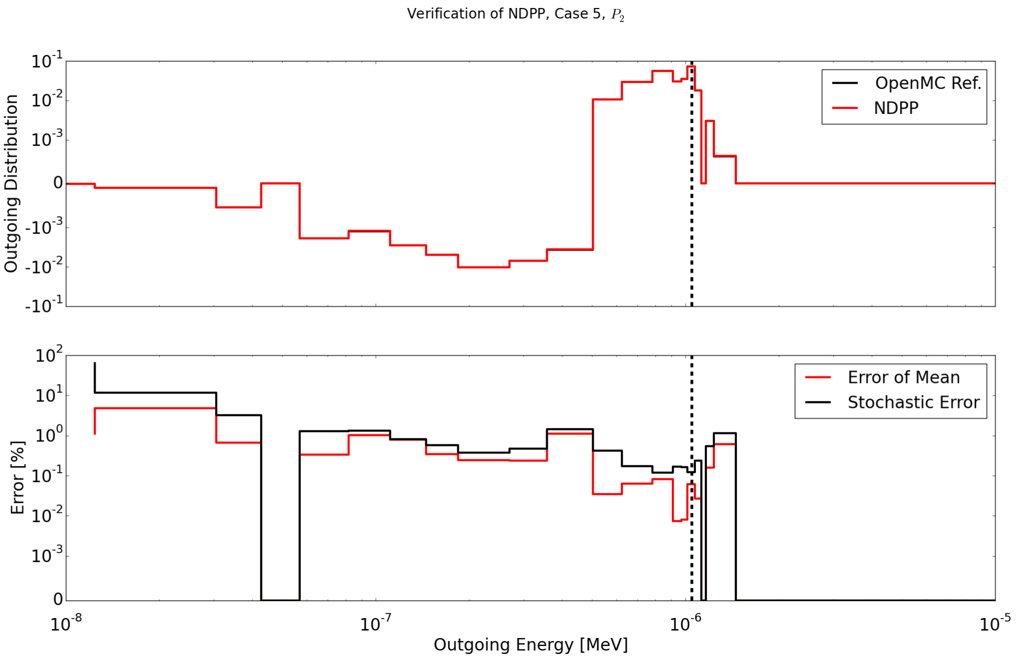

Figure 6.15: Case 5: $S(\alpha,\beta)$, with P_2 Scattering

6.2 Multi-Group Cross Section Accuracy Comparison

The previous sections analyzed accuracy by directly investigating the data produced by NDPP. This section, in contrast, will look at the accuracy of the MGXS data as tallied by OpenMC using data produced by NDPP. Doing so allows the analysis to factor in the interpolation of the NDPP data at tally time as well as look at the accuracy of the final end product of the method.

This evaluation will be performed with the same hot-zero power, beginning of cycle pin cell discussed in Appendix A and applied in Chapter 3. This model provides the simplest production-level case which can be analyzed. All data needed to produce a macroscopic MGXS library (using the 47-group structure) was then tallied including the P_2 scattering production. The reference solution for this work will be the traditional analog-based tallying discussed in Chapter 3. Both the reference analog solution and the NDPP-based solution will be simulated with 1 billion active particles in an eigenvalue calculation.

This analysis will first examine the complete scattering matrix of the fuel and moderator, comparing the P_0 matrices of the analog and improved method. The second comparison will be between the scattering moment matrices reduced over all outgoing groups. Third, the scattering moments for the three incoming groups previously studied in Chapter3 (groups 4, 14, and 44) will be analyzed and compared. This data will then be used by a deterministic transport code with anisotropic scattering, MPACT [18], to calculate the k_{eff} of the exact same pin cell in order to compare the error in resultant eigenvalues between the two tallying methods.

6.2.1 Scattering Matrix Comparison

In this section, the scattering moment matrices will be compared for the analog tallying and improved tallying methods. First, a side-by-side comparison of the analog and improved tallying methods will be shown to facilitate a qualitative comparison. The analog method is displayed on the left while the right shows that obtained by using the NDPP data. The color is used to denote the value according to the color scale located underneath the image. The incoming groups are located on the x-axis and outgoing groups on the y-axis. In this scheme down-scattering is represented as below the diagonal which connects the top left and lower right corners; up-scattering is above this diagonal. Self-scatter (scattering to the same group as the incident neutron) is of course the diagonal itself. Note that the color scale is a symmetric-log scale; this type of scale is a logarithmic scale which contains a linear scale from -10^{-5} to 10^{-5}. Finally, due to the high data dimensionality, the stochastic error of the tallies is not displayed.

Next, these separate plots will be combined in to a single plot which highlights the differences in the matrices generated by each of the two methods. The color scale on these plots are now linear to highlight the regions of highest error. Since a majority of group transfers have zero probability in the analog method but not the improved method (due to lack of those particular bins being sampled), the error plots were generated such that the percent error is shown if the values were above 1% of the maximum of the analog data for the given incoming energy group (the column). Below this 1% threshold, the absolute error was calculated instead. This was done to avoid the large errors which will arise when two numbers are very near zero, as will happen when the probabilities become negligible. Without this change, these large errors would overwhelm the error plots making it difficult to observe the more interesting effects.

Figures 6.16 through 6.18 show the side-by-side comparison of the P_0 through P_2 matrices for the fuel, respectively. The fuel moment matrices display some interesting phenomena worth discussing. At high energies (groups 1 to 8), the inelastic scattering leads to down-scattering to as low as group 10 (200 keV). Next, up-scattering begins at group 15; this is to be expected as the free-gas cutoff at this temperature is approximately 20 eV (which is within group 15). When comparing the analog and NDPP data for the three orders shown here, it is clear that NDPP is not missing any physics for the reactions present in the fuel.

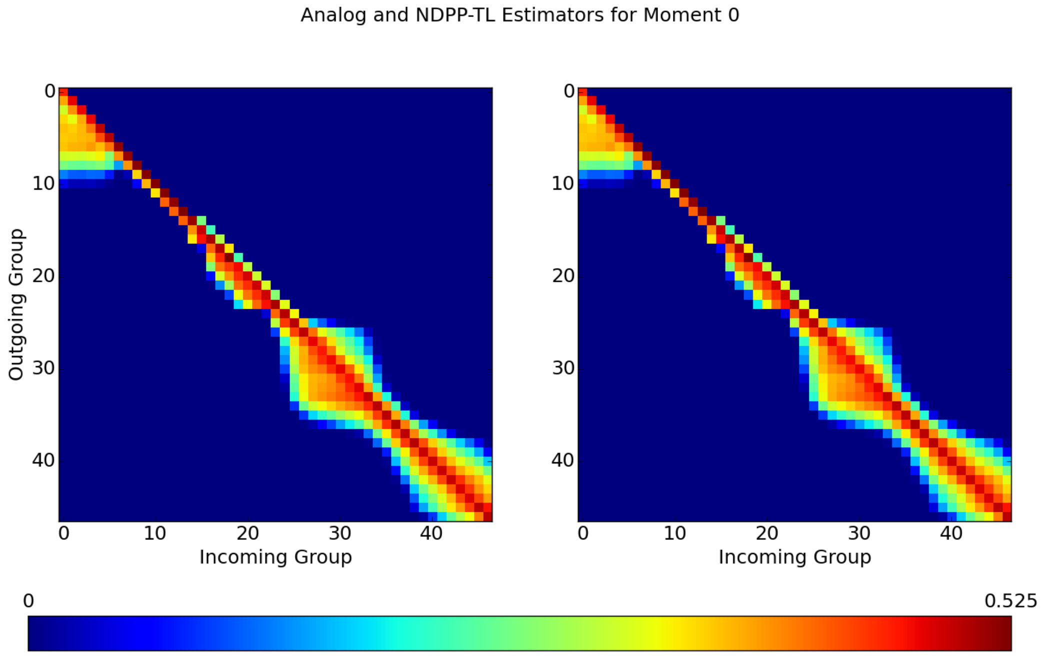

Figure 6.16: Fuel P_0 Scattering Matrix Comparison

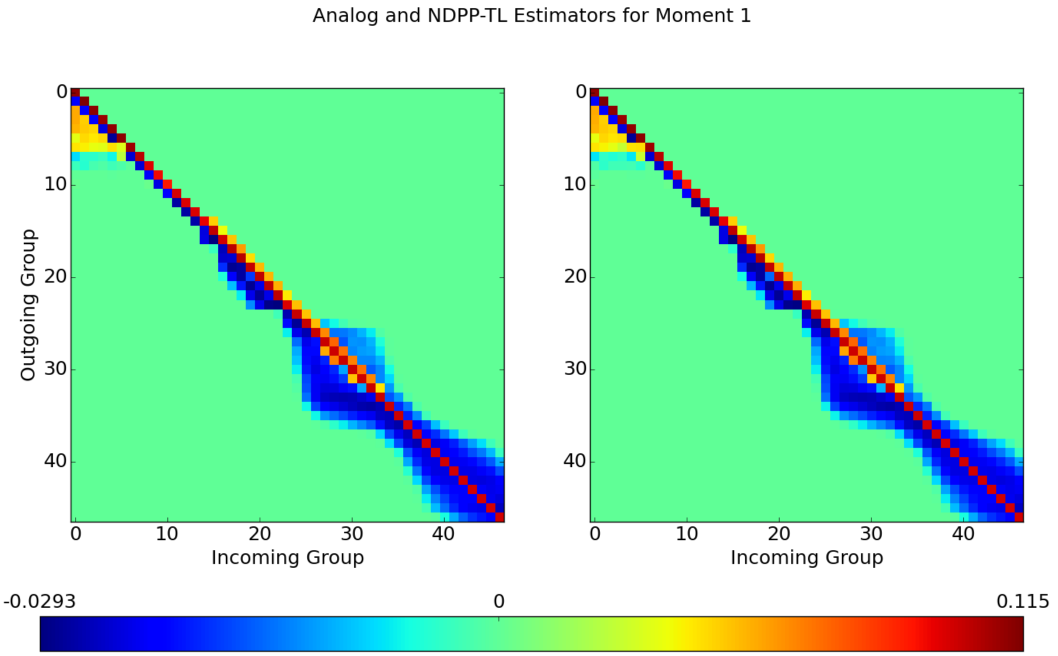

Figure 6.17: Fuel P_1 Scattering Matrix Comparison

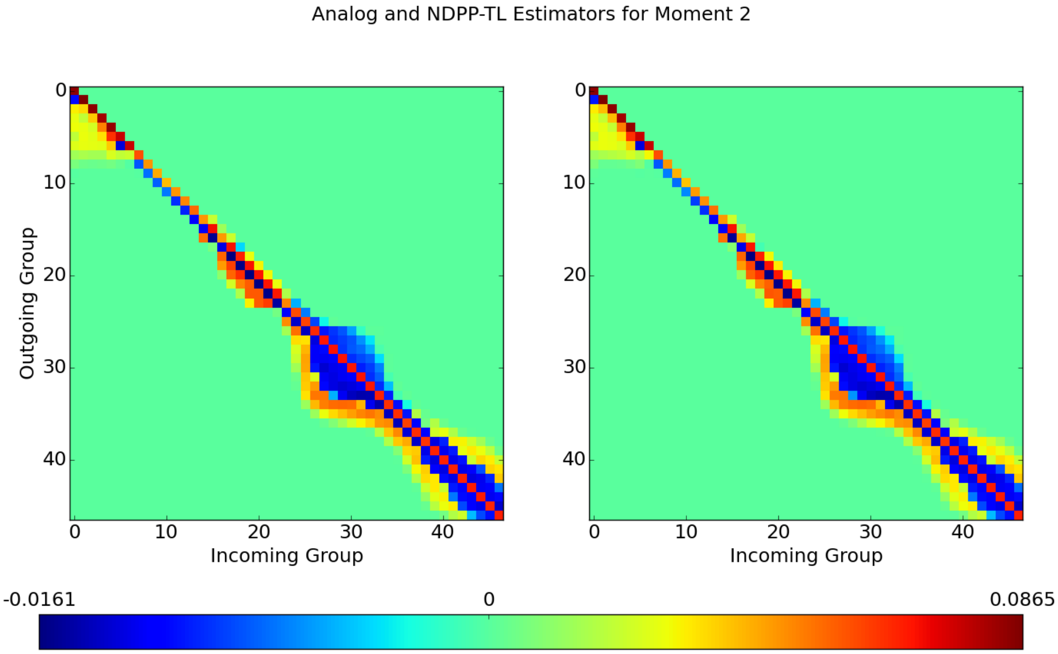

Figure 6.18: Fuel P_2 Scattering Matrix Comparison

The error comparison for the fuel is shown in Figures 6.19 through 6.21 for P_0 through

P_2, respectively. These results show the locations of maximum error; typically on the fringes of the distributions where the transition from percent error to absolute error is made. There is a region of relatively large errors in the inelastic regime (specifically in groups 3 and 4); this, like was shown in Section 6.1.4, is due to the difficulty in integrating the continuum distributions.

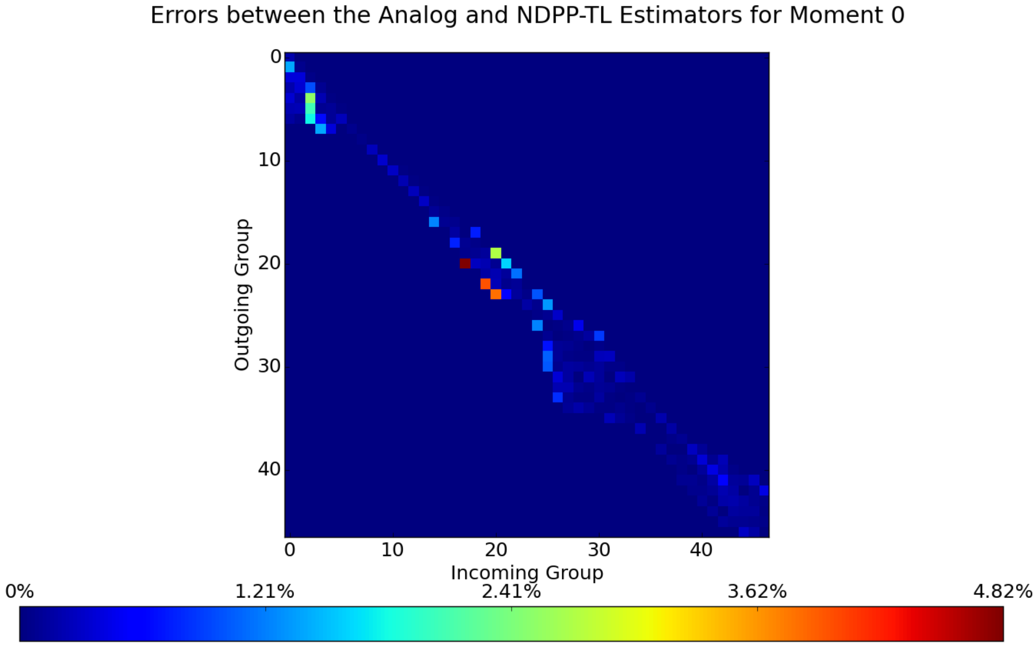

Figure 6.19: Fuel P_0 Scattering Matrix Errors

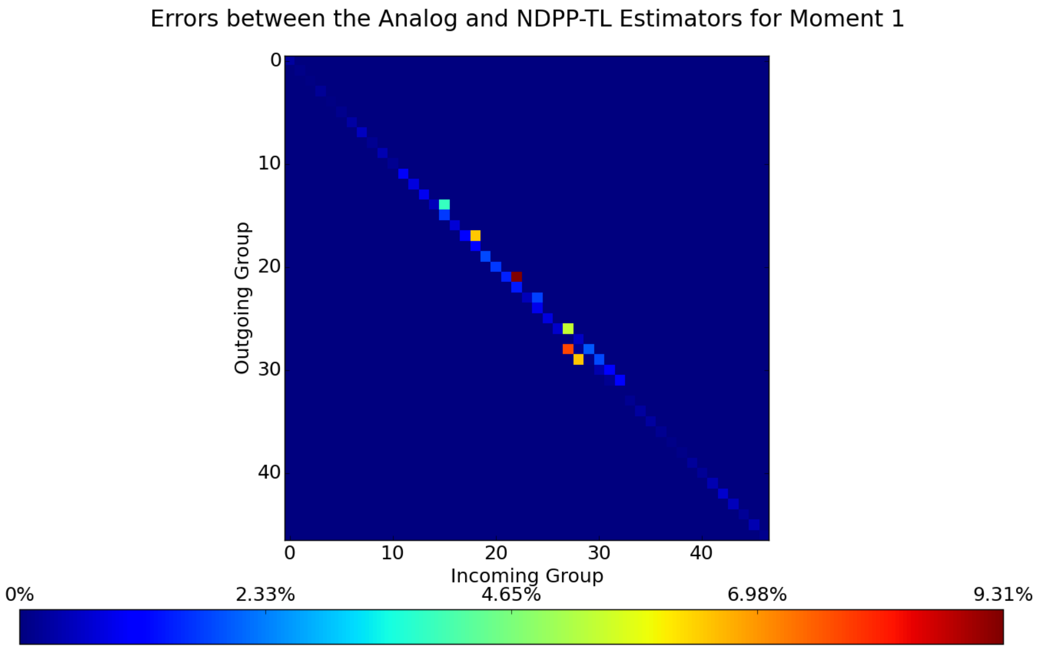

Figure 6.20: Fuel P_1 Scattering Matrix Errors

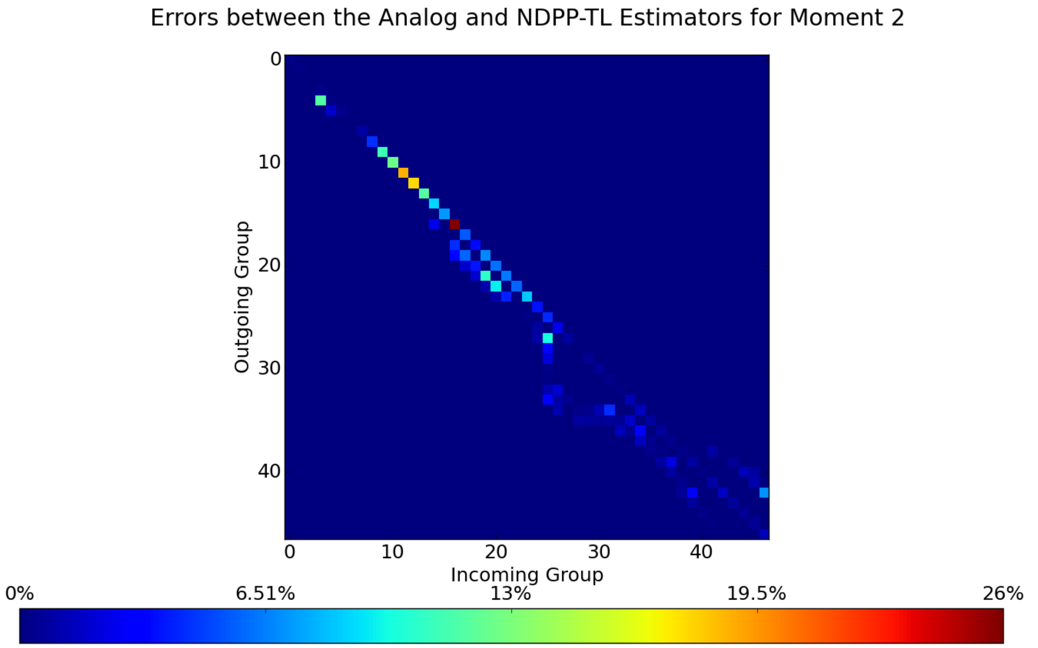

Figure 6.21: Fuel P_2 Scattering Matrix Errors

Figures 6.22 through 6.24 show the same qualitative comparison for the moderator.

When examining the data tallies from the moderator (borated water), three things are immediately obvious: first, the moderator material is dominated by down-scatter; second there are gaps in the data which are visible between incoming groups 16 and 34; and third, there are some differences where the scattering matrices approach zero around group 10.

The first is of course because of the light nuclei present in the moderator and thus the elastic scattering has an outgoing energy as low as seven orders of magnitude lower than the incoming energy.

The second item is an artifact of the discrete outgoing energies present in the inelastic scattering thermal scattering data (discussed in Chapter 4). The dark blue lines in Figure 6.22 are due to there being no outgoing energies in these outgoing groups and thus there is no energy transfer. This is fixed with continuous thermal scattering libraries provided with MCNP [23]; NDPP supports this data type but their analysis was not included in this work since their usage is not yet widespread and the format is not yet officially included in the ACE standard.

Overall, these figures give confidence that NDPP is not missing any important physics.

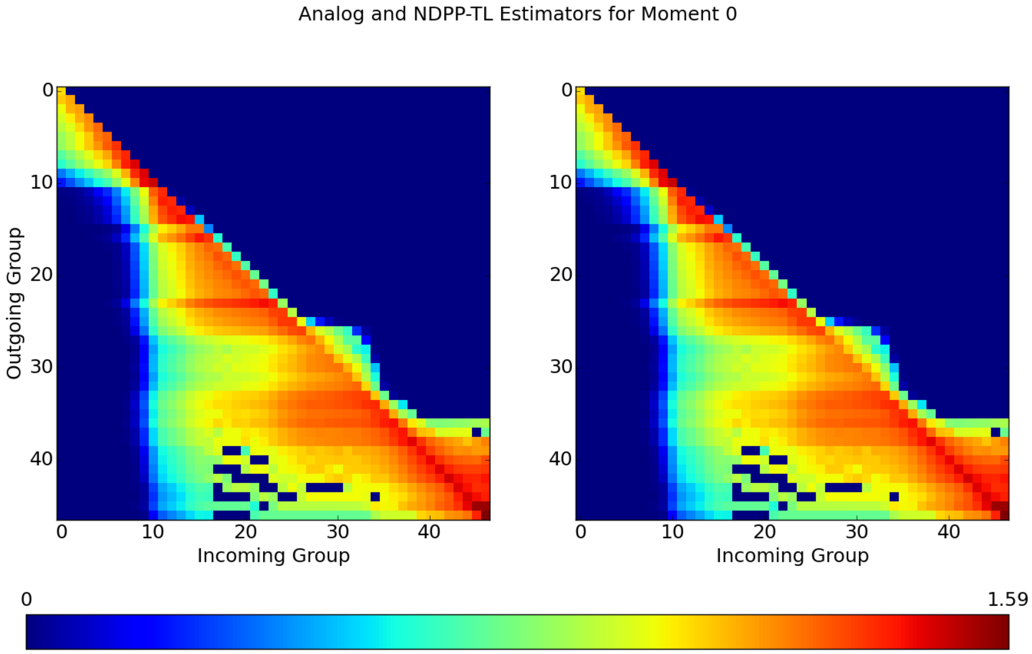

Figure 6.22: Moderator P_0 Scattering Matrix Comparison

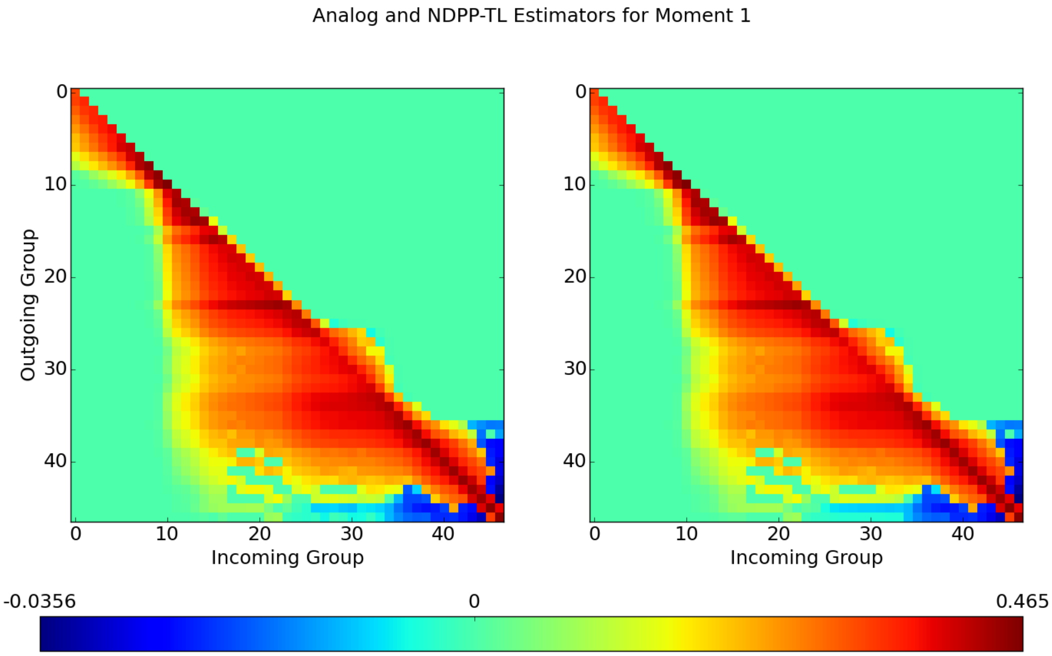

Figure 6.23: Moderator P_1 Scattering Matrix Comparison

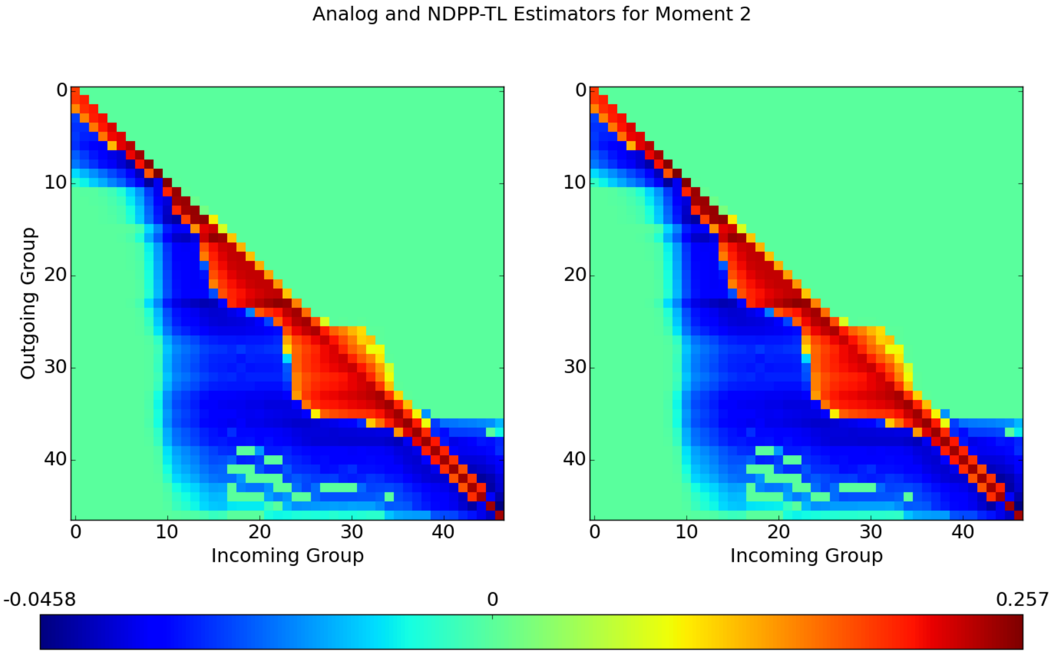

Figure 6.24: Moderator P_2 Scattering Matrix Comparison

The error comparison is presented in Figures 6.25 through 6.27. The maximum differences between the analog and NDPP methods are 1.89% for P_0, 2.1% for P_1, and 10% for P_2. For all orders, the worst performance occurs typically in the fast groups where the inelastic scattering (primarily of the ^{16}O here) has proven difficult to integrate, though the magnitude difference is not substantial. Note that since these plots show error on an absolute basis once the magnitude of the data becomes small enough, we see some large errors near the fringes of the possible transfers.

Despite the above, most of the matrices have errors less than 1% indicating very good agreement overall.

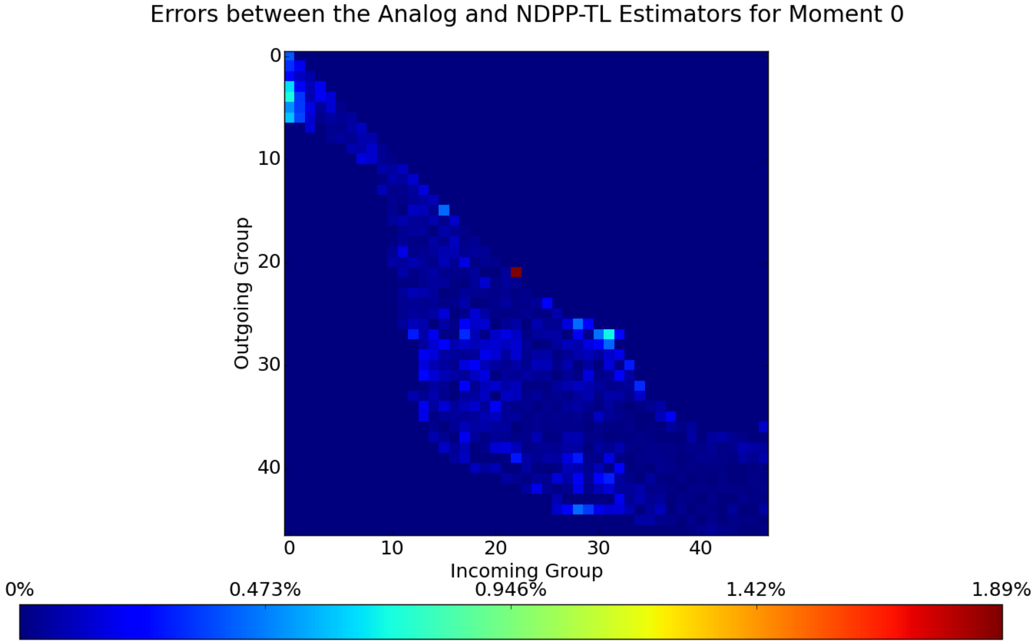

Figure 6.25: Moderator P_0 Scattering Matrix Errors

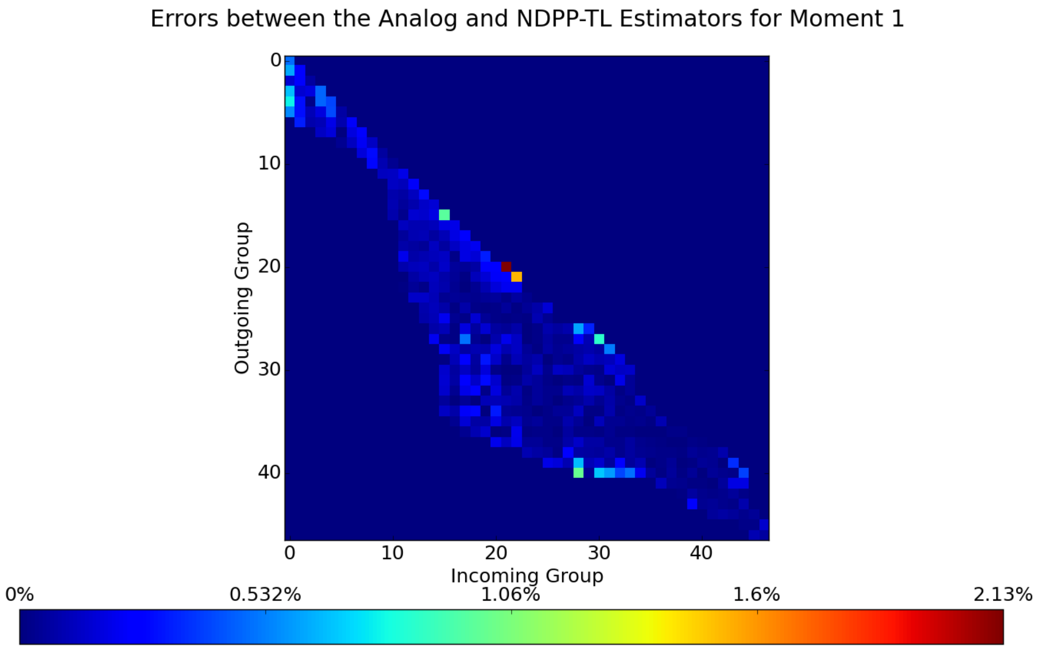

Figure 6.26: Moderator P_1 Scattering Matrix Errors

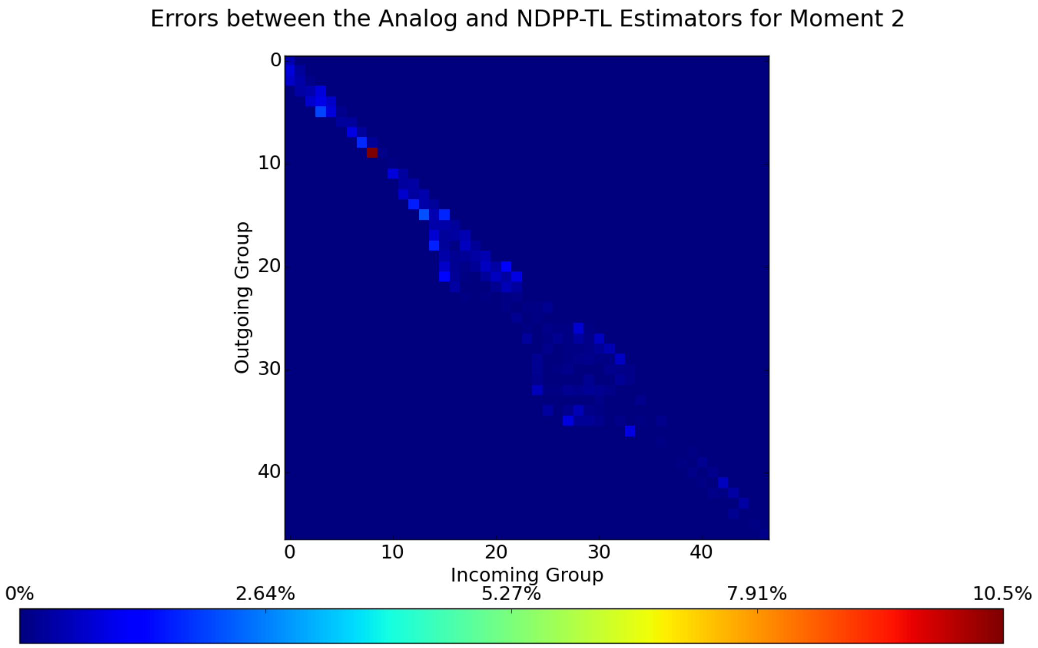

Figure 6.27: Moderator P_2 Scattering Matrix Errors

6.2.2 Total Scattering Comparison

In this section, the matrices presented above will be condensed over all of the outgoing groups to provide a less cluttered view of the results. In all of the following figures, the top plot is the average value of the tally and the bottom plot represents the error between the mean of the values. The percent error axes includes error bars which represent the 95% CI stochastic errors propagated through the error equation. These plots were generated such that bottom axis (the errors) provides the percent error if the values were above 1% of the maximum mean of the analog data. Below this 1% threshold, the absolute error was calculated instead. This was done to avoid the large errors which will arise when two numbers are very near zero, as will happen when the probabilities become negligible.

Figures 6.28 through 6.30 show this P_0 through P_2 data for the fuel, respectively; Figures 6.31 through 6.33 show the same for the moderator. The fuel cases match well with essentially no stochastically significant errors for the P_0 case. The errors for P_1 are less than two percent, but generally less than 0.5%. Finally, the P_2 errors are quite manageable, save for in the most thermal group, though since these values are very close to zero the error displayed is an absolute error, not percent.

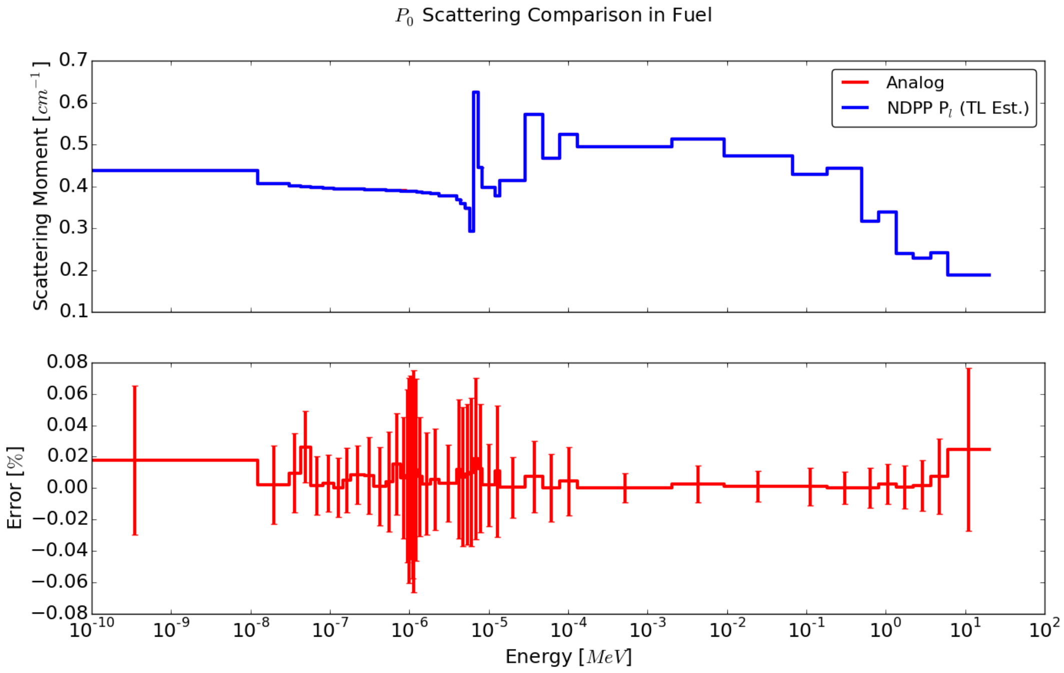

Figure 6.28: Fuel P_0 Total Scattering Comparison

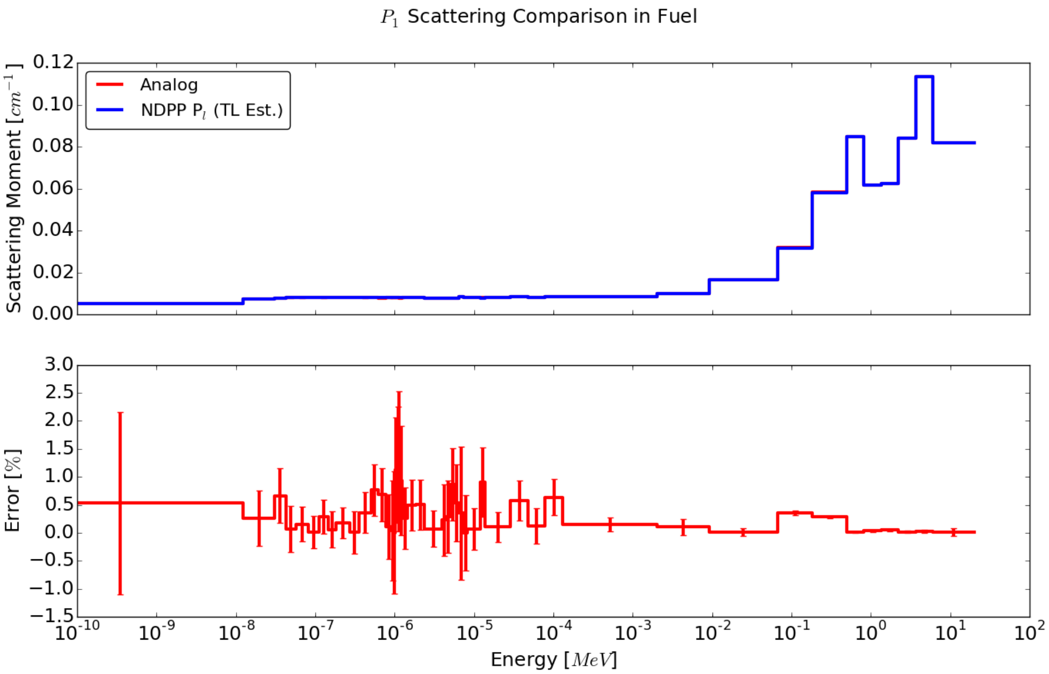

Figure 6.29: Fuel P_1 Total Scattering Comparison

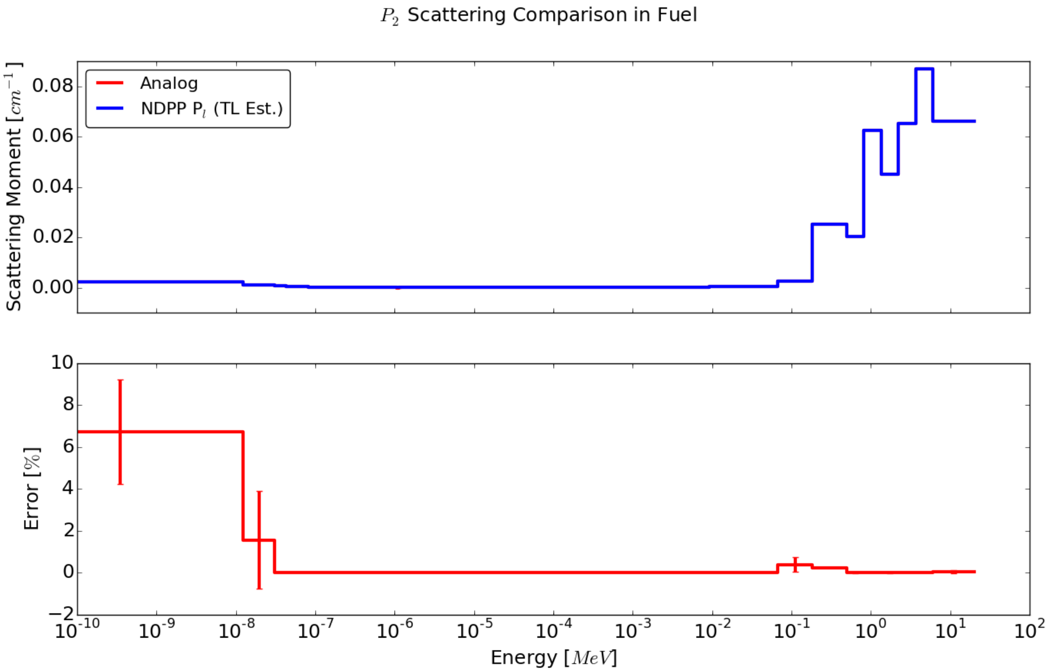

Figure 6.30: Fuel P_2 Total Scattering Comparison

The moderator data matches well, with the P_0 and P_1 results being within 0.2% of each other. The P_2 data grows to 1% in the fastest group, but again this is due to an absolute difference being presented. This is to be expected based on the verification results performed earlier; scattering in the moderator is dominated mostly be elastic scattering with the hydrogen. This elastic scattering is predicted very well by NDPP.

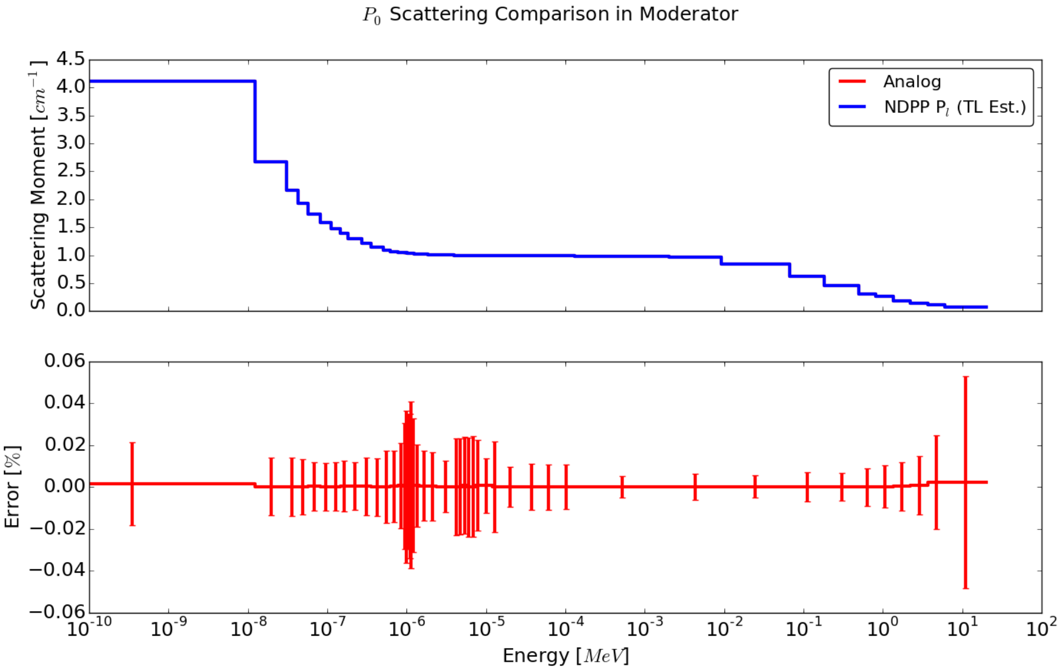

Figure 6.31: Moderator P_0 Total Scattering Comparison

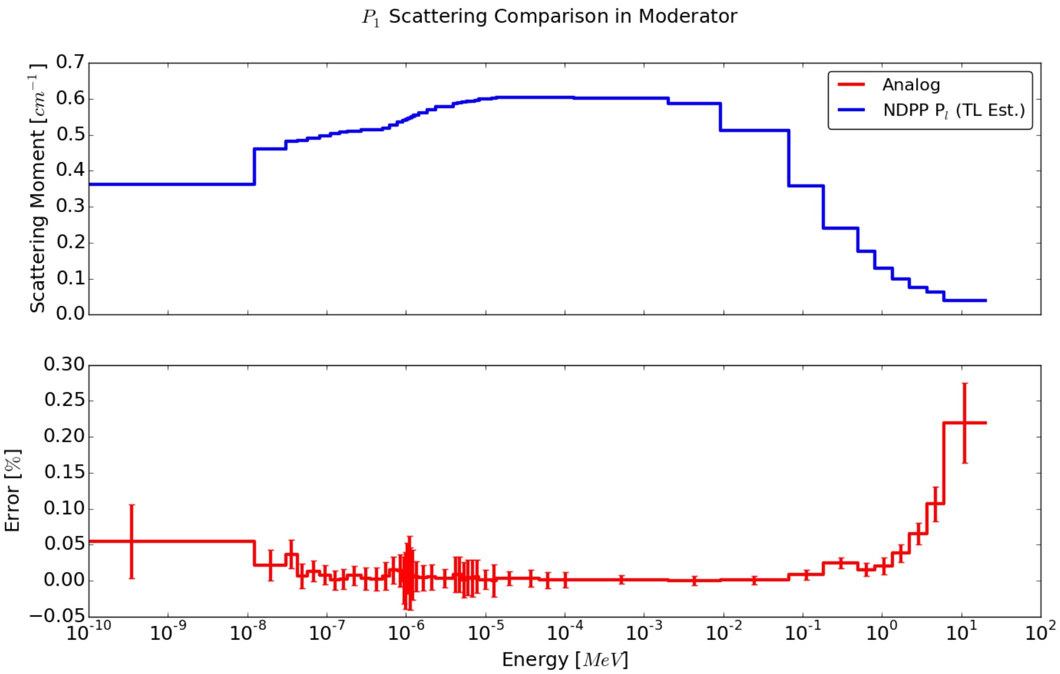

Figure 6.32: Moderator P_1 Total Scattering Comparison

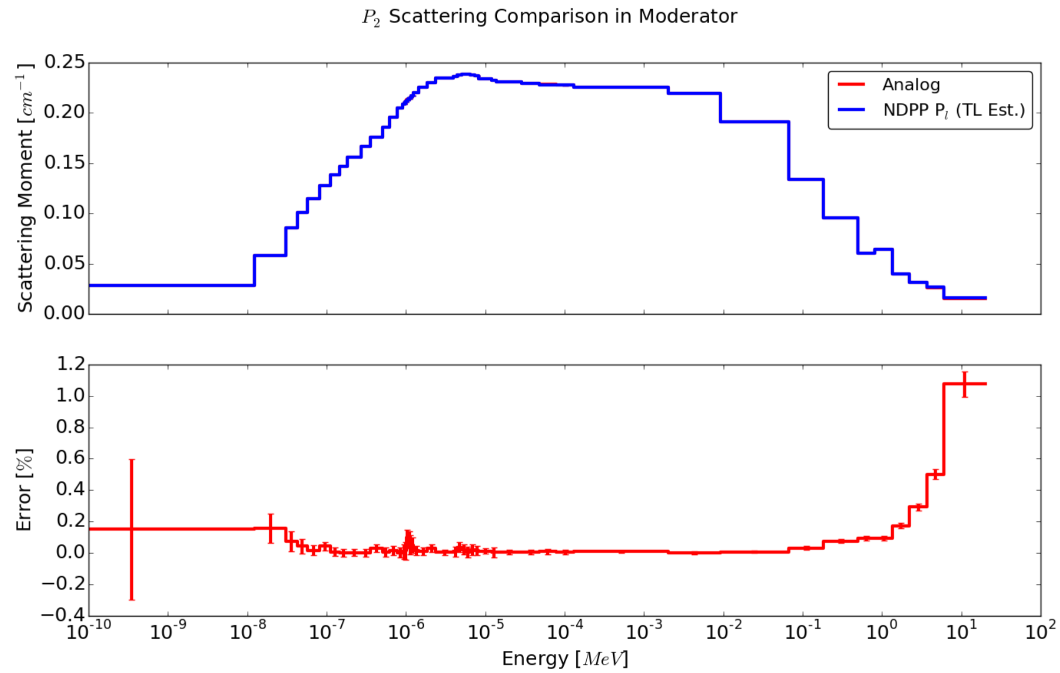

Figure 6.33: Moderator P_2 Total Scattering Comparison

6.2.3 Group-Wise Scattering Comparison

In this section, the complete outgoing data for incoming groups 4, 14, and 44 will be compared to provide a quantitative comparison of the outgoing data. These are the same groups investigated in Chapter 3. As a reminder, group 4 has energy bounds of 1.35 to 2.23 MeV, group 44 has energy bounds of 0.0428 to 0.0569 eV, and group 14 has energy bounds of 29.0 to 47.8 eV.

In all of the following figures, the top plot is the average value of the tally and the bottom plot represents the percent error between the mean of the values. The percent error axes includes error bars which represent the 95% CI stochastic errors propagated through the error equation. Like before, these plots were generated such that bottom axis, the errors, displayed the percent error if the values were above 1% of the maximum mean of the analog data. Below this 1% threshold, the absolute error was calculated instead. This was done to avoid the large errors which will arise when two numbers are very near zero, as will happen when the probabilities become negligible. Finally, the incoming group is highlighted in orange to provide for a quick understanding of the down-scatter, self-scatter and up-scatter regimes.

Figures 6.34 through 6.36 show this P_0 through P_2 data for group four in the fuel; Figures 6.37 through 6.39 show the same for the moderator. The group four data for both materials again show that the NDPP data matches very well. The large errors seen in the fuel's down-scatter regime are some of the worst performing regions in the scattering matrix (as seen when comparing the scattering moment matrices above). In this region, NDPP is having difficulty integrating the complicated inelastic routines. This is further indication that a user needs to make a value judgment on how much error is tolerable for their particular applications. Specifically, this could have been improved with more integration samples of this reaction and potentially more incoming energy grid points. Both these options increase the NDPP runtime. This should be balanced with the fact that, as will be seen, the magnitude of this error is mostly inconsequential to the accuracy of the integral parameters (the eigenvalue and pin powers).

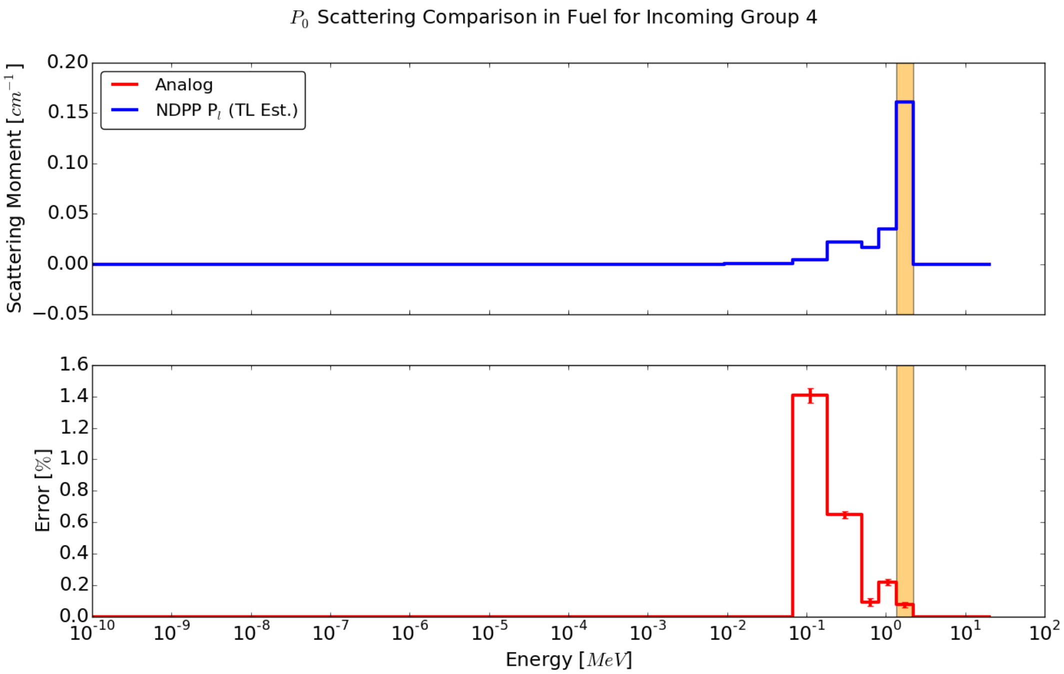

Figure 6.34: Fuel P_0 Group 4 Scattering Comparison

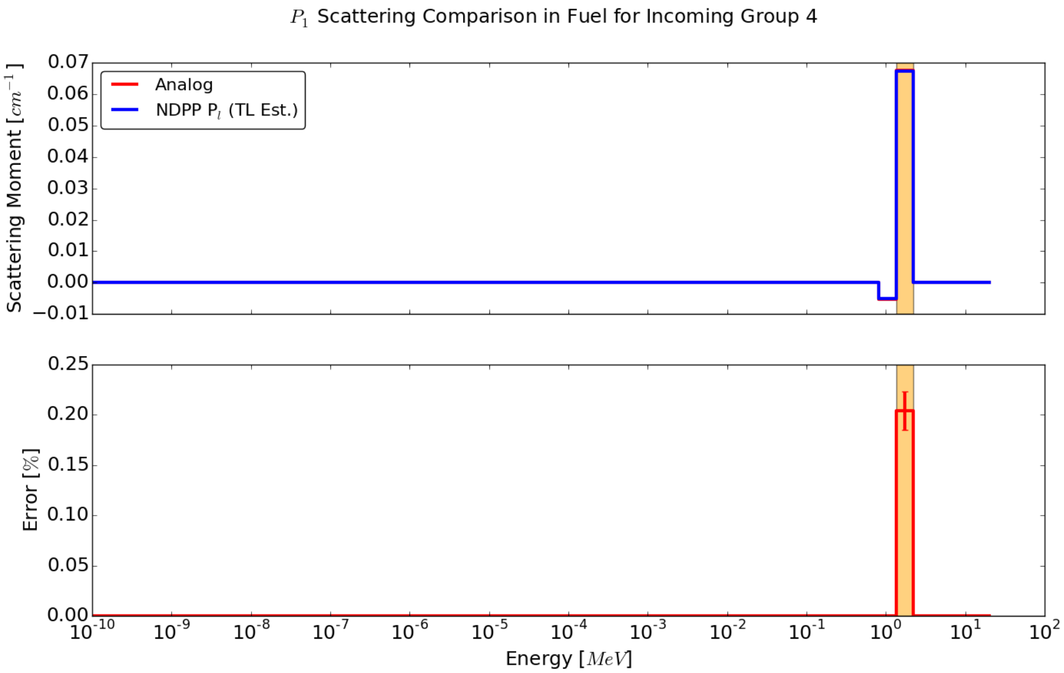

Figure 6.35: Fuel P_1 Group 4 Scattering Comparison

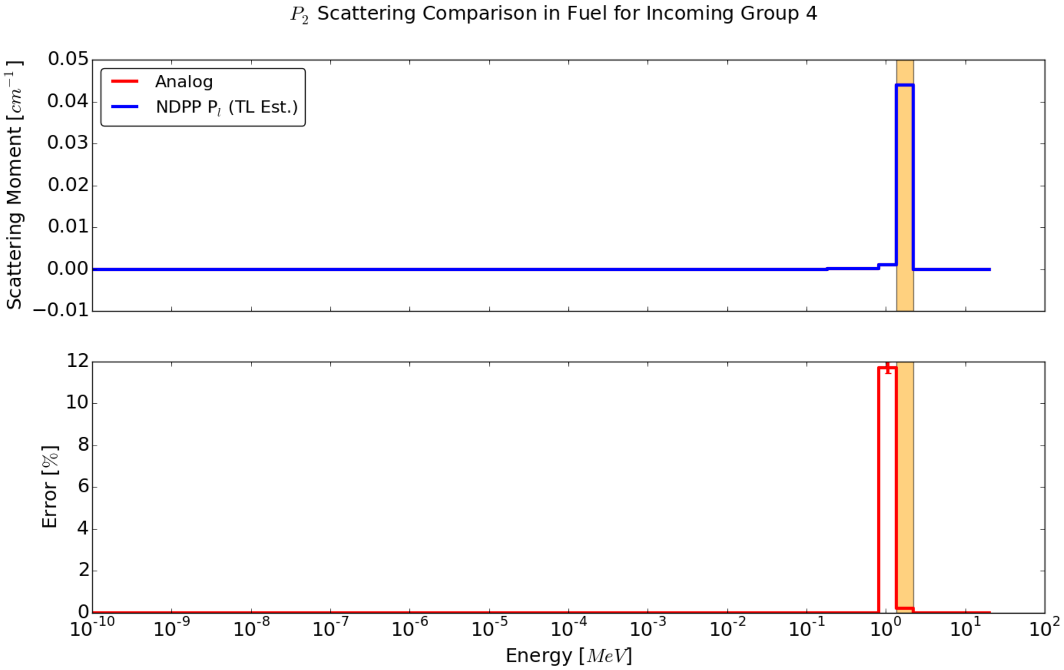

Figure 6.36: Fuel P_2 Group 4 Scattering Comparison

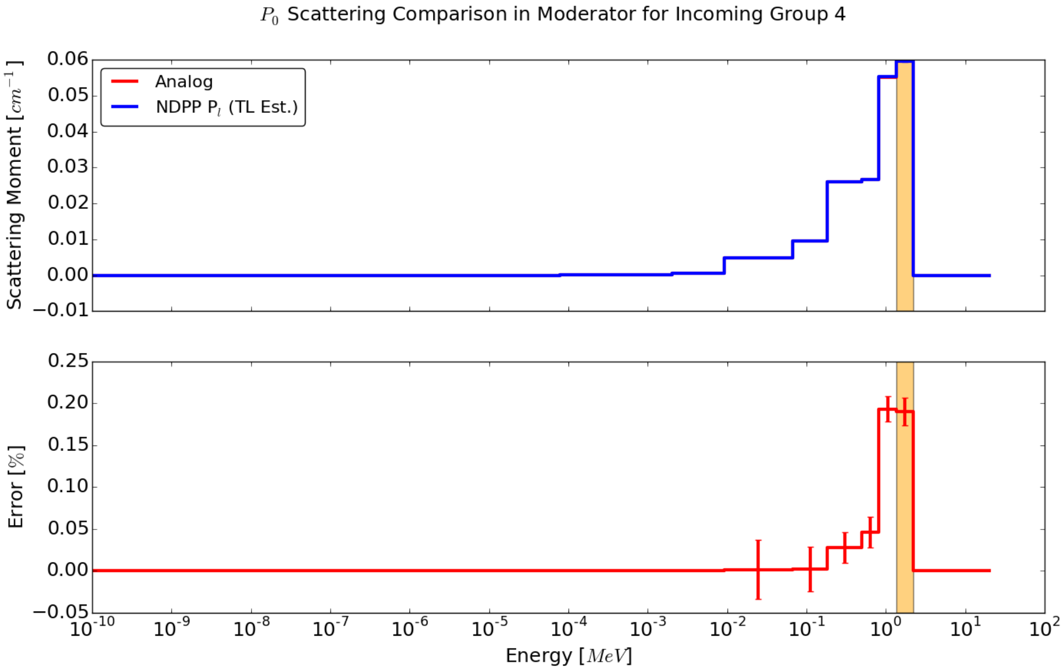

Figure 6.37: Moderator P_0 Group 4 Scattering Comparison

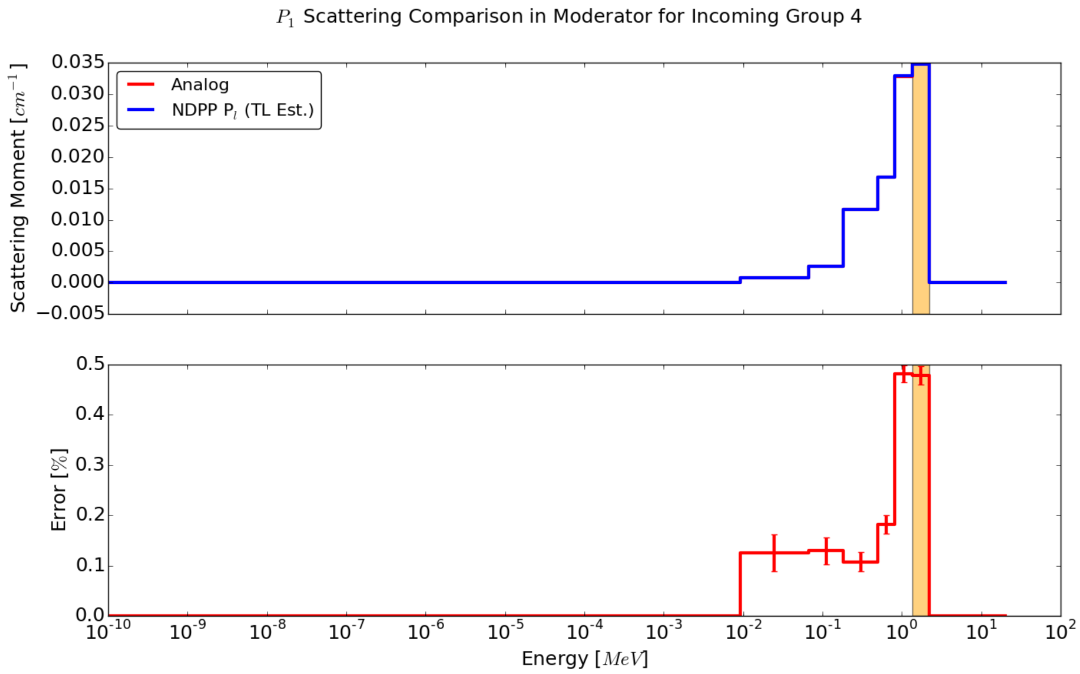

Figure 6.38: Moderator P_1 Group 4 Scattering Comparison

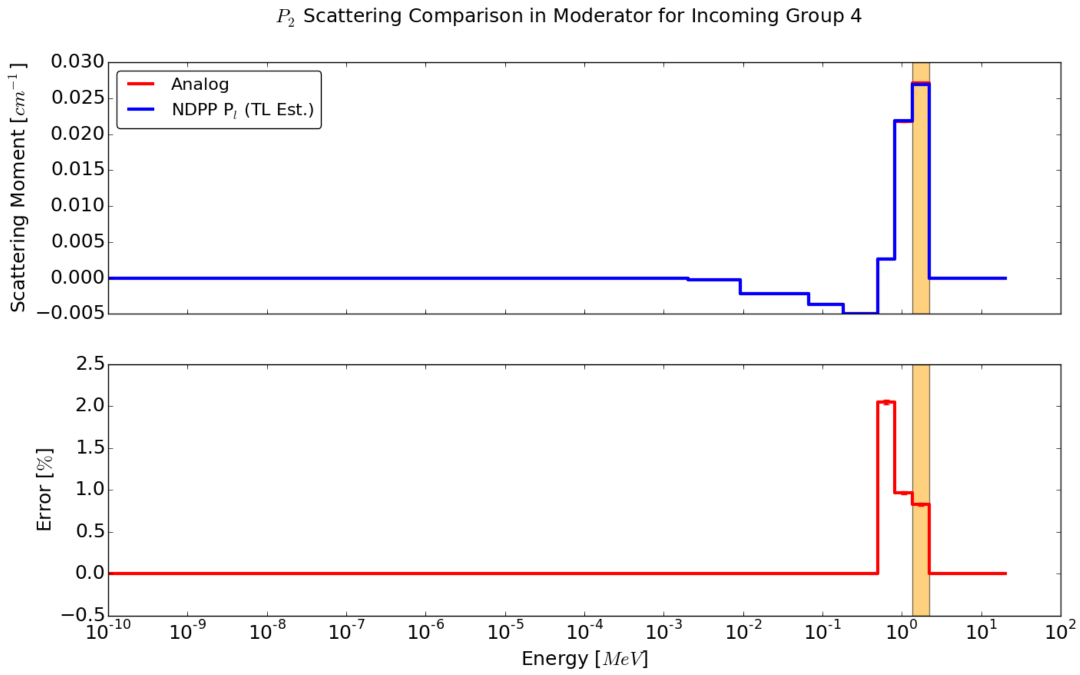

Figure 6.39: Moderator P_2 Group 4 Scattering Comparison

Figures 6.40 through 6.42 show this P_0 through P_2 data for group 14 in the fuel; Figures 6.43 through 6.45 show the same for the moderator. These figures show, for the most part, matching results accounting for differences in very small numbers like in the very low energy transfers. One area of concern, however, is the P_2 moment in the fuel, Figure 6.42. These differences in the P_2 magnitude are likely due to the interpolation of data on the NDPP grid and a higher-fidelity incoming energy grid could resolve the discrepancy because this group contains the onset of inelastic data (and thus rapidly increasing cross sections) in some of the uranium isotopes.

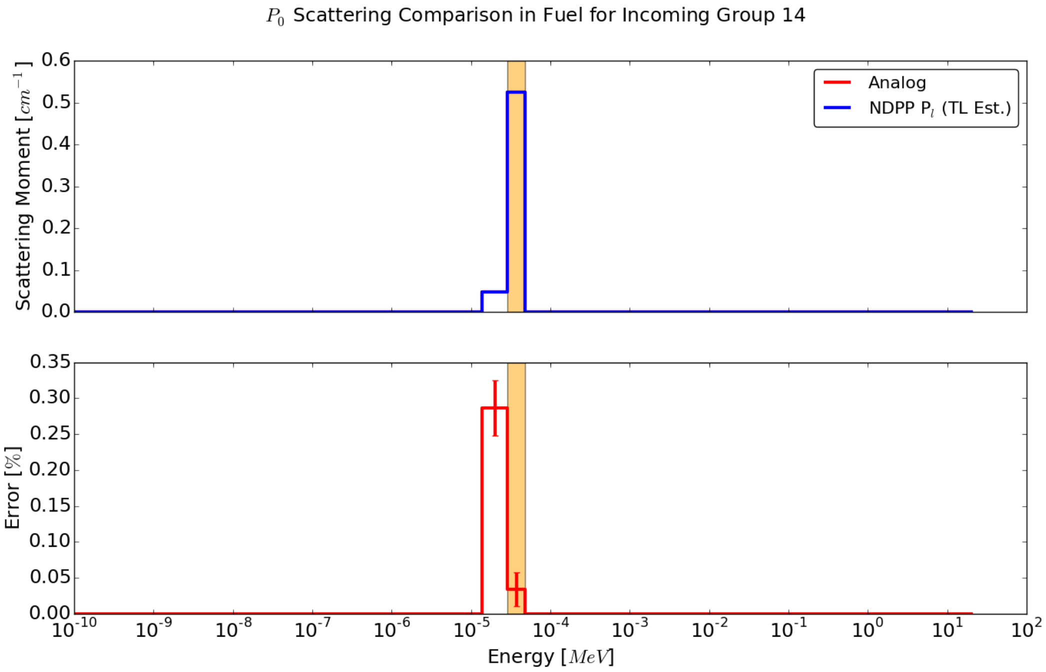

Figure 6.40: Fuel P_0 Group 14 Scattering Comparison

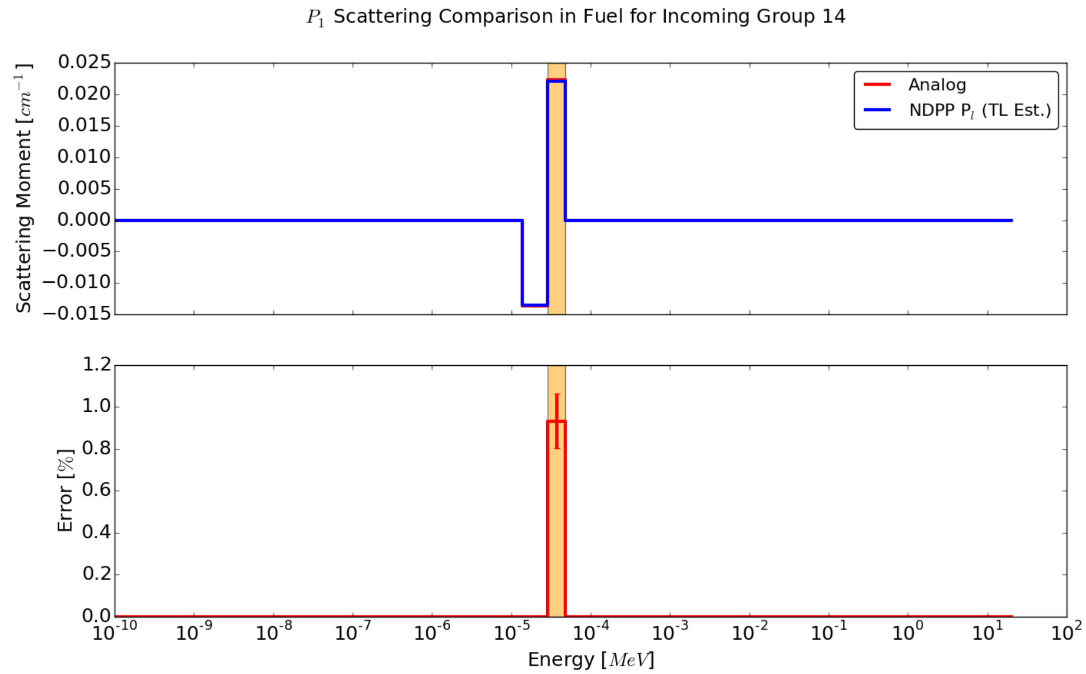

Figure 6.41: Fuel P_1 Group 14 Scattering Comparison

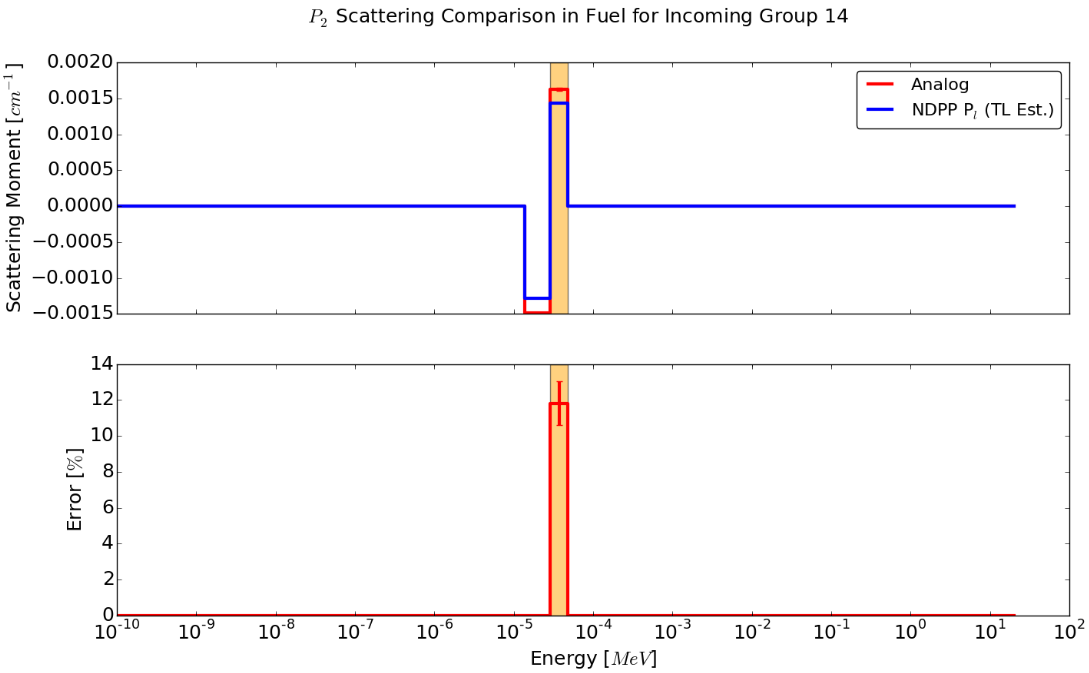

Figure 6.42: Fuel P_2 Group 14 Scattering Comparison

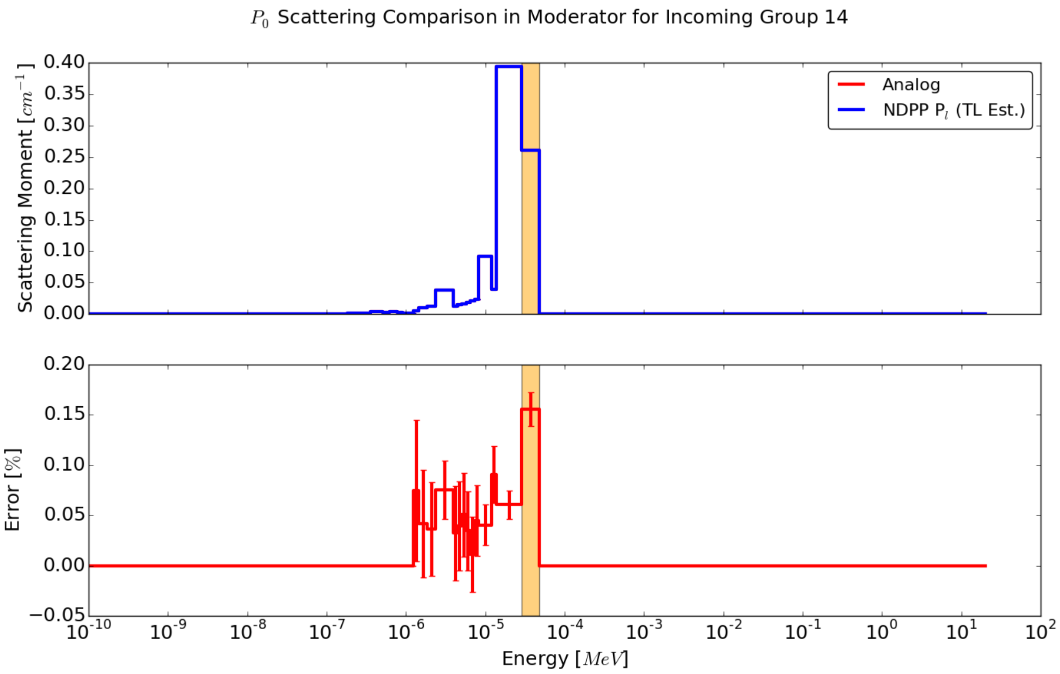

Figure 6.43: Moderator P_0 Group 14 Scattering Comparison

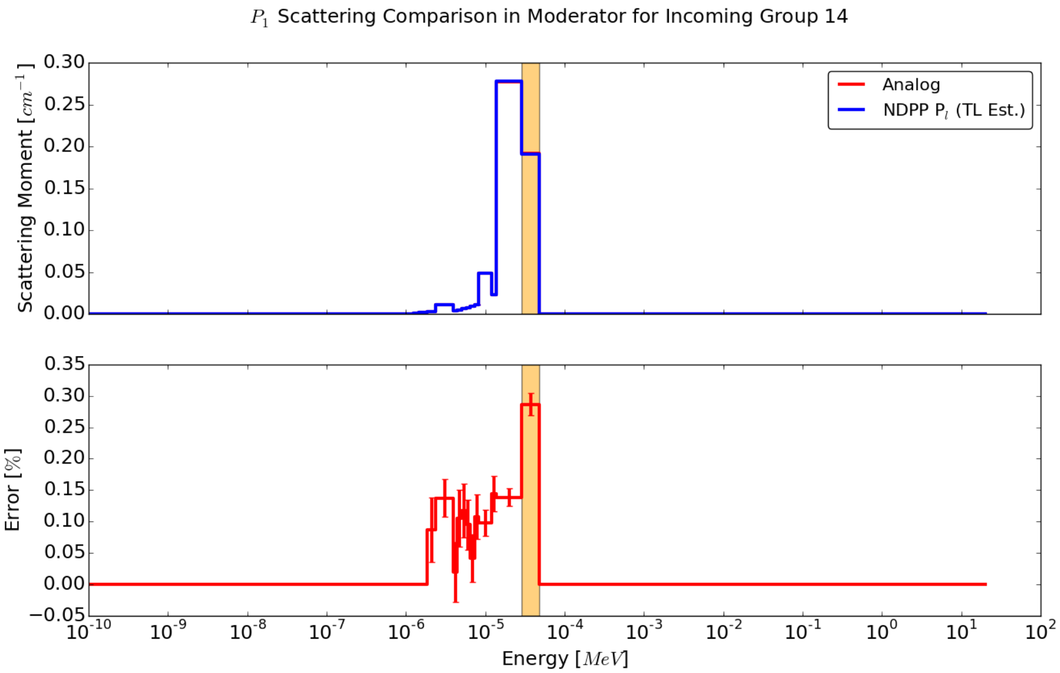

Figure 6.44: Moderator P_1 Group 14 Scattering Comparison

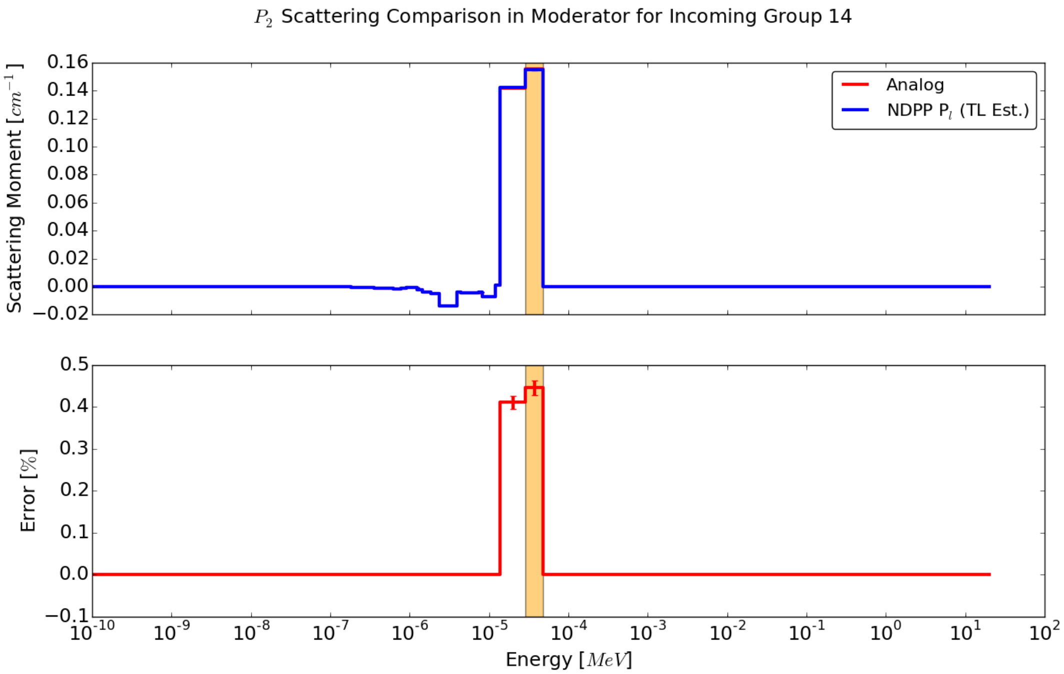

Figure 6.45: Moderator P_2 Group 14 Scattering Comparison

Figures 6.46 through 6.48 show this P_0 through P_2 data for group 44 in the fuel; Figures 6.49 through 6.51 show the same for the moderator. The methods again match well, as was expected since this regime only contains elastic and thermal scattering collisions which were earlier shown to match very well.

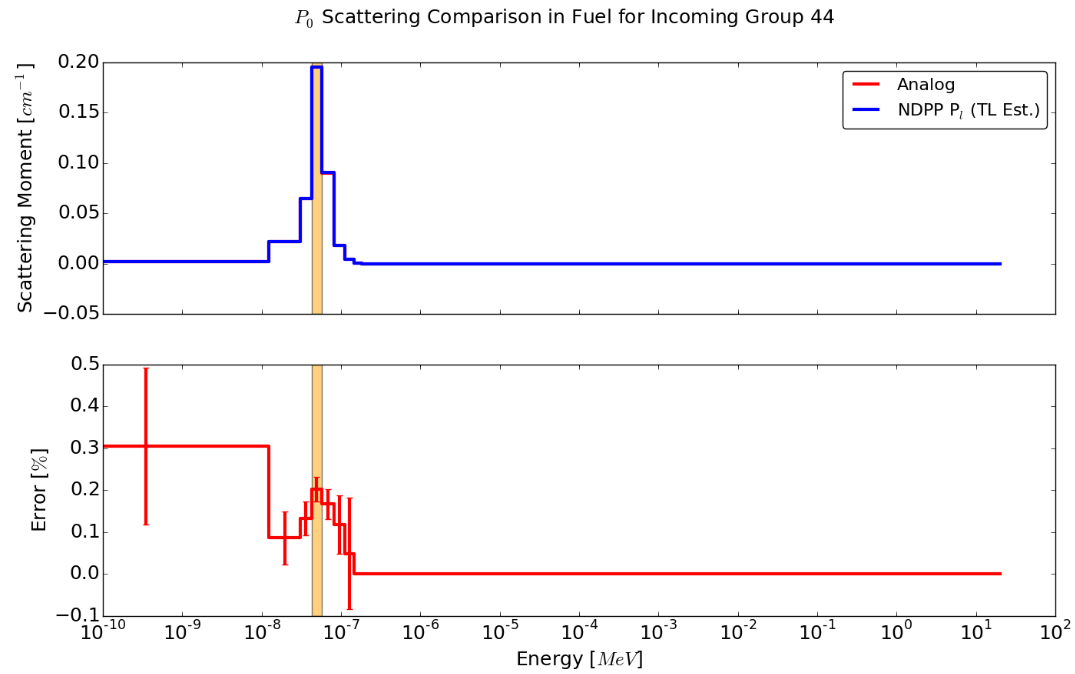

Figure 6.46: Fuel P_0 Group 44 Scattering Comparison

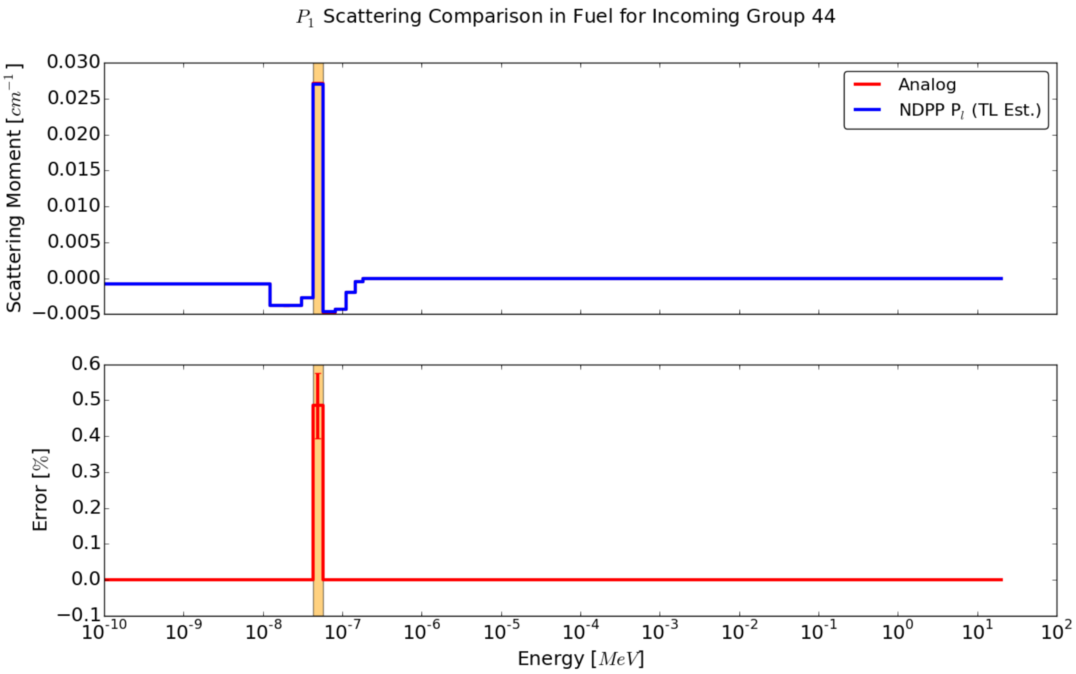

Figure 6.47: Fuel P_1 Group 44 Scattering Comparison

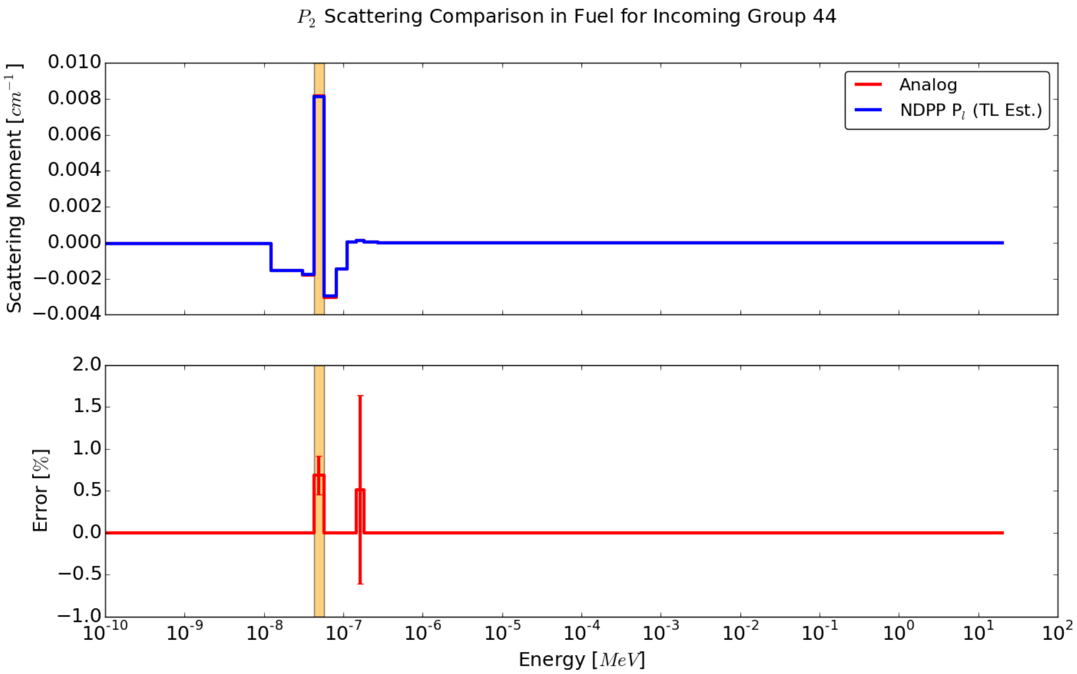

Figure 6.48: Fuel P_2 Group 44 Scattering Comparison

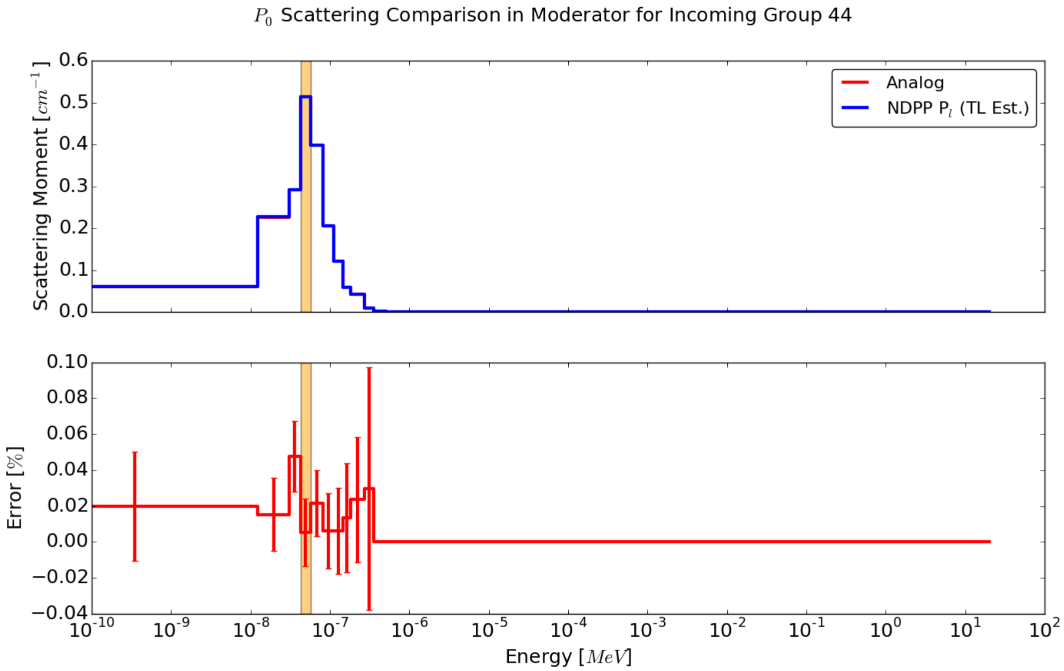

Figure 6.49: Moderator P_0 Group 44 Scattering Comparison

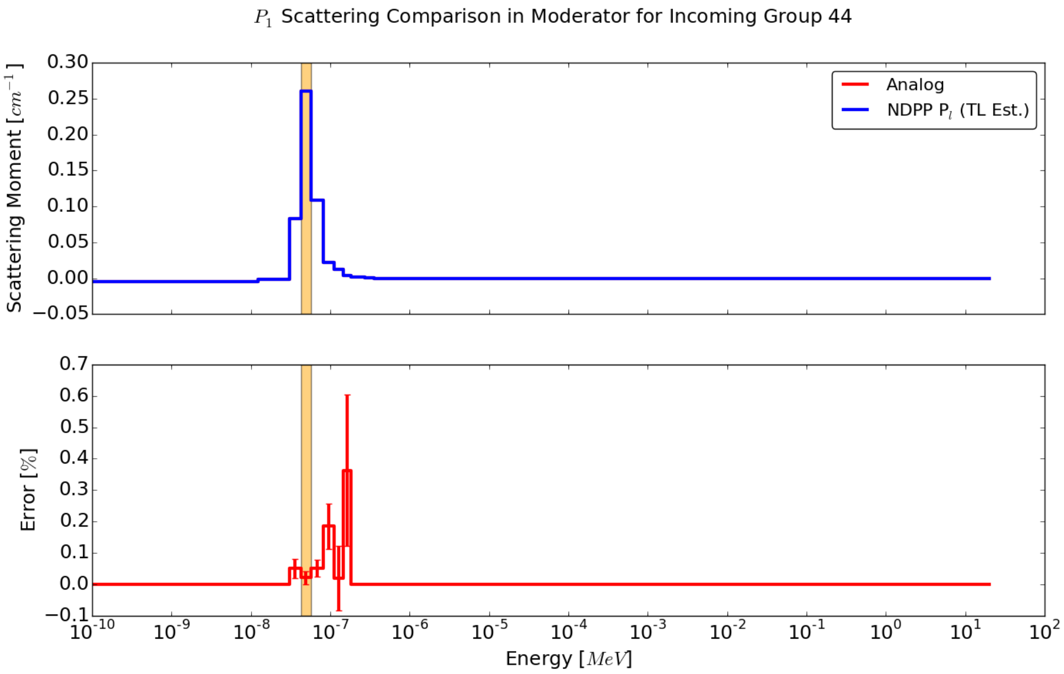

Figure 6.50: Moderator P_1 Group 44 Scattering Comparison

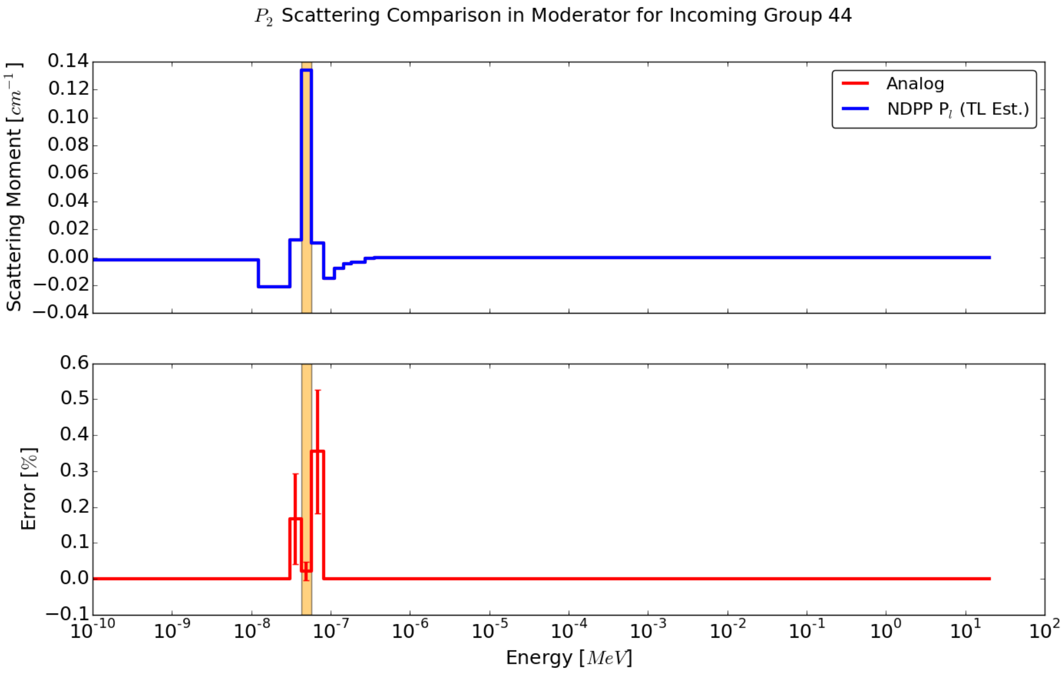

Figure 6.51: Moderator P_2 Group 44 Scattering Comparison

6.2.4 MPACT Eigenvalue Comparison

The final accuracy comparison to make for this case is to input the MGXS libraries generated by both the analog and NDPP-based tallies into a deterministic transport code and compare the resultant eigenvalues for the exact same pin cell problem in which the cross sections were generated. This was done using the MPACT MOC code with both isotropic and P_2 scattering treatments. The MPACT model utilized for this case is described in Appendix A. Table 6.1 shows the results of this analysis.

Table 6.1: MPACT Pin Cell Eigenvalue

Case	OpenMC k_{eff}	Analog k_{eff}	Analog to OpenMC Bias $[pcm]$	NDPP k_{eff}	NDPP to Analog Bias $[pcm]$
P_0	1.181820 ± 0.000029	1.1775166	-364.2	1.1773651	-12.9
P_2	1.181820 ± 0.000029	1.1777991	-340.2	1.1776487	-12.8

A 13 pcm difference is observed between the analog and improved methods of tallying the scattering production moments. It is not ideal that a difference exists; however, the difference is quite small when compared to typical Monte Carlo to deterministic bias, which is typically at least ten times as large when using specially-generated libraries [37].

This nearly negligible difference is due to a combination of many factors, including: numerical truncation error of the integration performed in NDPP as well as interpolation error when generating the NDPP data and when tallying the data in OpenMC. This bias can therefore be reduced by a finer set of NDPP integration parameters or perhaps by researching better interpolation schemes, though this requires a value judgment by the user as to the desired accuracy and computational costs involved. Finally, so long as this NDPP-to-analog bias is consistently around a certain value for a class of calculations (such as Light Water Reactor (LWR) analyses), then the magnitude of the bias is inconsequential to important reactivity design parameters.

6.3 Multi-Group Cross Section Tallying Efficiency Comparison

The previous section has established that the method does indeed work; however this effort was undertaken in order to provide a benefit and not merely replicate current functionality.

Therefore the goal of this section is to quantify the benefits of using the improved method of tallying. The questions to be considered in this section are:

1. What is the effect of NDPP-based tallies on Monte Carlo memory usage?
2. What is the effect of NDPP-based tallies on Monte Carlo run time?
3. To what degree is the tallying efficiency improved?
4. How does this tallying efficiency impact important parameters such as the neutron multiplication factor and power distribution?
5. What is the figure-of-merit of the improved method, factoring in the tallying efficiency and run-time implications?

These will be treated (in the order presented above) in the following sections.

6.3.1 Improved Method Memory Impact

Table 6.2 shows the storage size required of the Monte Carlo code for each of the nuclides present in the pin cell model. This is important as the memory usage changes the size of a problem you can fit on a fixed machine. Before entering this discussion, it is important to reiterate that the target application of this method is cross section generation and not full-core analysis, thus the memory burden may not be a significant hurdle since multi-GigaByte mesh tallies and are not necessary for this application.

The data in Table 6.2 provides the number of incoming energy points of the elastic and inelastic grids and their associate storage requirements. The inelastic data is only reported for either scattering or scattering production. This is done because the size of the scattering data is the same as the scattering production data, and because it is expected that MGXS libraries will be generated using either scattering or scattering production tallies, but not both. Since OpenMC has the capability to discard the scattering data if only scattering production data is needed, then including both types in the total memory burden is not realistic. As a reminder, data in this set is available for up to P_2 scattering, a thinning tolerance of 1E-5% and a printing tolerance of 1E-10 was applied.

This table shows that the inelastic data storage is larger even than the upstream ACE data set for a given nuclide and temperature; a total of 27.3 MB are required for the elastic data in the pin-cell problem and another 524 MB for the inelastic data. This is not a favorable result, but is acceptable for the reasons of problem size given above, and because the inelastic data does not scale with temperature as does the elastic temperature.

As was discussed in Chapter 5, the inelastic data size grows proportionally with the number of groups multiplied by the number of inelastic levels of a nuclide. Therefore, as the number of groups increase (like in the case of fast reactor analyses), it is expected that this inelastic data will become all-consuming and require either increasing the thinning tolerances and researching higher-order interpolation schemes such that fewer points are needed to describe each critical point.

On the other hand, the elastic data is quite small, being on the order of 0.5 MB and a maximum of 1.52 MB for ^1H. The hydrogen data is the largest (yet still reasonable) because its maximum energy transfer is 7 orders of magnitude, hence there are many outgoing energy groups for each incoming point. This storage size is good news since this is the data that will need to be provided at varying temperatures within the model.

This storage size could be further reduced by further subdividing elastic data in to a truly temperature-dependent portion of the elastic data and set of elastic data which is temperature-independent. Specifically, all elastic data was kept separate from inelastic since the free-gas kernel and resonances imply a temperature dependence of the elastic data; however, the variance of the cross section that is due to resonance Doppler broadening does not affect the NDPP calculations since the applicable cross section is not applied until the Monte Carlo simulation. Therefore the temperature-dependent portion of the elastic data includes the points up to an energy matching the maximum free-gas cutoff energy in the problem. It is expected that this could reduce the temperature-dependent storage by roughly one third. This was not done in this work but can be easily implemented in the future. Other options include utilizing better interpolation schemes and applying looser thinning than was done here.

No study has been performed to understand how many temperature points are necessary to capture the temperature dependence of the outgoing distributions as the ability to perform temperature interpolation is not yet available in OpenMC. While the temperature interval of data needed for interpolation is not known, it is known that the thermal motion effect on the energy-angle distributions is strongest for lighter nuclei; luckily the range of temperatures of these nuclei will generally be 30K about nominal. This limits the actual number of data sets needed during a cross section generation calculation.

Table 6.2: NDPP Storage Requirements

Isotope	Elastic Points	Elastic Size (MB)	Inelastic Points	Inelastic Size (MB)
^{1}H	2,161	1.52	0	0.00
^{10}B	2,359	0.48	38,100	23.67
^{11}B	3,861	0.54	16,708	6.97
^{16}O	4,227	0.46	14,860	5.93
^{50}Cr	11,872	0.61	11,197	8.00
^{52}Cr	13,630	0.65	17,223	12.00
^{53}Cr	9,690	0.54	21,572	15.23
^{54}Cr	10,653	0.58	8,818	5.67
^{54}Fe	13,369	0.63	11,925	8.69
^{56}Fe	17,049	0.73	37,785	26.38
^{57}Fe	11,896	0.58	19,393	8.73
^{58}Fe	10,422	0.55	7,253	4.64
^{90}Zr	4,285	0.37	17,230	11.22
^{91}Zr	6,810	0.43	27,280	16.88
^{92}Zr	7,473	0.45	33,315	21.34
^{94}Zr	6,913	0.43	28,475	18.22
^{96}Zr	6,540	0.42	17,935	10.86
^{112}Sn	6,009	0.40	32,648	18.35
^{114}Sn	6,063	0.39	36,541	20.56
^{115}Sn	5,588	0.38	23,409	12.29
^{116}Sn	8,251	0.45	15,242	7.85
^{117}Sn	7,327	0.44	18,305	9.46
^{118}Sn	5,651	0.38	11,205	5.49
^{119}Sn	6,255	0.41	28,078	15.32
^{120}Sn	7,641	0.43	23,060	12.72
^{122}Sn	8,828	0.48	13,714	7.06
^{124}Sn	7,868	0.44	28,103	15.57
^{174}Hf	4,187	0.35	3,766	1.57
^{176}Hf	3,964	0.33	3,768	1.54
^{177}Hf	5,376	0.43	12,346	6.25
^{178}Hf	3,966	0.33	3,759	1.57
^{179}Hf	4,172	0.34	6,340	3.08
^{180}Hf	3,761	0.32	3,757	1.54
^{234}U	6,993	0.39	57,672	44.05
^{235}U	7,902	0.47	56,091	46.11
^{236}U	6,841	0.38	56,471	44.82
^{238}U	8,849	0.45	57,011	44.43
H-H_2O	28,407	9.36	0	0.00
Total	-	27.32	-	524.06

Finally, to test the potential for further memory reductions, the same data was produced but this time using a thinning tolerance of 1E-3% and a printing tolerance of 1E-8 was applied. Each of these is two orders of magnitude coarser than in the previous case. The total size of the elastic data for this case was 15.7 MB; the same for the inelastic was 297.6 MB, for a total storage requirement of 313.3 MB. Each of these is roughly 30% the size of the data reported in Table 6.2. Note that this data was not applied to any of the analyses in this work.

6.3.2 Improved Method Run-Time Impact

To test the run-time impact of this method, the pin cell problem will be used and run with only the tallies required to generate MGXS data using the analog method and then again using the improved method for the scattering data. This will be repeated for utilizing NDPP data with and without the track-length estimators. All comparisons are made on the basis of number of neutrons simulated per second in the active batches (those which accumulate tallies) when using a single CPU thread. These cases were run with batch sizes of 10,000 particles per batch with 1,900 inactive batches like before, but only 100 active batches (totaling one million active histories) were necessary to obtain adequate timing estimates.

Before examining the data closely, it is important to understand that the improved method requires more operations to be performed than the analog estimator at each tally event. This is because more information is being tallied each event. So the following tables are for information, but are only a step along the way to understanding the merits of the method. The final examination of the merits of the improved method will be discussed in Section 6.3.5.

Table 6.3 shows the active history calculation rate when using analog tallying for the scattering moments, improved method (using a collision estimator), and finally the improved method with a track-length estimator. This data shows a modest slow down of only 11% when applying the NDPP collision estimator but a quite heavy (81%) impact when applying the track-length estimator.

As a reminder, the analog method simply evaluates the Legendre polynomial of the change in angle at each order requested (P_0 through P_2 in this case) after a collision has occurred with a single nuclide The NDPP collision estimator has to first find the correct elastic and inelastic NDPP data sets to apply for the nuclide which underwent the collision, combine them (via Eqn. (5.3) or (5.4)), and then sum the resultant two-dimensional matrix (with size up to $G \times L$) data to the tally object. The track-length estimator form does the exact same operation as the NDPP collision estimator, but does 1) this for every nuclide in the material instead of just the chosen target atom, and 2) every time a neutron moves through a material, let alone has a collision in it. For this reason, the track-length estimator is much costlier than the collision estimator version.

The choice of which tally type to use is of course up to the user and the model being run: if the full benefit of track-length estimation is not needed the collision can be used to increase speed. This decision is no different than when choosing to utilize track-length or collision estimation for all the other tally types available.

Table 6.3: Timing Impact of Scattering Data

Case	Calculation Rate (#/sec)	Slow Down
Analog	5,153	-
NDPP Collision	4,570	11%
NDPP Track-Length	1,001	81%

6.3.3 Improved Method Tallying Efficiency

This section will study the ability of the improved method to increase the tallying efficiency. This will be performed by examining both the mean values and reported relative uncertainties as a function of the number of particles simulated for both the original analog and improved methods of tallying.

6.3.3.1 Examination of Scattering Moment Tallying Efficiency

This analysis will again focus on the same groups studied previously in this chapter; that is, the fast, epithermal, and thermal groups (groups 4, 14, and 44, respectively). These results will also be shown and discussed for each the fuel and the moderator.

This work will limit the study towards just efficiency of tallying the scattering from the given incoming group to all outgoing groups at once. This is the same as examining the root-sum-squared convergence behavior of each of the outgoing data for each incoming group.

In each of the figures which follow, two sets of lines are shown on the same axes as functions of the number of batches simulated (on the x-axis). The first line (the solid line) provides the percent deviation of the accumulated solution compared with the reference solution (the analog solution at one billion active histories). The second dotted line provides the reported stochastic error (on a 95% CI relative basis). These lines exist for both the analog method (in red), and the improved method with NDPP data (in blue) using a track-length estimator.

Figures 6.52 through 6.54 show the P_0 through P_2 results (respectively) of this work for the fuel in the fast group (group 4). These plots show the following trends, which typically hold for the remaining cases:

- The mean estimated with NDPP data typically reaches its converged value significantly faster than does the analog
    - This is to be expected as the improved method does not have outgoing information to stochastically resolve; once the incoming dimensions have been resolved (i.e., the collapsing flux spectra), then the NDPP method is “done”
- NDPP tallies show a smaller relative error than the analog method through the histories
    - This is because there is less volatility in the tallies since the outgoing dimensions are no longer stochastically integrated
- The benefit of the improved method to the relative uncertainties is increased with increasing scattering order
    - As the Legendre order increases, the oscillatory nature of the functions also increases; this increases the noise of the analog tally
    - The improved method is not subject to this weakness since the angular variable is not sampled, thus its volatility has no effect.
- When the NDPP tallies reach their converged values, the relative uncertainties continue to follow the expected $\frac{1}{\sqrt{N}}$ convergence
    - This is because the variance of the mean (discussed in Chapter 3 and shown in Eq. (3.3)) is still obtaining samples and thus N is still growing
- NDPP tallies exhibit a truncation error as this final value is typically between 0.001% and 0.1% of the reference analog solution
    - This is an artifact of the fact that NDPP utilizes numerical integration methods and must interpolate the integrated data from the incoming energy grid

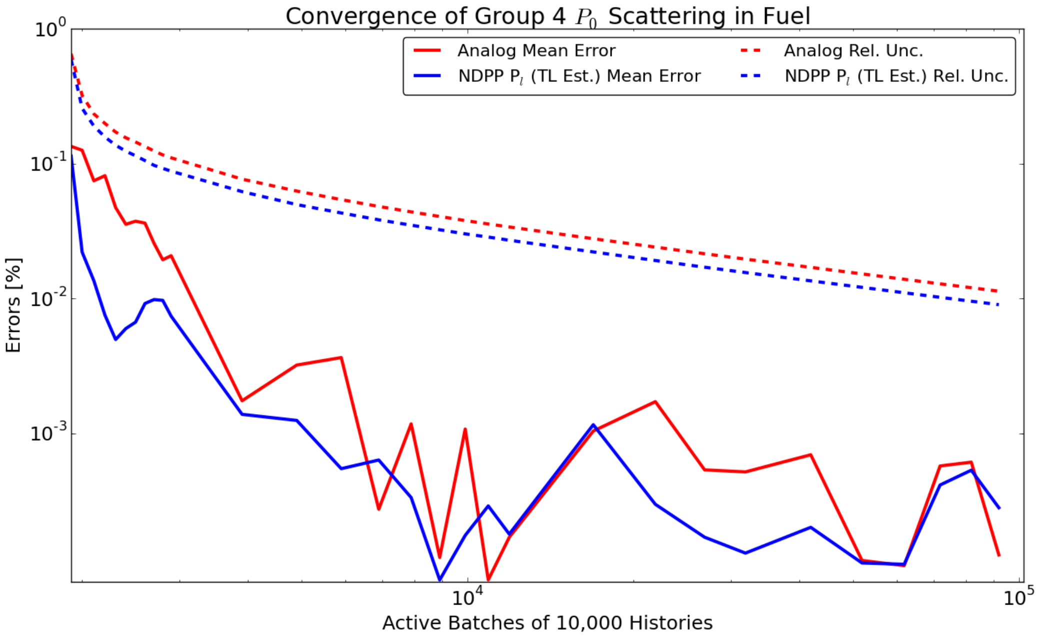

Figure 6.52: Fuel P_0 Group 4 Scattering Comparison

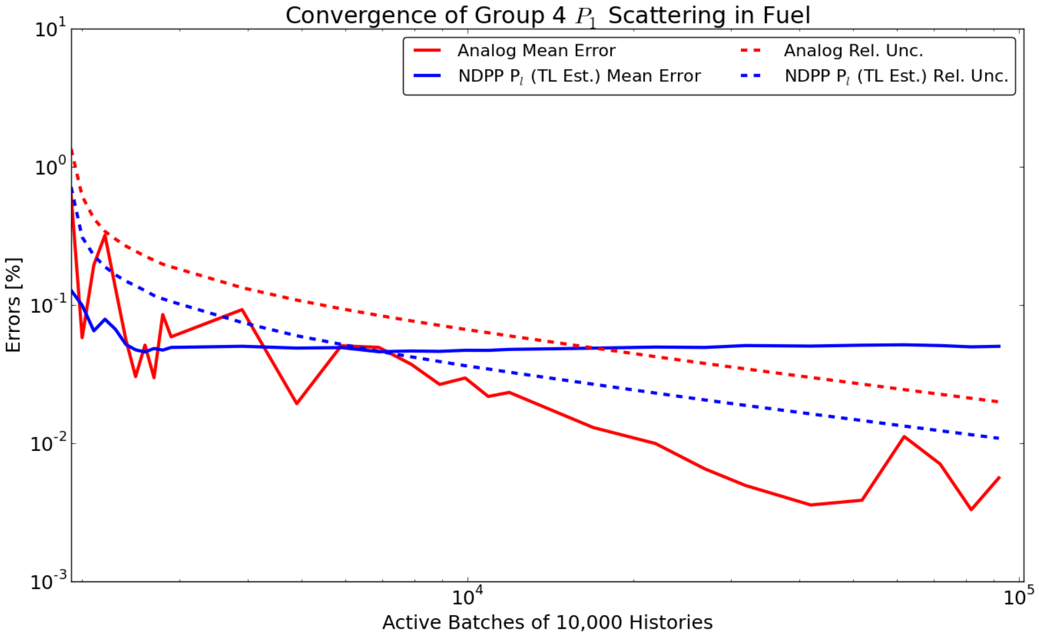

Figure 6.53: Fuel P_1 Group 4 Scattering Comparison

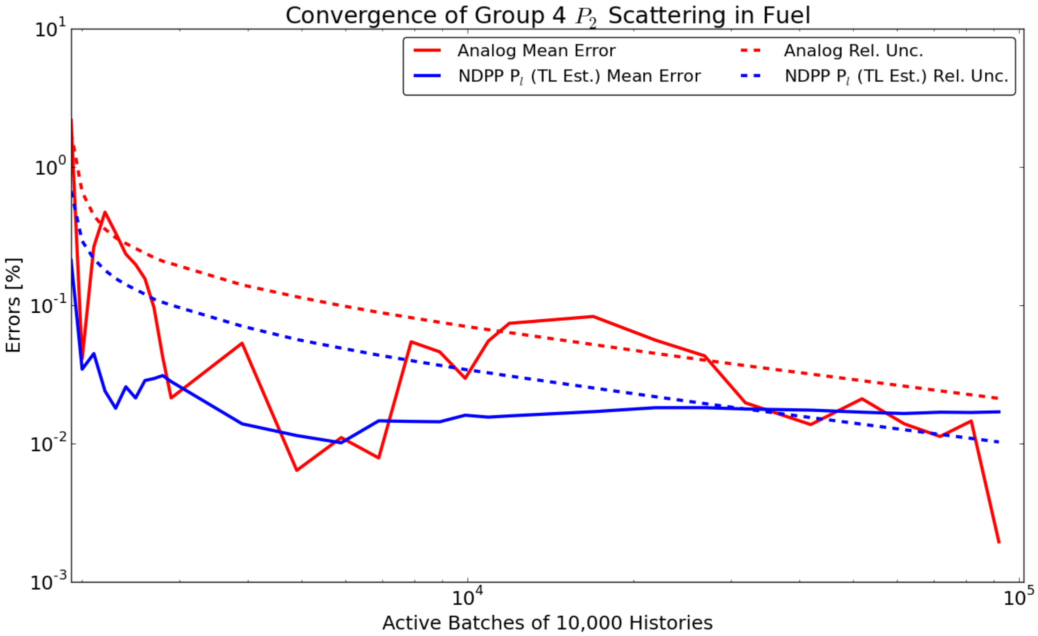

Figure 6.54: Fuel P_2 Group 4 Scattering Comparison

Figures 6.55 through 6.57 show the P_0 through P_2 results (respectively) of this work for the moderator in the fast group. The worst the truncation error for this material is found in the P_2 moments at approximately 0.15%. This is likely due to the difficult in interpolating between the inelastic scattering reactions present in the oxygen as has been discussed before.

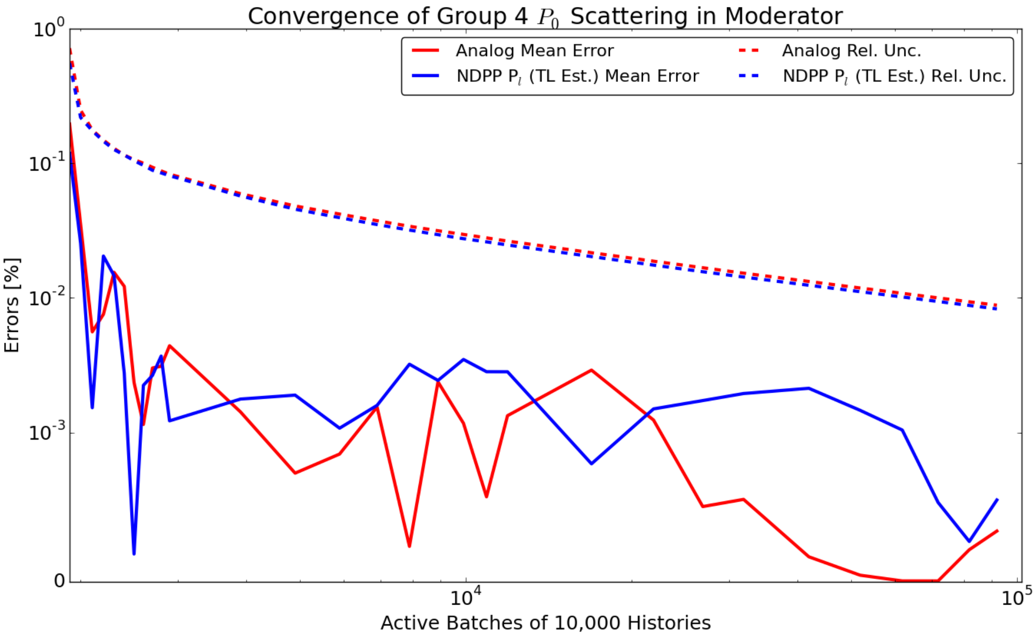

Figure 6.55: Moderator P_0 Group 4 Scattering Comparison

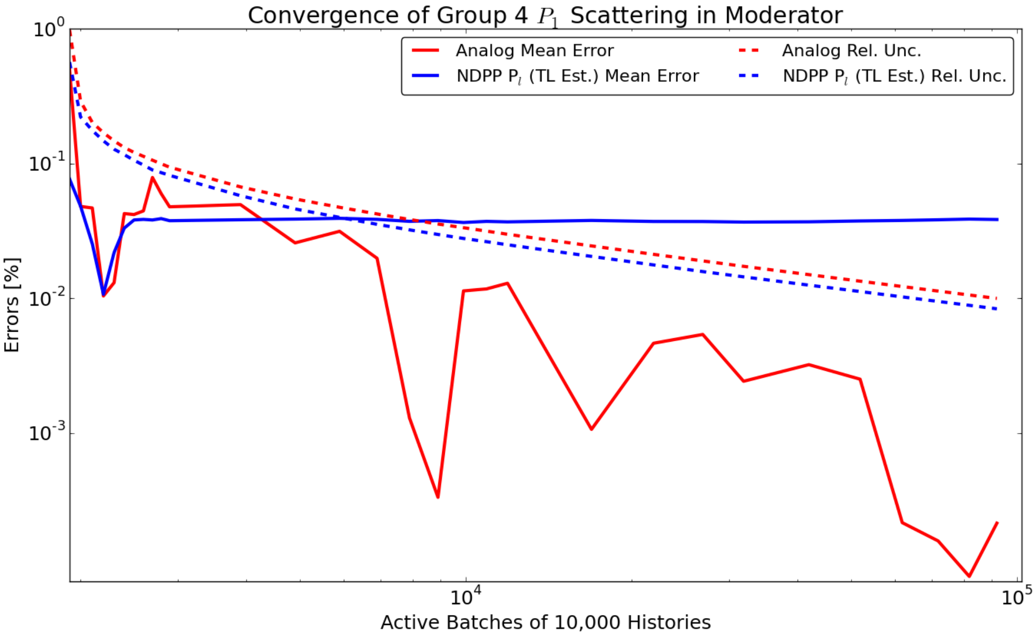

Figure 6.56: Moderator P_1 Group 4 Scattering Comparison

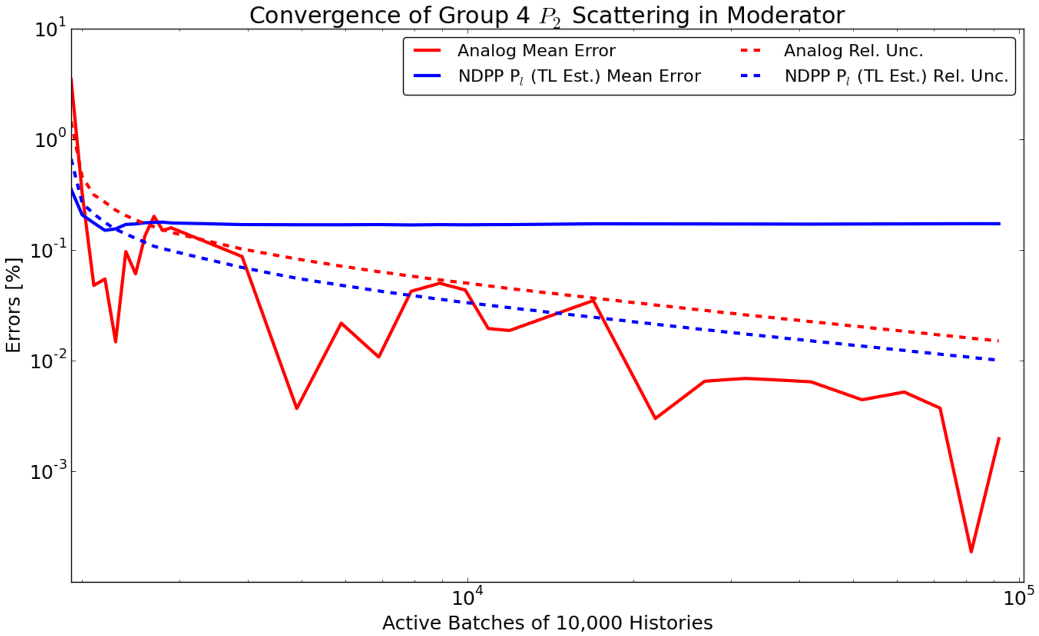

Figure 6.57: Moderator P_2 Group 4 Scattering Comparison

Figures 6.58 through 6.60 show the P_0 through P_2 results of this work for the fuel in the epithermal group, group 14. In this group, scattering is nearly isotropic; therefore it should be expected that the analog method will have difficulty resolving the higher order moments. This behavior was exactly seen, as the NDPP tallies have an order of magnitude improvement in relative uncertainty over the analog.

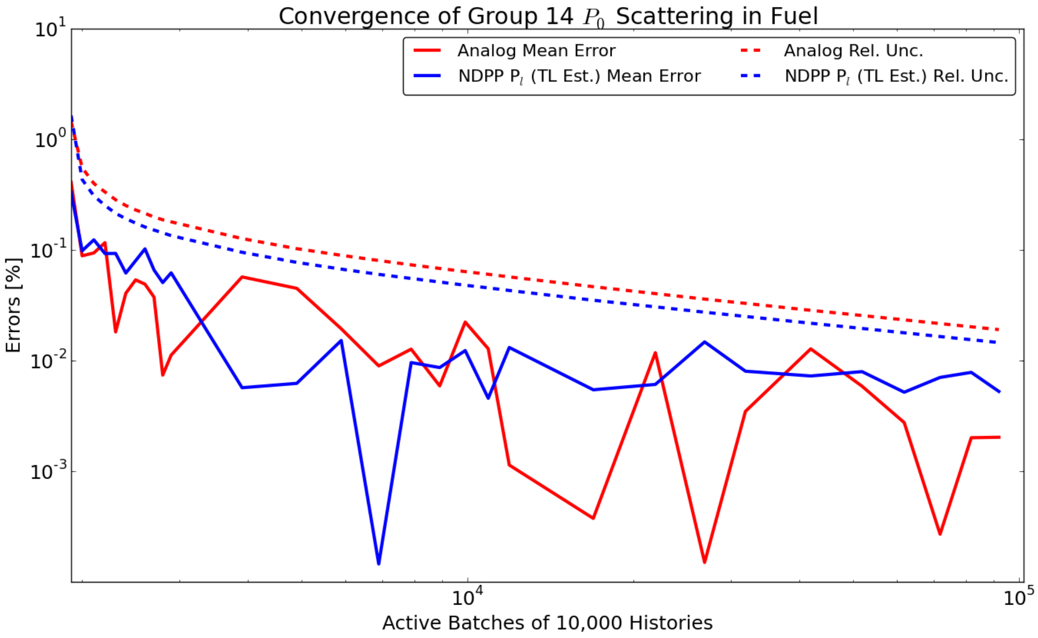

Figure 6.58: Fuel P_0 Group 14 Scattering Comparison

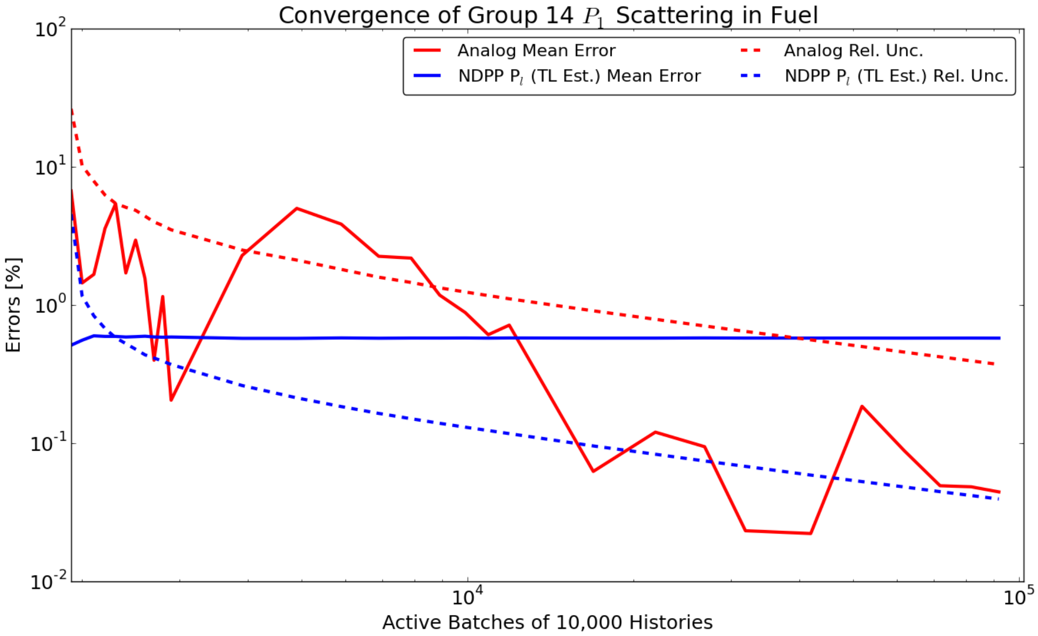

Figure 6.59: Fuel P_1 Group 14 Scattering Comparison

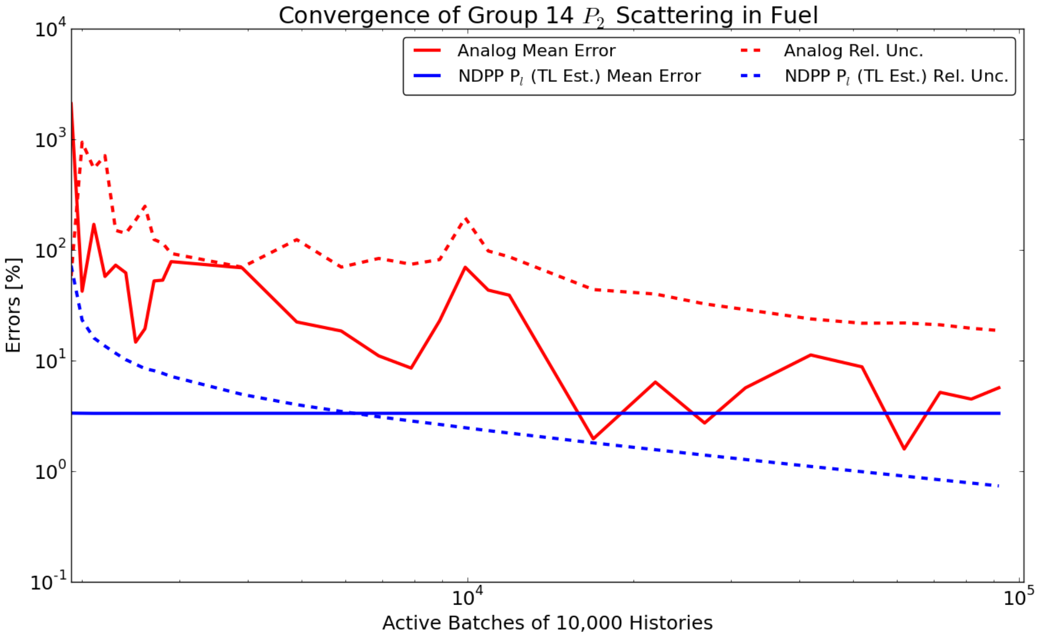

Figure 6.60: Fuel P_2 Group 14 Scattering Comparison

Figures 6.61 through 6.63 show the P_0 through P_2 results of this work for the moderator in the epithermal group, group 14. Since the moderator scattering in this group is still anisotropic, the improvement due to the NDPP data is not as extensive as for the fuel. It is instructive to note that since the moderator has no inelastic collisions in this group, the target-in-motion elastic kernel is performing very well with essentially negligible truncation errors just above $10^{-4}\%$ for P_0 and $2 \times 10^{-3}\%$ for P_2.

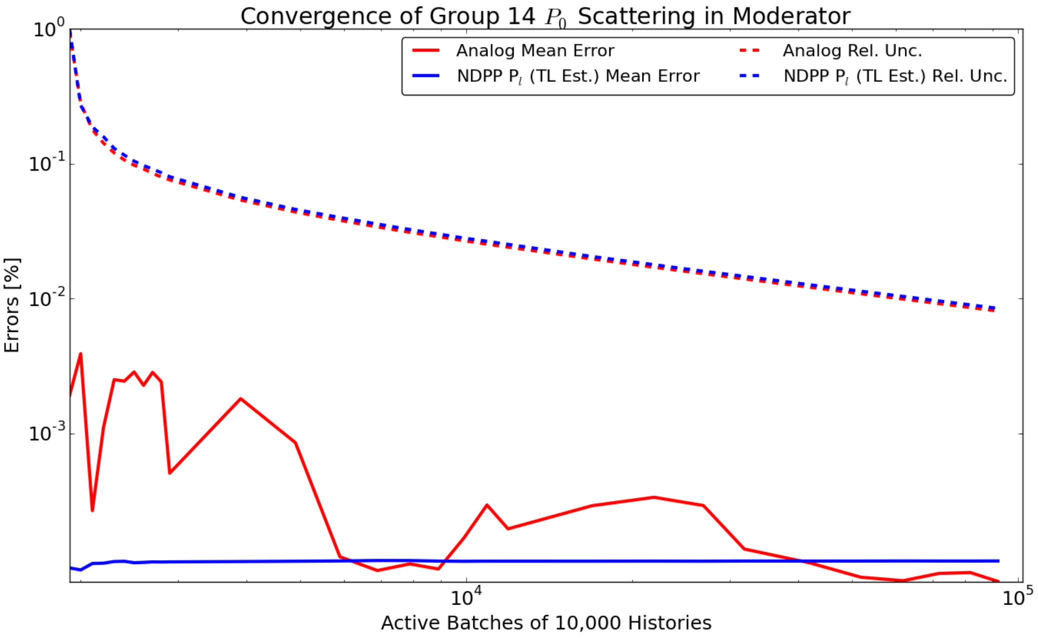

Figure 6.61: Moderator P_0 Group 14 Scattering Comparison

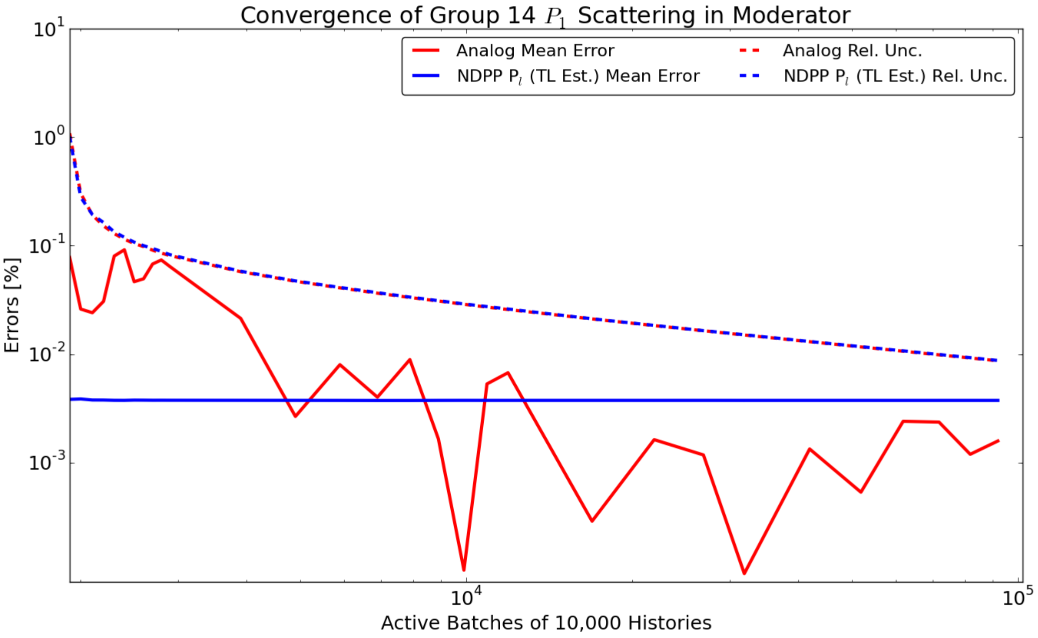

Figure 6.62: Moderator P_1 Group 14 Scattering Comparison

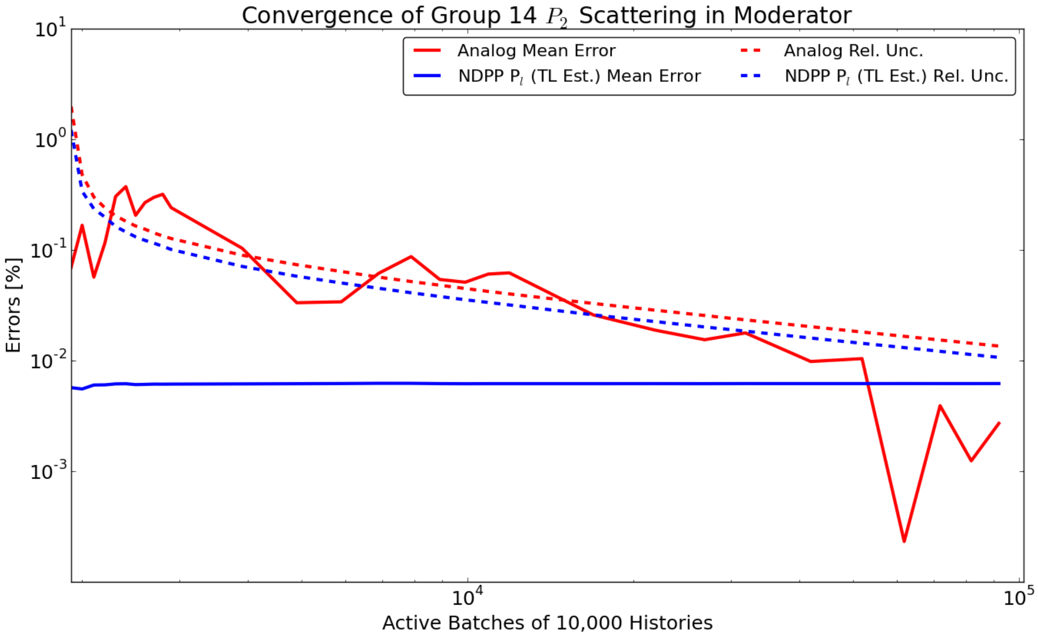

Figure 6.63: Moderator P_2 Group 14 Scattering Comparison

The thermal group (group 44) data for both materials Figures 6.64 through 6.69 show the P_0 through P_2 results of this work for the fuel then moderator in the thermal group, group 44. Since the thermal collisions are typically isotropic, these results are quite similar to those seen for the epithermal fuel data above. The P_1 and higher moments are difficult to resolve stochastically and the NDPP method performs quite well compared to the analog.

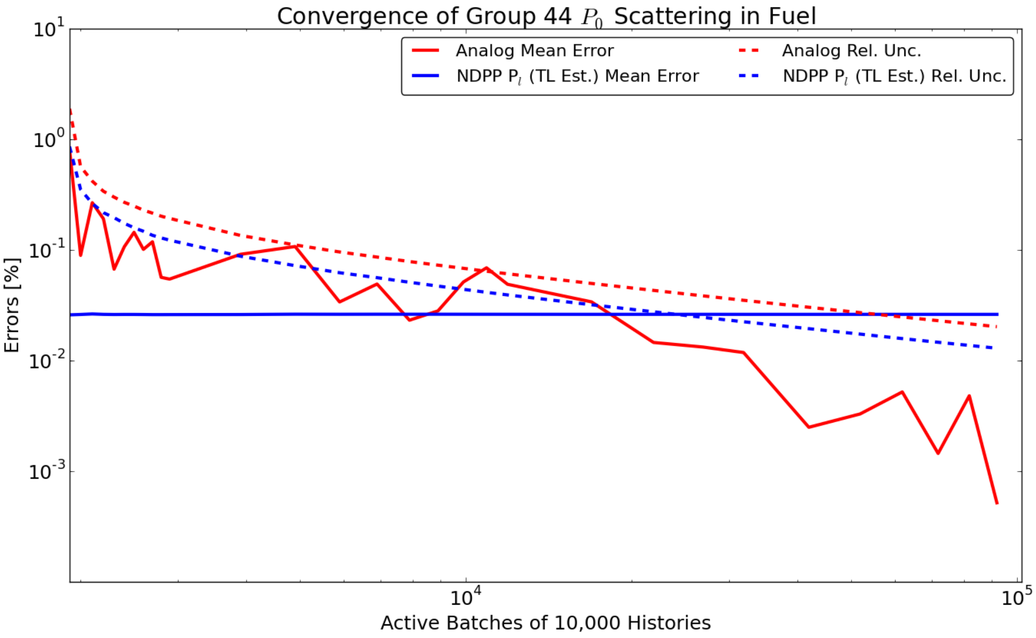

Figure 6.64: Fuel P_0 Group 44 Scattering Comparison

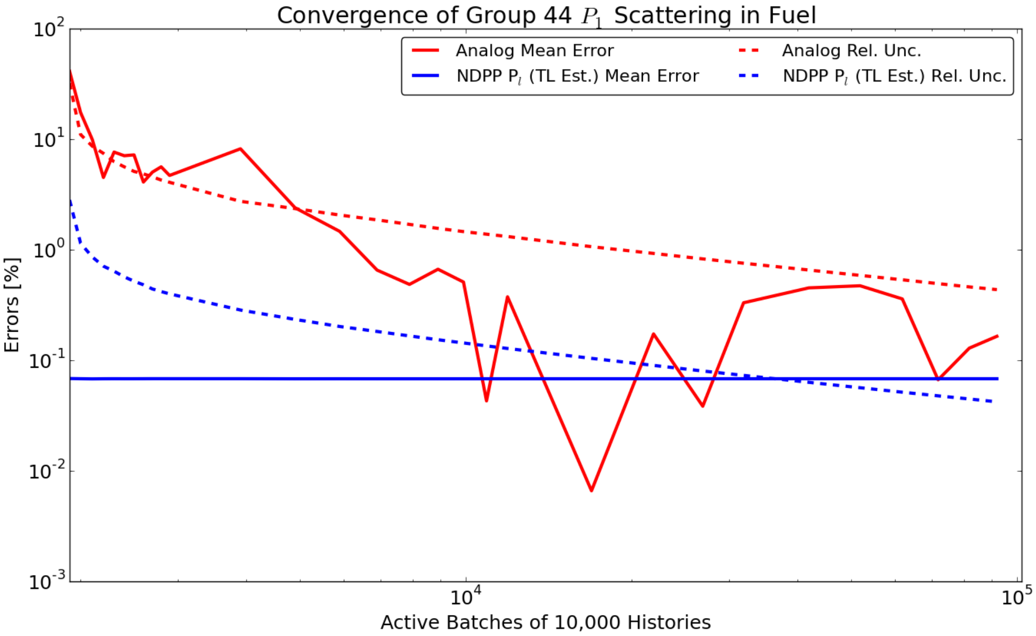

Figure 6.65: Fuel P_1 Group 44 Scattering Comparison

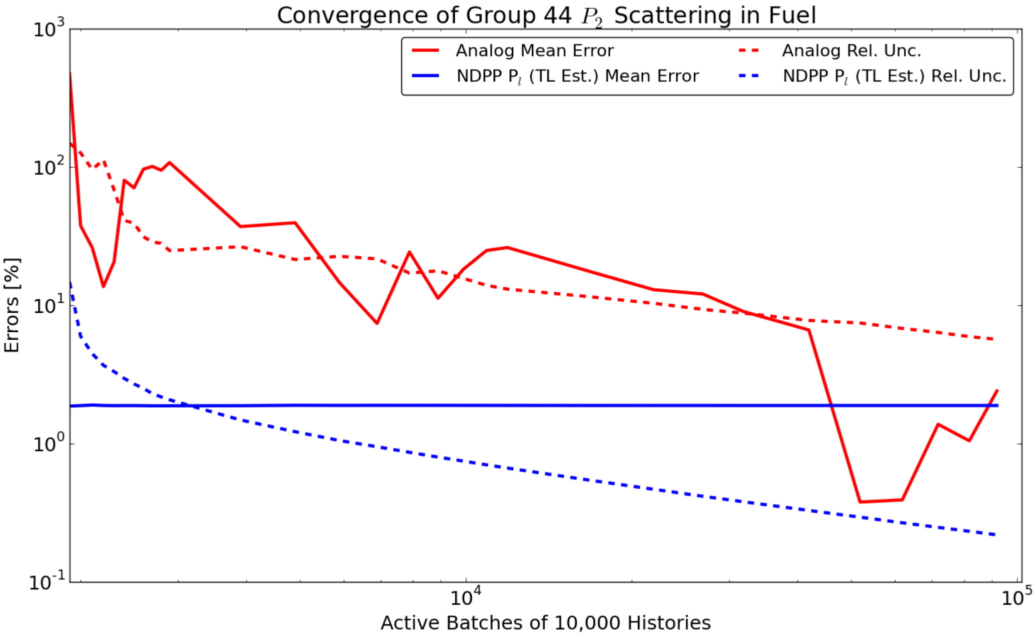

Figure 6.66: Fuel P_2 Group 44 Scattering Comparison

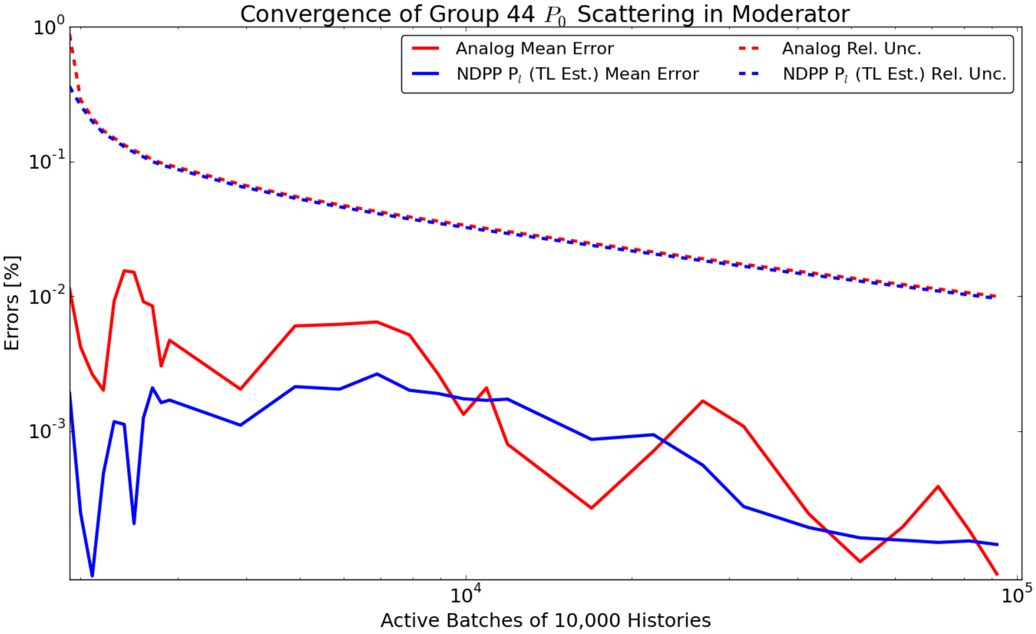

Figure 6.67: Moderator P_0 Group 44 Scattering Comparison

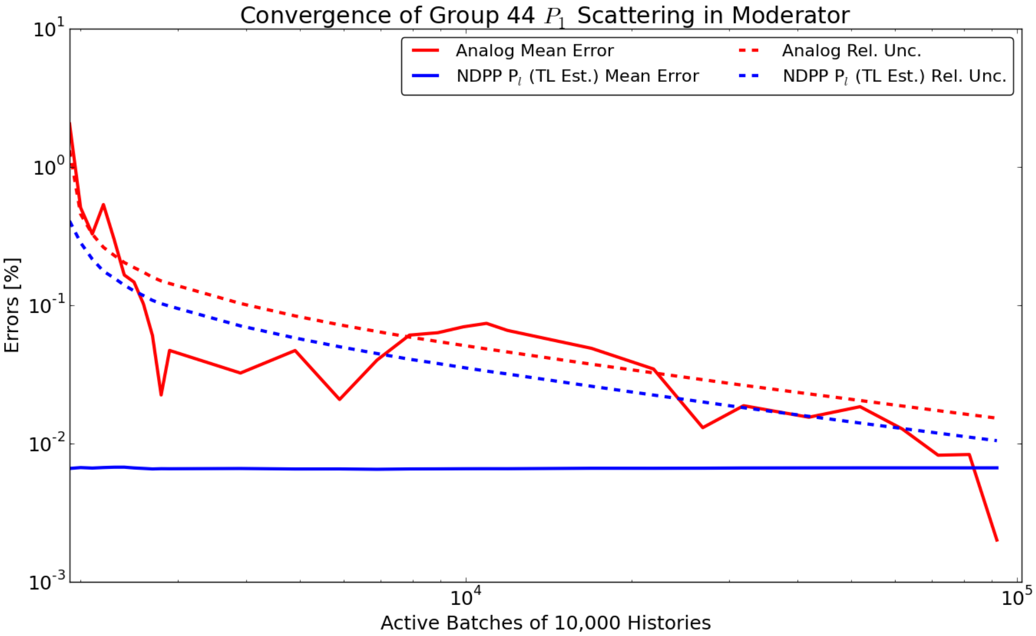

Figure 6.68: Moderator P_1 Group 44 Scattering Comparison

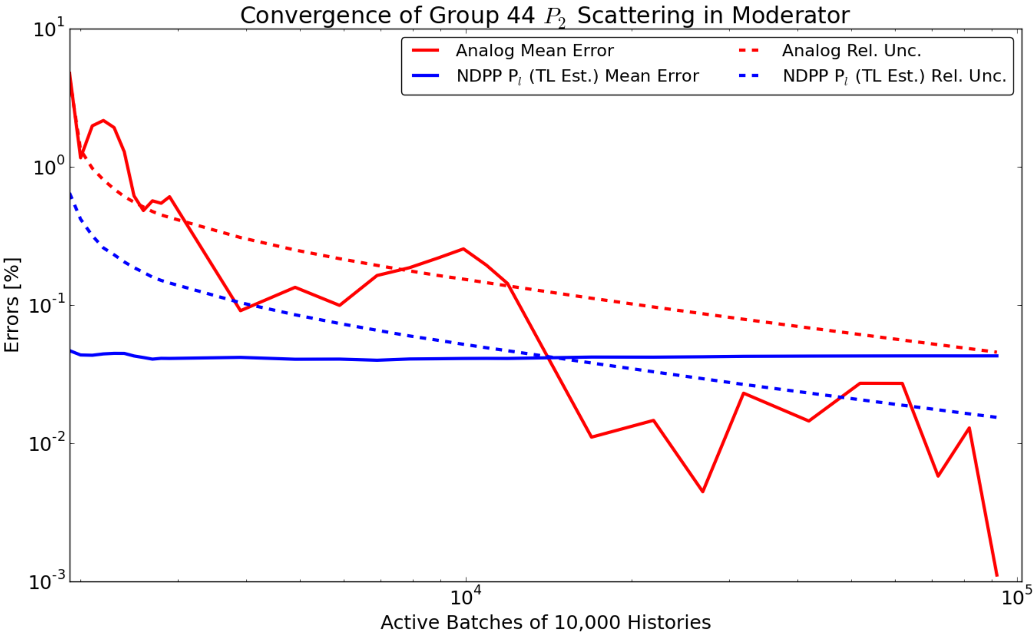

Figure 6.69: Moderator P_2 Group 44 Scattering Comparison

6.3.3.2 Track-Length and Collision Estimator Comparison

The previous sections showed that the improved method lives up to its name. This comparison took advantage of the fact that the improved method enables track-length tallying by utilizing the track-length form of the NDPP tallies. This section will back up slightly and verify that the efficiency gains are only improved by the enabling of track-length tallies, and not *because* of them. This will be tested by running the same pin cell problem but this time using collision estimators with the NDPP tallies instead of track-length estimators.

Instead of providing the entire set of figures shown previously, some of the best performing cases from above will be re-examined with the collision estimators. The cases to examine include the P_1 scattering moments obtained for Groups 14 and 44 in the fuel. These results are shown in Figures 6.70 and 6.71. As can be seen, the difference in relative errors between the collision and track-length estimators is responsible for only a small portion of the benefit indicating that most of the benefit was obtained simply because of the pre-processed data.

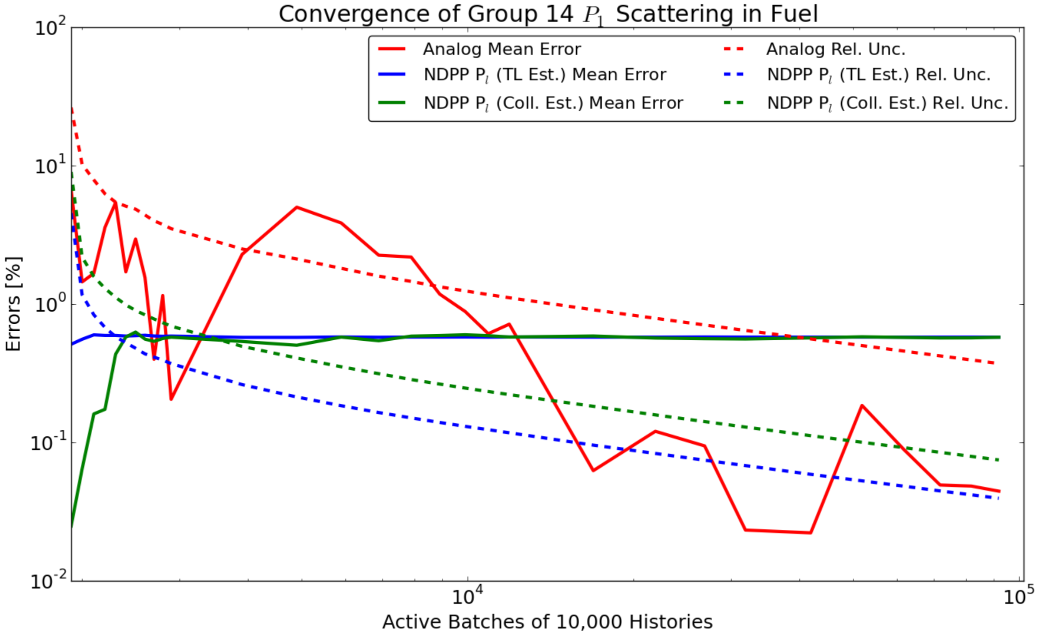

Figure 6.70: Fuel P_1 Group 14 Scattering Comparison

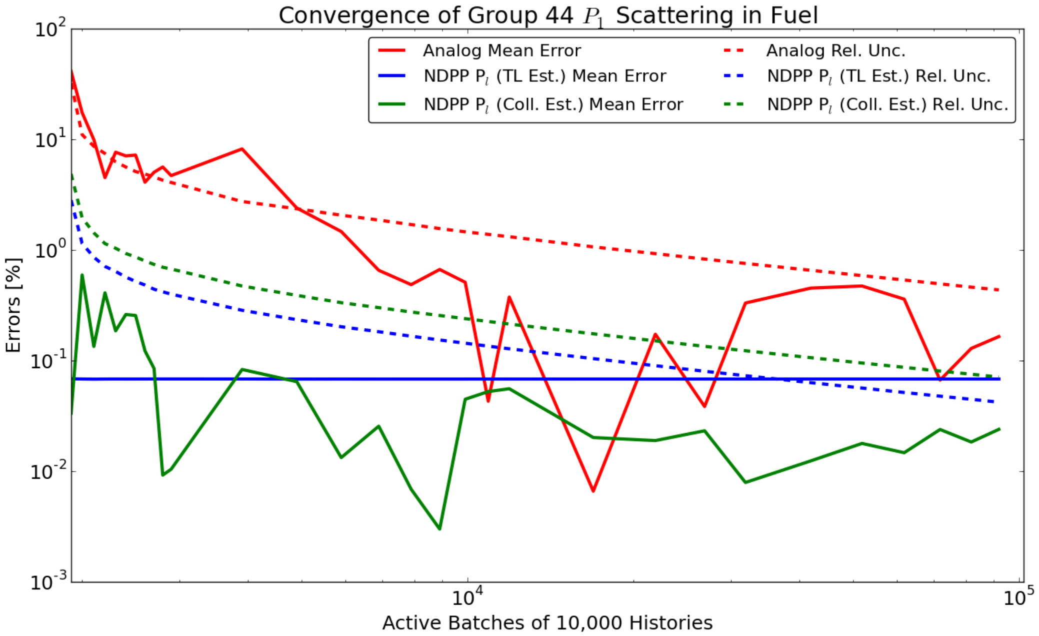

Figure 6.71: Fuel P_1 Group 44 Scattering Comparison

A pin cell case with data being shown in only the fuel and moderator is not an ideal situation to compare collision and track-length estimators, however. A single pin cell will have sufficient collisions occurring in these two regions such that the difference between the two should be minimal. A more extreme case would be examining collisions within the fuel-clad gap. This region contains helium gas which does not experience a significant number of collisions and therefore the difference between the track-length and collision estimators should be exacerbated. Therefore, the same investigation as above will be performed except this time for group 4 of the gap. Group four was chosen simply because the other groups did not experience any collisions at all for a up to thousands of batches.

These results, in Figures 6.72 through 6.74, show that the track-length estimator was responsible for most of the improvement in the method because the collision estimator relative uncertainties nearly overlaps with the analog.

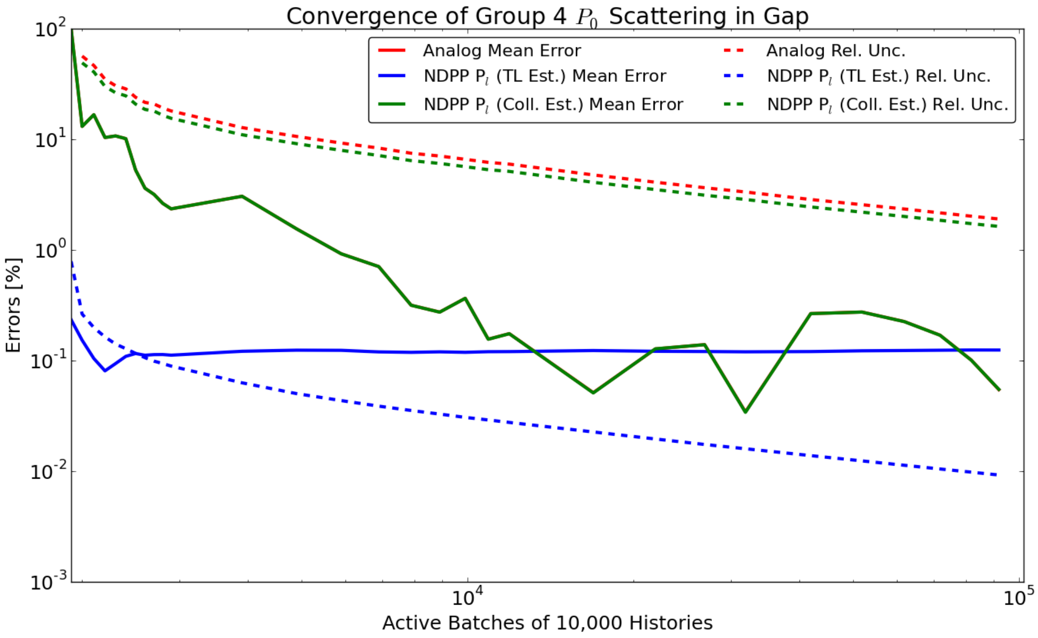

Figure 6.72: Gap P_0 Group 4 Scattering Comparison

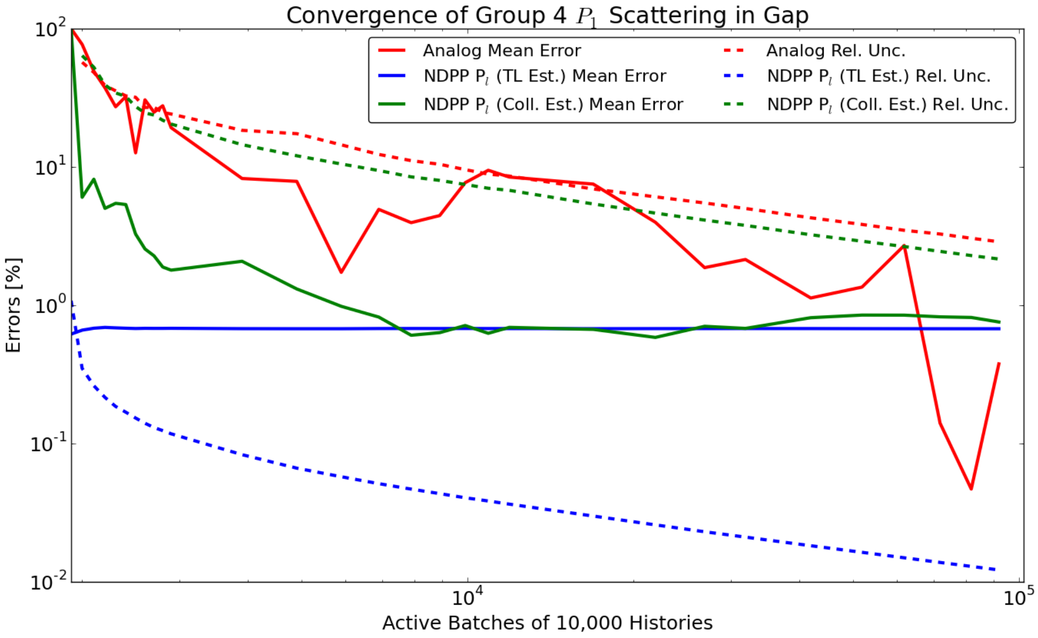

Figure 6.73: Gap P_1 Group 4 Scattering Comparison

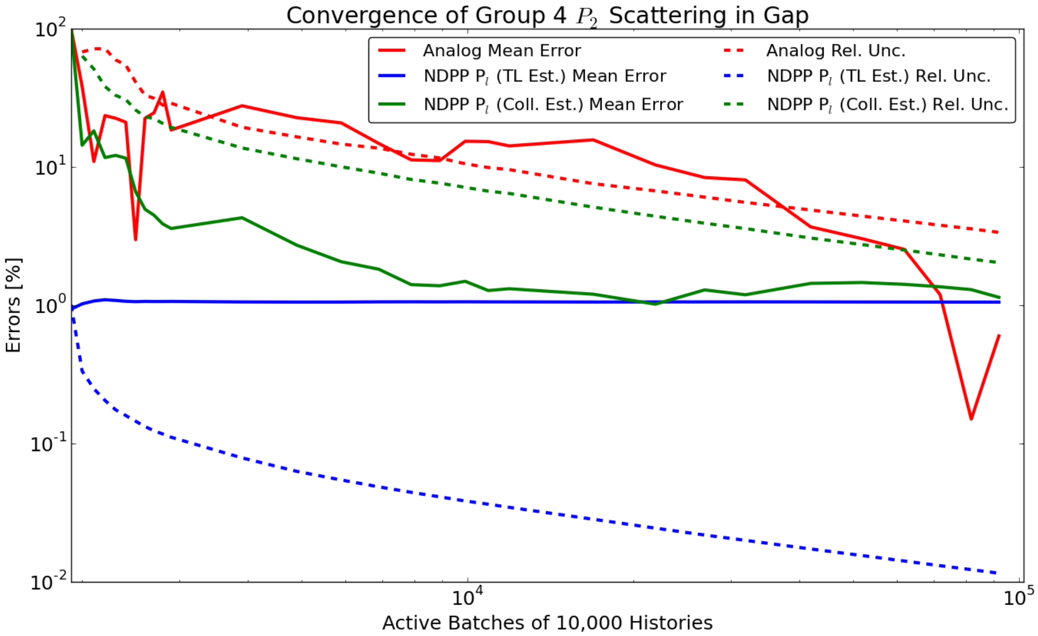

Figure 6.74: Gap P_2 Group 4 Scattering Comparison

6.3.4 Improved Method Design Parameters Impact

In this section, the performance of the design method relative to parameters important for design will be tested. This will be examined by taking the cross section libraries generated by both the analog and improved methods and using them in a deterministic transport solver and calculating both the eigenvalue and pin powers. This study will use the two models used earlier in this dissertation and fully defined in Appendix A: the pin cell model and the 5x5 sub-assembly problem. The pin cell model will only consider the eigenvalue convergence, while the sub-assembly problem will be used to investigate the convergence of both the eigenvalue and pin powers.

6.3.4.1 Pin Cell Eigenvalue Convergence

To evaluate the eigenvalue convergence, the OpenMC tallies were converted to an MPACT MGXS library at varying numbers of batches throughout the entire billion history simulation. MPACT was then run with both isotropic and P_2 scattering and the resultant value of k_{eff} plotted along with the running OpenMC eigenvalue. The models utilized for this case are described in Appendix A.

The resultant P_0 eigenvalue trajectory is shown in Figure 6.75 for both the analog and improved method, the latter using the track-length estimator form of the scattering moments. Figure 6.76 shows the same information, but this time the data is converted to a percent difference (with units of percent-mille, or *pcm*) between the MPACT solutions and the OpenMC final and converged (billion history) solution. Figures 6.77 and 6.78 show the same, but with P_2 scattering in MPACT.

These results show a very promising result: the NDPP track-length based library yields data which approaches the billion-particle eigenvalue with a minimum number of histories. The analog method does not reach (and exceed) the NDPP method's eigenvalue until around 10,000 batches (for a total of 100 million active histories). Another measure to state the benefit of the improved method is to look at the "eigenvalue swing"; for the purposes of this work, this is swing is defined as the difference between the MPACT solution at the first available batch count (10 active batches or 100,000 active histories) and the one billion history MPACT solution. The analog-based tallies undergo an eigenvalue swing of 225 pcm in the P_2 case while the NDPP-based tallies have a swing of only 41 pcm (again for P_2). This difference is because the NDPP tallies are converged nearly immediately and do not vary significantly thereafter so long as the fission source has been adequately converged.

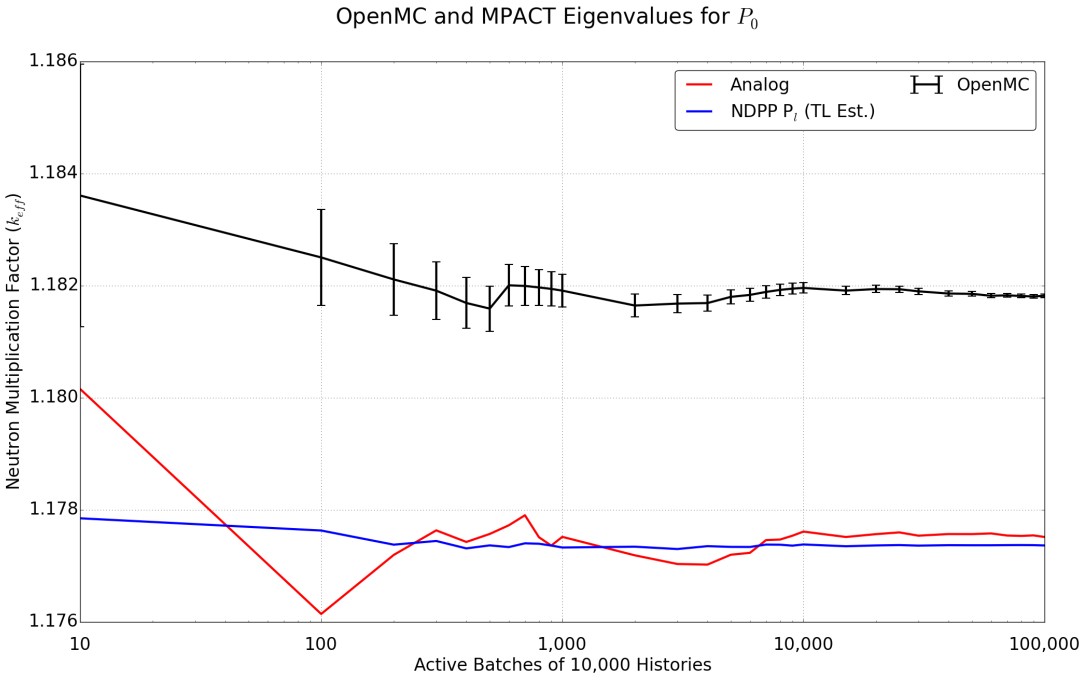

Figure 6.75: Pin Cell Problem MPACT P_0 Eigenvalue Convergence

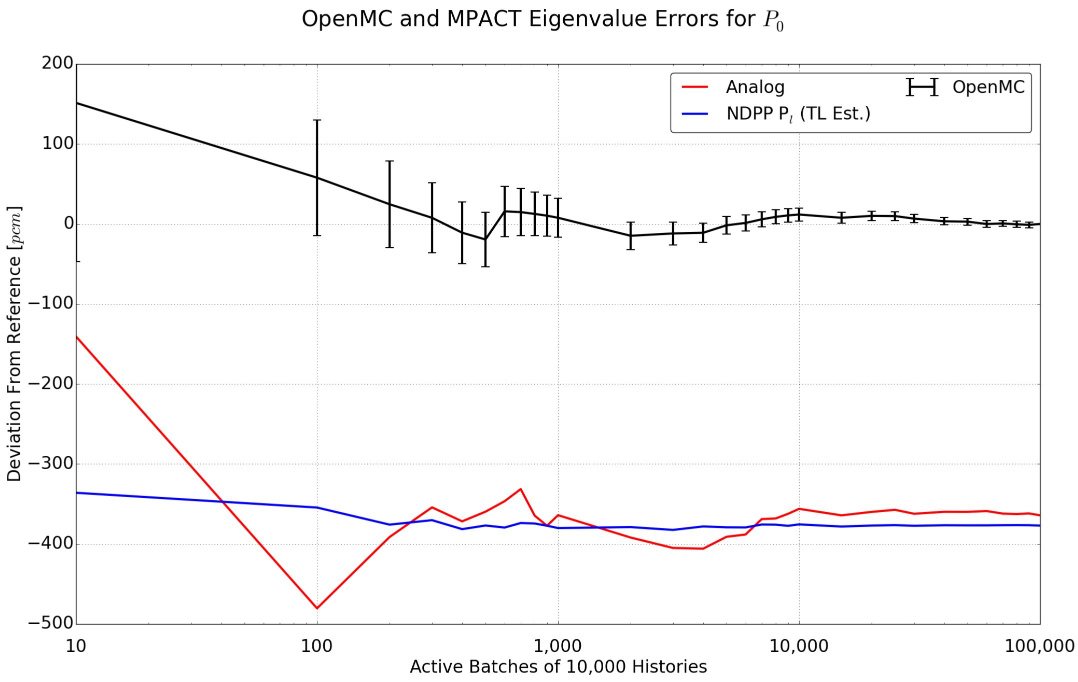

Figure 6.76: Pin Cell Problem MPACT P_0 Eigenvalue Convergence [pcm]

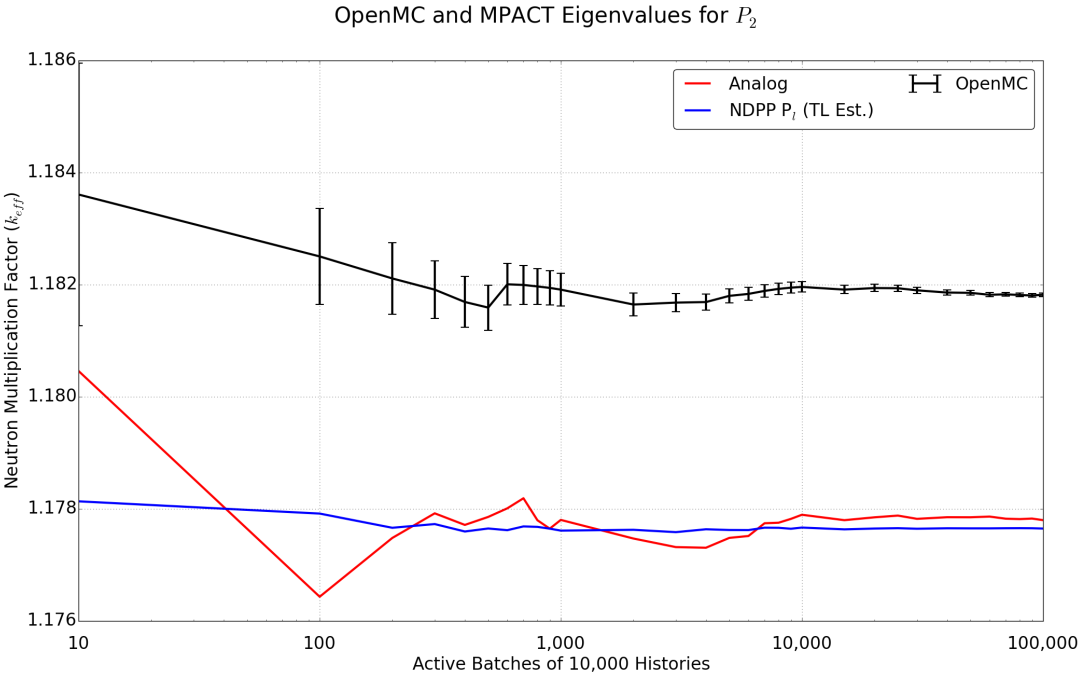

Figure 6.77: Pin Cell Problem MPACT P_2 Eigenvalue Convergence

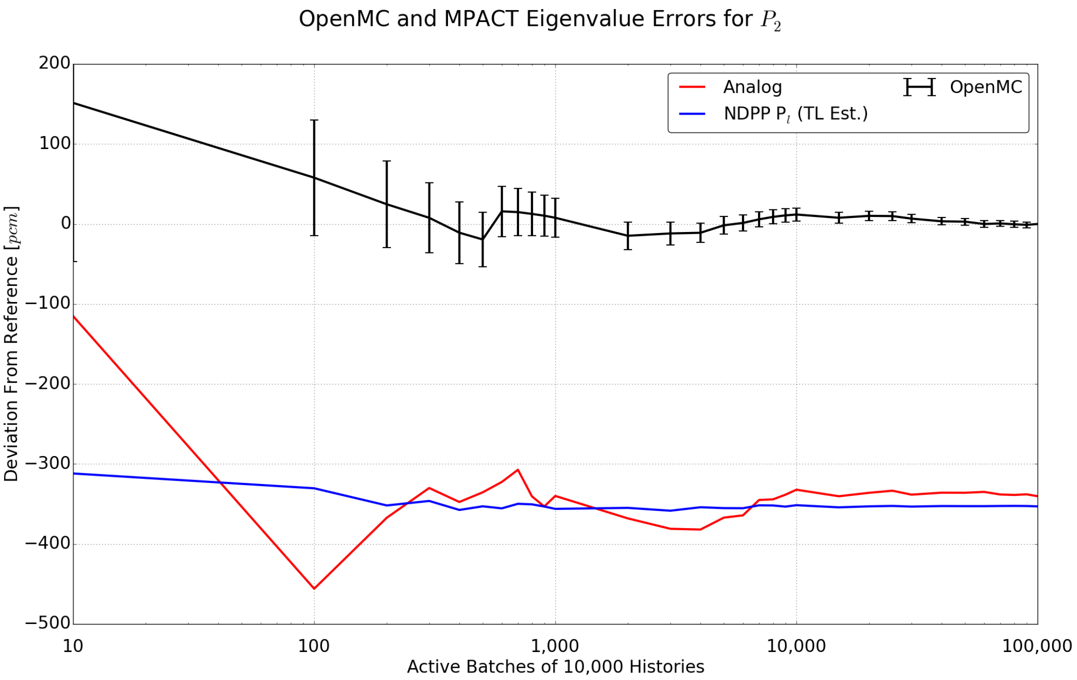

Figure 6.78: Pin Cell Problem MPACT P_2 Eigenvalue Convergence [pcm]

A previous section discussed the difference between the collision and track-length estimators. Figure (6.79) shows the same data as in Figure (6.78), except this time also including the cases of using the NDPP collision estimator data (in green). First, we see that this problem does depend heavily on the enabling of the track-length estimator; this is responsible for most of the benefit of using the NDPP data for this problem.

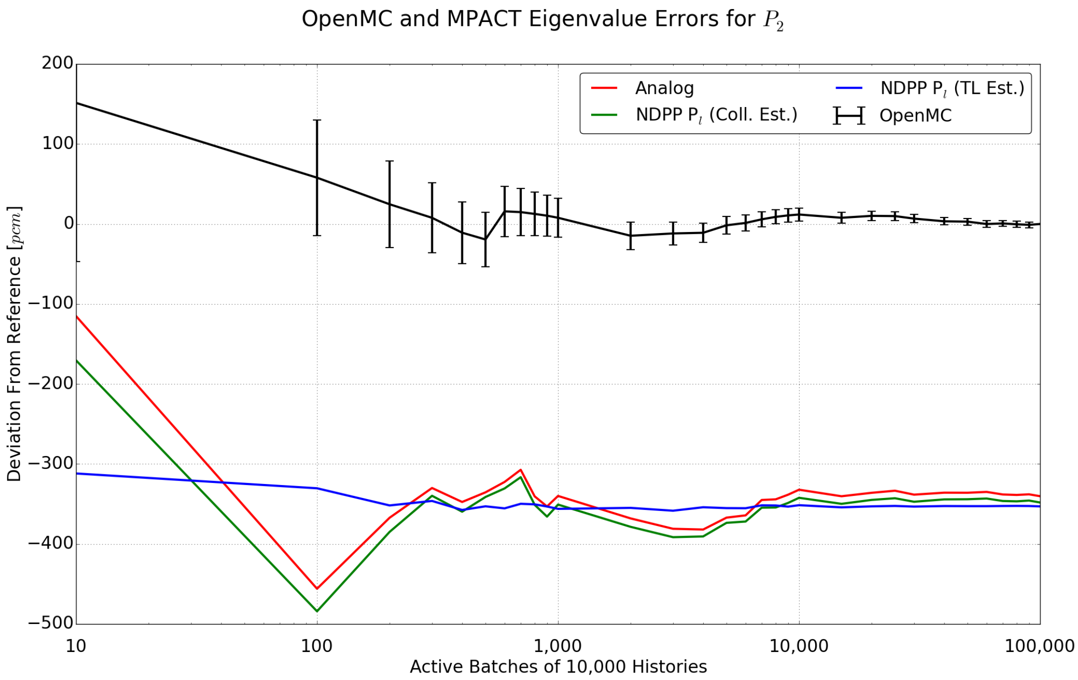

Figure 6.79: MPACT P_2 Eigenvalue Convergence With All Estimator Types [pcm]

6.3.4.2 Sub-Assembly Eigenvalue Convergence

The pin cell problem was one which would be realistically encountered when generating multi-group cross section libraries; but did not show a strong scattering dependence. To scale up the dimensions of the problem examined with the NDPP data, this eigenvalue convergence study will be performed with the 5x5 sub-assembly problem described in Appendix A and previously used in Chapter 3. The models utilized for this case are described in Appendix A.

The results of the P_0 calculations are shown in Figure 6.80; Figure 6.81 shows the same information but is normalized with the y-axis being the percent-mille difference between the MPACT solution and the 1 billion particle OpenMC solution. The same results are shown for P_2 scattering in Figures 6.82 and 6.83. In all these figures, the red line is the same as was shown in Chapter 3.

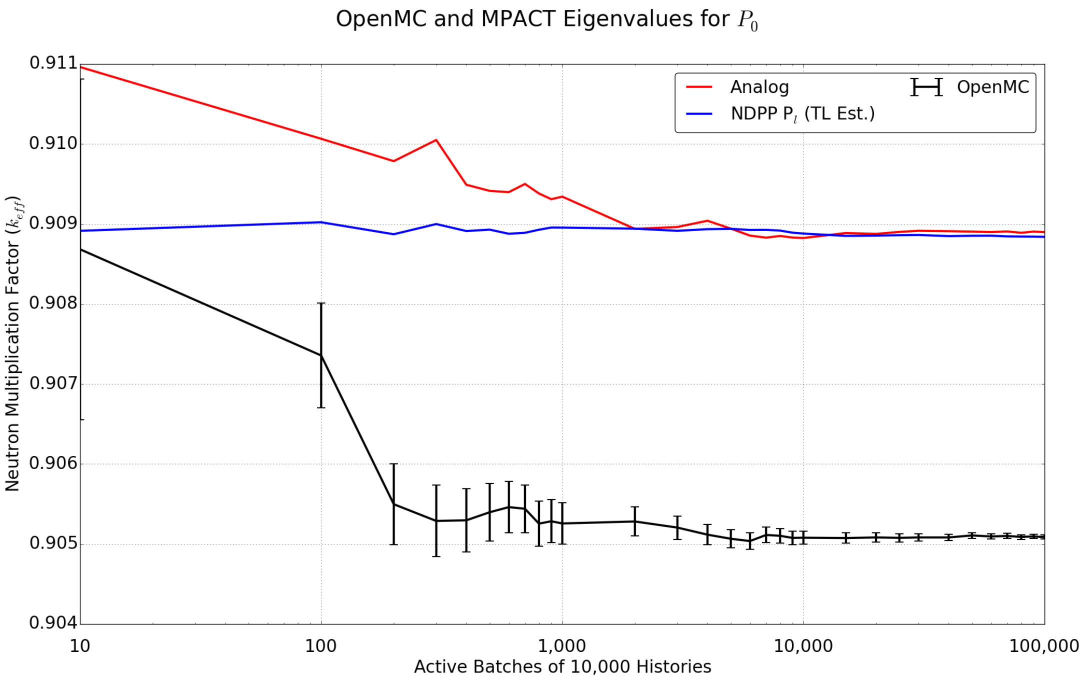

Figure 6.80: Sub-Assembly Problem MPACT P_0 Eigenvalue Convergence

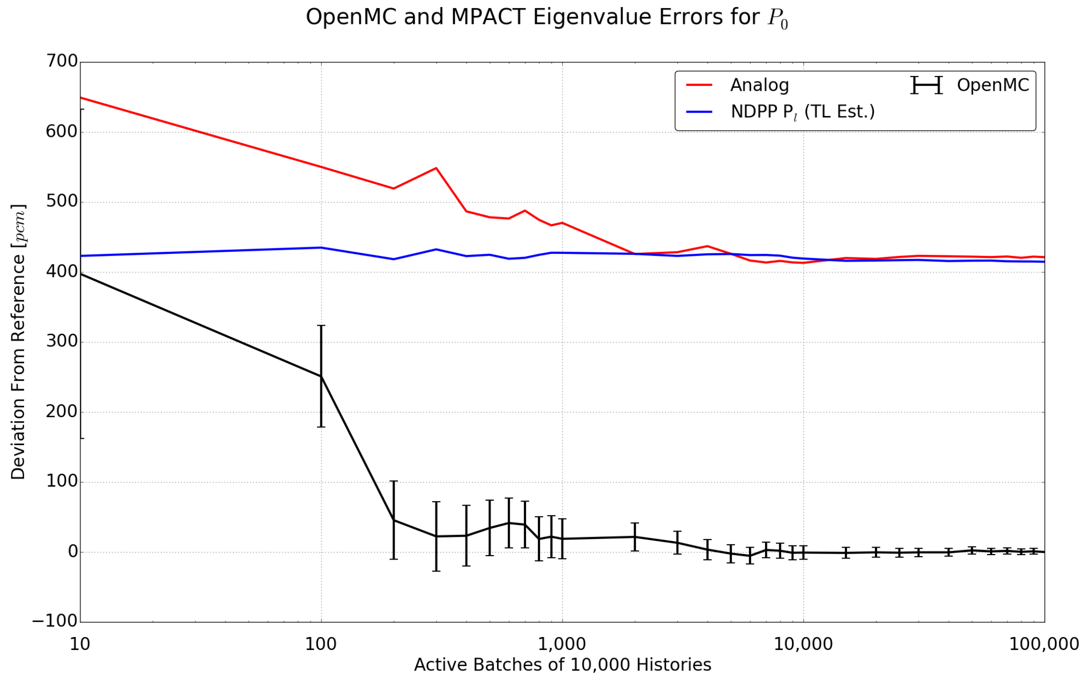

Figure 6.81: Sub-Assembly Problem MPACT P_0 Eigenvalue Convergence [pcm]

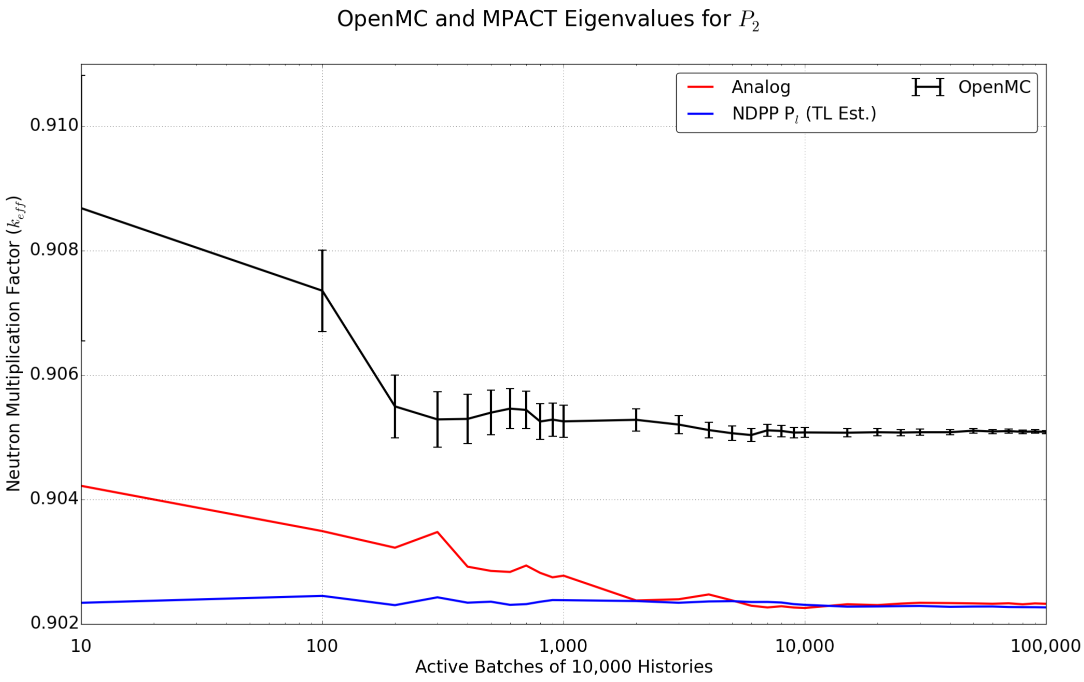

Figure 6.82: Sub-Assembly Problem MPACT P_2 Eigenvalue Convergence

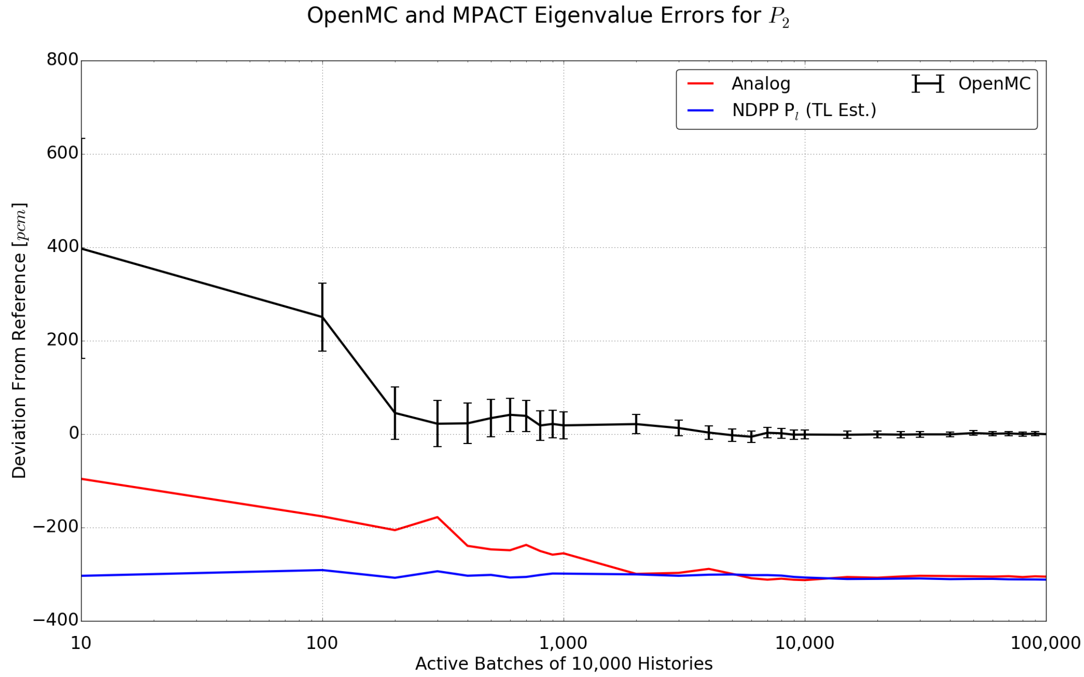

Figure 6.83: Sub-Assembly Problem MPACT P_2 Eigenvalue Convergence [pcm]

First, we see that the bias between the analog and NDPP-based methods is only 6.5 pcm for both the P_0 and P_2 cases. This is half the 13 pcm bias observed for the pin cell case (Table 6.1), though both are small enough to be considered negligible.

Next, these results also show that the NDPP library with track-length estimators is only 8 pcm different than the final value after only ten batches. The analog method does not reach such levels until around 8,000 batches. Like the pin cell model, this difference is because the NDPP tallies do not vary with increasing histories so long as the fission source has been adequately converged.

6.3.4.3 Sub-Assembly Pin Power Convergence

Figures 6.84 and 6.85 show the convergence of the maximum pin power error (top) and the root-mean-squared error (bottom) of all 21 fuel-bearing pins with both the Direct-P$_n$ and improved method-based tallies. In this case, the maximum pin power error is defined as the percent difference between the pin power of the highest-power pin in the sub-assembly value at the particular batch count and the OpenMC reference peak pin power presented in Appendix A. The root-mean-squared is the same, but showing the root-mean-square error of all pins instead of the error in the hottest pin.

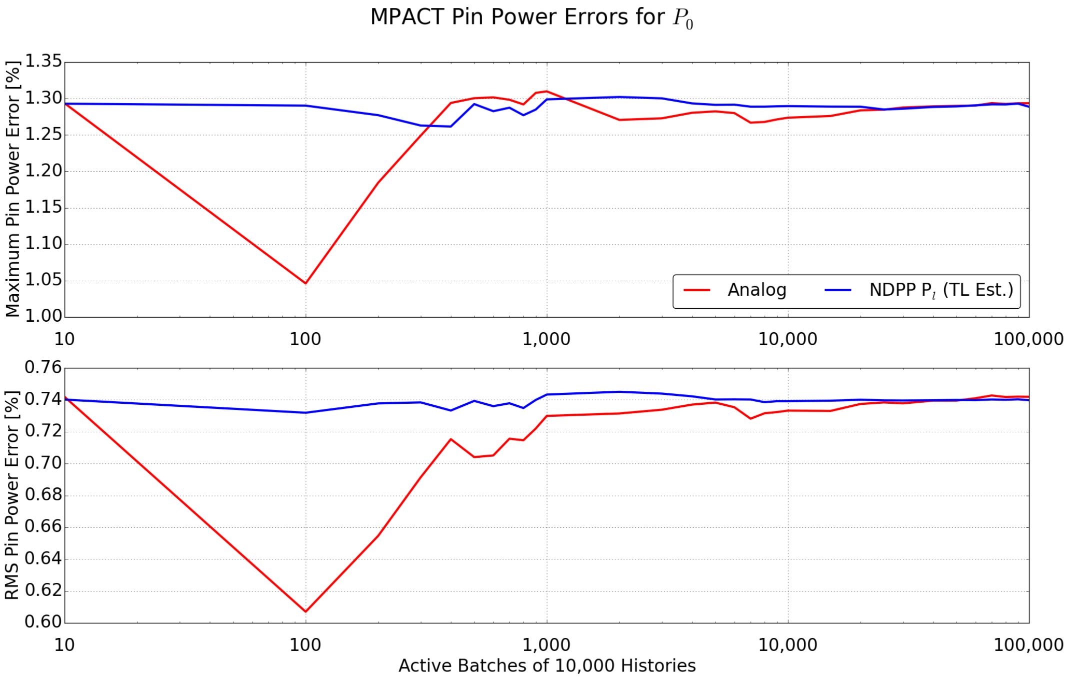

Figure 6.84: Sub-Assembly Problem MPACT P_0 Pin Power Convergence

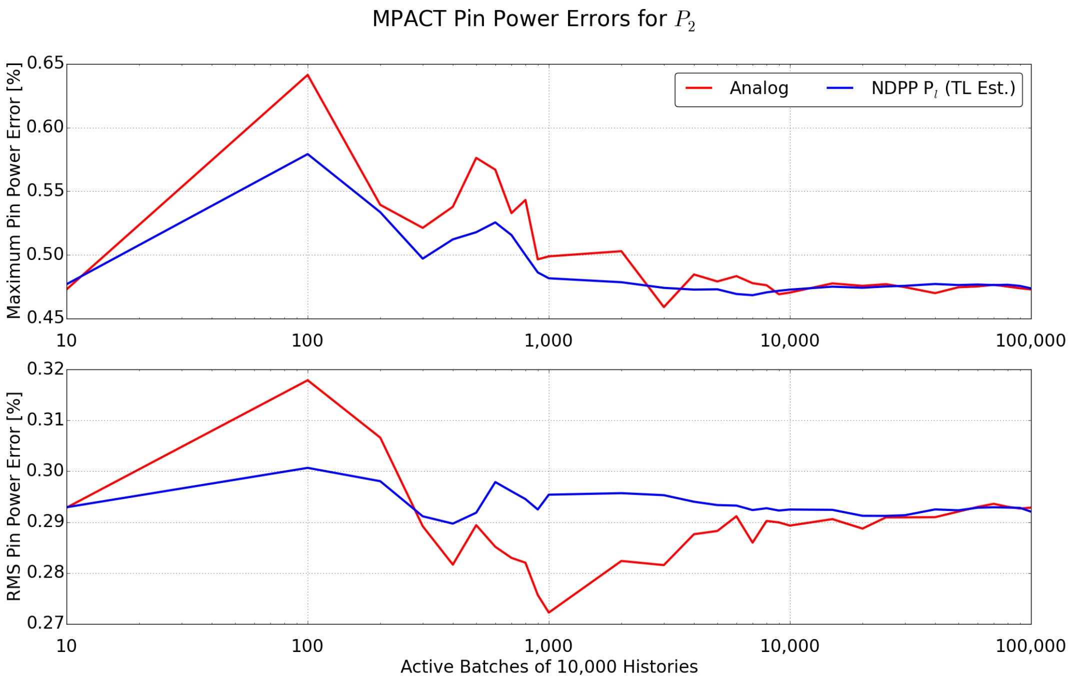

Figure 6.85: Sub-Assembly Problem MPACT P_2 Pin Power Convergence

Like the eigenvalue comparison, we see here that the NDPP method approaches the average value within a few hundred batches for both the hottest pin and root-mean-square of all the pins; the analog method requires substantially more histories.

Finally, note that the NDPP method does not introduce a large bias in these measures of pin power. The analog method had a final maximum pin power error for the P_0 case of 1.2935%; the improved method tallies resulted in a final maximum pin power error of 1.2929% resulting in only a negligible difference. The root-mean-square error results were similarly negligible, as the analog RMS error was 0.7419% while the improved method error was 0.7397%. The same held true for the P_2 case. The final max power error was 0.4729% for the analog and 0.4737% for the improved method. The RMS error was 0.2929% for the analog and 0.2921% for the improved method.

Both of these findings indicate that the improved method of tallying can significantly reduce the number of histories needed to obtain both the eigenvalue and power distribution without severely impacting the accuracy.

6.3.5 Improved Method Figure-of-Merit

The figure-of-merit used when comparing two methods of variance reduction is shown in Eq. (6.1) [2]. This equation is used to quantify the amount of accuracy obtained in a given unit of computation time and therefore comparing the value of Eq. (6.1) for one method and another provides for an easy comparison of multiple methods.

$$FOM = \frac{1}{\sigma^2 t} \tag{6.1}$$

For the purposes of this work, the figure-of-merit can be defined as it is above, or it can be in a form more which describes the effect of the method on downstream analyses such as eigenvalues and pin powers. This section will consider both formulations.

6.3.5.1 Cross Section Figure-of-Merit

To examine the figure-of-merit of the tallied cross sections themselves, the analog and improved method scattering moment matrices were taken from the final, one billion history result. The relative uncertainty of each entry of the scattering moment matrices was then used (with the run time) in Eq. 6.1 to provide a useful figure-of-merit for these cross sections.

To limit the data, this analysis will focus on the same fast, epithermal, and thermal groups (groups 4, 14, and 44, respectively) used throughout this work. This time, only the P_0 and P_2 data will be shown since the P_1 does not provide additional information to this discussion.

Figures 6.86 through 6.89 show this data for the fast group in the fuel and moderator. These results show that the improved method provides a substantial (many orders of magnitude) improvement over the analog method for most of the outgoing energy space. The analog method does well at or near the top of the energy range (self-scatter), but this should have been expected due to the similar relative uncertainty trajectories shown in Section 6.3.3.1.

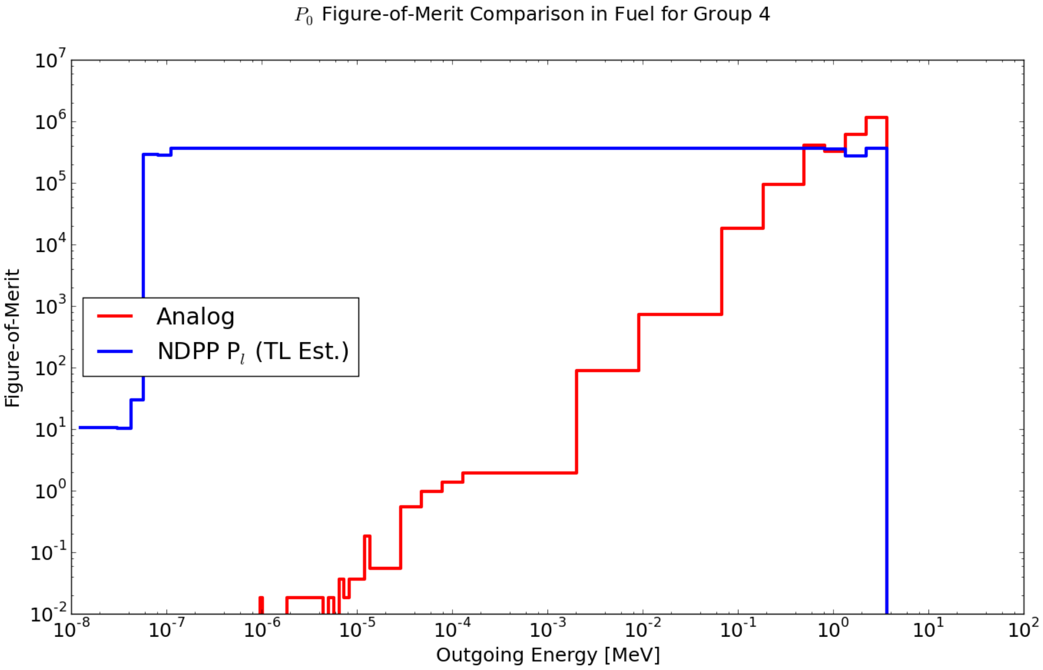

Figure 6.86: Fuel P_0 Group 4 FOM Comparison

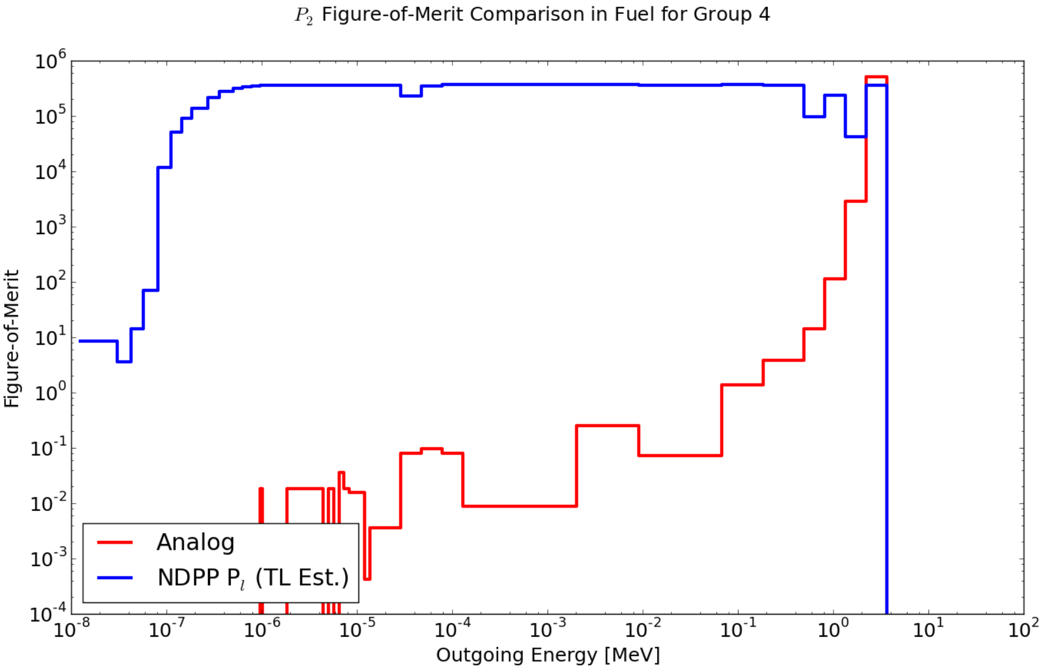

Figure 6.87: Fuel P_2 Group 4 FOM Comparison

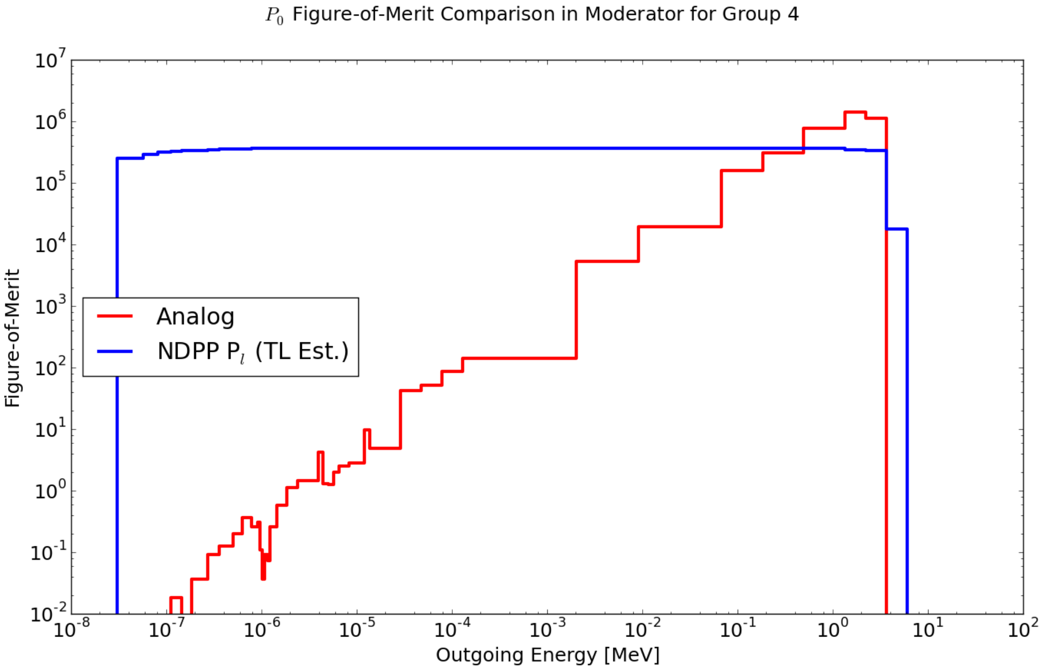

Figure 6.88: Moderator P_0 Group 4 FOM Comparison

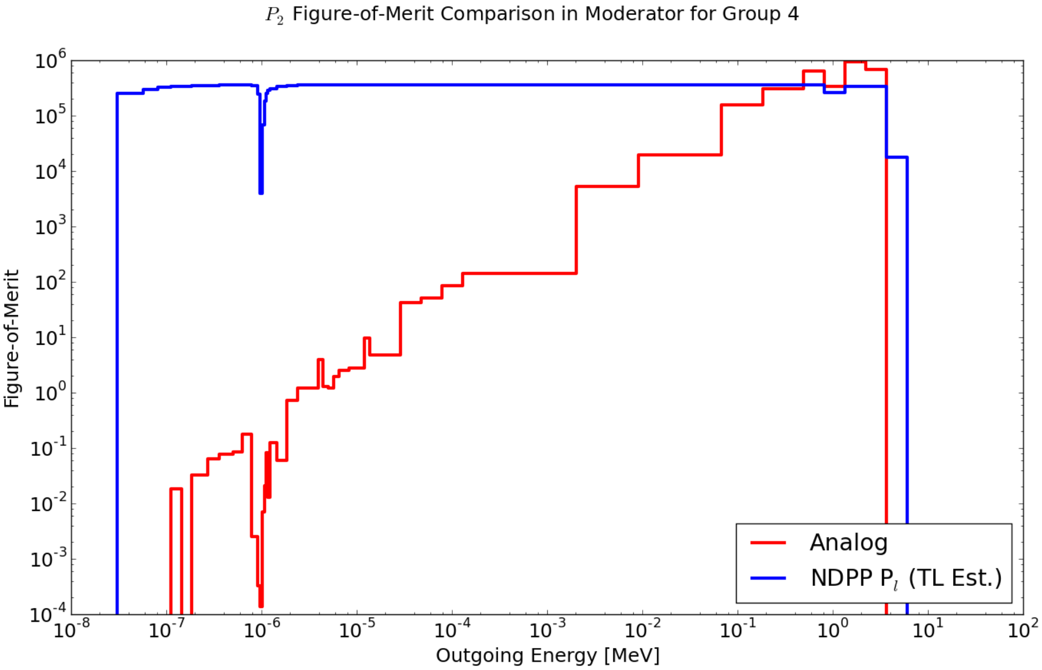

Figure 6.89: Moderator P_2 Group 4 FOM Comparison

Figures 6.90 through 6.93 show this data for the epithermal group in the fuel and moderator. This data shows the same trends as for the fast group, though the analog method does well in the fuel for the P_0 data. This is because the mass of the fuel limits the amount of down-scatter, and thus most collisions in the fuel only result in outgoing energies in one of two groups. When this is the case, the improved method does not provide enough benefit to outweigh the runtime penalty.

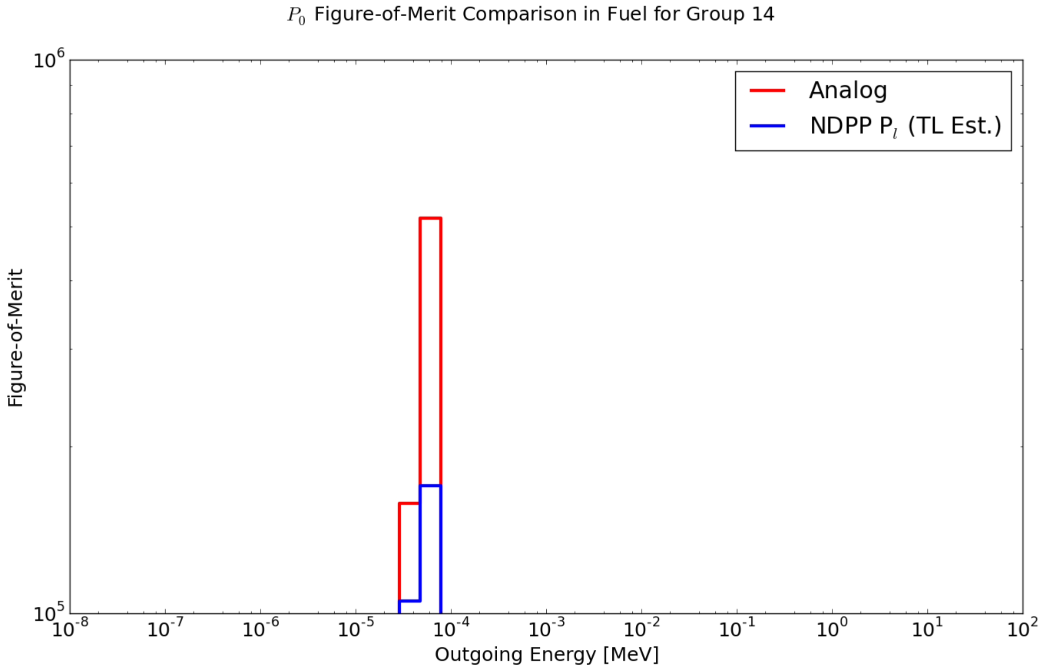

Figure 6.90: Fuel P_0 Group 14 FOM Comparison

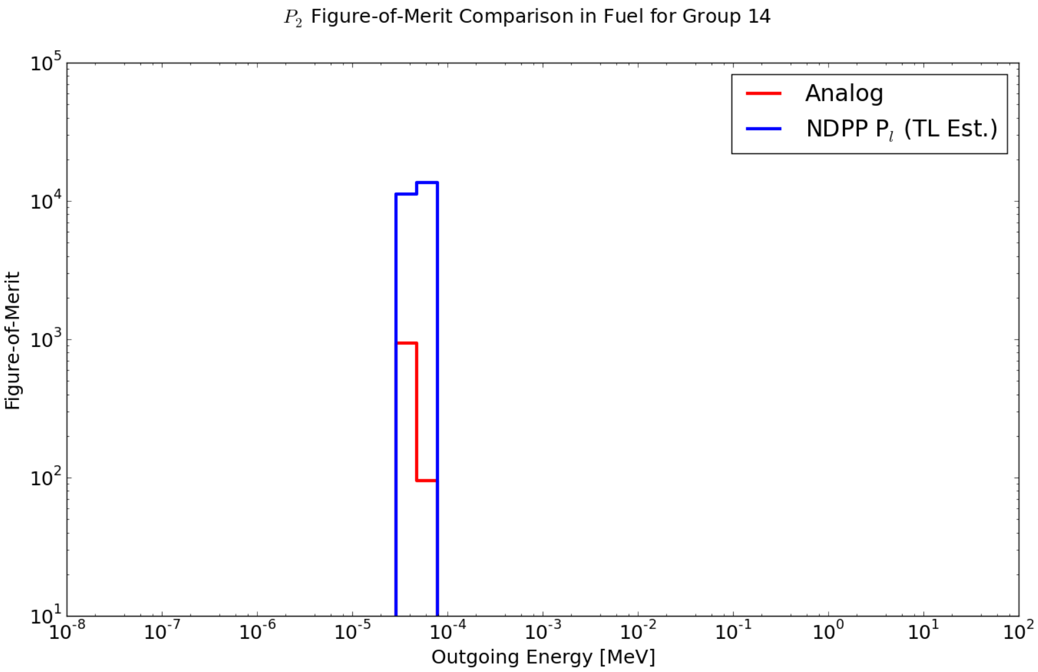

Figure 6.91: Fuel P_2 Group 14 FOM Comparison

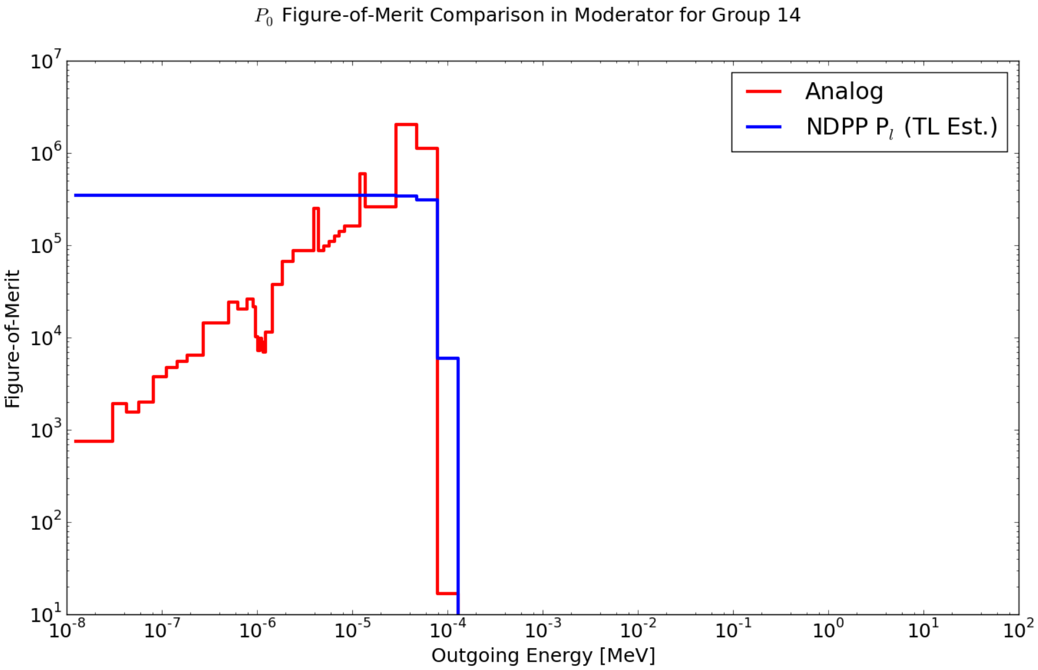

Figure 6.92: Moderator P_0 Group 14 FOM Comparison

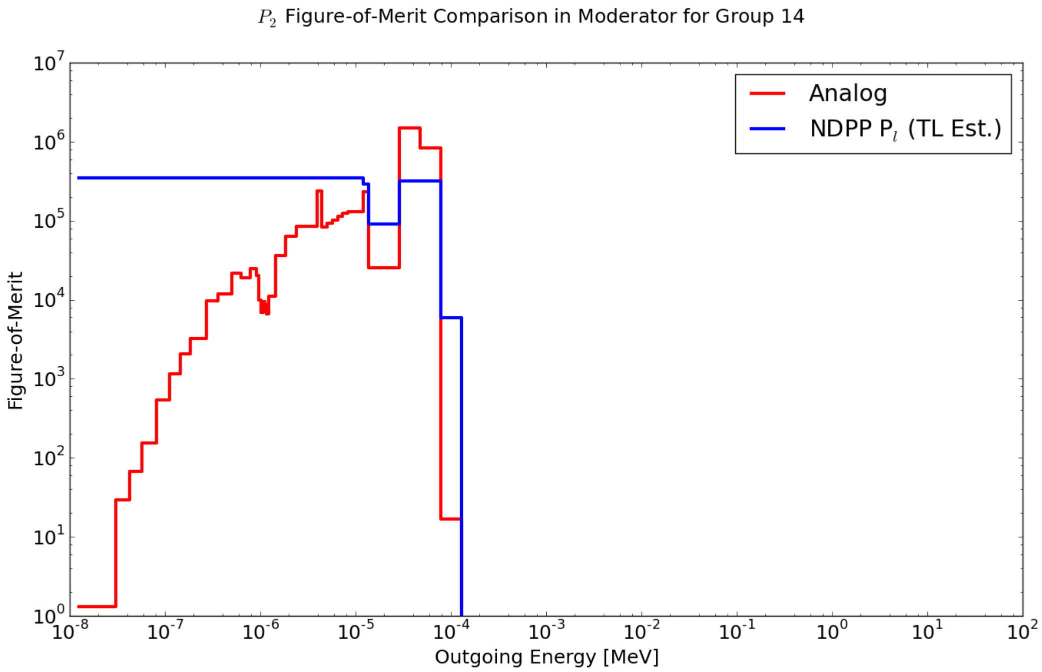

Figure 6.93: Moderator P_2 Group 14 FOM Comparison

Figures 6.94 through 6.97 show this data for the thermal group in the fuel and moderator. These data show the same story as the fast group: the improved method provides a large amount of information to many groups at once, but the analog method performs well with P_0 data for groups near the incoming energy.

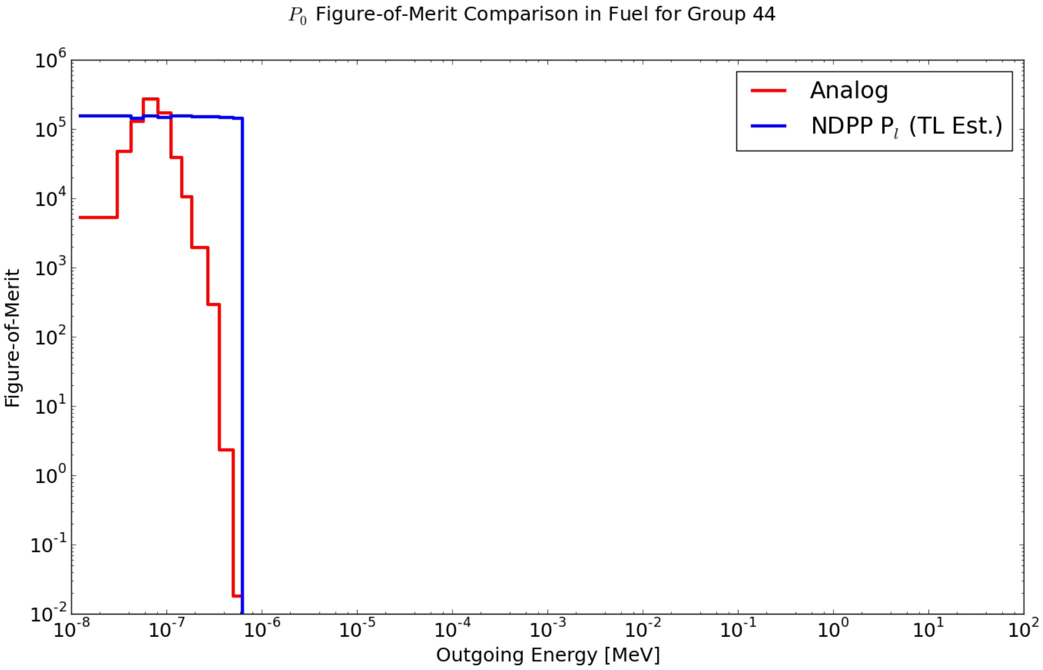

Figure 6.94: Fuel P_0 Group 44 FOM Comparison

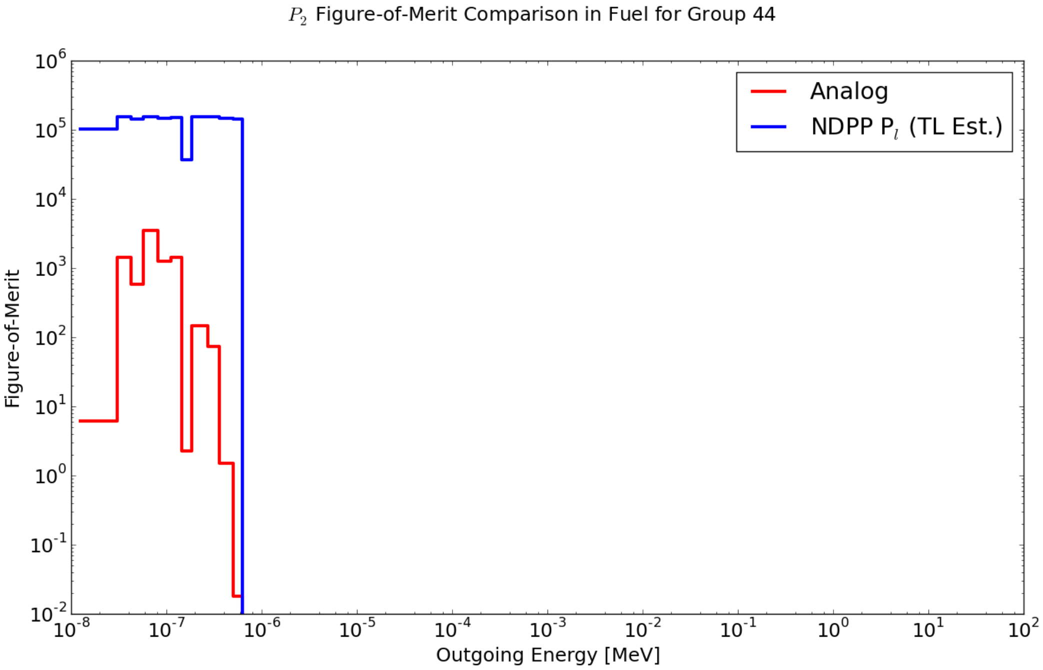

Figure 6.95: Fuel P_2 Group 44 FOM Comparison

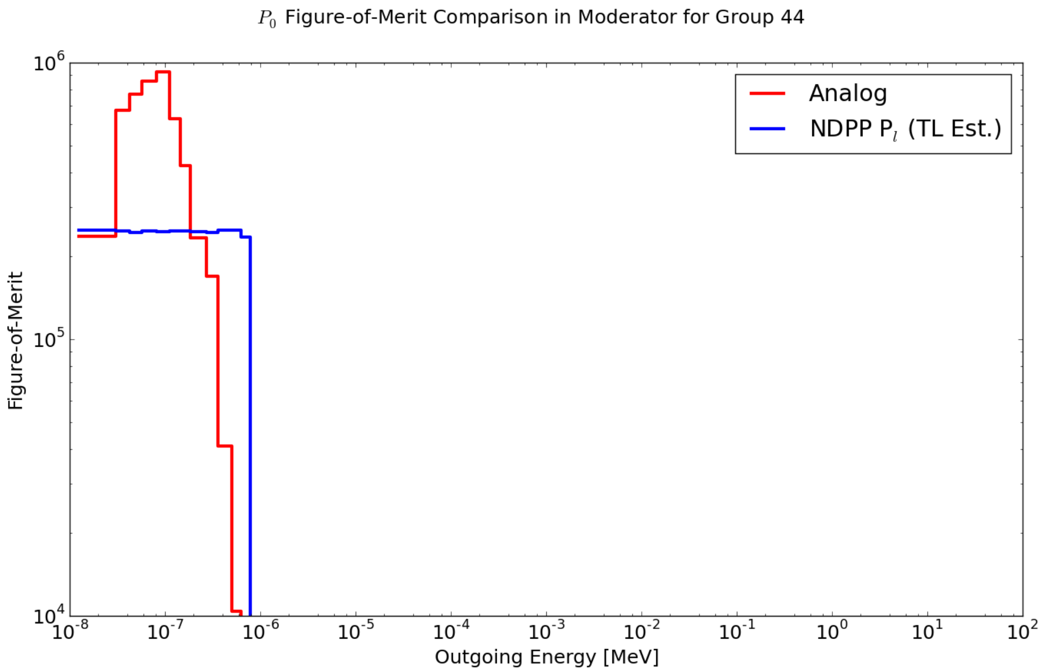

Figure 6.96: Moderator P_0 Group 44 FOM Comparison

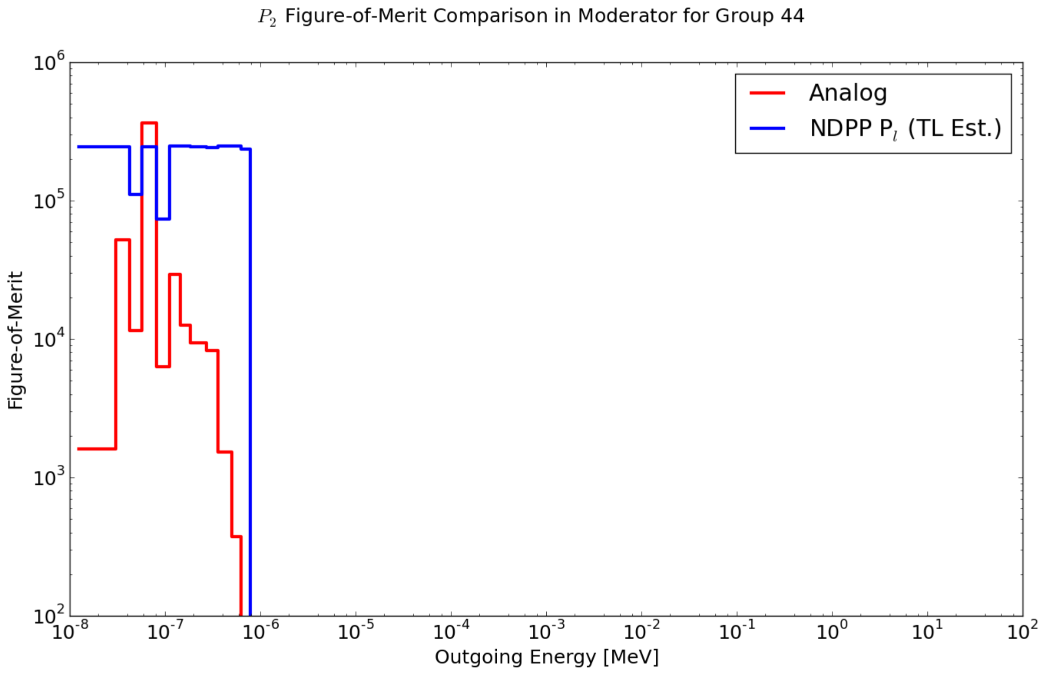

Figure 6.97: Moderator P_2 Group 44 FOM Comparison

As shown in Eq. 6.1, the figure-of-merit is inversely proportional to the run-time. The improved methods figure-of-merit could therefore be improved by only optimizing its code further. Therefore this is an item noted for future work in the conclusion of this dissertation.

6.3.5.2 Eigenvalue and Pin Power Figure-of-Merit

Since the quantities of main interest of this data are the resultant eigenvalues and pin powers, using the traditional Eq. (6.1) approach to compare the analog and improved methods would require a uncertainty propagation of the generated MGXS libraries through the deterministic solver. This would be an intensely time-consuming process as uncertainty propagation, in its most basic form, would require a Monte Carlo sampling of all the cross sections about their reported distributions with sufficiently large number of samples.

Instead a much simpler approach will be taken: finding the time to obtain a sufficiently converged MPACT solution. The word solution is vague and here it will be the quantities of high importance to reactor designers: k_{eff} and both the maximum pin power error and root-mean-square pin power error. The k_{eff} figure-of-merit will be examined for both the pin cell and sub-assembly problems; the pin power figure-of-merits will only be examined for the sub-assembly problem. The word "sufficiently" is also vague at best, for the purposes of this work it will be defined as when the quantity of interest reaches a certain deviation from its one billion history value. For the k_{eff} comparisons, "sufficiently" will be defined to be the point at which all subsequent results remain within ten pcm; pin power comparisons will be called converged when all subsequent results remain within 0.01 percentage points. In all cases, only the P_2 solution will be considered.

The first to consider is eigenvalue convergence of the pin cell. Figure 6.98 shows the same results as Figure 6.78, though this time the y-axis scaled to show the percent error from the one billion history result and the x-axis is the run time. The solid black horizontal lines are the ±10 pcm lines. We see here that the analog method requires around three hours to satisfactorily achieve the criteria of ten pcm from the final solution. The NDPP-based method requires around twenty-four minutes to realize the same. This is an improvement of nearly a factor of eight in the total time required to achieve a result to within a certain level of convergence.

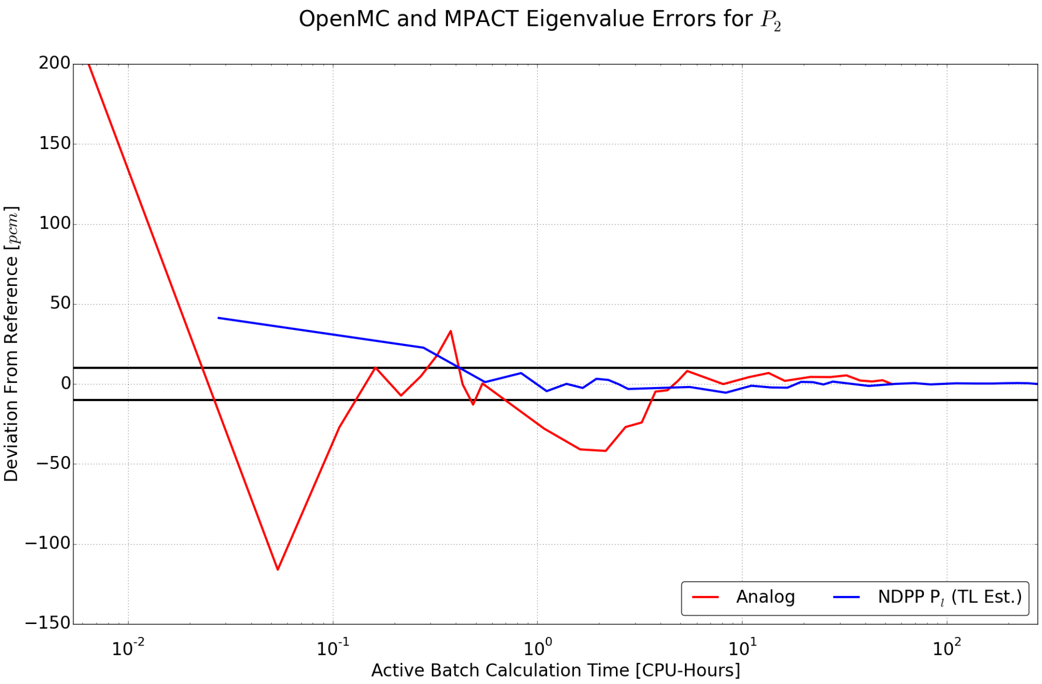

Figure 6.98: Pin Cell Problem k_{eff} Figure-of-Merit Determination

Moving on to the sub-assembly problem, Figure 6.99 shows that the analog method reaches the ten pcm marker at around two hours. Unfortunately, this milestone occurs for the improved method at 10-11 hours. This seems to indicate that the improved method is worse, though it should be noted that the 5 pcm criteria was chosen arbitrarily; if this was increased to 10 pcm, then the improved method would have met the criteria within a few minutes.

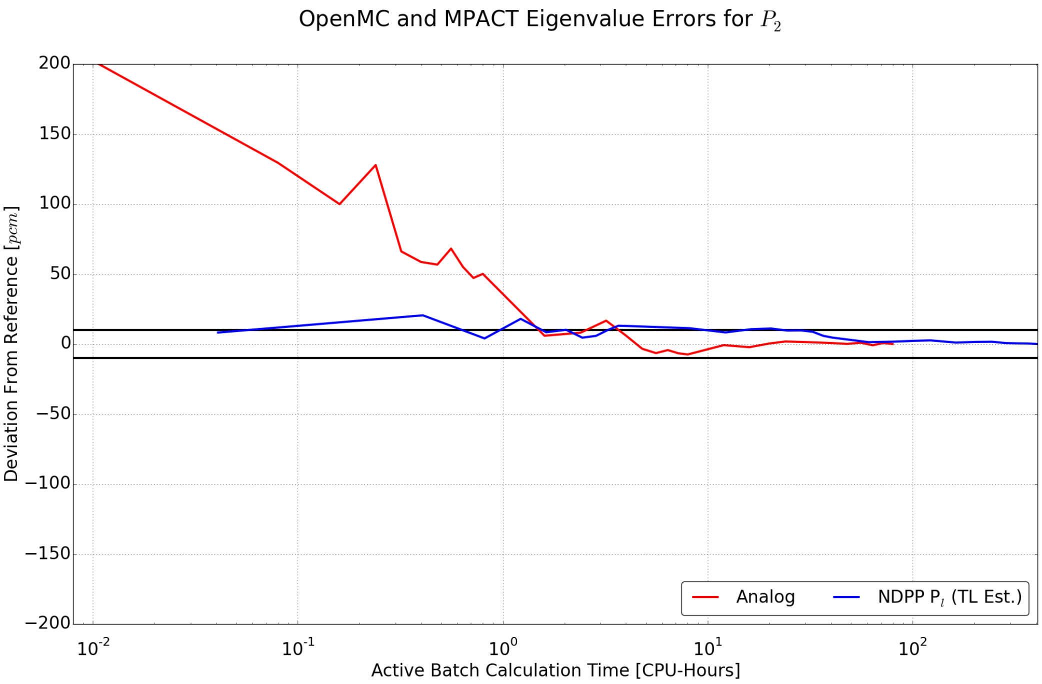

Figure 6.99: Sub-Assembly Problem k_{eff} Figure-of-Merit Determination

Next, Figure 6.100 shows the results for the maximum and root-mean square pin power errors. The solid black horizontal lines are the ± 0.01 percentage point lines. The analog method reaches the maximum pin power error criterion at around 5 hours; the NDPP method reaches the same at 4 hours. This result is not as impressive as the other results, with a savings of only one hour, or twenty percent; this implies more work is necessary to improve the run-time performance of OpenMC when using NDPP-based tallies. Finally, the analog method reaches the root-mean-squared pin power error criterion at around 2.5 hours and the NDPP method reaches this threshold with the very first data point, which was achieved in less than three minutes. This is again an impressive improvement of more than a factor of fifty in the total time required to achieve a result to within a certain level of convergence for all of the pin powers.

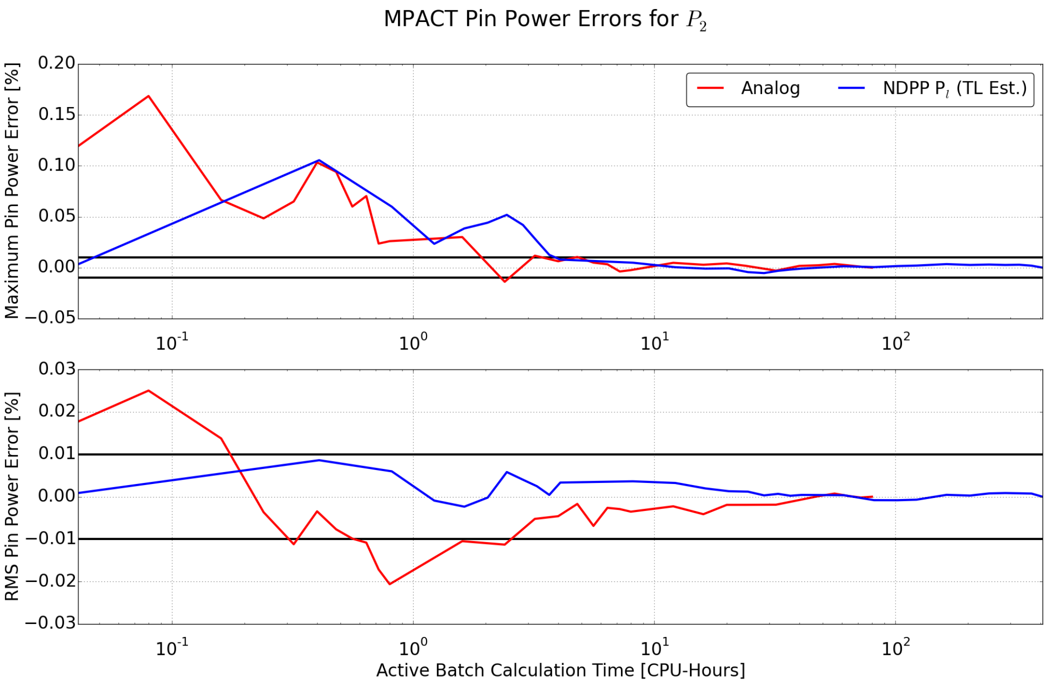

Figure 6.100: Sub-Assembly Problem Maximum Pin Power Figure-of-Merit Determination

6.4 Summary of Results

The goal of this chapter were three-fold:

1. Examine the accuracy of the NDPP data
2. Determine the accuracy of tallies utilizing the NDPP data with the improved method
    - This examination included cross section values, eigenvalues and power distributions resulting from the use of the library
3. Comparing the tallying efficiency of the improved and analog methods
    - This examination included the memory and run-time implications of the improved method, as well as examining the efficiency of cross section values, eigenvalues and power distributions resulting from the use of the library.

For the first item, the NDPP output data matched well with a Monte Carlo tallied reference solution as most data of the scattering distributions were less than the Monte Carlo stochastic uncertainty. Noticeable differences, though still small, were observed with the inelastic continuum case due to different interpolation mechanisms in NDPP and OpenMC.

The tally accuracy examination showed that excellent agreement was observed with the differences being isolated to either when the magnitude of the data in question was very small (and thus percent errors were highly sensitive to differences), or again in cases when tighter integration and interpolation schemes could have been applied such as for the P_2 moment in the fuel for group 14 scattering (Figure (6.42)).

When comparing the eigenvalues after the MC-generated libraries were used in MPACT, a maximum 13 pcm bias was observed between the analog and improved tallying schemes. This bias is due to differences in interpolation schemes (as seen earlier) as well as interpolation and truncation error which is necessarily present in the NDPP-based data.

The tally efficiency comparison showed that the additional memory usage totaled 551 MB for the pin cell problem which included 38 different libraries. Fortunately only 5% of this memory burden was temperature dependent data which will limit the amount that the memory usage scales for realistic problems.

The run-time study showed that using NDPP data with track-length tallies slowed down the history calculation rate by as much as 81%, the majority of which was due to the macroscopic scattering moment tallying. This slow down is an unfortunate side-effect which is only 11% when the NDPP collision tallies are used instead. Since the only difference in code execution for these two different cases is the frequency this data is tallied, its stands to reason that reducing the number of times the tally operation is performed will have a significant impact on the run-time. One means of doing this will be to combine all microscopic data to macroscopic data before the Monte Carlo simulation begins; this will significantly reduce the time spent tallying since there will be one tally event per material as opposed to one per nuclide.

When comparing the convergence of the reported mean and relative uncertainties, it was seen that the improved method did reduce the relative errors; sometimes by more than an order of magnitude. Further, the means approached their converged value with relatively few histories necessary. For some data, this benefit was mostly due to the enabling of track-length scoring while other data benefited tremendously from the reduction in the number of dimensions that had to be stochastically integrated.

Finally, like the mean values of the cross section data, the eigenvalues and pin powers obtained using the improved method converged after sometimes 1% the number of batches necessary for the analog method. This is a tremendous benefit and means that the method performs as it should and meets its goal of reducing the effort required to create MGXS libraries with Monte Carlo. As discussed previously, the method does need work in reducing the run-time as this slow down reduces the convergence benefit just stated. Fortunately the significantly improved tallying efficiency outweighs the run-time penalty such that the method still produces converged solutions hours faster than the currently used state of the art based on analog sampling of the scattering moment matrices.

CHAPTER 7

Summary and Future Work

7.1 Summary

This thesis begins by identifying a need for using Monte Carlo solvers to generate multi-group cross section libraries for deterministic transport. Unfortunately, it has been known (and this work has shown) that the cost in calculating these libraries would be prohibitive, mostly due to the poor tallying efficiency of multi-group scattering moment matrices. To reduce this "long pole in the tent", this work identified a method, called the "improved method" of tallying which reduced the number of dimensions needed to tally these scattering moment matrices. This was done by deterministically scoring the outgoing particle's angular and energy probability distribution functions instead of stochastically sampling them; a process which also adds the possibility of using track-length estimators instead of only collision-based estimators.

Since these distributions are complicated and exist in multiple forms, they must be converted to a useful form before the particle simulation begins. To achieve this, a pre-processor, NDPP, was written. NDPP takes the continuous-energy outgoing energy-angle distributions and integrates over a the outgoing angle and a user-defined energy group structure for a set of incoming energy points. This data will then be interpolated "on-the-fly" during the random walk to reproduce continuous-energy distributions by the downstream Monte Carlo code.

This work then used the NDPP data for both a pin cell and 5x5 subassembly problem and found that the tallying efficiency was significantly improved while only incurring a 13 pcm bias on the value of k_{eff} due to truncation and interpolation errors. Finally, this work noted that the using the improved method with NDPP did hurt the run-time performance of the Monte Carlo code: the pin cell problem, for example, ran 81% slower when using these tallies than when using the traditional analog scheme. Fortunately, this slow down did not outweigh the significant tallying efficiency benefit such that the time needed to yield a k_{eff}

or pin power within a given stochastic error was reduced by as little as 16% and as much as 80% in the cases studied.

These results show that the improved method successfully reduces the time requirement to generate MGXS libraries with a MC solver. This goes a long way towards achieving the goal of a hybrid system where a local MC solver generates MGXS for a global deterministic transport solver. Furthermore, the relative uncertainties in the elements of the scattering moment matrices were significantly reduced, leading to lower design uncertainties applied to all relevant nuclear design products.

7.2 Future Work

The following present possible avenues of improvement of the improved method of tallying and the pre-processor, NDPP, in general.

7.2.1 Improved Energy Interpolation Techniques

The improved method with the NDPP pre-processor is unfortunately a memory intensive proposition. The majority of the memory usage for an isothermal case is due to the number of points necessary to provide for accurate interpolation of the temperature independent inelastic scattering data. To relax this burden, effort should be expended to reduce the number of points needed by investigating higher-order interpolation techniques such as interpolating polynomials or spline interpolation. This would be especially useful for use-cases desiring a very fine group structure.

7.2.2 Explore Temperature Interpolation Techniques

When considering problems with multiple temperatures (which is expected to be the majority of cases analyzed), it may become possible for the temperature-dependent (elastic) data to become prohibitively large. Since the elastic data is quite small in memory (generally less than 0.75 MB per Table 6.2), then this would become an issue only if interpolating between temperature tables requires the NDPP data to be generated on a very fine temperature grid. The desired grid spacing nor the type of interpolation to use has not yet been investigated.

7.2.3 Improving Tallying Performance with NDPP Data

This work limited itself to implementing a method which can be applied to generate either nuclide or material-specific (or both) cross-section libraries. Unfortunately this decision meant that some efficiency gains which can only be applied to one of the two paths were not undertaken. The biggest impact of this was that the NDPP data was that the run-time can be increased significantly for the case of generating material-specific cross-sections by combining the isotopic data into one set of data to tally for each material in the problem. The addition of this capability would mean not having to fetch and sum the data for every nuclide at tally time and thus would reduce the time spent in tallies and thus could significantly speed up the NDPP-based tallying scheme.

To estimate the impact of this change, the pin cell and sub-assembly timing studies were re-run, but this time the improved method tallies only tallied data for one nuclide per material. This was done to simulate what the computational burden would be if there was only one set of NDPP data to tally per material as opposed to one set of NDPP data to tally for every nuclide in a material. The resultant slow down factors of this study are shown in Table 7.1 and show that the run-time increased substantially, as expected. This would be immediately useful in the case of this work's over-arching goal of a hybrid Monte Carlo/deterministic transport system where the MC solver is used to generate local MGXS. In addition, if an organization's current cross-section generation strategy does include material-wise cross-sections (likely as part of some hybrid strategy) then this path should be explored to significantly increase the figure-of-merit of this improved method of tallying.

Table 7.1: Material-Based Data Run-Time Improvement

Case	Pin Cell Slow Down	Sub-Assembly Slow Down
Original NDPP Track-Length	81%	81%
Modified NDPP Track-Length	46%	57%

7.2.4 Examine Other Areas of Potential Benefit

The benefits of the method have not yet been applied to areas besides cross section generation for deterministic neutron transport. One area outside of just generating libraries is to further accelerate hybrid Monte Carlo/deterministic schemes to reduce the number of total batches necessary to achieve a desired result. Another area thus far has not yet considered is to generate this source term to reduce the number of total batches necessary in coupled neutron-gamma problems.

APPENDIX A

Model Descriptions

The work discussed in this dissertation is focused on the generation of a multi-group cross section library by a Monte Carlo solver. Typical LWR cross section generation problems are as small as single fuel pins (in an infinite lattice of similar pins) or as large as a few assemblies. This work will explore the single fuel pin model as well as an intermediate-sized five-by-five grid of pins with large spatial heterogeneity mimic important features of the multiple assembly case.

The Consortium for Advanced Simulation of Light Water Reactors (CASL) program has produced a series of core physics benchmark problems designed to "...assist software and methods developers and analysts in progressing through capabilities needed to model U.S. nuclear power reactors and their operations" [38]. This benchmark suite includes eight classes of problems, from pin cells up to simulating full-core zero power physics test through life and a plant startup evolution including thermal-feedback and short-term depletion (i.e., xenon and samarium) capabilities. This CASL suite of models is the source of the two models used in this analysis. The pin cell model corresponds exactly to problem 1B defined on page 20 of the CASL benchmark document, reference [38]. The five-by-five, or sub-assembly, problem is composed of 2.619% enriched (by-weight) UO_2 fuel pins, guide tubes and Pyrex rods all as described in reference [38]. A description of each of these problems and their modeling in both OpenMC and MPACT will be described in the sections which follow.

A.1 Pin-Cell Model

The geometric and material definition of this pin cell is Problem 1B as defined by the CASL benchmark series of problems. The fuel rod parameters are based on publicly available information about the initial loading of the Watts Bar Nuclear 1 core, with supplemental information provided from similar core designs where needed.

The fuel in this rod is 3.1% (by weight) enriched UO_2 with a density of 10.257 g/cc. The fuel pellet itself has a radius of 0.4096 cm. A ^4He gap surrounds the fuel pin. The rod is clad in Zircaloy-4 with many alloying elements included as well as impurities, such as hafnium isotopes; the density of this Zircaloy is 6.56 g/cc. Finally, the moderator is light water with 1300 ppm of boric acid; no deuterium is modeled. The density of this moderator is 0.661 g/cc. The pin cell is isothermal and modeled at 600K; the densities are consistent with this temperature. This material information is provided in Table A.1 and the geometric information is provided in Table A.2.

Table A.1: Pin Cell Geometry Definition

Quantity	Dimension [cm]
Pellet Radius	0.4096
Inner Clad Radius	0.418
Outer Clad Radius	0.475
Rod Pitch	1.26

Table A.2: Pin Cell Material Definition

Material	Isotope	Atom Density $\left[\frac{\#}{barn-cm}\right]$	Isotope	Atom Density $\left[\frac{\#}{barn-cm}\right]$
Fuel	^{234}U	6.11864E-6	^{238}U	2.21546E-2
(3.1% enriched)	^{235}U	7.18132E-4	^{16}O	4.57642E-2
	^{236}U	3.29861E-6		
Cladding	^{90}Zr	2.18865E-2	^{54}Fe	8.68307E-6
(Zircaloy-4)	^{91}Zr	4.77292E-3	^{56}Fe	1.36306E-4
	^{92}Zr	7.29551E-3	^{57}Fe	3.14789E-6
	^{94}Zr	7.39335E-3	^{58}Fe	4.18926E-7
	^{96}Zr	1.19110E-3	^{50}Cr	3.30121E-6
	^{112}Sn	4.68066E-6	^{52}Cr	6.36606E-5
	^{114}Sn	3.18478E-6	^{53}Cr	7.21860E-6
	^{115}Sn	1.64064E-6	^{54}Cr	1.79686E-6
	^{116}Sn	7.01616E-5	^{174}Hf	3.54138E-9
	^{117}Sn	3.70592E-5	^{176}Hf	1.16423E-7
	^{118}Sn	1.16872E-4	^{177}Hf	4.11686E-7
	^{119}Sn	4.14504E-5	^{178}Hf	6.03806E-7
	^{120}Sn	1.57212E-4	^{179}Hf	3.01460E-7
	^{122}Sn	2.23417E-5	^{180}Hf	7.76449E-7
	^{124}Sn	2.79392E-5		
Moderator	^{1}H	4.41459E-2	^{10}B	9.52537E-6
(Borated Water)	^{16}O	2.20729E-2	^{11}B	3.83408E-5

This model was set up in OpenMC [17] without geometric or material approximation. The 600K continuous-energy data was provided by the ENDF/B-VII.0 ACE library which ships with the RSICC version of MCNP (versions 5 and 6) [23]. The problem was run with 10,000 particles per batch, 1,900 inactive batches and 100,000 active batches for a total of one billion histories simulated which contribute to the tallies.

MGXS libraries were tallied in macroscopic format with one tally region set up per region of the pin cell. This corresponds to one set of macroscopic tallies per material since this model has the same number of geometric entities as materials. This is not ideal as doing so ignores the spatial dependence of resonance self-shielding. Doing so is acceptable for this study because it does not affect the success determination of the proposed method. In general, if track-length tallies could be utilized then they were; if not collision estimators were used.

1. The total, fission production, and fission energy production (Σ_t, $\nu\Sigma_f$, and $\kappa\Sigma_f$ respectively) reaction rates were tallied with a track-length estimator.
   (a) These were tallied with an incoming energy filter applied.
2. The scattering production P_2 matrices are tallied with a collision estimator of using the previous analog method, and either a collision or track-length estimator of using the NDPP-based improved method.
   (a) Scattering production was used vice scattering to maintain a neutron economy as consistent as possible with the MC reference solution.
   (b) The analog method of scattering production moment tallying is enabled with the “nu-scatter-p2” score type.
   (c) Similarly, the NDPP method is enabled with the “ndpp-nu-scatter-p2”.
   (d) The “analog” keyword in the estimator tag simply means an analog, or collision, estimator is used vice a track-length estimator; the use of “analog” here does not mean the analog method of tallying scattering moments was used.
   (e) These were tallied with both an incoming energy and outgoing energy filter applied in order to produce the scattering matrix.
3. The fission energy spectrum was determined with the “nu-fission” score.
   (a) This score was tallied with both an incoming and outgoing energy filter applied; the outgoing filter bins matched the individual group boundaries while the incoming just supplied the minimum and maximum energies.

    (b) This tally can only be tallied with a collision estimator.

4. A collision and track-length estimate of the flux were tallied as necessary for consistency with the reaction rate estimators used.
    (a) These were tallied with only an incoming energy filter applied.

OpenMC requires separate files to define geometry, materials, tallies and general settings information. A set of input files used to model this case with all the different tally types necessary for the studies within this work are provided below.

Listing A.1: OpenMC Pin Cell Geometry File

```xml
<?xml version="1.0"?>
<geometry>

  <!--
    Define fuel pellet radius (1), clad inner radius (2), and
    clad outer radius (3)
  -->

  <surface id="1" type="z-cylinder" coeffs="0. 0. 0.4096" />
  <surface id="2" type="z-cylinder" coeffs="0. 0. 0.4180" />
  <surface id="3" type="z-cylinder" coeffs="0. 0. 0.4750" />

  <!-- Reflective surfaces on outside of pin-cell. -->
  <surface id="20" type="x-plane" coeffs="-0.63" boundary="reflective"/>
  <surface id="21" type="x-plane" coeffs=" 0.63" boundary="reflective"/>
  <surface id="22" type="y-plane" coeffs="-0.63" boundary="reflective"/>
  <surface id="23" type="y-plane" coeffs=" 0.63" boundary="reflective"/>

  <!-- Combine to surfaces to make pin cell -->
  <cell id="1"  material="1" surfaces="  -1" />
  <cell id="2"  material="2" surfaces="1 -2" />
  <cell id="3"  material="3" surfaces="2 -3" />
  <cell id="4"  material="4" surfaces="3 20 -21 22 -23" />

</geometry>
```

Listing A.2: OpenMC Pin Cell Materials File

```xml
<?xml version="1.0"?>
<materials>
  <!-- Set default xs set to 71c, which is ENDF-B/VII.0 at 600K -->
  <default_xs>71c</default_xs>

  <!-- 3.1 w/o enriched UO2 -->
  <material id="1">
    <density units="sum" />
    <nuclide name="U-234"   ao="6.11864E-6" />
    <nuclide name="U-235"   ao="7.18132E-4" />
    <nuclide name="U-236"   ao="3.29861E-6" />
```

```
    <nuclide name="U-238"   ao="2.21546E-2" />
    <nuclide name="O-16"    ao="4.57642E-2" />
  </material>

  <!-- Gap -->
  <material id="2">
    <density units="sum" />
    <nuclide name="He-4" ao="2.68714E-5" />
  </material>

  <!-- Cladding -->
  <material id="3">
    <density units="sum" />
    <nuclide name="Zr-90"  ao="2.18865E-2" />
    <nuclide name="Zr-91"  ao="4.77292E-3" />
    <nuclide name="Zr-92"  ao="7.29551E-3" />
    <nuclide name="Zr-94"  ao="7.39335E-3" />
    <nuclide name="Zr-96"  ao="1.19110E-3" />
    <nuclide name="Sn-112" ao="4.68066E-6" />
    <nuclide name="Sn-114" ao="3.18478E-6" />
    <nuclide name="Sn-115" ao="1.64064E-6" />
    <nuclide name="Sn-116" ao="7.01616E-5" />
    <nuclide name="Sn-117" ao="3.70592E-5" />
    <nuclide name="Sn-118" ao="1.16872E-4" />
    <nuclide name="Sn-119" ao="4.14504E-5" />
    <nuclide name="Sn-120" ao="1.57212E-4" />
    <nuclide name="Sn-122" ao="2.23417E-5" />
    <nuclide name="Sn-124" ao="2.79392E-5" />
    <nuclide name="Fe-54"  ao="8.68307E-6" />
    <nuclide name="Fe-56"  ao="1.36306E-4" />
    <nuclide name="Fe-57"  ao="3.14789E-6" />
    <nuclide name="Fe-58"  ao="4.18926E-7" />
    <nuclide name="Cr-50"  ao="3.30121E-6" />
    <nuclide name="Cr-52"  ao="6.36606E-5" />
    <nuclide name="Cr-53"  ao="7.21860E-6" />
    <nuclide name="Cr-54"  ao="1.79686E-6" />
    <nuclide name="Hf-174" ao="3.54138E-9" />
    <nuclide name="Hf-176" ao="1.16423E-7" />
    <nuclide name="Hf-177" ao="4.11686E-7" />
    <nuclide name="Hf-178" ao="6.03806E-7" />
    <nuclide name="Hf-179" ao="3.01460E-7" />
    <nuclide name="Hf-180" ao="7.76449E-7" />
</material>

  <!-- Water -->
  <material id="4">
    <density units="sum" />
    <nuclide name="O-16"   ao="2.20729E-2" />
    <nuclide name="H-1"    ao="4.41459E-2" />
    <nuclide name="B-10"   ao="9.52537E-6" />
    <nuclide name="B-11"   ao="3.83408E-5" />
    <!--
      Set the thermal scattering table to H-H20
      16t is the library for 600K
    -->
```

```
    <sab name="lwtr" xs="16t" />
  </material>

</materials>
```

Listing A.3: OpenMC Pin Cell Tallies File

```
<?xml version="1.0"?>
<tallies>
  <tally>
    <id>1</id>
    <filter>
      <type>cell</type>
      <bins> 1 2 3 4 </bins>
    </filter>
    <filter>
      <type>energy</type>
      <bins>
        0.0000E0   1.2396E-8 3.0613E-8 4.2755E-8 5.6922E-8 8.1968E-8
        1.1157E-7 1.4572E-7 1.8443E-7 2.7052E-7 3.5767E-7 5.0323E-7
        6.2506E-7 7.8208E-7 9.1000E-7 9.7100E-7 1.0137E-6 1.0722E-6
        1.1254E-6 1.1664E-6 1.2351E-6 1.4574E-6 1.8554E-6 2.3824E-6
        3.9279E-6 4.4509E-6 5.0435E-6 5.7150E-6 6.4760E-6 7.3382E-6
        8.3153E-6 1.2099E-5 1.3710E-5 2.9023E-5 4.7851E-5 7.8893E-5
        1.3007E-4 2.0347E-3 9.1188E-3 6.7379E-2 1.8316E-1 4.9787E-1
        8.2085E-1 1.3534     2.2313     3.6788     6.0653     20.0
      </bins>
    </filter>
    <scores>
       total
       kappa-fission
       nu-fission
       flux
    </scores>
    <estimator>tracklength</estimator>
  </tally>

  <tally>
    <id>2</id>
    <filter>
     <type>cell</type>
       <bins> 1 2 3 4 </bins>
    </filter>
    <filter>
      <type>energy</type>
      <bins>
        0.0000E0   1.2396E-8 3.0613E-8 4.2755E-8 5.6922E-8 8.1968E-8
        1.1157E-7 1.4572E-7 1.8443E-7 2.7052E-7 3.5767E-7 5.0323E-7
        6.2506E-7 7.8208E-7 9.1000E-7 9.7100E-7 1.0137E-6 1.0722E-6
        1.1254E-6 1.1664E-6 1.2351E-6 1.4574E-6 1.8554E-6 2.3824E-6
        3.9279E-6 4.4509E-6 5.0435E-6 5.7150E-6 6.4760E-6 7.3382E-6
        8.3153E-6 1.2099E-5 1.3710E-5 2.9023E-5 4.7851E-5 7.8893E-5
        1.3007E-4 2.0347E-3 9.1188E-3 6.7379E-2 1.8316E-1 4.9787E-1
        8.2085E-1 1.3534     2.2313     3.6788     6.0653     20.0
      </bins>
```

```
    </filter>
    <filter>
      <type>energyout</type>
      <bins>
        0.0000E0  1.2396E-8 3.0613E-8 4.2755E-8 5.6922E-8 8.1968E-8
        1.1157E-7 1.4572E-7 1.8443E-7 2.7052E-7 3.5767E-7 5.0323E-7
        6.2506E-7 7.8208E-7 9.1000E-7 9.7100E-7 1.0137E-6 1.0722E-6
        1.1254E-6 1.1664E-6 1.2351E-6 1.4574E-6 1.8554E-6 2.3824E-6
        3.9279E-6 4.4509E-6 5.0435E-6 5.7150E-6 6.4760E-6 7.3382E-6
        8.3153E-6 1.2099E-5 1.3710E-5 2.9023E-5 4.7851E-5 7.8893E-5
        1.3007E-4 2.0347E-3 9.1188E-3 6.7379E-2 1.8316E-1 4.9787E-1
        8.2085E-1 1.3534    2.2313    3.6788    6.0653    20.0
      </bins>
    </filter>
    <scores>
      nu-scatter-p2
      ndpp-nu-scatter-p2
    </scores>
    <estimator>analog</estimator>
  </tally>

  <tally>
    <id>3</id>
    <filter>
     <type>cell</type>
      <bins> 1 2 3 4 </bins>
    </filter>
    <filter>
      <type>energy</type>
      <bins>
        0.0000E0  1.2396E-8 3.0613E-8 4.2755E-8 5.6922E-8 8.1968E-8
        1.1157E-7 1.4572E-7 1.8443E-7 2.7052E-7 3.5767E-7 5.0323E-7
        6.2506E-7 7.8208E-7 9.1000E-7 9.7100E-7 1.0137E-6 1.0722E-6
        1.1254E-6 1.1664E-6 1.2351E-6 1.4574E-6 1.8554E-6 2.3824E-6
        3.9279E-6 4.4509E-6 5.0435E-6 5.7150E-6 6.4760E-6 7.3382E-6
        8.3153E-6 1.2099E-5 1.3710E-5 2.9023E-5 4.7851E-5 7.8893E-5
        1.3007E-4 2.0347E-3 9.1188E-3 6.7379E-2 1.8316E-1 4.9787E-1
        8.2085E-1 1.3534    2.2313    3.6788    6.0653    20.0
      </bins>
    </filter>
    <scores>
      flux
    </scores>
    <estimator>analog</estimator>
  </tally>

  <tally>
    <id>4</id>
    <filter>
     <type>cell</type>
       <bins> 1 2 3 4 </bins>
    </filter>
    <filter>
      <type>energy</type>
      <bins>
```

```
        0.0000E0  1.2396E-8 3.0613E-8 4.2755E-8 5.6922E-8 8.1968E-8
        1.1157E-7 1.4572E-7 1.8443E-7 2.7052E-7 3.5767E-7 5.0323E-7
        6.2506E-7 7.8208E-7 9.1000E-7 9.7100E-7 1.0137E-6 1.0722E-6
        1.1254E-6 1.1664E-6 1.2351E-6 1.4574E-6 1.8554E-6 2.3824E-6
        3.9279E-6 4.4509E-6 5.0435E-6 5.7150E-6 6.4760E-6 7.3382E-6
        8.3153E-6 1.2099E-5 1.3710E-5 2.9023E-5 4.7851E-5 7.8893E-5
        1.3007E-4 2.0347E-3 9.1188E-3 6.7379E-2 1.8316E-1 4.9787E-1
        8.2085E-1 1.3534    2.2313    3.6788    6.0653    20.0
      </bins>
    </filter>
    <filter>
      <type>energyout</type>
      <bins>
        0.0000E0  1.2396E-8 3.0613E-8 4.2755E-8 5.6922E-8 8.1968E-8
        1.1157E-7 1.4572E-7 1.8443E-7 2.7052E-7 3.5767E-7 5.0323E-7
        6.2506E-7 7.8208E-7 9.1000E-7 9.7100E-7 1.0137E-6 1.0722E-6
        1.1254E-6 1.1664E-6 1.2351E-6 1.4574E-6 1.8554E-6 2.3824E-6
        3.9279E-6 4.4509E-6 5.0435E-6 5.7150E-6 6.4760E-6 7.3382E-6
        8.3153E-6 1.2099E-5 1.3710E-5 2.9023E-5 4.7851E-5 7.8893E-5
        1.3007E-4 2.0347E-3 9.1188E-3 6.7379E-2 1.8316E-1 4.9787E-1
        8.2085E-1 1.3534    2.2313    3.6788    6.0653    20.0
      </bins>
    </filter>
    <scores>
      ndpp-nu-scatter-p2
    </scores>
    <estimator>tracklength</estimator>
  </tally>

  <tally>
    <id>5</id>
    <filter>
     <type>cell</type>
      <bins> 1 2 3 4 </bins>
    </filter>
    <filter>
      <type>energy</type>
      <bins> 0.0 20.0 </bins>
    </filter>
    <filter>
      <type>energyout</type>
      <bins>
        0.0000E0  1.2396E-8 3.0613E-8 4.2755E-8 5.6922E-8 8.1968E-8
        1.1157E-7 1.4572E-7 1.8443E-7 2.7052E-7 3.5767E-7 5.0323E-7
        6.2506E-7 7.8208E-7 9.1000E-7 9.7100E-7 1.0137E-6 1.0722E-6
        1.1254E-6 1.1664E-6 1.2351E-6 1.4574E-6 1.8554E-6 2.3824E-6
        3.9279E-6 4.4509E-6 5.0435E-6 5.7150E-6 6.4760E-6 7.3382E-6
        8.3153E-6 1.2099E-5 1.3710E-5 2.9023E-5 4.7851E-5 7.8893E-5
        1.3007E-4 2.0347E-3 9.1188E-3 6.7379E-2 1.8316E-1 4.9787E-1
        8.2085E-1 1.3534    2.2313    3.6788    6.0653    20.0
      </bins>
    </filter>
    <scores>
      nu-fission
    </scores>
```

```
    <estimator>analog</estimator>
  </tally>

  <assume_separate>false</assume_separate>

  <ndpp_library>/home/nelsonag/cases/diss/ndpp/47g/ndpp_lib.xml</ndpp_library>

</tallies>
```

Listing A.4: OpenMC Pin Cell Settings File

```
<?xml version="1.0"?>
<settings>

  <!--
    Define how many particles to run and for how many batches
    in an eigenvalue calculation mode
  -->
  <eigenvalue>
    <batches>101900</batches>
    <inactive>1900</inactive>
    <particles>10000</particles>
  </eigenvalue>

  <!--
    Start with uniformally distributed neutron source
    with the default energy spectrum of a Maxwellian
    and isotropic distribution.
  -->
  <source>
    <space type="box">
      <parameters>
        -0.63 -0.63 -1E50
         0.63  0.63  1E50
      </parameters>
    </space>
  </source>

  <!-- Establish statepoints to aid in examining convergence -->
  <state_point>
    <batches>
      1910 2000 2100 2200 2300 2400 2500 2600 2700 2800 2900
      3900 4900 5900 6900 7900 8900 9900 10900 11900
      16900 21900 26900 31900 41900 51900 61900 71900 81900 91900 101900
    </batches>
    <source_write>true</source_write>
  </state_point>

  <output>
    <cross_sections>true</cross_sections>
    <summary>true</summary>
    <tallies>false</tallies>
  </output>

  <cross_sections>/home/nelsonag/cases/diss/endf70.xml</cross_sections>
```

```

</settings>
```

Finally, the matching MPACT input file is provided below. In this model, a ray spacing of 0.005 cm is used. The angular quadrature is Chebyshev-Yamamoto (with 32 azimuthal and 3 polar angles). The fission source and eigenvalue are converged to 10^{-6}.

Listing A.5: MPACT Pin Cell Input File

```
CASEID p2

MATERIAL
   mat  1 2 :: m1
   mat  2 2 :: m2
   mat  3 2 :: m3
   mat  4 0 :: m4

GEOM
  !Ray tracing module dimensions
  mod_dim 1.26 1.26 1.0

  !Pin mesh
  pinmesh 1 cyl 0.4096 0.4180 0.475 0.575 / 1.26 /  1.0  / 10 2 2 10 / 10*8 2*8 2*8 10*8 1 / 1

  pin 1 1 / 1 2 3 4 4

 !Pin modular ray tracing
  module 1 3*1
   1

  !Define lattices, assemblies and core
  lattice 1 2*1
   1

  assembly 1
   1

  core 360
   1

XSEC
   addpath ./
   xslib USER data.xs

OPTION
   bound_cond 1 1 1 1 1 1
   solver 1 2
   ray 0.005 CHEBYSHEV-YAMAMOTO 16 3
   parallel 1 1 1 4
   conv_crit 2*1.e-6
   iter_lim 2000 2 3
   vis_edits F
   validation T
```

```
  cmfd T
  scatt_meth P2
.
```

In this case, the materials are listed as simply being m1, m2, m3, and m4. These are code names needed for an external python script to use; this script takes the OpenMC tally data, normalizes by flux as necessary and prints out data in a format that MPACT expects.

A.2 Sub-Assembly Model

The sub-assembly model was developed to provide a problem which would challenge both the analog and improved methods of tallying described in this work. To that end, a problem was needed which had high spatial fidelity of the tallying regions and a highly anisotropic nature. As is usually the case, a smaller problem was needed to accommodate the high spatial fidelity. Therefore a 5x5 sub-assembly cluster of pin-cells was chosen, with guide tubes and Pyrex poison added within the grid in order to induce the desired degree of anisotropy. This five-by-five grid has a total of four guide tube locations located on the diagonals of the second ring; two of the guide tubes opposite each other contain the Pyrex poison rods. Figure A.1 provides a view of this sub-assembly pin lay-down. This image was produced by OpenMC and each color represents the different materials in use (as identified in Table A.2). The red areas are the 2.619% enriched fuel, the location of the Pyrex is shown with black, steel is shown in light gray, zircaloy cladding regions are green, moderator regions are blue, and helium-filled regions are white. Reflective boundary conditions are assigned on all problem boundaries.

Each of the fuel pins, guide tubes, and Pyrex rods are exactly as defined by the CASL benchmark specifications. This model was modeled at 600K and 1300ppm boron, but the coolant density was set to 0.743 g/cc, corresponding to 565K at 2250 psia; 600K was used by CASL as the data temperature to be consistent with the libraries available at the time. Table A.2 contains the material properties used for all the materials. The fuel, guide tube, and Pyrex geometries are provided in Table A.5. All pins have a pitch of 1.26 cm. The fuel rod is as was defined in the pin-cell problem. The guide tube is simply a cylinder of Zircaloy-4 with water inside and out. The Pyrex rods are fixed inserts located in the guide tube locations and contain the borosilicate glass clad on both the inner and outer annuli with Stainless Steel 304.

Table A.3: Sub-Assembly Material Definition

Material	Isotope	Atom Density $\left[\frac{\#}{barn-cm}\right]$	Isotope	Atom Density $\left[\frac{\#}{barn-cm}\right]$
Fuel (2.619% enriched)	^{234}U	5.09503E-6	^{238}U	2.22663E-2
	^{235}U	6.06709E-4	^{16}O	4.57617E-2
	^{236}U	2.76809E-6		
Gap	^{4}He	2.68714E-5		
Cladding (Zircaloy-4)	^{90}Zr	2.18865E-2	^{54}Fe	8.68307E-6
	^{91}Zr	4.77292E-3	^{56}Fe	1.36306E-4
	^{92}Zr	7.29551E-3	^{57}Fe	3.14789E-6
	^{94}Zr	7.39335E-3	^{58}Fe	4.18926E-7
	^{96}Zr	1.19110E-3	^{50}Cr	3.30121E-6
	^{112}Sn	4.68066E-6	^{52}Cr	6.36606E-5
	^{114}Sn	3.18478E-6	^{53}Cr	7.21860E-6
	^{115}Sn	1.64064E-6	^{54}Cr	1.79686E-6
	^{116}Sn	7.01616E-5	^{174}Hf	3.54138E-9
	^{117}Sn	3.70592E-5	^{176}Hf	1.16423E-7
	^{118}Sn	1.16872E-4	^{177}Hf	4.11686E-7
	^{119}Sn	4.14504E-5	^{178}Hf	6.03806E-7
	^{120}Sn	1.57212E-4	^{179}Hf	3.01460E-7
	^{122}Sn	2.23417E-5	^{180}Hf	7.76449E-7
	^{124}Sn	2.79392E-5		
Moderator (Borated Water)	^{1}H	4.96224E-2	^{10}B	1.07070E-5
	^{16}O	2.48112E-2	^{11}B	4.30971E-5
Pyrex	^{28}Si	1.81980E-2	^{10}B	9.63266E-4
	^{29}Si	9.24474E-4	^{11}B	3.90172E-3
	^{30}Si	6.10133E-4	^{16}O	4.67761E-2
Stainless Steel (304)	Natural C	3.20895E-4	^{54}Fe	3.44776E-3
	^{28}Si	1.58197E-3	^{56}Fe	5.41225E-2
	^{29}Si	8.03653E-5	^{57}Fe	1.24992E-3
	^{30}Si	5.30394E-5	^{58}Fe	1.66342E-4
	^{31}P	6.99938E-5	^{58}Ni	5.30854E-3
	^{50}Cr	7.64915E-4	^{60}Ni	2.04484E-3
	^{52}Cr	1.47506E-2	^{61}Ni	8.88879E-5
	^{53}Cr	1.67260E-3	^{62}Ni	2.83413E-4
	^{54}Cr	4.16346E-4	^{64}Ni	7.21770E-5
	^{55}Mn	1.75387E-3		

Table A.5: Sub-Assembly Geometry Definition

	Quantity	Dimension [cm]
Fuel Rod	Pellet Radius	0.4096
	Inner Clad Radius	0.418
	Outer Clad Radius	0.475
	Rod Pitch	1.26
Guide Tube	Inner Radius	0.561
	Outer Radius	0.602
Pyrex	Inner Tube Inner Radius	0.214
	Inner Tube Outer Radius	0.231
	Pyrex Inner Radius	0.241
	Pyrex Outer Radius	0.427
	Cladding Inner Radius	0.437
	Cladding Outer Radius	0.484

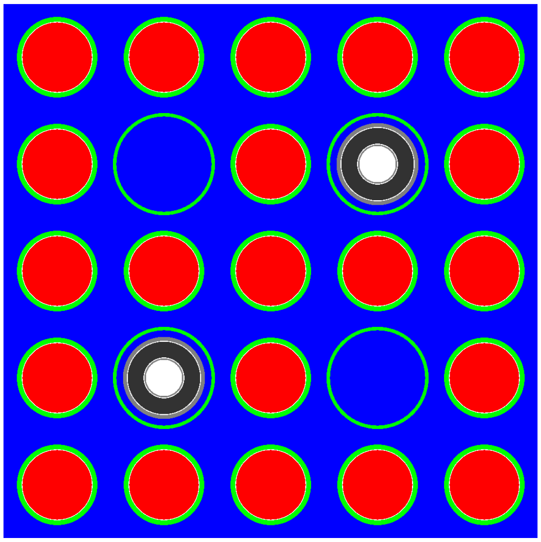

Figure A.1: Sub-Assembly Model

Like the pin cell model, this model was set up in OpenMC [17] without geometric or material approximation. The same 600K continuous-energy ACE data was used. The problem was run with 10,000 particles per batch, 900 inactive batches and 100,000 active batches for a total of one billion histories simulated which contribute to the tallies.

The calculated OpenMC eigenvalue is $0.905095 \pm 2.6 \times 10^-5$. The OpenMC-generated pin power distribution is shown in Table A.6 and the uncertainties are shown in Table A.7. As expected, the power is pushed towards outside the water-filled guide tube due to the high moderation present there and pulled away from the regions outside the Pyrex pins.

Table A.6: Sub-Assembly Normalized Pin Powers

1.0739	1.0775	1.0000	0.9193	0.9389
1.0775	0.0000	0.9856	0.0000	0.9195
0.9999	0.9860	0.9896	0.9857	0.9998
0.9197	0.0000	0.9858	0.0000	1.0776
0.9395	0.9196	0.9998	1.0776	1.0736

Table A.7: Sub-Assembly Normalized Pin Power Uncertainties [%]

0.0420	0.0390	0.0360	0.0341	0.0382
0.0387	0.0000	0.0307	0.0000	0.0316
0.0358	0.0304	0.0303	0.0306	0.0330
0.0340	0.0000	0.0305	0.0000	0.0355
0.0382	0.0315	0.0332	0.0355	0.0383

The OpenMC input files used to model this sub-assembly problem are provided below. For this problem, the tallies were set up so that each material within each pin produced its own tallies. Further, to increase the spatial fidelity of the tallied cross section library, the fuel and Pyrex materials were subdivided into five and two (respectively) tally regions of equal volume. This method netted a total of 194 total tally regions, each capturing data to generate all the different macroscopic MGXS types.

Listing A.6: OpenMC Sub-Assembly Geometry File

```
<?xml version=”1.0”?>
<geometry>
<!--
  This represents the following layout of Fuel (F), Guide Tube (GT)
  and Pyrex (PY):
```

```
    F F  F F  F
    F GT F PY F
    F F  F F  F
    F PY F GT F
    F F  F F  F
  -->

<!--
    The first index of surface number will be the pin type:
    1 if fuel, 2 if guide tube, 3 if pyrex.
    The next digit is the surface index.

    For tallying purposes the fuel pins will contain 5 additional rings
    in the fuel.
    The pyrex pins will contain 2 additional rings inside the Pyrex material.
    All of these tallying rings will be equi-volume.
-->

  <!-- Fuel Pin Surfaces-->
  <!-- First, our 5 equivolume rings -->
  <surface id="11" type="z-cylinder" coeffs="0. 0. 0.1832" />
  <surface id="12" type="z-cylinder" coeffs="0. 0. 0.2591" />
  <surface id="13" type="z-cylinder" coeffs="0. 0. 0.3173" />
  <surface id="14" type="z-cylinder" coeffs="0. 0. 0.3664" />
  <surface id="15" type="z-cylinder" coeffs="0. 0. 0.4096" />
  <surface id="16" type="z-cylinder" coeffs="0. 0. 0.4180" />
  <surface id="17" type="z-cylinder" coeffs="0. 0. 0.4750" />

  <!-- Guide tube Surfaces -->
  <surface id="21" type="z-cylinder" coeffs="0. 0. 0.5610" />
  <surface id="22" type="z-cylinder" coeffs="0. 0. 0.6020" />

  <!-- Pyrex rod Surfaces -->
  <!-- Will use guide tube surfaces for the containing clad -->
  <surface id="31" type="z-cylinder" coeffs="0. 0. 0.2140" />
  <surface id="32" type="z-cylinder" coeffs="0. 0. 0.2310" />
  <surface id="33" type="z-cylinder" coeffs="0. 0. 0.2410" />
  <surface id="34" type="z-cylinder" coeffs="0. 0. 0.3467" />
  <surface id="35" type="z-cylinder" coeffs="0. 0. 0.4270" />
  <surface id="36" type="z-cylinder" coeffs="0. 0. 0.4370" />
  <surface id="37" type="z-cylinder" coeffs="0. 0. 0.4840" />

  <!--
      Build 25 pins, starting with lower left and index (1,1)
      Each of the 25 pins will be defined separately so they have their own cell
      ids.
      The pins are numbered such that 11 is pin (1,1); with indices counting from
      the bottom left to the upper right
      Therefore the grid will look like:
      15 25 35 45 55
      14 24 34 44 54
      13 23 33 43 53
      12 22 32 42 52
      11 21 31 41 51

```

```
    This makes up the 1st two digits of the cell id;
    the last two are the material number.
    The universe number will simply be this 2 digit location index.
  −−>

<!−− Bottom Row, Row 1 −−>
  <cell id=”1101”  universe=”11” material=”1” surfaces=”   −11” />
  <cell id=”1102”  universe=”11” material=”1” surfaces=”11 −12” />
  <cell id=”1103”  universe=”11” material=”1” surfaces=”12 −13” />
  <cell id=”1104”  universe=”11” material=”1” surfaces=”13 −14” />
  <cell id=”1105”  universe=”11” material=”1” surfaces=”14 −15” />
  <cell id=”1106”  universe=”11” material=”2” surfaces=”15 −16” />
  <cell id=”1107”  universe=”11” material=”3” surfaces=”16 −17” />
  <cell id=”1108”  universe=”11” material=”4” surfaces=”17” />

  <cell id=”2101”  universe=”21” material=”1” surfaces=”   −11” />
  <cell id=”2102”  universe=”21” material=”1” surfaces=”11 −12” />
  <cell id=”2103”  universe=”21” material=”1” surfaces=”12 −13” />
  <cell id=”2104”  universe=”21” material=”1” surfaces=”13 −14” />
  <cell id=”2105”  universe=”21” material=”1” surfaces=”14 −15” />
  <cell id=”2106”  universe=”21” material=”2” surfaces=”15 −16” />
  <cell id=”2107”  universe=”21” material=”3” surfaces=”16 −17” />
  <cell id=”2108”  universe=”21” material=”4” surfaces=”17” />

  <cell id=”3101”  universe=”31” material=”1” surfaces=”   −11” />
  <cell id=”3102”  universe=”31” material=”1” surfaces=”11 −12” />
  <cell id=”3103”  universe=”31” material=”1” surfaces=”12 −13” />
  <cell id=”3104”  universe=”31” material=”1” surfaces=”13 −14” />
  <cell id=”3105”  universe=”31” material=”1” surfaces=”14 −15” />
  <cell id=”3106”  universe=”31” material=”2” surfaces=”15 −16” />
  <cell id=”3107”  universe=”31” material=”3” surfaces=”16 −17” />
  <cell id=”3108”  universe=”31” material=”4” surfaces=”17” />

  <cell id=”4101”  universe=”41” material=”1” surfaces=”   −11” />
  <cell id=”4102”  universe=”41” material=”1” surfaces=”11 −12” />
  <cell id=”4103”  universe=”41” material=”1” surfaces=”12 −13” />
  <cell id=”4104”  universe=”41” material=”1” surfaces=”13 −14” />
  <cell id=”4105”  universe=”41” material=”1” surfaces=”14 −15” />
  <cell id=”4106”  universe=”41” material=”2” surfaces=”15 −16” />
  <cell id=”4107”  universe=”41” material=”3” surfaces=”16 −17” />
  <cell id=”4108”  universe=”41” material=”4” surfaces=”17” />

  <cell id=”5101”  universe=”51” material=”1” surfaces=”   −11” />
  <cell id=”5102”  universe=”51” material=”1” surfaces=”11 −12” />
  <cell id=”5103”  universe=”51” material=”1” surfaces=”12 −13” />
  <cell id=”5104”  universe=”51” material=”1” surfaces=”13 −14” />
  <cell id=”5105”  universe=”51” material=”1” surfaces=”14 −15” />
  <cell id=”5106”  universe=”51” material=”2” surfaces=”15 −16” />
  <cell id=”5107”  universe=”51” material=”3” surfaces=”16 −17” />
  <cell id=”5108”  universe=”51” material=”4” surfaces=”17” />

<!−− Row 2 −−>
  <cell id=”1201”  universe=”12” material=”1” surfaces=”   −11” />
  <cell id=”1202”  universe=”12” material=”1” surfaces=”11 −12” />
  <cell id=”1203”  universe=”12” material=”1” surfaces=”12 −13” />
```

```
  <cell id=”1204”  universe=”12”  material=”1”  surfaces=”13 −14”  />
  <cell id=”1205”  universe=”12”  material=”1”  surfaces=”14 −15”  />
  <cell id=”1206”  universe=”12”  material=”2”  surfaces=”15 −16”  />
  <cell id=”1207”  universe=”12”  material=”3”  surfaces=”16 −17”  />
  <cell id=”1208”  universe=”12”  material=”4”  surfaces=”17”  />

  <cell id=”2201”  universe=”22”  material=”2”  surfaces=”    −31”  />
  <cell id=”2202”  universe=”22”  material=”6”  surfaces=”31 −32”  />
  <cell id=”2203”  universe=”22”  material=”2”  surfaces=”32 −33”/>
  <cell id=”2204”  universe=”22”  material=”5”  surfaces=”33 −34”/>
  <cell id=”2205”  universe=”22”  material=”5”  surfaces=”34 −35”/>
  <cell id=”2206”  universe=”22”  material=”2”  surfaces=”35 −36”/>
  <cell id=”2207”  universe=”22”  material=”6”  surfaces=”36 −37”/>
  <cell id=”2208”  universe=”22”  material=”4”  surfaces=”37 −21”/>
  <cell id=”2209”  universe=”22”  material=”3”  surfaces=”21 −22”  />
  <cell id=”2210”  universe=”22”  material=”4”  surfaces=”22”  />

  <cell id=”3201”  universe=”32”  material=”1”  surfaces=”    −11”  />
  <cell id=”3202”  universe=”32”  material=”1”  surfaces=”11 −12”  />
  <cell id=”3203”  universe=”32”  material=”1”  surfaces=”12 −13”  />
  <cell id=”3204”  universe=”32”  material=”1”  surfaces=”13 −14”  />
  <cell id=”3205”  universe=”32”  material=”1”  surfaces=”14 −15”  />
  <cell id=”3206”  universe=”32”  material=”2”  surfaces=”15 −16”  />
  <cell id=”3207”  universe=”32”  material=”3”  surfaces=”16 −17”  />
  <cell id=”3208”  universe=”32”  material=”4”  surfaces=”17”  />

  <cell id=”4201”  universe=”42”  material=”4”  surfaces=”    −21”  />
  <cell id=”4202”  universe=”42”  material=”3”  surfaces=”21 −22”  />
  <cell id=”4203”  universe=”42”  material=”4”  surfaces=”22”  />

  <cell id=”5201”  universe=”52”  material=”1”  surfaces=”    −11”  />
  <cell id=”5202”  universe=”52”  material=”1”  surfaces=”11 −12”  />
  <cell id=”5203”  universe=”52”  material=”1”  surfaces=”12 −13”  />
  <cell id=”5204”  universe=”52”  material=”1”  surfaces=”13 −14”  />
  <cell id=”5205”  universe=”52”  material=”1”  surfaces=”14 −15”  />
  <cell id=”5206”  universe=”52”  material=”2”  surfaces=”15 −16”  />
  <cell id=”5207”  universe=”52”  material=”3”  surfaces=”16 −17”  />
  <cell id=”5208”  universe=”52”  material=”4”  surfaces=”17”  />

<!−− Row 3 −−>
  <cell id=”1301”  universe=”13”  material=”1”  surfaces=”    −11”  />
  <cell id=”1302”  universe=”13”  material=”1”  surfaces=”11 −12”  />
  <cell id=”1303”  universe=”13”  material=”1”  surfaces=”12 −13”  />
  <cell id=”1304”  universe=”13”  material=”1”  surfaces=”13 −14”  />
  <cell id=”1305”  universe=”13”  material=”1”  surfaces=”14 −15”  />
  <cell id=”1306”  universe=”13”  material=”2”  surfaces=”15 −16”  />
  <cell id=”1307”  universe=”13”  material=”3”  surfaces=”16 −17”  />
  <cell id=”1308”  universe=”13”  material=”4”  surfaces=”17”  />

  <cell id=”2301”  universe=”23”  material=”1”  surfaces=”    −11”  />
  <cell id=”2302”  universe=”23”  material=”1”  surfaces=”11 −12”  />
  <cell id=”2303”  universe=”23”  material=”1”  surfaces=”12 −13”  />
  <cell id=”2304”  universe=”23”  material=”1”  surfaces=”13 −14”  />
  <cell id=”2305”  universe=”23”  material=”1”  surfaces=”14 −15”  />
  <cell id=”2306”  universe=”23”  material=”2”  surfaces=”15 −16”  />
```

```
  <cell id="2307"  universe="23" material="3" surfaces="16 -17" />
  <cell id="2308"  universe="23" material="4" surfaces="17" />

  <cell id="3301"  universe="33" material="1" surfaces="   -11" />
  <cell id="3302"  universe="33" material="1" surfaces="11 -12" />
  <cell id="3303"  universe="33" material="1" surfaces="12 -13" />
  <cell id="3304"  universe="33" material="1" surfaces="13 -14" />
  <cell id="3305"  universe="33" material="1" surfaces="14 -15" />
  <cell id="3306"  universe="33" material="2" surfaces="15 -16" />
  <cell id="3307"  universe="33" material="3" surfaces="16 -17" />
  <cell id="3308"  universe="33" material="4" surfaces="17" />

  <cell id="4301"  universe="43" material="1" surfaces="   -11" />
  <cell id="4302"  universe="43" material="1" surfaces="11 -12" />
  <cell id="4303"  universe="43" material="1" surfaces="12 -13" />
  <cell id="4304"  universe="43" material="1" surfaces="13 -14" />
  <cell id="4305"  universe="43" material="1" surfaces="14 -15" />
  <cell id="4306"  universe="43" material="2" surfaces="15 -16" />
  <cell id="4307"  universe="43" material="3" surfaces="16 -17" />
  <cell id="4308"  universe="43" material="4" surfaces="17" />

  <cell id="5301"  universe="53" material="1" surfaces="   -11" />
  <cell id="5302"  universe="53" material="1" surfaces="11 -12" />
  <cell id="5303"  universe="53" material="1" surfaces="12 -13" />
  <cell id="5304"  universe="53" material="1" surfaces="13 -14" />
  <cell id="5305"  universe="53" material="1" surfaces="14 -15" />
  <cell id="5306"  universe="53" material="2" surfaces="15 -16" />
  <cell id="5307"  universe="53" material="3" surfaces="16 -17" />
  <cell id="5308"  universe="53" material="4" surfaces="17" />

<!-- Row 4 -->
  <cell id="1401"  universe="14" material="1" surfaces="   -11" />
  <cell id="1402"  universe="14" material="1" surfaces="11 -12" />
  <cell id="1403"  universe="14" material="1" surfaces="12 -13" />
  <cell id="1404"  universe="14" material="1" surfaces="13 -14" />
  <cell id="1405"  universe="14" material="1" surfaces="14 -15" />
  <cell id="1406"  universe="14" material="2" surfaces="15 -16" />
  <cell id="1407"  universe="14" material="3" surfaces="16 -17" />
  <cell id="1408"  universe="14" material="4" surfaces="17" />

  <cell id="2401"  universe="24" material="4" surfaces="   -21" />
  <cell id="2402"  universe="24" material="3" surfaces="21 -22" />
  <cell id="2403"  universe="24" material="4" surfaces="22" />

  <cell id="3401"  universe="34" material="1" surfaces="   -11" />
  <cell id="3402"  universe="34" material="1" surfaces="11 -12" />
  <cell id="3403"  universe="34" material="1" surfaces="12 -13" />
  <cell id="3404"  universe="34" material="1" surfaces="13 -14" />
  <cell id="3405"  universe="34" material="1" surfaces="14 -15" />
  <cell id="3406"  universe="34" material="2" surfaces="15 -16" />
  <cell id="3407"  universe="34" material="3" surfaces="16 -17" />
  <cell id="3408"  universe="34" material="4" surfaces="17" />

  <cell id="4401"  universe="44" material="2" surfaces="   -31" />
  <cell id="4402"  universe="44" material="6" surfaces="31 -32" />
```

```
  <cell id=”4403”  universe=”44” material=”2” surfaces=”32 −33”/>
  <cell id=”4404”  universe=”44” material=”5” surfaces=”33 −34”/>
  <cell id=”4405”  universe=”44” material=”5” surfaces=”34 −35”/>
  <cell id=”4406”  universe=”44” material=”2” surfaces=”35 −36”/>
  <cell id=”4407”  universe=”44” material=”6” surfaces=”36 −37”/>
  <cell id=”4408”  universe=”44” material=”4” surfaces=”37 −21”/>
  <cell id=”4409”  universe=”44” material=”3” surfaces=”21 −22” />
  <cell id=”4410”  universe=”44” material=”4” surfaces=”22” />

  <cell id=”5401”  universe=”54” material=”1” surfaces=”   −11” />
  <cell id=”5402”  universe=”54” material=”1” surfaces=”11 −12” />
  <cell id=”5403”  universe=”54” material=”1” surfaces=”12 −13” />
  <cell id=”5404”  universe=”54” material=”1” surfaces=”13 −14” />
  <cell id=”5405”  universe=”54” material=”1” surfaces=”14 −15” />
  <cell id=”5406”  universe=”54” material=”2” surfaces=”15 −16” />
  <cell id=”5407”  universe=”54” material=”3” surfaces=”16 −17” />
  <cell id=”5408”  universe=”54” material=”4” surfaces=”17” />

<!−− Row 5 −−>
  <cell id=”1501”  universe=”15” material=”1” surfaces=”   −11” />
  <cell id=”1502”  universe=”15” material=”1” surfaces=”11 −12” />
  <cell id=”1503”  universe=”15” material=”1” surfaces=”12 −13” />
  <cell id=”1504”  universe=”15” material=”1” surfaces=”13 −14” />
  <cell id=”1505”  universe=”15” material=”1” surfaces=”14 −15” />
  <cell id=”1506”  universe=”15” material=”2” surfaces=”15 −16” />
  <cell id=”1507”  universe=”15” material=”3” surfaces=”16 −17” />
  <cell id=”1508”  universe=”15” material=”4” surfaces=”17” />

  <cell id=”2501”  universe=”25” material=”1” surfaces=”   −11” />
  <cell id=”2502”  universe=”25” material=”1” surfaces=”11 −12” />
  <cell id=”2503”  universe=”25” material=”1” surfaces=”12 −13” />
  <cell id=”2504”  universe=”25” material=”1” surfaces=”13 −14” />
  <cell id=”2505”  universe=”25” material=”1” surfaces=”14 −15” />
  <cell id=”2506”  universe=”25” material=”2” surfaces=”15 −16” />
  <cell id=”2507”  universe=”25” material=”3” surfaces=”16 −17” />
  <cell id=”2508”  universe=”25” material=”4” surfaces=”17” />

  <cell id=”3501”  universe=”35” material=”1” surfaces=”   −11” />
  <cell id=”3502”  universe=”35” material=”1” surfaces=”11 −12” />
  <cell id=”3503”  universe=”35” material=”1” surfaces=”12 −13” />
  <cell id=”3504”  universe=”35” material=”1” surfaces=”13 −14” />
  <cell id=”3505”  universe=”35” material=”1” surfaces=”14 −15” />
  <cell id=”3506”  universe=”35” material=”2” surfaces=”15 −16” />
  <cell id=”3507”  universe=”35” material=”3” surfaces=”16 −17” />
  <cell id=”3508”  universe=”35” material=”4” surfaces=”17” />

  <cell id=”4501”  universe=”45” material=”1” surfaces=”   −11” />
  <cell id=”4502”  universe=”45” material=”1” surfaces=”11 −12” />
  <cell id=”4503”  universe=”45” material=”1” surfaces=”12 −13” />
  <cell id=”4504”  universe=”45” material=”1” surfaces=”13 −14” />
  <cell id=”4505”  universe=”45” material=”1” surfaces=”14 −15” />
  <cell id=”4506”  universe=”45” material=”2” surfaces=”15 −16” />
  <cell id=”4507”  universe=”45” material=”3” surfaces=”16 −17” />
  <cell id=”4508”  universe=”45” material=”4” surfaces=”17” />

```

```
  <cell id=”5501”  universe=”55” material=”1” surfaces=”   -11” />
  <cell id=”5502”  universe=”55” material=”1” surfaces=”11 -12” />
  <cell id=”5503”  universe=”55” material=”1” surfaces=”12 -13” />
  <cell id=”5504”  universe=”55” material=”1” surfaces=”13 -14” />
  <cell id=”5505”  universe=”55” material=”1” surfaces=”14 -15” />
  <cell id=”5506”  universe=”55” material=”2” surfaces=”15 -16” />
  <cell id=”5507”  universe=”55” material=”3” surfaces=”16 -17” />
  <cell id=”5508”  universe=”55” material=”4” surfaces=”17” />

<!-- Assemblies -->

  <!-- Our Assembly -->
  <lattice id=”100”>
    <type>rectangular</type>
    <dimension>5 5</dimension>
    <lower_left>-3.15 -3.15</lower_left>
    <width>1.26 1.26</width>
    <universes>
      15 25 35 45 55
      14 24 34 44 54
      13 23 33 43 53
      12 22 32 42 52
      11 21 31 41 51
    </universes>
    <outside>5</outside>
  </lattice>

  <surface id=”1000” type=”z-plane” coeffs=”-100” boundary=”reflective”/>
  <surface id=”1100” type=”z-plane” coeffs=”100”  boundary=”reflective”/>


  <!-- Problem Boundaries -->
  <surface id=”1001” type=”x-plane” coeffs=”-3.15” boundary=”reflective”/>
  <surface id=”1002” type=”x-plane” coeffs=”3.15”  boundary=”reflective”/>
  <surface id=”1003” type=”y-plane” coeffs=”-3.15” boundary=”reflective”/>
  <surface id=”1004” type=”y-plane” coeffs=”3.15”  boundary=”reflective”/>

  <!-- And Universe 0: -->
  <cell id=”1” fill=”100” universe=”0”
     surfaces=”1001 -1002 1003 -1004 1000 -1100”/>


</geometry>
```

Listing A.7: OpenMC Sub-Assembly Materials File

```
<?xml version=”1.0”?>
<materials>
<!-- Based on AMA 1B -->
  <default_xs>71c</default_xs>

  <!-- 2.619 % UO2 Fuel composition -->
  <material id=”1”>
    <density units=”g/cm3” value=”10.257”/>
    <nuclide name=”O-16”    ao=”4.57617E-2” />
```

```
    <nuclide name="U-234"    ao="5.09503E-6" />
    <nuclide name="U-235"    ao="6.06709E-4" />
    <nuclide name="U-236"    ao="2.76809E-6" />
    <nuclide name="U-238"    ao="2.22663E-2" />
  </material>

  <!-- Gap composition -->
  <material id="2">
    <density units="g/cm3" value="1.786e-4"/>
    <nuclide name="He-4" ao="2.68714E-5" />
  </material>

  <!-- Cladding composition -->
  <material id="3">
    <density units="g/cm3" value="6.56"/>
    <nuclide name="Cr-50"  ao="3.30121E-6" />
    <nuclide name="Cr-52"  ao="6.36606E-5" />
    <nuclide name="Cr-53"  ao="7.21860E-6" />
    <nuclide name="Cr-54"  ao="1.79686E-6" />
    <nuclide name="Fe-54"  ao="8.68307E-6" />
    <nuclide name="Fe-56"  ao="1.36306E-4" />
    <nuclide name="Fe-57"  ao="3.14789E-6" />
    <nuclide name="Fe-58"  ao="4.18926E-7" />
    <nuclide name="Zr-90"  ao="2.18865E-2" />
    <nuclide name="Zr-91"  ao="4.77292E-3" />
    <nuclide name="Zr-92"  ao="7.29551E-3" />
    <nuclide name="Zr-94"  ao="7.39335E-3" />
    <nuclide name="Zr-96"  ao="1.19110E-3" />
    <nuclide name="Sn-112" ao="4.68066E-6" />
    <nuclide name="Sn-114" ao="3.18478E-6" />
    <nuclide name="Sn-115" ao="1.64064E-6" />
    <nuclide name="Sn-116" ao="7.01616E-5" />
    <nuclide name="Sn-117" ao="3.70592E-5" />
    <nuclide name="Sn-118" ao="1.16872E-4" />
    <nuclide name="Sn-119" ao="4.14504E-5" />
    <nuclide name="Sn-120" ao="1.57212E-4" />
    <nuclide name="Sn-122" ao="2.23417E-5" />
    <nuclide name="Sn-124" ao="2.79392E-5" />
    <nuclide name="Hf-174" ao="3.54138E-9" />
    <nuclide name="Hf-176" ao="1.16423E-7" />
    <nuclide name="Hf-177" ao="4.11686E-7" />
    <nuclide name="Hf-178" ao="6.03806E-7" />
    <nuclide name="Hf-179" ao="3.01460E-7" />
    <nuclide name="Hf-180" ao="7.76449E-7" />
  </material>

  <!-- Borated Water, 0.743 g/cm3 -->
  <material id="4">
    <density units="g/cm3" value="0.743"/>
    <nuclide name="O-16"   ao="2.48112E-2" />
    <nuclide name="H-1"    ao="4.96224E-2" />
    <nuclide name="B-10"   ao="1.07070E-5" />
    <nuclide name="B-11"   ao="4.30971E-5" />
    <sab name="lwtr" xs="16t" />
  </material>
```

```

  <!-- Pyrex -->
  <material id=”5”>
    <density units=”g/cm3” value=”2.25”/>
    <nuclide name=”B-10”   ao=”9.63266E-4”  />
    <nuclide name=”B-11”   ao=”3.90172E-3”  />
    <nuclide name=”O-16”   ao=”4.67761E-2”  />
    <nuclide name=”Si-28”  ao=”1.81980E-2”  />
    <nuclide name=”Si-29”  ao=”9.24474E-4”  />
    <nuclide name=”Si-30”  ao=”6.10133E-4”  />
    <!-- SiO2 S(a,b)? -->
  </material>

  <!-- SS304 -->
  <material id=”6”>
    <density units=”g/cm3” value=”8.00”/>
    <nuclide name=”C-Nat”  ao=”3.20895E-4”  />
    <nuclide name=”Si-28”  ao=”1.58197E-3”  />
    <nuclide name=”Si-29”  ao=”8.03653E-5”  />
    <nuclide name=”Si-30”  ao=”5.30394E-5”  />
    <nuclide name=”P-31”   ao=”6.99938E-5”  />
    <nuclide name=”Cr-50”  ao=”7.64915E-4”  />
    <nuclide name=”Cr-52”  ao=”1.47506E-2”  />
    <nuclide name=”Cr-53”  ao=”1.67260E-3”  />
    <nuclide name=”Cr-54”  ao=”4.16346E-4”  />
    <nuclide name=”Mn-55”  ao=”1.75387E-3”  />
    <nuclide name=”Fe-54”  ao=”3.44776E-3”  />
    <nuclide name=”Fe-56”  ao=”5.41225E-2”  />
    <nuclide name=”Fe-57”  ao=”1.24992E-3”  />
    <nuclide name=”Fe-58”  ao=”1.66342E-4”  />
    <nuclide name=”Ni-58”  ao=”5.30854E-3”  />
    <nuclide name=”Ni-60”  ao=”2.04484E-3”  />
    <nuclide name=”Ni-61”  ao=”8.88879E-5”  />
    <nuclide name=”Ni-62”  ao=”2.83413E-4”  />
    <nuclide name=”Ni-64”  ao=”7.21770E-5”  />
  </material>


</materials>
```

Listing A.8: OpenMC Sub-Assembly Tallies File

```
<?xml version=”1.0”?>
<tallies>
  <tally>
    <id>1</id>
    <filter>
      <type>cell</type>
      <bins>
        1101 1102 1103 1104 1105 1106 1107 1108
        2101 2102 2103 2104 2105 2106 2107 2108
        3101 3102 3103 3104 3105 3106 3107 3108
        4101 4102 4103 4104 4105 4106 4107 4108
        5101 5102 5103 5104 5105 5106 5107 5108

```

```
      1201 1202 1203 1204 1205 1206 1207 1208
      2201 2202 2203 2204 2205 2206 2207 2208 2209 2210
      3201 3202 3203 3204 3205 3206 3207 3208
      4201 4202 4203
      5201 5202 5203 5204 5205 5206 5207 5208

      1301 1302 1303 1304 1305 1306 1307 1308
      2301 2302 2303 2304 2305 2306 2307 2308
      3301 3302 3303 3304 3305 3306 3307 3308
      4301 4302 4303 4304 4305 4306 4307 4308
      5301 5302 5303 5304 5305 5306 5307 5308

      1401 1402 1403 1404 1405 1406 1407 1408
      2401 2402 2403
      3401 3402 3403 3404 3405 3406 3407 3408
      4401 4402 4403 4404 4405 4406 4407 4408 4409 4410
      5401 5402 5403 5404 5405 5406 5407 5408

      1501 1502 1503 1504 1505 1506 1507 1508
      2501 2502 2503 2504 2505 2506 2507 2508
      3501 3502 3503 3504 3505 3506 3507 3508
      4501 4502 4503 4504 4505 4506 4507 4508
      5501 5502 5503 5504 5505 5506 5507 5508
    </bins>
  </filter>
  <filter>
    <type>energy</type>
    <bins>
      0.0000E0  1.2396E-8 3.0613E-8 4.2755E-8 5.6922E-8 8.1968E-8
      1.1157E-7 1.4572E-7 1.8443E-7 2.7052E-7 3.5767E-7 5.0323E-7
      6.2506E-7 7.8208E-7 9.1000E-7 9.7100E-7 1.0137E-6 1.0722E-6
      1.1254E-6 1.1664E-6 1.2351E-6 1.4574E-6 1.8554E-6 2.3824E-6
      3.9279E-6 4.4509E-6 5.0435E-6 5.7150E-6 6.4760E-6 7.3382E-6
      8.3153E-6 1.2099E-5 1.3710E-5 2.9023E-5 4.7851E-5 7.8893E-5
      1.3007E-4 2.0347E-3 9.1188E-3 6.7379E-2 1.8316E-1 4.9787E-1
      8.2085E-1 1.3534    2.2313    3.6788    6.0653    20.0
    </bins>
  </filter>
  <scores>
     total
     kappa-fission
     nu-fission
     flux
  </scores>
  <estimator>tracklength</estimator>
</tally>

<tally>
  <id>2</id>
  <filter>
    <type>cell</type>
    <bins>
      1101 1102 1103 1104 1105 1106 1107 1108
      2101 2102 2103 2104 2105 2106 2107 2108
      3101 3102 3103 3104 3105 3106 3107 3108
```

```
        4101 4102 4103 4104 4105 4106 4107 4108
        5101 5102 5103 5104 5105 5106 5107 5108

        1201 1202 1203 1204 1205 1206 1207 1208
        2201 2202 2203 2204 2205 2206 2207 2208 2209 2210
        3201 3202 3203 3204 3205 3206 3207 3208
        4201 4202 4203
        5201 5202 5203 5204 5205 5206 5207 5208

        1301 1302 1303 1304 1305 1306 1307 1308
        2301 2302 2303 2304 2305 2306 2307 2308
        3301 3302 3303 3304 3305 3306 3307 3308
        4301 4302 4303 4304 4305 4306 4307 4308
        5301 5302 5303 5304 5305 5306 5307 5308

        1401 1402 1403 1404 1405 1406 1407 1408
        2401 2402 2403
        3401 3402 3403 3404 3405 3406 3407 3408
        4401 4402 4403 4404 4405 4406 4407 4408 4409 4410
        5401 5402 5403 5404 5405 5406 5407 5408

        1501 1502 1503 1504 1505 1506 1507 1508
        2501 2502 2503 2504 2505 2506 2507 2508
        3501 3502 3503 3504 3505 3506 3507 3508
        4501 4502 4503 4504 4505 4506 4507 4508
        5501 5502 5503 5504 5505 5506 5507 5508
      </bins>
    </filter>
    <filter>
      <type>energy</type>
      <bins>
        0.0000E0  1.2396E-8 3.0613E-8 4.2755E-8 5.6922E-8 8.1968E-8
        1.1157E-7 1.4572E-7 1.8443E-7 2.7052E-7 3.5767E-7 5.0323E-7
        6.2506E-7 7.8208E-7 9.1000E-7 9.7100E-7 1.0137E-6 1.0722E-6
        1.1254E-6 1.1664E-6 1.2351E-6 1.4574E-6 1.8554E-6 2.3824E-6
        3.9279E-6 4.4509E-6 5.0435E-6 5.7150E-6 6.4760E-6 7.3382E-6
        8.3153E-6 1.2099E-5 1.3710E-5 2.9023E-5 4.7851E-5 7.8893E-5
        1.3007E-4 2.0347E-3 9.1188E-3 6.7379E-2 1.8316E-1 4.9787E-1
        8.2085E-1 1.3534    2.2313    3.6788    6.0653    20.0
      </bins>
    </filter>
    <filter>
      <type>energyout</type>
      <bins>
        0.0000E0  1.2396E-8 3.0613E-8 4.2755E-8 5.6922E-8 8.1968E-8
        1.1157E-7 1.4572E-7 1.8443E-7 2.7052E-7 3.5767E-7 5.0323E-7
        6.2506E-7 7.8208E-7 9.1000E-7 9.7100E-7 1.0137E-6 1.0722E-6
        1.1254E-6 1.1664E-6 1.2351E-6 1.4574E-6 1.8554E-6 2.3824E-6
        3.9279E-6 4.4509E-6 5.0435E-6 5.7150E-6 6.4760E-6 7.3382E-6
        8.3153E-6 1.2099E-5 1.3710E-5 2.9023E-5 4.7851E-5 7.8893E-5
        1.3007E-4 2.0347E-3 9.1188E-3 6.7379E-2 1.8316E-1 4.9787E-1
        8.2085E-1 1.3534    2.2313    3.6788    6.0653    20.0
      </bins>
    </filter>
    <scores>
```

```
      nu-scatter-p2
      ndpp-nu-scatter-p2
    </scores>
    <estimator>analog</estimator>
  </tally>

  <tally>
    <id>3</id>
    <filter>
      <type>cell</type>
      <bins>
        1101 1102 1103 1104 1105 1106 1107 1108
        2101 2102 2103 2104 2105 2106 2107 2108
        3101 3102 3103 3104 3105 3106 3107 3108
        4101 4102 4103 4104 4105 4106 4107 4108
        5101 5102 5103 5104 5105 5106 5107 5108

        1201 1202 1203 1204 1205 1206 1207 1208
        2201 2202 2203 2204 2205 2206 2207 2208 2209 2210
        3201 3202 3203 3204 3205 3206 3207 3208
        4201 4202 4203
        5201 5202 5203 5204 5205 5206 5207 5208

        1301 1302 1303 1304 1305 1306 1307 1308
        2301 2302 2303 2304 2305 2306 2307 2308
        3301 3302 3303 3304 3305 3306 3307 3308
        4301 4302 4303 4304 4305 4306 4307 4308
        5301 5302 5303 5304 5305 5306 5307 5308

        1401 1402 1403 1404 1405 1406 1407 1408
        2401 2402 2403
        3401 3402 3403 3404 3405 3406 3407 3408
        4401 4402 4403 4404 4405 4406 4407 4408 4409 4410
        5401 5402 5403 5404 5405 5406 5407 5408

        1501 1502 1503 1504 1505 1506 1507 1508
        2501 2502 2503 2504 2505 2506 2507 2508
        3501 3502 3503 3504 3505 3506 3507 3508
        4501 4502 4503 4504 4505 4506 4507 4508
        5501 5502 5503 5504 5505 5506 5507 5508
      </bins>
    </filter>
    <filter>
      <type>energy</type>
      <bins>
        0.0000E0  1.2396E-8 3.0613E-8 4.2755E-8 5.6922E-8 8.1968E-8
        1.1157E-7 1.4572E-7 1.8443E-7 2.7052E-7 3.5767E-7 5.0323E-7
        6.2506E-7 7.8208E-7 9.1000E-7 9.7100E-7 1.0137E-6 1.0722E-6
        1.1254E-6 1.1664E-6 1.2351E-6 1.4574E-6 1.8554E-6 2.3824E-6
        3.9279E-6 4.4509E-6 5.0435E-6 5.7150E-6 6.4760E-6 7.3382E-6
        8.3153E-6 1.2099E-5 1.3710E-5 2.9023E-5 4.7851E-5 7.8893E-5
        1.3007E-4 2.0347E-3 9.1188E-3 6.7379E-2 1.8316E-1 4.9787E-1
        8.2085E-1 1.3534    2.2313    3.6788    6.0653    20.0
      </bins>
    </filter>
```

```
    <scores>
      flux
    </scores>
    <estimator>analog</estimator>
  </tally>

  <tally>
    <id>4</id>
    <filter>
      <type>cell</type>
      <bins>
        1101 1102 1103 1104 1105 1106 1107 1108
        2101 2102 2103 2104 2105 2106 2107 2108
        3101 3102 3103 3104 3105 3106 3107 3108
        4101 4102 4103 4104 4105 4106 4107 4108
        5101 5102 5103 5104 5105 5106 5107 5108

        1201 1202 1203 1204 1205 1206 1207 1208
        2201 2202 2203 2204 2205 2206 2207 2208 2209 2210
        3201 3202 3203 3204 3205 3206 3207 3208
        4201 4202 4203
        5201 5202 5203 5204 5205 5206 5207 5208

        1301 1302 1303 1304 1305 1306 1307 1308
        2301 2302 2303 2304 2305 2306 2307 2308
        3301 3302 3303 3304 3305 3306 3307 3308
        4301 4302 4303 4304 4305 4306 4307 4308
        5301 5302 5303 5304 5305 5306 5307 5308

        1401 1402 1403 1404 1405 1406 1407 1408
        2401 2402 2403
        3401 3402 3403 3404 3405 3406 3407 3408
        4401 4402 4403 4404 4405 4406 4407 4408 4409 4410
        5401 5402 5403 5404 5405 5406 5407 5408

        1501 1502 1503 1504 1505 1506 1507 1508
        2501 2502 2503 2504 2505 2506 2507 2508
        3501 3502 3503 3504 3505 3506 3507 3508
        4501 4502 4503 4504 4505 4506 4507 4508
        5501 5502 5503 5504 5505 5506 5507 5508
      </bins>
    </filter>
    <filter>
      <type>energy</type>
      <bins>
        0.0000E0  1.2396E-8 3.0613E-8 4.2755E-8 5.6922E-8 8.1968E-8
        1.1157E-7 1.4572E-7 1.8443E-7 2.7052E-7 3.5767E-7 5.0323E-7
        6.2506E-7 7.8208E-7 9.1000E-7 9.7100E-7 1.0137E-6 1.0722E-6
        1.1254E-6 1.1664E-6 1.2351E-6 1.4574E-6 1.8554E-6 2.3824E-6
        3.9279E-6 4.4509E-6 5.0435E-6 5.7150E-6 6.4760E-6 7.3382E-6
        8.3153E-6 1.2099E-5 1.3710E-5 2.9023E-5 4.7851E-5 7.8893E-5
        1.3007E-4 2.0347E-3 9.1188E-3 6.7379E-2 1.8316E-1 4.9787E-1
        8.2085E-1 1.3534    2.2313    3.6788    6.0653    20.0
      </bins>
    </filter>
```

```
    <filter>
      <type>energyout</type>
      <bins>
        0.0000E0  1.2396E-8 3.0613E-8 4.2755E-8 5.6922E-8 8.1968E-8
        1.1157E-7 1.4572E-7 1.8443E-7 2.7052E-7 3.5767E-7 5.0323E-7
        6.2506E-7 7.8208E-7 9.1000E-7 9.7100E-7 1.0137E-6 1.0722E-6
        1.1254E-6 1.1664E-6 1.2351E-6 1.4574E-6 1.8554E-6 2.3824E-6
        3.9279E-6 4.4509E-6 5.0435E-6 5.7150E-6 6.4760E-6 7.3382E-6
        8.3153E-6 1.2099E-5 1.3710E-5 2.9023E-5 4.7851E-5 7.8893E-5
        1.3007E-4 2.0347E-3 9.1188E-3 6.7379E-2 1.8316E-1 4.9787E-1
        8.2085E-1 1.3534    2.2313    3.6788    6.0653    20.0
      </bins>
    </filter>
    <scores>
      ndpp-nu-scatter-p2
    </scores>
    <estimator>tracklength</estimator>
  </tally>

  <tally>
    <id>5</id>
    <filter>
      <type>cell</type>
      <bins>
        1101 1102 1103 1104 1105 1106 1107 1108
        2101 2102 2103 2104 2105 2106 2107 2108
        3101 3102 3103 3104 3105 3106 3107 3108
        4101 4102 4103 4104 4105 4106 4107 4108
        5101 5102 5103 5104 5105 5106 5107 5108

        1201 1202 1203 1204 1205 1206 1207 1208
        2201 2202 2203 2204 2205 2206 2207 2208 2209 2210
        3201 3202 3203 3204 3205 3206 3207 3208
        4201 4202 4203
        5201 5202 5203 5204 5205 5206 5207 5208

        1301 1302 1303 1304 1305 1306 1307 1308
        2301 2302 2303 2304 2305 2306 2307 2308
        3301 3302 3303 3304 3305 3306 3307 3308
        4301 4302 4303 4304 4305 4306 4307 4308
        5301 5302 5303 5304 5305 5306 5307 5308

        1401 1402 1403 1404 1405 1406 1407 1408
        2401 2402 2403
        3401 3402 3403 3404 3405 3406 3407 3408
        4401 4402 4403 4404 4405 4406 4407 4408 4409 4410
        5401 5402 5403 5404 5405 5406 5407 5408

        1501 1502 1503 1504 1505 1506 1507 1508
        2501 2502 2503 2504 2505 2506 2507 2508
        3501 3502 3503 3504 3505 3506 3507 3508
        4501 4502 4503 4504 4505 4506 4507 4508
        5501 5502 5503 5504 5505 5506 5507 5508
      </bins>
    </filter>
```

```
    <filter>
      <type>energy</type>
      <bins> 0.0  20.0 </bins>
    </filter>
    <filter>
      <type>energyout</type>
      <bins>
        0.0000E0  1.2396E-8 3.0613E-8 4.2755E-8 5.6922E-8 8.1968E-8
        1.1157E-7 1.4572E-7 1.8443E-7 2.7052E-7 3.5767E-7 5.0323E-7
        6.2506E-7 7.8208E-7 9.1000E-7 9.7100E-7 1.0137E-6 1.0722E-6
        1.1254E-6 1.1664E-6 1.2351E-6 1.4574E-6 1.8554E-6 2.3824E-6
        3.9279E-6 4.4509E-6 5.0435E-6 5.7150E-6 6.4760E-6 7.3382E-6
        8.3153E-6 1.2099E-5 1.3710E-5 2.9023E-5 4.7851E-5 7.8893E-5
        1.3007E-4 2.0347E-3 9.1188E-3 6.7379E-2 1.8316E-1 4.9787E-1
        8.2085E-1 1.3534    2.2313    3.6788    6.0653    20.0
      </bins>
    </filter>
    <scores>
      nu-fission
    </scores>
    <estimator>analog</estimator>
  </tally>

  <assume_separate>false</assume_separate>

  <ndpp_library>/home/nelsonag/cases/diss/ndpp/47g/ndpp_lib.xml</ndpp_library>

</tallies>
```

Listing A.9: OpenMC Sub-Assembly Settings File

```
<?xml version="1.0"?>
<settings>

  <!-- Define how many particles to run and for how many batches -->
  <eigenvalue>
    <batches>100900</batches>
    <inactive>900</inactive>
    <particles>10000</particles>
  </eigenvalue>

  <source>
    <space type="box">
      <parameters>
        -3.15  -3.15  -100
        3.15    3.15   100
      </parameters>
    </space>
  </source>

  <state_point>
    <batches>
      910  1000  1100  1200  1300  1400  1500  1600  1700  1800  1900
      2900  3900  4900  5900  6900  7900  8900  9900  10900  15900  20900  25900
      30900  40900  50900  60900  70900  80900  90900  100900
```

```
    </batches>
    <source_write>true</source_write>
  </state_point>

  <output>
    <cross_sections>true</cross_sections>
    <summary>true</summary>
    <tallies>false</tallies>
  </output>

  <cross_sections>/home/nelsonag/cases/diss/endf70.xml</cross_sections>

</settings>
```

The matching MPACT input file is provided below. In this model, a ray spacing of 0.005 cm is used. The angular quadrature is Chebyshev-Yamamoto (with 32 azimuthal and 3 polar angles). The fission source and eigenvalue are converged to 10^{-6}.

Listing A.10: MPACT Sub-Assembly Input File

```
CASEID  p2

MATERIAL
  mat  1101  2  ::  m1
  mat  1102  2  ::  m2
  mat  1103  2  ::  m3
  mat  1104  2  ::  m4
  mat  1105  2  ::  m5
  mat  1106  2  ::  m6
  mat  1107  2  ::  m7
  mat  1108  2  ::  m8
  mat  2101  2  ::  m9
  mat  2102  2  ::  m10
  mat  2103  2  ::  m11
  mat  2104  2  ::  m12
  mat  2105  2  ::  m13
  mat  2106  2  ::  m14
  mat  2107  2  ::  m15
  mat  2108  2  ::  m16
  mat  3101  2  ::  m17
  mat  3102  2  ::  m18
  mat  3103  2  ::  m19
  mat  3104  2  ::  m20
  mat  3105  2  ::  m21
  mat  3106  2  ::  m22
  mat  3107  2  ::  m23
  mat  3108  2  ::  m24
  mat  4101  2  ::  m25
  mat  4102  2  ::  m26
  mat  4103  2  ::  m27
  mat  4104  2  ::  m28
  mat  4105  2  ::  m29
  mat  4106  2  ::  m30
  mat  4107  2  ::  m31
```

```
mat 4108 2 :: m32
mat 5101 2 :: m33
mat 5102 2 :: m34
mat 5103 2 :: m35
mat 5104 2 :: m36
mat 5105 2 :: m37
mat 5106 2 :: m38
mat 5107 2 :: m39
mat 5108 2 :: m40
mat 1201 2 :: m41
mat 1202 2 :: m42
mat 1203 2 :: m43
mat 1204 2 :: m44
mat 1205 2 :: m45
mat 1206 2 :: m46
mat 1207 2 :: m47
mat 1208 2 :: m48
mat 2201 2 :: m49
mat 2202 2 :: m50
mat 2203 2 :: m51
mat 2204 2 :: m52
mat 2205 2 :: m53
mat 2206 2 :: m54
mat 2207 2 :: m55
mat 2208 2 :: m56
mat 2209 2 :: m57
mat 2210 2 :: m58
mat 3201 2 :: m59
mat 3202 2 :: m60
mat 3203 2 :: m61
mat 3204 2 :: m62
mat 3205 2 :: m63
mat 3206 2 :: m64
mat 3207 2 :: m65
mat 3208 2 :: m66
mat 4201 2 :: m67
mat 4202 2 :: m68
mat 4203 2 :: m69
mat 5201 2 :: m70
mat 5202 2 :: m71
mat 5203 2 :: m72
mat 5204 2 :: m73
mat 5205 2 :: m74
mat 5206 2 :: m75
mat 5207 2 :: m76
mat 5208 2 :: m77
mat 1301 2 :: m78
mat 1302 2 :: m79
mat 1303 2 :: m80
mat 1304 2 :: m81
mat 1305 2 :: m82
mat 1306 2 :: m83
mat 1307 2 :: m84
mat 1308 2 :: m85
mat 2301 2 :: m86
```

```
mat 2302 2 :: m87
mat 2303 2 :: m88
mat 2304 2 :: m89
mat 2305 2 :: m90
mat 2306 2 :: m91
mat 2307 2 :: m92
mat 2308 2 :: m93
mat 3301 2 :: m94
mat 3302 2 :: m95
mat 3303 2 :: m96
mat 3304 2 :: m97
mat 3305 2 :: m98
mat 3306 2 :: m99
mat 3307 2 :: m100
mat 3308 2 :: m101
mat 4301 2 :: m102
mat 4302 2 :: m103
mat 4303 2 :: m104
mat 4304 2 :: m105
mat 4305 2 :: m106
mat 4306 2 :: m107
mat 4307 2 :: m108
mat 4308 2 :: m109
mat 5301 2 :: m110
mat 5302 2 :: m111
mat 5303 2 :: m112
mat 5304 2 :: m113
mat 5305 2 :: m114
mat 5306 2 :: m115
mat 5307 2 :: m116
mat 5308 2 :: m117
mat 1401 2 :: m118
mat 1402 2 :: m119
mat 1403 2 :: m120
mat 1404 2 :: m121
mat 1405 2 :: m122
mat 1406 2 :: m123
mat 1407 2 :: m124
mat 1408 2 :: m125
mat 2401 2 :: m126
mat 2402 2 :: m127
mat 2403 2 :: m128
mat 3401 2 :: m129
mat 3402 2 :: m130
mat 3403 2 :: m131
mat 3404 2 :: m132
mat 3405 2 :: m133
mat 3406 2 :: m134
mat 3407 2 :: m135
mat 3408 2 :: m136
mat 4401 2 :: m137
mat 4402 2 :: m138
mat 4403 2 :: m139
mat 4404 2 :: m140
mat 4405 2 :: m141
```

```
    mat 4406 2 :: m142
    mat 4407 2 :: m143
    mat 4408 2 :: m144
    mat 4409 2 :: m145
    mat 4410 2 :: m146
    mat 5401 2 :: m147
    mat 5402 2 :: m148
    mat 5403 2 :: m149
    mat 5404 2 :: m150
    mat 5405 2 :: m151
    mat 5406 2 :: m152
    mat 5407 2 :: m153
    mat 5408 2 :: m154
    mat 1501 2 :: m155
    mat 1502 2 :: m156
    mat 1503 2 :: m157
    mat 1504 2 :: m158
    mat 1505 2 :: m159
    mat 1506 2 :: m160
    mat 1507 2 :: m161
    mat 1508 2 :: m162
    mat 2501 2 :: m163
    mat 2502 2 :: m164
    mat 2503 2 :: m165
    mat 2504 2 :: m166
    mat 2505 2 :: m167
    mat 2506 2 :: m168
    mat 2507 2 :: m169
    mat 2508 2 :: m170
    mat 3501 2 :: m171
    mat 3502 2 :: m172
    mat 3503 2 :: m173
    mat 3504 2 :: m174
    mat 3505 2 :: m175
    mat 3506 2 :: m176
    mat 3507 2 :: m177
    mat 3508 2 :: m178
    mat 4501 2 :: m179
    mat 4502 2 :: m180
    mat 4503 2 :: m181
    mat 4504 2 :: m182
    mat 4505 2 :: m183
    mat 4506 2 :: m184
    mat 4507 2 :: m185
    mat 4508 2 :: m186
    mat 5501 2 :: m187
    mat 5502 2 :: m188
    mat 5503 2 :: m189
    mat 5504 2 :: m190
    mat 5505 2 :: m191
    mat 5506 2 :: m192
    mat 5507 2 :: m193
    mat 5508 2 :: m194

GEOM
```

```

 !Ray tracing module dimensions
 mod_dim 6.3 6.3 1.0

 !Pin mesh
  pinMesh 1  cyl  0.1832 0.2591 0.3173 0.3664 0.4096 0.418 0.475 0.575 / 1.26 / 1.0 / 5*1 1 1 1 / 5*8 8 8 8 8 / 1
  pinMesh 2  cyl  0.561 0.602 / 1.26 / 1.0 / 2 1 / 2*8 8 8 / 1
  pinMesh 3  cyl  0.214 0.231 0.241 0.3467 0.427 0.437 0.484 0.561 0.602 / 1.26 / 1.0 / 8*1 1 / 10*8 / 1

 pin 11 1 / 1101 1102 1103 1104 1105 1106 1107 1108 1108
 pin 21 1 / 2101 2102 2103 2104 2105 2106 2107 2108 2108
 pin 31 1 / 3101 3102 3103 3104 3105 3106 3107 3108 3108
 pin 41 1 / 4101 4102 4103 4104 4105 4106 4107 4108 4108
 pin 51 1 / 5101 5102 5103 5104 5105 5106 5107 5108 5108

 pin 12 1 / 1201 1202 1203 1204 1205 1206 1207 1208 1208
 pin 22 3 / 2201 2202 2203 2204 2205 2206 2207 2208 2209 2210
 pin 32 1 / 3201 3202 3203 3204 3205 3206 3207 3208 3208
 pin 42 2 / 4201 4202 4203
 pin 52 1 / 5201 5202 5203 5204 5205 5206 5207 5208 5208

 pin 13 1 / 1301 1302 1303 1304 1305 1306 1307 1308 1308
 pin 23 1 / 2301 2302 2303 2304 2305 2306 2307 2308 2308
 pin 33 1 / 3301 3302 3303 3304 3305 3306 3307 3308 3308
 pin 43 1 / 4301 4302 4303 4304 4305 4306 4307 4308 4308
 pin 53 1 / 5301 5302 5303 5304 5305 5306 5307 5308 5308

 pin 14 1 / 1401 1402 1403 1404 1405 1406 1407 1408 1408
 pin 24 2 / 2401 2402 2403
 pin 34 1 / 3401 3402 3403 3404 3405 3406 3407 3408 3408
 pin 44 3 / 4401 4402 4403 4404 4405 4406 4407 4408 4409 4410
 pin 54 1 / 5401 5402 5403 5404 5405 5406 5407 5408 5408

 pin 15 1 / 1501 1502 1503 1504 1505 1506 1507 1508 1508
 pin 25 1 / 2501 2502 2503 2504 2505 2506 2507 2508 2508
 pin 35 1 / 3501 3502 3503 3504 3505 3506 3507 3508 3508
 pin 45 1 / 4501 4502 4503 4504 4505 4506 4507 4508 4508
 pin 55 1 / 5501 5502 5503 5504 5505 5506 5507 5508 5508


!Pin modular ray tracing
 module  1 2*5 1
  15 25 35 45 55
  14 24 34 44 54
  13 23 33 43 53
  12 22 32 42 52
  11 21 31 41 51

 lattice  1  1 1
  1

!Define assemblies
 assembly  1
```

```
  1

 core 360
  1

XSEC
  addpath ./
  xslib USER data.xs

OPTION
  bound_cond 1 1 1 1 1 1
  solver 1 2
  ray 0.005 CHEBYSHEV-YAMAMOTO 16 3
  parallel 1 1 1 4
  conv_crit 2*1.e-6
  iter_lim 2000 2 3
  vis_edits T
  validation T
  scatt_meth P2
.
```

APPENDIX B

Group Structures

This appendix presents the two group structures used within this report, the seven-group and the forty-seven group structures.

Table B.1 provides the seven energy group structure utilized within this report. This group structure is the one utilized with the widely used C5G7 deterministic transport benchmark [30].

Table B.2 provides the forty-seven energy group structure utilized within this report. This group structure is traditionally associated with the HELIOS code and is documented within the HELIOS manual [36].

Table B.1: C5G7 Seven Group Energy Structure

Group Number	Upper Bound (MeV)	Group Number	Upper Bound (MeV)
7	1.34E-7	3	9.11882E-3
6	6.25E-7	2	1.35335
5	4.0E-6	1	20.0
4	5.55951E-5	-	-

Table B.2: HELIOS Forty-Seven Group Energy Structure

Group Number	Upper Bound (MeV)	Group Number	Upper Bound (MeV)
47	1.2396E-8	23	4.4509E-6
46	3.0613E-8	22	5.0435E-6
45	4.2755E-8	21	5.7150E-6
44	5.6922E-8	20	6.4760E-6
43	8.1968E-8	19	7.3382E-6
42	1.1157E-7	18	8.3153E-6
41	1.4572E-7	17	1.2099E-5
40	1.8443E-7	16	1.3710E-5
39	2.7052E-7	15	2.9023E-5
38	3.5767E-7	14	4.7851E-5
37	5.0323E-7	13	7.8893E-5
36	6.2506E-7	12	1.3007E-4
35	7.8208E-7	11	2.0347E-3
34	9.1000E-7	10	9.1188E-3
33	9.7100E-7	9	6.7379E-2
32	1.0137E-6	8	1.8316E-1
31	1.0722E-6	7	4.9787E-1
30	1.1254E-6	6	8.2085E-1
29	1.1664E-6	5	1.3534
28	1.2351E-6	4	2.2313
27	1.4574E-6	3	3.6788
26	1.8554E-6	2	6.0653
25	2.3824E-6	1	20.0
24	3.9279E-6	-	-

APPENDIX C

NDPP Input Files

This appendix provides the NDPP input files (*ndpp.xml* and *cross_sections.xml*) as well as the resultant library descriptor file, *ndpp_lib.xml* for information. These files were the same as used to generate the 47-group data used in both the pin cell and sub-assembly models of this work.

Listing C.1: NDPP Options Input File

```
<?xml version=”1.0” ?>

<ndpp>
  <scatt_type>legendre</scatt_type>
  <scatt_order>2</scatt_order>
  <cross_sections>../../endf70.xml</cross_sections>
  <energy_bins>
    0.0000E0  1.2396E−8 3.0613E−8 4.2755E−8 5.6922E−8 8.1968E−8 1.1157E−7 1.4572E−7 1.8443E−7 2.7052E−7 3.5767E−7
    5.0323E−7 6.2506E−7 7.8208E−7 9.1000E−7 9.7100E−7 1.0137E−6 1.0722E−6 1.1254E−6 1.1664E−6 1.2351E−6 1.4574E−6
    1.8554E−6 2.3824E−6 3.9279E−6 4.4509E−6 5.0435E−6 5.7150E−6 6.4760E−6 7.3382E−6 8.3153E−6 1.2099E−5 1.3710E−5
    2.9023E−5 4.7851E−5 7.8893E−5 1.3007E−4 2.0347E−3 9.1188E−3 6.7379E−2 1.8316E−1 4.9787E−1 8.2085E−1 1.3534
    2.2313  3.6788  6.0653  20
  </energy_bins>
  <nuscatter>true</nuscatter>
  <integrate_chi>true</integrate_chi>
  <output_format>binary</output_format>
  <freegas_cutoff>400.0</freegas_cutoff>
  <mu_bins>501</mu_bins>
  <print_tol>1.0E−10</print_tol>
  <thinning_tol>1E−5</thinning_tol>
  <threads>4</threads>
</ndpp>
```

Listing C.2: NDPP Cross-Sections Description File

```
<?xml version=”1.0” ?>
<cross_sections>
```

```
<directory>/opt/xsdata/endf70</directory>
<filetype>binary</filetype>
<record_length>4096</record_length>
<entries>512</entries>

<!-- Fuels -->
<ace_table alias=”O-16.71c” awr=”15.85751” location=”12050” name=”8016.71c” path=”xdata/endf70a” temperature=”5.1704e-08” zaid=”8016”/>
<ace_table alias=”U-234.71c” awr=”232.0304” location=”6610” name=”92234.71c” path=”xdata/endf70j” temperature=”5.1704e-08” zaid=”92234”/>
<ace_table alias=”U-235.71c” awr=”233.0248” location=”11327” name=”92235.71c” path=”xdata/endf70j” temperature=”5.1704e-08” zaid=”92235”/>
<ace_table alias=”U-236.71c” awr=”234.0178” location=”16818” name=”92236.71c” path=”xdata/endf70j” temperature=”5.1704e-08” zaid=”92236”/>
<ace_table alias=”U-238.71c” awr=”236.0058” location=”24190” name=”92238.71c” path=”xdata/endf70j” temperature=”5.1704e-08” zaid=”92238”/>
<ace_table awr=”15.85751” location=”34136” name=”o2/u.13t” path=”xdata/endf70sab” temperature=”5.1704e-08” zaid=”0”/>
<ace_table awr=”236.0058” location=”37200” name=”u/o2.13t” path=”xdata/endf70sab” temperature=”5.1704e-08” zaid=”0”/>

<!-- Gap -->
<ace_table alias=”He-4.71c” awr=”3.968219” location=”429” name=”2004.71c” path=”xdata/endf70a” temperature=”5.1704e-08” zaid=”2004”/>

<!-- Clad -->
<ace_table alias=”Cr-50.71c” awr=”49.517” location=”847” name=”24050.71c” path=”xdata/endf70b” temperature=”5.1704e-08” zaid=”24050”/>
<ace_table alias=”Cr-52.71c” awr=”51.494” location=”4760” name=”24052.71c” path=”xdata/endf70b” temperature=”5.1704e-08” zaid=”24052”/>
<ace_table alias=”Cr-53.71c” awr=”52.486” location=”8161” name=”24053.71c” path=”xdata/endf70b” temperature=”5.1704e-08” zaid=”24053”/>
<ace_table alias=”Cr-54.71c” awr=”53.476” location=”10990” name=”24054.71c” path=”xdata/endf70b” temperature=”5.1704e-08” zaid=”24054”/>
<ace_table alias=”Fe-54.71c” awr=”53.476” location=”16492” name=”26054.71c” path=”xdata/endf70b” temperature=”5.1704e-08” zaid=”26054”/>
<ace_table alias=”Fe-56.71c” awr=”55.454” location=”19974” name=”26056.71c” path=”xdata/endf70b” temperature=”5.1704e-08” zaid=”26056”/>
<ace_table alias=”Fe-57.71c” awr=”56.446” location=”24437” name=”26057.71c” path=”xdata/endf70b” temperature=”5.1704e-08” zaid=”26057”/>
<ace_table alias=”Fe-58.71c” awr=”57.436” location=”27379” name=”26058.71c” path=”xdata/endf70b” temperature=”5.1704e-08” zaid=”26058”/>
<ace_table alias=”Zr-90.71c” awr=”89.1324” location=”47188” name=”40090.71c” path=”xdata/endf70c” temperature=”5.1704e-08” zaid=”40090”/>
<ace_table alias=”Zr-91.71c” awr=”90.1247” location=”49225” name=”40091.71c” path=”xdata/endf70c” temperature=”5.1704e-08” zaid=”40091”/>
<ace_table alias=”Zr-92.71c” awr=”91.1155” location=”51364” name=”40092.71c” path=”xdata/endf70c” temperature=”5.1704e-08” zaid=”40092”/>
<ace_table alias=”Zr-94.71c” awr=”93.0996” location=”54984” name=”40094.71c” path=”xdata/endf70c” temperature=”5.1704e-08” zaid=”40094”/>
<ace_table alias=”Zr-96.71c” awr=”95.0844” location=”57855” name=”40096.71c” path=”xdata/endf70c” temperature=”5.1704e-08” zaid=”40096”/>
<ace_table alias=”Sn-112.71c” awr=”110.944” location=”4356” name=”50112.71c” path=”xdata/endf70e” temperature=”5.1704e-08” zaid=”50112”/>
```

```
<ace_table alias="Sn-114.71c" awr="112.925" location="10984" name="50114.71c" path="xdata/endf70e" temperature="5.1704e-08" zaid="50114"/>
<ace_table alias="Sn-115.71c" awr="113.916" location="12148" name="50115.71c" path="xdata/endf70e" temperature="5.1704e-08" zaid="50115"/>
<ace_table alias="Sn-116.71c" awr="114.906" location="13378" name="50116.71c" path="xdata/endf70e" temperature="5.1704e-08" zaid="50116"/>
<ace_table alias="Sn-117.71c" awr="115.899" location="15534" name="50117.71c" path="xdata/endf70e" temperature="5.1704e-08" zaid="50117"/>
<ace_table alias="Sn-118.71c" awr="116.889" location="16750" name="50118.71c" path="xdata/endf70e" temperature="5.1704e-08" zaid="50118"/>
<ace_table alias="Sn-119.71c" awr="117.882" location="17543" name="50119.71c" path="xdata/endf70e" temperature="5.1704e-08" zaid="50119"/>
<ace_table alias="Sn-120.71c" awr="118.872" location="18940" name="50120.71c" path="xdata/endf70e" temperature="5.1704e-08" zaid="50120"/>
<ace_table alias="Sn-122.71c" awr="120.856" location="21329" name="50122.71c" path="xdata/endf70e" temperature="5.1704e-08" zaid="50122"/>
<ace_table alias="Sn-124.71c" awr="122.841" location="24952" name="50124.71c" path="xdata/endf70e" temperature="5.1704e-08" zaid="50124"/>
<ace_table alias="Sn-126.71c" awr="124.826" location="28491" name="50126.71c" path="xdata/endf70e" temperature="5.1704e-08" zaid="50126"/>
<ace_table alias="Hf-174.71c" awr="172.446" location="1887" name="72174.71c" path="xdata/endf70i" temperature="5.1704e-08" zaid="72174"/>
<ace_table alias="Hf-176.71c" awr="174.430" location="2324" name="72176.71c" path="xdata/endf70i" temperature="5.1704e-08" zaid="72176"/>
<ace_table alias="Hf-177.71c" awr="175.423" location="3266" name="72177.71c" path="xdata/endf70i" temperature="5.1704e-08" zaid="72177"/>
<ace_table alias="Hf-178.71c" awr="176.415" location="4733" name="72178.71c" path="xdata/endf70i" temperature="5.1704e-08" zaid="72178"/>
<ace_table alias="Hf-179.71c" awr="177.409" location="5470" name="72179.71c" path="xdata/endf70i" temperature="5.1704e-08" zaid="72179"/>
<ace_table alias="Hf-180.71c" awr="178.401" location="6546" name="72180.71c" path="xdata/endf70i" temperature="5.1704e-08" zaid="72180"/>

<!-- Borated Water -->
<ace_table alias="H-1.71c" freegas_cutoff="-1" awr="0.999167" location="18" name="1001.71c" path="xdata/endf70a" temperature="5.1704e-08" zaid="1001"/>
<ace_table alias="B-10.71c" awr="9.926921" location="6814" name="5010.71c" path="xdata/endf70a" temperature="5.1704e-08" zaid="5010"/>
<ace_table alias="B-11.71c" awr="10.9147" location="7541" name="5011.71c" path="xdata/endf70a" temperature="5.1704e-08" zaid="5011"/>
<ace_table awr="0.999167" location="22984" name="lwtr.16t" path="xdata/endf70sab" temperature="5.1704e-08" zaid="0"/>

<!-- Pyrex -->
<ace_table alias="Si-28.71c" awr="27.737" location="21649" name="14028.71c" path="xdata/endf70a" temperature="5.1704e-08" zaid="14028"/>
<ace_table alias="Si-29.71c" awr="28.728" location="24261" name="14029.71c" path="xdata/endf70a" temperature="5.1704e-08" zaid="14029"/>
<ace_table alias="Si-30.71c" awr="29.716" location="26640" name="14030.71c" path="xdata/endf70a" temperature="5.1704e-08" zaid="14030"/>


<!-- Stainless -->
<ace_table alias="C-Nat.71c" awr="11.898" location="8877" name="6000.71c" path="xdata/endf70a" temperature="5.1704e-08" zaid="6000"/>
```

```
<ace_table alias="P-31.71c" awr="30.708" location="28341" name="15031.71c" path="xdata/endf70a" temperature="5.1704e-08" zaid="15031"/>
<ace_table alias="Mn-55.71c" awr="54.4661" location="13668" name="25055.71c" path="xdata/endf70b" temperature="5.1704e-08" zaid="25055"/>
<ace_table alias="Ni-58.71c" awr="57.438" location="33156" name="28058.71c" path="xdata/endf70b" temperature="5.1704e-08" zaid="28058"/>
<ace_table alias="Ni-60.71c" awr="59.416" location="40128" name="28060.71c" path="xdata/endf70b" temperature="5.1704e-08" zaid="28060"/>
<ace_table alias="Ni-61.71c" awr="60.408" location="44085" name="28061.71c" path="xdata/endf70b" temperature="5.1704e-08" zaid="28061"/>
<ace_table alias="Ni-62.71c" awr="61.396" location="46510" name="28062.71c" path="xdata/endf70b" temperature="5.1704e-08" zaid="28062"/>
<ace_table alias="Ni-64.71c" awr="63.379" location="48787" name="28064.71c" path="xdata/endf70b" temperature="5.1704e-08" zaid="28064"/>

<!-- AIC -->
<ace_table alias="Ag-107.71c" awr="105.987" location="54537" name="47107.71c" path="xdata/endf70d" temperature="5.1704e-08" zaid="47107"/>
<ace_table alias="Ag-109.71c" awr="107.969" location="58255" name="47109.71c" path="xdata/endf70d" temperature="5.1704e-08" zaid="47109"/>
<ace_table alias="Cd-106.71c" awr="104.996" location="65734" name="48106.71c" path="xdata/endf70d" temperature="5.1704e-08" zaid="48106"/>
<ace_table alias="Cd-108.71c" awr="106.977" location="67152" name="48108.71c" path="xdata/endf70d" temperature="5.1704e-08" zaid="48108"/>
<ace_table alias="Cd-110.71c" awr="108.959" location="68202" name="48110.71c" path="xdata/endf70d" temperature="5.1704e-08" zaid="48110"/>
<ace_table alias="Cd-111.71c" awr="109.951" location="69792" name="48111.71c" path="xdata/endf70d" temperature="5.1704e-08" zaid="48111"/>
<ace_table alias="Cd-112.71c" awr="110.942" location="71987" name="48112.71c" path="xdata/endf70d" temperature="5.1704e-08" zaid="48112"/>
<ace_table alias="Cd-113.71c" awr="111.930" location="74188" name="48113.71c" path="xdata/endf70d" temperature="5.1704e-08" zaid="48113"/>
<ace_table alias="Cd-114.71c" awr="112.925" location="77638" name="48114.71c" path="xdata/endf70d" temperature="5.1704e-08" zaid="48114"/>
<ace_table alias="Cd-116.71c" awr="114.909" location="80763" name="48116.71c" path="xdata/endf70d" temperature="5.1704e-08" zaid="48116"/>
<ace_table alias="In-113.71c" awr="111.934" location="352" name="49113.71c" path="xdata/endf70e" temperature="5.1704e-08" zaid="49113"/>
<ace_table alias="In-115.71c" awr="113.917" location="2227" name="49115.71c" path="xdata/endf70e" temperature="5.1704e-08" zaid="49115"/>

<!-- B4C: all nuclides included above -->

<!-- WABA -->
<ace_table alias="Al-27.71c" awr="26.74975" location="19280" name="13027.71c" path="xdata/endf70a" temperature="5.1704e-08" zaid="13027"/>

<!-- Gd -->
<ace_table alias="Gd-152.71c" awr="150.615" location="1023" name="64152.71c" path="xdata/endf70h" temperature="5.1704e-08" zaid="64152"/>
<ace_table alias="Gd-153.71c" awr="151.608" location="5390" name="64153.71c" path="xdata/endf70h" temperature="5.1704e-08" zaid="64153"/>
<ace_table alias="Gd-154.71c" awr="152.599" location="9191" name="64154.71c" path="xdata/endf70h" temperature="5.1704e-08" zaid="64154"/>
```

```
  <ace_table alias="Gd-155.71c" awr="153.592" location="14263" name="64155.71c" path="xdata/endf70h" temperature="5.1704e-08" zaid="64155"/>
  <ace_table alias="Gd-156.71c" awr="154.583" location="17531" name="64156.71c" path="xdata/endf70h" temperature="5.1704e-08" zaid="64156"/>
  <ace_table alias="Gd-157.71c" awr="155.576" location="21605" name="64157.71c" path="xdata/endf70h" temperature="5.1704e-08" zaid="64157"/>
  <ace_table alias="Gd-158.71c" awr="156.567" location="25390" name="64158.71c" path="xdata/endf70h" temperature="5.1704e-08" zaid="64158"/>
  <ace_table alias="Gd-160.71c" awr="158.553" location="29431" name="64160.71c" path="xdata/endf70h" temperature="5.1704e-08" zaid="64160"/>

</cross_sections>
```

Listing C.3: NDPP Library Description File

```
<?xml version="1.0"?>
<ndpp_lib>
  <directory> /home/nelsonag/cases/diss/ndpp/47g/  </directory>
  <filetype> binary </filetype>
  <entries> 73  </entries>
  <nuscatter> true </nuscatter>
  <chi_present> true </chi_present>
  <scatt_type> 0 </scatt_type>
  <scatt_order> 2 </scatt_order>
  <print_tol> 1.00000E-10 </print_tol>
  <thin_tol> 1.00000E-07 </thin_tol>
  <mu_bins> 501 </mu_bins>
  <energy_bins>
   0.000000000000E+00   1.239600000000E-08   3.061300000000E-08   4.275500000000E-08
   5.692200000000E-08   8.196800000000E-08   1.115700000000E-07   1.457200000000E-07
   1.844300000000E-07   2.705200000000E-07   3.576700000000E-07   5.032300000000E-07
   6.250600000000E-07   7.820800000000E-07   9.100000000000E-07   9.710000000000E-07
   1.013700000000E-06   1.072200000000E-06   1.125400000000E-06   1.166400000000E-06
   1.235100000000E-06   1.457400000000E-06   1.855400000000E-06   2.382400000000E-06
   3.927900000000E-06   4.450900000000E-06   5.043500000000E-06   5.715000000000E-06
   6.476000000000E-06   7.338200000000E-06   8.315300000000E-06   1.209900000000E-05
   1.371000000000E-05   2.902300000000E-05   4.785100000000E-05   7.889300000000E-05
   1.300700000000E-04   2.034700000000E-03   9.118800000000E-03   6.737900000000E-02
   1.831600000000E-01   4.978700000000E-01   8.208500000000E-01   1.353400000000E+00
   2.231300000000E+00   3.678800000000E+00   6.065300000000E+00   2.000000000000E+01
  </energy_bins>

  <ndpp_table alias="O-16.71c" awr="15.8575" location="1" name="8016.71c" path="8016.71c.g47" temperature="5.17040E-08" zaid="8016" freegas_cutoff="2.06816E-05"/>
  <ndpp_table alias="U-234.71c" awr="232.030" location="1" name="92234.71c" path="92234.71c.g47" temperature="5.17040E-08" zaid="92234" freegas_cutoff="2.06816E-05"/>
  <ndpp_table alias="U-235.71c" awr="233.025" location="1" name="92235.71c" path="92235.71c.g47" temperature="5.17040E-08" zaid="92235" freegas_cutoff="2.06816E-05"/>
  <ndpp_table alias="U-236.71c" awr="234.018" location="1" name="92236.71c" path="92236.71c.g47" temperature="5.17040E-08" zaid="92236" freegas_cutoff="2.06816E-05"/>
  <ndpp_table alias="U-238.71c" awr="236.006" location="1" name="92238.71c" path="92238.71c.g47" temperature="5.17040E-08" zaid="92238" freegas_cutoff="2.06816E-05"/>
  <ndpp_table alias="o2/u.13t" awr="15.8575" location="1" name="o2/u.13t" path="o2-u.13t.g47" temperature="5.17040E-08" zaid="0" freegas_cutoff="-2.00000"/>
```

```
<ndpp_table alias="u/o2.13t" awr="236.006" location="1" name="u/o2.13t" path="u-o2.13t.g47" temperature="5.17040E-08" zaid="0" freegas_cutoff="-2.00000"/>
<ndpp_table alias="He-4.71c" awr="3.96822" location="1" name="2004.71c" path="2004.71c.g47" temperature="5.17040E-08" zaid="2004" freegas_cutoff="2.06816E-05"/>
<ndpp_table alias="Cr-50.71c" awr="49.5170" location="1" name="24050.71c" path="24050.71c.g47" temperature="5.17040E-08" zaid="24050" freegas_cutoff="2.06816E-05"/>
<ndpp_table alias="Cr-52.71c" awr="51.4940" location="1" name="24052.71c" path="24052.71c.g47" temperature="5.17040E-08" zaid="24052" freegas_cutoff="2.06816E-05"/>
<ndpp_table alias="Cr-53.71c" awr="52.4860" location="1" name="24053.71c" path="24053.71c.g47" temperature="5.17040E-08" zaid="24053" freegas_cutoff="2.06816E-05"/>
<ndpp_table alias="Cr-54.71c" awr="53.4760" location="1" name="24054.71c" path="24054.71c.g47" temperature="5.17040E-08" zaid="24054" freegas_cutoff="2.06816E-05"/>
<ndpp_table alias="Fe-54.71c" awr="53.4760" location="1" name="26054.71c" path="26054.71c.g47" temperature="5.17040E-08" zaid="26054" freegas_cutoff="2.06816E-05"/>
<ndpp_table alias="Fe-56.71c" awr="55.4540" location="1" name="26056.71c" path="26056.71c.g47" temperature="5.17040E-08" zaid="26056" freegas_cutoff="2.06816E-05"/>
<ndpp_table alias="Fe-57.71c" awr="56.4460" location="1" name="26057.71c" path="26057.71c.g47" temperature="5.17040E-08" zaid="26057" freegas_cutoff="2.06816E-05"/>
<ndpp_table alias="Fe-58.71c" awr="57.4360" location="1" name="26058.71c" path="26058.71c.g47" temperature="5.17040E-08" zaid="26058" freegas_cutoff="2.06816E-05"/>
<ndpp_table alias="Zr-90.71c" awr="89.1324" location="1" name="40090.71c" path="40090.71c.g47" temperature="5.17040E-08" zaid="40090" freegas_cutoff="2.06816E-05"/>
<ndpp_table alias="Zr-91.71c" awr="90.1247" location="1" name="40091.71c" path="40091.71c.g47" temperature="5.17040E-08" zaid="40091" freegas_cutoff="2.06816E-05"/>
<ndpp_table alias="Zr-92.71c" awr="91.1155" location="1" name="40092.71c" path="40092.71c.g47" temperature="5.17040E-08" zaid="40092" freegas_cutoff="2.06816E-05"/>
<ndpp_table alias="Zr-94.71c" awr="93.0996" location="1" name="40094.71c" path="40094.71c.g47" temperature="5.17040E-08" zaid="40094" freegas_cutoff="2.06816E-05"/>
<ndpp_table alias="Zr-96.71c" awr="95.0844" location="1" name="40096.71c" path="40096.71c.g47" temperature="5.17040E-08" zaid="40096" freegas_cutoff="2.06816E-05"/>
<ndpp_table alias="Sn-112.71c" awr="110.944" location="1" name="50112.71c" path="50112.71c.g47" temperature="5.17040E-08" zaid="50112" freegas_cutoff="2.06816E-05"/>
<ndpp_table alias="Sn-114.71c" awr="112.925" location="1" name="50114.71c" path="50114.71c.g47" temperature="5.17040E-08" zaid="50114" freegas_cutoff="2.06816E-05"/>
<ndpp_table alias="Sn-115.71c" awr="113.916" location="1" name="50115.71c" path="50115.71c.g47" temperature="5.17040E-08" zaid="50115" freegas_cutoff="2.06816E-05"/>
<ndpp_table alias="Sn-116.71c" awr="114.906" location="1" name="50116.71c" path="50116.71c.g47" temperature="5.17040E-08" zaid="50116" freegas_cutoff="2.06816E-05"/>
<ndpp_table alias="Sn-117.71c" awr="115.899" location="1" name="50117.71c" path="50117.71c.g47" temperature="5.17040E-08" zaid="50117" freegas_cutoff="2.06816E-05"/>
<ndpp_table alias="Sn-118.71c" awr="116.889" location="1" name="50118.71c" path="50118.71c.g47" temperature="5.17040E-08" zaid="50118" freegas_cutoff="2.06816E-05"/>
<ndpp_table alias="Sn-119.71c" awr="117.882" location="1" name="50119.71c" path="50119.71c.g47" temperature="5.17040E-08" zaid="50119" freegas_cutoff="2.06816E-05"/>
<ndpp_table alias="Sn-120.71c" awr="118.872" location="1" name="50120.71c" path="50120.71c.g47" temperature="5.17040E-08" zaid="50120" freegas_cutoff="2.06816E-05"/>
<ndpp_table alias="Sn-122.71c" awr="120.856" location="1" name="50122.71c" path="50122.71c.g47" temperature="5.17040E-08" zaid="50122" freegas_cutoff="2.06816E-05"/>
<ndpp_table alias="Sn-124.71c" awr="122.841" location="1" name="50124.71c" path="50124.71c.g47" temperature="5.17040E-08" zaid="50124" freegas_cutoff="2.06816E-05"/>
<ndpp_table alias="Sn-126.71c" awr="124.826" location="1" name="50126.71c" path="50126.71c.g47" temperature="5.17040E-08" zaid="50126" freegas_cutoff="2.06816E-05"/>
<ndpp_table alias="Hf-174.71c" awr="172.446" location="1" name="72174.71c" path="72174.71c.g47" temperature="5.17040E-08" zaid="72174" freegas_cutoff="2.06816E-05"/>
```

```
<ndpp_table alias="Hf-176.71c" awr="174.430" location="1" name="72176.71c" path="72176.71c.g47" temperature="5.17040E-08" zaid="72176" freegas_cutoff="2.06816E-05"/>
<ndpp_table alias="Hf-177.71c" awr="175.423" location="1" name="72177.71c" path="72177.71c.g47" temperature="5.17040E-08" zaid="72177" freegas_cutoff="2.06816E-05"/>
<ndpp_table alias="Hf-178.71c" awr="176.415" location="1" name="72178.71c" path="72178.71c.g47" temperature="5.17040E-08" zaid="72178" freegas_cutoff="2.06816E-05"/>
<ndpp_table alias="Hf-179.71c" awr="177.409" location="1" name="72179.71c" path="72179.71c.g47" temperature="5.17040E-08" zaid="72179" freegas_cutoff="2.06816E-05"/>
<ndpp_table alias="Hf-180.71c" awr="178.401" location="1" name="72180.71c" path="72180.71c.g47" temperature="5.17040E-08" zaid="72180" freegas_cutoff="2.06816E-05"/>
<ndpp_table alias="H-1.71c" awr="0.999167" location="1" name="1001.71c" path="1001.71c.g47" temperature="5.17040E-08" zaid="1001" freegas_cutoff="2.06816E-05"/>
<ndpp_table alias="B-10.71c" awr="9.92692" location="1" name="5010.71c" path="5010.71c.g47" temperature="5.17040E-08" zaid="5010" freegas_cutoff="2.06816E-05"/>
<ndpp_table alias="B-11.71c" awr="10.9147" location="1" name="5011.71c" path="5011.71c.g47" temperature="5.17040E-08" zaid="5011" freegas_cutoff="2.06816E-05"/>
<ndpp_table alias="lwtr.16t" awr="0.999167" location="1" name="lwtr.16t" path="lwtr.16t.g47" temperature="5.17040E-08" zaid="0" freegas_cutoff="-2.00000"/>
<ndpp_table alias="Si-28.71c" awr="27.7370" location="1" name="14028.71c" path="14028.71c.g47" temperature="5.17040E-08" zaid="14028" freegas_cutoff="2.06816E-05"/>
<ndpp_table alias="Si-29.71c" awr="28.7280" location="1" name="14029.71c" path="14029.71c.g47" temperature="5.17040E-08" zaid="14029" freegas_cutoff="2.06816E-05"/>
<ndpp_table alias="Si-30.71c" awr="29.7160" location="1" name="14030.71c" path="14030.71c.g47" temperature="5.17040E-08" zaid="14030" freegas_cutoff="2.06816E-05"/>
<ndpp_table alias="C-Nat.71c" awr="11.8980" location="1" name="6000.71c" path="6000.71c.g47" temperature="5.17040E-08" zaid="6000" freegas_cutoff="2.06816E-05"/>
<ndpp_table alias="P-31.71c" awr="30.7080" location="1" name="15031.71c" path="15031.71c.g47" temperature="5.17040E-08" zaid="15031" freegas_cutoff="2.06816E-05"/>
<ndpp_table alias="Ni-58.71c" awr="57.4380" location="1" name="28058.71c" path="28058.71c.g47" temperature="5.17040E-08" zaid="28058" freegas_cutoff="2.06816E-05"/>
<ndpp_table alias="Ni-60.71c" awr="59.4160" location="1" name="28060.71c" path="28060.71c.g47" temperature="5.17040E-08" zaid="28060" freegas_cutoff="2.06816E-05"/>
<ndpp_table alias="Ni-61.71c" awr="60.4080" location="1" name="28061.71c" path="28061.71c.g47" temperature="5.17040E-08" zaid="28061" freegas_cutoff="2.06816E-05"/>
<ndpp_table alias="Ni-62.71c" awr="61.3960" location="1" name="28062.71c" path="28062.71c.g47" temperature="5.17040E-08" zaid="28062" freegas_cutoff="2.06816E-05"/>
<ndpp_table alias="Ni-64.71c" awr="63.3790" location="1" name="28064.71c" path="28064.71c.g47" temperature="5.17040E-08" zaid="28064" freegas_cutoff="2.06816E-05"/>
<ndpp_table alias="Ag-107.71c" awr="105.987" location="1" name="47107.71c" path="47107.71c.g47" temperature="5.17040E-08" zaid="47107" freegas_cutoff="2.06816E-05"/>
<ndpp_table alias="Ag-109.71c" awr="107.969" location="1" name="47109.71c" path="47109.71c.g47" temperature="5.17040E-08" zaid="47109" freegas_cutoff="2.06816E-05"/>
<ndpp_table alias="Cd-106.71c" awr="104.996" location="1" name="48106.71c" path="48106.71c.g47" temperature="5.17040E-08" zaid="48106" freegas_cutoff="2.06816E-05"/>
<ndpp_table alias="Cd-108.71c" awr="106.977" location="1" name="48108.71c" path="48108.71c.g47" temperature="5.17040E-08" zaid="48108" freegas_cutoff="2.06816E-05"/>
<ndpp_table alias="Cd-110.71c" awr="108.959" location="1" name="48110.71c" path="48110.71c.g47" temperature="5.17040E-08" zaid="48110" freegas_cutoff="2.06816E-05"/>
<ndpp_table alias="Cd-111.71c" awr="109.951" location="1" name="48111.71c" path="48111.71c.g47" temperature="5.17040E-08" zaid="48111" freegas_cutoff="2.06816E-05"/>
<ndpp_table alias="Cd-112.71c" awr="110.942" location="1" name="48112.71c" path="48112.71c.g47" temperature="5.17040E-08" zaid="48112" freegas_cutoff="2.06816E-05"/>
<ndpp_table alias="Cd-113.71c" awr="111.930" location="1" name="48113.71c" path="48113.71c.g47" temperature="5.17040E-08" zaid="48113" freegas_cutoff="2.06816E-05"/>
```

```
  <ndpp_table alias="Cd-114.71c" awr="112.925" location="1" name="48114.71c" path="48114.71c.g47" temperature="5.17040E-08" zaid="48114" freegas_cutoff="2.06816E-05"/>
  <ndpp_table alias="Cd-116.71c" awr="114.909" location="1" name="48116.71c" path="48116.71c.g47" temperature="5.17040E-08" zaid="48116" freegas_cutoff="2.06816E-05"/>
  <ndpp_table alias="In-113.71c" awr="111.934" location="1" name="49113.71c" path="49113.71c.g47" temperature="5.17040E-08" zaid="49113" freegas_cutoff="2.06816E-05"/>
  <ndpp_table alias="In-115.71c" awr="113.917" location="1" name="49115.71c" path="49115.71c.g47" temperature="5.17040E-08" zaid="49115" freegas_cutoff="2.06816E-05"/>
  <ndpp_table alias="Al-27.71c" awr="26.7497" location="1" name="13027.71c" path="13027.71c.g47" temperature="5.17040E-08" zaid="13027" freegas_cutoff="2.06816E-05"/>
  <ndpp_table alias="Gd-152.71c" awr="150.615" location="1" name="64152.71c" path="64152.71c.g47" temperature="5.17040E-08" zaid="64152" freegas_cutoff="2.06816E-05"/>
  <ndpp_table alias="Gd-153.71c" awr="151.608" location="1" name="64153.71c" path="64153.71c.g47" temperature="5.17040E-08" zaid="64153" freegas_cutoff="2.06816E-05"/>
  <ndpp_table alias="Gd-154.71c" awr="152.599" location="1" name="64154.71c" path="64154.71c.g47" temperature="5.17040E-08" zaid="64154" freegas_cutoff="2.06816E-05"/>
  <ndpp_table alias="Gd-155.71c" awr="153.592" location="1" name="64155.71c" path="64155.71c.g47" temperature="5.17040E-08" zaid="64155" freegas_cutoff="2.06816E-05"/>
  <ndpp_table alias="Gd-156.71c" awr="154.583" location="1" name="64156.71c" path="64156.71c.g47" temperature="5.17040E-08" zaid="64156" freegas_cutoff="2.06816E-05"/>
  <ndpp_table alias="Gd-157.71c" awr="155.576" location="1" name="64157.71c" path="64157.71c.g47" temperature="5.17040E-08" zaid="64157" freegas_cutoff="2.06816E-05"/>
  <ndpp_table alias="Gd-158.71c" awr="156.567" location="1" name="64158.71c" path="64158.71c.g47" temperature="5.17040E-08" zaid="64158" freegas_cutoff="2.06816E-05"/>
  <ndpp_table alias="Gd-160.71c" awr="158.553" location="1" name="64160.71c" path="64160.71c.g47" temperature="5.17040E-08" zaid="64160" freegas_cutoff="2.06816E-05"/>
</ndpp_lib>
```

BIBLIOGRAPHY

[1] G. I. BELL and S. GLASSTONE, *Nuclear Reactor Theory*, Van Nostrand Reinhold Company, New York (1970).

[2] E. E. LEWIS AND W. F. MILLER JR., *Computational Methods of Neutron Transport*, American Nuclear Society, Inc., La Grange Park, Illinois, USA (1993).

[3] D. KELLY, T. SUTTON, and S. WILSON, "MC21 analysis of the nuclear energy agency Monte Carlo performance benchmark problem," American Nuclear Society, La Grange Park, IL (Jul 2012).

[4] E. L. REDMOND, *Multigroup Cross Section Generation via Monte Carlo Methods*, Ph.D. thesis, Massachusetts Institute of Technology (June 1997).

[5] J. LEPPÄNEN, "Development of a New Monte Carlo Reactor Physics Code," (2007).

[6] J. E. HOOGENBOOM, V. A. KHOTYLEV, and J. M. THOLAMMAKKIL, "Generation of multi-group cross sections and scattering matrices with the Monte Carlo code MCNP5," in "Joint International Topical Meeting on Mathematics & Computation and Supercomputing in Nuclear Applications (M&C+ SNA 2007), Monterey, California, April 15-19 2007, on CD-ROM," American Nuclear Society, La Grange Park, IL (2007).

[7] K. YOSHIOKA, Y. TAKEUCHI, and T. KITAMURA, "Multi-Group Constants Generation System for 3D-Core Simulation Using a Continuous Energy Monte Carlo Technique," *Progress in nuclear science and technology*, **2**, 334–340 (2011).

[8] M. TOHJOH, M. WATANABE, and A. YAMAMOTO, "Application of Continuous-Energy Monte Carlo Code as a Cross-Section Generator of BWR Core Calculations," *Annals of Nuclear Energy*, **32**, 8, 857–875 (2005).

[9] Y. A. K. YOSHIOKA, "Multigroup Scattering Matrix Generation Method Using Weight-to-Flux Ratio Based on a Continuous Energy Monte Carlo Technique," *Journal of Nuclear Science and Technology*, **47**, 10, 90–916 (2010).

[10] H. J. PARK, H. J. SHIM, H. G. JOO, and C. H. KIM, "Generation of Few-Group Diffusion Theory Constants by Monte Carlo Code McCARD," *Nuclear Science and Engineering*, **172**, 1, 66–77 (2012).

[11] E. FRIDMAN and J. LEPPÄNEN, "On the Use of the Serpent Monte Carlo Code for Few-Group Cross Section Generation," *Annals of Nuclear Energy*, **38**, 6, 1399–1405 (2011).

[12] D. G. CACUCI, *Handbook of Nuclear Engineering: Vol. 1: Nuclear Engineering Fundamentals*, vol. 1, Springer (2010).

[13] A. HÉBERT, *Applied Reactor Physics*, Presses internationales Polytechnique (2009).

[14] G. I. BELL, G. E. HANSEN, and H. A. SANDMEIER, "Multitable Treatments of Anisotropic Scattering in Sn Multigroup Transport Calculations," *Nuclear Science and Engineering*, **28**, 3, 376–383 (1967).

[15] E. A. CHADWICK, M. B., "ENDF/B-VII.1 Nuclear Data for Science and Technology: Cross Sections, Covariances, Fission Product Yields and Decay Data," *Nuclear Data Sheets*, **112**, 2887–2996 (2011).

[16] R. E. MACFARLANE and A. C. KAHLER, "Methods for Processing ENDF/B-VII with NJOY," *Nuclear Data Sheets, Volume 111, Issue 12, p. 2739-2890.*, **111**, 2739–2890 (dec 2010).

[17] P. K. ROMANO and B. FORGET, "The OpenMC Monte Carlo Particle transport code," *Annals of Nuclear Energy*, **51**, 274–281 (2013).

[18] MPACT TEAM, *MPACT Theory Manual, Version 1.0*, University of Michigan, Ann Arbor, Michigan (October 2013).

[19] W. BOYD, S. SHANER, L. LI, B. FORGET, and K. SMITH, "The OpenMOC Method of Characteristics Neutral Particle Transport Code," *Annals of Nuclear Energy*, **68**, 43–52 (2014).

[20] J. K. SHULTIS and R. E. FAW, *Radiation Shielding*, American Nuclear Society, La Grange Park, Il (2000).

[21] M. H. KALOS and P. A. WHITLOCK, *Monte Carlo Methods*, John Wiley & Sons (2008).

[22] R. Y. RUBINSTEIN, *Simulation and the Monte Carlo Method*, Wiley, New York (1981).

[23] X-5 MONTE CARLO TEAM, "MCNP User Manual, Version 5," *LA-UR-03-1987* (February 2008).

[24] D. W. MUIR, R. M. BOICOURT, and A. C. KAHLER, "The NJOY Nuclear Data Processing System, Version 2012," *"LA-UR-12-27079"* (2012).

[25] E. A. CHADWICK, M. B., "ENDF/B-VII.0: Next Generation Evaluated Nuclear Data Library for Nuclear Science and Technology," *Nuclear Data Sheets*, **107**, 2931–3060 (2006).

[26] A. TRKOV, M. HERMAN, and D. A. BROWN, “ENDF-6 Formats Manual,” Tech. rep. (2011).

[27] M. M. R. WILLIAMS, *The Slowing Down and Thermalization of Neutrons*, North-Holland Publishing Company, Amsterdam (1966).

[28] J. DONGARRA and OTHERS, “MPI: A Message-Passing Interface Standard, Version 3.0,” *Message Passing Interface Forum* (2012).

[29] OPENMP ARCHITECTURE REVIEW BOARD, “OpenMP Application Program Interface, v. 3.0,” *OpenMP Architecture Review Board* (2008).

[30] OECD/NEA, “Benchmark on Deterministic Transport Calculations Without Spatial Homogenisation,” Tech. Rep. NEA/NSC/DOC(2003)16, Paris, France (2003).

[31] G. F. KUNCIR, “Algorithm 103: Simpson’s Rule Integrator,” *Communications of the ACM 5*, **6**, 347 (1963).

[32] W. H. PRESS, S. A. TEUKOLSKY, T. W. VETERLING, and B. FLANNERY, “Numerical Recipes 3rd Edition,” *The Art of Scientific Computing* (2007).

[33] R. DAGAN, “On the angular distribution of the ideal gas scattering kernel,” *Annals of Nuclear Energy*, **35**, 6, 1109 (2008).

[34] S. Z. GHRAYEB, M. OUISLOUMEN, A. M. OUGOUAG, and K. N. IVANOV, “Deterministic modeling of higher angular moments of resonant neutron scattering,” *Annals of Nuclear Energy*, **38**, 10, 2291 (2011).

[35] E. E. SUNNY, *On-the-Fly Generation of Differential Resonance Scattering Probability Distribution Functions for Monte Carlo Codes*, Ph.D. thesis, University of Michigan (2013).

[36] R. J. STAMM’LER, *HELIOS Methods (version 1.10)*, Studsvik Scandpower (April 2008).

[37] B. COLLINS, B. KOCHUNAS, AND T. DOWNAR, “Assessment of the 2D MOC Solver in MPACT,” in “International Conference on Mathematics and Computational Methods Applied to Nuclear Science & Engineering (M&C 2013), Sun Valley, Idaho, USA, May 5-9, 2013 on CD-ROM,” American Nuclear Society, La Grange Park, IL (2013).

[38] A. T. GODFREY, “VERA Core Physics Benchmark Progression Problems Specifications,” Tech. rep., Consortium for Advanced Simulation of LWRs, CASL-U-2012-0131-003 (2014), revision 3.